

**Simultaneous Heavy Flavor Fractions
and Top Cross Section Measurement
at the
Collider Detector at Fermilab**

by

Mark J. Mathis

A dissertation submitted to The Johns Hopkins University in conformity with the
requirements for the degree of Doctor of Philosophy.

Baltimore, Maryland

April, 2010

© Mark J. Mathis 2010

All rights reserved

Abstract

This dissertation describes the measurement of the top pair production cross section, using data from proton–antiproton collisions at a center-of-mass energy of 1.96 TeV, with $2.7 \pm 0.2 \text{ fb}^{-1}$ of data collected by the Collider Detector at Fermilab.

Background contributions are measured concurrently with the top cross section in the b -tagged lepton-plus-jets sample using a kinematic fit, which simultaneously determines the cross sections and normalizations of $t\bar{t}$, $W + \text{jets}$, QCD, and electroweak processes. This is the first application of a procedure of this kind.

The top cross section is measured to be $\sigma_{t\bar{t}} = 7.64 \pm 0.57(\text{stat} + \text{syst}) \pm 0.45(\text{lumi}) \text{ pb}$ and the Monte Carlo simulation scale factors $K_{Wb\bar{b}} = 1.57 \pm 0.25$, $K_{Wc\bar{c}} = 0.94 \pm 0.79$, $K_{Wc} = 1.9 \pm 0.3$, and $K_{Wq\bar{q}} = 1.1 \pm 0.3$. These results are consistent with existing measurements using other procedures. More data will reduce the systematic uncertainties and will lead to the most precise of any single analysis to date.

Author: Mark J. Mathis

Advisor: Dr. Petar Maksimović

Acknowledgements

I want to thank my parents and family above all. I would not have been able to make it this far without their love, encouragement, and support. Even if they didn't quite understand what I was doing or why, their support for me was unquestionable and unending, and I cannot thank them enough. I only wish Mom were here to see this.

I would like to thank my sister Tricia for taking time out of her busy schedule to read this entire dissertation, and also for spending more than 12 hours on the phone with me going over her comments in detail. To think what she could have done with more than a few days is mind-boggling!

My advisor Petar Maksimović has taught me so much in these past seven years. Not only did he provide advice on the physics side, but also on the thought processes necessary to succeed as a scientist. I truly would not have made it this far without his patience, his support, and his belief in my success and I thank him greatly for those.

I would also like to thank the physics department staff at Johns Hopkins, who

made sure my paychecks arrived on time, my travel reimbursements were filed properly, and exams were scheduled. Bonnie Bosley, Lonnie Clark, Mike McDonnell, Mark Hall, Connie Fliegel, and Carm King in particular made sure I didn't encounter any problems in an already-hectic graduate student life. The faculty and staff in the physics department, particularly the experimental high energy group, have provided me with valuable advice which I'm grateful for.

I would not have all of the great data to perform this analysis without the hard work of many people at Fermilab. The staff, scientists, and engineers who keep the accelerator and CDF running at such high intensities and high efficiencies deserve a special thanks. I'd also like to thank Jen Pursley, who helped me learn the ropes at Fermilab when I moved out there, as well as offered valuable advice about subjects as varied as ROOT, silicon power supplies, and writing a dissertation. I thank Satyajit Behari for taking care of the silicon power supplies until I could get out to Fermilab and for providing expert knowledge about them — and about many other subjects — when I needed it.

Charles Plager and Andrew Ivanov provided immense support in the analysis, and I wouldn't have finished it without their help. I asked them question after question, and they patiently gave me answer after answer, and for that I thank them. The rest of the Method III team —in particular, Sal Rappoccio, Gavril Giurgiu, and Tom Schwarz — have provided numerous comments and advice to improve my talks and the CDFNote.

I thank Dee Hahn and the CDF QLC committee for happy hour on Fridays (and homemade salsa!). The Fermilab GSA provided much needed breaks for pub nights and summer BBQs, and the Fermi Ultimate team gave a not-so-needed excuse to get out of the trailers and into the sun.

My friends at both Hopkins and Fermilab provided much needed moral support. Greg, Jenny, Tim, Kendrah, Lynn, Derek, Nate, Grimey, Kylea, Ken, Amelia, John, Sarah!, Sarah, Mika, Zeynep, Tim, Joe, Homer, Warren, Kristi, Carrie, Carley, Craig, Nicole, and Karaoke Dave and Sandy have kept me sane throughout graduate school. The best parties were always at 2934 (physicists know how to party!), something I missed after moving out to Illinois.

I must thank the Academy, because ... well, because it's the Academy. Can you accept anything without thanking the Academy?

Lastly, but certainly not leastly, I want to thank Michelle. Her love, support, patience, and encouragement have made this last year and a half wonderful, despite the pressure of finishing this analysis and writing this dissertation.

Contents

Abstract	ii
Acknowledgements	iii
List of Tables	x
List of Figures	xii
1 Overview of the Standard Model of Particle Interactions	1
1.1 Quantum Electrodynamics	3
1.2 Quantum Chromodynamics	6
1.3 The Weak Force and Electroweak Symmetry Breaking	9
1.3.1 The Higgs Mechanism	11
1.4 Beyond the Standard Model	15
2 $t\bar{t}$ Production at the Tevatron	18
2.1 Top Quarks at the Tevatron	20

2.1.1	Top Production	22
2.1.2	Top Decay	24
2.2	Measuring the Cross Section	26
3	Experimental Apparatus	28
3.1	The Tevatron	28
3.1.1	Proton Source, Preacceleration, and the Linac	29
3.1.2	Booster, Main Injector, Accumulator, and Recycler	31
3.1.3	Tevatron Collider	32
3.2	The Collider Detector at Fermilab	33
3.2.1	Silicon System	36
3.2.2	Central Outer Tracker	38
3.2.3	Calorimeters	39
3.2.4	Muon Chambers and Scintillators	40
3.2.5	Time of Flight	41
3.2.6	Cerenkov Luminosity Counters	42
3.2.7	Trigger System	43
4	Introduction to the Measurement	49
5	Event Selection	59
6	Signal and Background Modeling	63

6.1	W + Heavy Flavor	65
6.2	W + Light Flavor	65
6.3	QCD	66
6.4	Other Electroweak Processes	68
6.5	Mistags	68
7	Fitter	69
7.1	Treatment of Systematic Effects	70
7.2	Preparing for the Fit	73
7.3	Pseudoexperiments	76
8	Systematic Uncertainties	99
8.1	Initial- and Final-State Radiation	100
8.2	Jet Energy Scale	101
8.3	Q^2 Energy Scale	102
8.4	b -tag Scale Factor	103
8.5	Mistag Rate	103
8.6	Parton Showering	104
8.7	QCD Shape	105
8.8	KIT Flavor Separator	105
8.9	Parton Distribution Functions	106
8.10	Luminosity	106

9 Results	107
9.1 Kinematic Validation Plots	113
10 Conclusions and Outlook	181
A Trigger Paths	184
B Analysis Appendices	186
B.1 Monte Carlo Simulation Parameters	186
B.2 Monte Carlo Simulation Data-sets	189
B.3 Building and Using the Fitter	197
B.4 Fitter PolyNoids	198
Glossary	226
Bibliography	229
Vita	236

List of Tables

3.1	Summary of basic specifications for L00, SVX, and ISL subsystems. . .	38
5.1	Information about the data-sets used in this analysis	60
5.2	Lepton-plus-jets selection criteria	60
5.3	Event selection and QCD veto	62
5.4	Event acceptances for each sample requiring tight tags	62
6.1	Values of lepton ID and trigger efficiency	64
6.2	Values of the QCD scale factors	67
7.1	The parameters included in the fit	76
9.1	Fit results	108
9.2	Correlation matrix of floating fit parameters	111
9.3	Comparison of uncertainties	112
B.1	ALPGEN parameters used	187
B.2	PYTHIA parameters used	188
B.3	Data-set details for Monte Carlo simulation samples	189
B.4	Data-set details for Monte Carlo simulation samples	190
B.5	Data-set details for Monte Carlo simulation samples	191
B.6	Data-set details for Monte Carlo simulation samples	192
B.7	Data-set details for Monte Carlo simulation samples	192
B.8	Data-set details for Monte Carlo simulation samples	193
B.9	Data-set details for Monte Carlo simulation samples	194
B.10	Data-set details for Monte Carlo simulation samples	195
B.11	Data-set details for Monte Carlo simulation samples	196
B.12	Functional form describing the b -tag scale factor uncertainty	216
B.13	Functional form describing the Mistag rate uncertainty	217
B.14	Functional form describing the JES uncertainty	220
B.15	Functional form describing the Q^2 uncertainty	223

B.16 Functional form describing the I/FSR uncertainty	225
---	-----

List of Figures

1.1	The classifications of the different particles in the Standard Model. . .	4
1.2	Example Feynman diagram	6
1.3	Visual representations of the Higgs potential	12
1.4	Corrections to the W and Z boson masses	14
1.5	Higgs exclusions	16
2.1	Top pair quark production modes	21
2.2	Parton distribution functions	23
2.3	W boson decay modes	25
2.4	Lepton-plus-jets channel	26
3.1	Aerial view of the Tevatron accelerator	29
3.2	Schematic of the Tevatron collider chain	30
3.3	Schematic of the CDF detector	34
3.4	Schematic of the inner tracking components of CDF	35
3.5	Views of the silicon system at CDF	36
3.6	Block diagram of the first two levels of the trigger system at CDF . .	44
4.1	Cartoon of jet flavor vs n_{jet} for different samples	51
4.2	Sample output of the KIT Flavor Separator	52
4.3	Cartoon illustrating the effects of top cross section and tagging efficiency	53
4.4	KIT Flavor Separator in the 1-jet 1-tag bin	54
4.5	KIT Flavor Separator in the 4-jet 1-tag bin	55
4.6	KIT Flavor Separator in the 4-jet 2-tag bin	56
4.7	Complete set of templates	57
4.8	Complete set of templates projected onto the n_{jet} distribution	58
6.1	Fit of the missing transverse energy distribution to data	67
7.1	Functional forms of the template normalizations as different parameters are shifted	72

7.2	Generated values from pseudoexperiments	78
7.3	Generated values from pseudoexperiments	79
7.4	Generated values from pseudoexperiments	80
7.5	Generated values from pseudoexperiments	81
7.6	Generated values from pseudoexperiments	82
7.7	Generated values from pseudoexperiments	83
7.8	Generated values from pseudoexperiments	84
7.9	Expected errors from pseudoexperiments	85
7.10	Expected errors from pseudoexperiments	86
7.11	Expected errors from pseudoexperiments	87
7.12	Expected errors from pseudoexperiments	88
7.13	Expected errors from pseudoexperiments	89
7.14	Expected errors from pseudoexperiments	90
7.15	Expected errors from pseudoexperiments	91
7.16	Pull distributions from pseudoexperiments	92
7.17	Pull distributions from pseudoexperiments	93
7.18	Pull distributions from pseudoexperiments	94
7.19	Pull distributions from pseudoexperiments	95
7.20	Pull distributions from pseudoexperiments	96
7.21	Pull distributions from pseudoexperiments	97
7.22	Pull distributions from pseudoexperiments	98
9.1	Templates after being fit to the data	109
9.2	Templates after being fit to the data, projected onto the n_{jet} distribution	110
9.3	Kinematic plots of the missing transverse energy	114
9.4	Kinematic plots of the missing transverse energy	115
9.5	Kinematic plots of the missing transverse energy	116
9.6	Kinematic plots of the missing transverse energy	117
9.7	Kinematic plots of the missing transverse energy	118
9.8	Kinematic plots of the total transverse energy in the event	119
9.9	Kinematic plots of the total transverse energy in the event	120
9.10	Kinematic plots of the total transverse energy in the event	121
9.11	Kinematic plots of the total transverse energy in the event	122
9.12	Kinematic plots of the total transverse energy in the event	123
9.13	Kinematic plots of the transverse mass of the W	124
9.14	Kinematic plots of the transverse mass of the W	125
9.15	Kinematic plots of the transverse mass of the W	126
9.16	Kinematic plots of the transverse mass of the W	127
9.17	Kinematic plots of the transverse mass of the W	128
9.18	Kinematic plots of the transverse momentum of the lepton	129
9.19	Kinematic plots of the transverse momentum of the lepton	130
9.20	Kinematic plots of the transverse momentum of the lepton	131

9.21	Kinematic plots of the transverse momentum of the lepton	132
9.22	Kinematic plots of the transverse momentum of the lepton	133
9.23	Kinematic plots of the pseudorapidity of the lepton	134
9.24	Kinematic plots of the pseudorapidity of the lepton	135
9.25	Kinematic plots of the pseudorapidity of the lepton	136
9.26	Kinematic plots of the pseudorapidity of the lepton	137
9.27	Kinematic plots of the pseudorapidity of the lepton	138
9.28	Kinematic plots of the transverse energy of the leading jet	139
9.29	Kinematic plots of the transverse energy of the leading jet	140
9.30	Kinematic plots of the transverse energy of the leading jet	141
9.31	Kinematic plots of the transverse energy of the leading jet	142
9.32	Kinematic plots of the transverse energy of the leading jet	143
9.33	Kinematic plots of the pseudorapidity of the leading jet	144
9.34	Kinematic plots of the pseudorapidity of the leading jet	145
9.35	Kinematic plots of the pseudorapidity of the leading jet	146
9.36	Kinematic plots of the pseudorapidity of the leading jet	147
9.37	Kinematic plots of the pseudorapidity of the leading jet	148
9.38	Kinematic plots of the transverse energy of the secondary jet	149
9.39	Kinematic plots of the transverse energy of the secondary jet	150
9.40	Kinematic plots of the transverse energy of the secondary jet	151
9.41	Kinematic plots of the transverse energy of the secondary jet	152
9.42	Kinematic plots of the pseudorapidity of the secondary jet	153
9.43	Kinematic plots of the pseudorapidity of the secondary jet	154
9.44	Kinematic plots of the pseudorapidity of the secondary jet	155
9.45	Kinematic plots of the pseudorapidity of the secondary jet	156
9.46	Kinematic plots of the transverse energy of the leading tagged jet . .	157
9.47	Kinematic plots of the transverse energy of the leading tagged jet . .	158
9.48	Kinematic plots of the transverse energy of the leading tagged jet . .	159
9.49	Kinematic plots of the transverse energy of the leading tagged jet . .	160
9.50	Kinematic plots of the transverse energy of the leading tagged jet . .	161
9.51	Kinematic plots of the pseudorapidity of the leading tagged jet	162
9.52	Kinematic plots of the pseudorapidity of the leading tagged jet	163
9.53	Kinematic plots of the pseudorapidity of the leading tagged jet	164
9.54	Kinematic plots of the pseudorapidity of the leading tagged jet	165
9.55	Kinematic plots of the pseudorapidity of the leading tagged jet	166
9.56	Kinematic plots of the transverse energy of the secondary tagged jet .	167
9.57	Kinematic plots of the transverse energy of the secondary tagged jet .	168
9.58	Kinematic plots of the $ \eta $ of the secondary tagged jet	169
9.59	Kinematic plots of the $ \eta $ of the secondary tagged jet	170
9.60	Kinematic plots of the secondary vertex mass in the leading tagged jet	171
9.61	Kinematic plots of the secondary vertex mass in the leading tagged jet	172
9.62	Kinematic plots of the secondary vertex mass in the leading tagged jet	173

9.63	Kinematic plots of the secondary vertex mass in the leading tagged jet	174
9.64	Kinematic plots of the secondary vertex mass in the leading tagged jet	175
9.65	Kinematic plots of the displacement of the leading tagged jet	176
9.66	Kinematic plots of the displacement of the leading tagged jet	177
9.67	Kinematic plots of the displacement of the leading tagged jet	178
9.68	Kinematic plots of the displacement of the leading tagged jet	179
9.69	Kinematic plots of the displacement of the leading tagged jet	180
10.1	Expected uncertainties with additional data	182
B.1	Function parameterizing the form of the Btag uncertainty	199
B.2	Function parameterizing the form of the Btag uncertainty	200
B.3	Function parameterizing the form of the Btag uncertainty	201
B.4	Function parameterizing the form of the Btag uncertainty	202
B.5	Function parameterizing the form of the Btag uncertainty	203
B.6	Function parameterizing the form of the Mistag uncertainty	204
B.7	Function parameterizing the form of the Mistag uncertainty	205
B.8	Function parameterizing the form of the Mistag uncertainty	206
B.9	Function parameterizing the form of the Mistag uncertainty	207
B.10	Function parameterizing the form of the Mistag uncertainty	208
B.11	Function parameterizing the form of the Mistag uncertainty	209
B.12	Function parameterizing the form of the Jet Energy Scale uncertainty	210
B.13	Function parameterizing the form of the Jet Energy Scale uncertainty	211
B.14	Function parameterizing the form of the Jet Energy Scale uncertainty	212
B.15	Function parameterizing the form of the Q^2 energy scale uncertainty .	213
B.16	Function parameterizing the form of the Jet Energy Scale uncertainty	214
B.17	Function parameterizing the form of the I/FSR uncertainty	215

Chapter 1

Overview of the Standard Model of Particle Interactions

The universe consists of a vast number of matter particles that interact with each other via a small number of force-carrying particles. These particles can be divided into two major groups based on their spin - *fermions*, which have half-integer spin, and *bosons*, which have integer spin. All force-carrying particles are bosons, while the other elementary particles are fermions.

The Standard Model (SM) of high-energy physics is a theoretical description of the interactions between all of those particles. There are four known forces in nature — electromagnetic, strong nuclear (also referred to as strong), weak nuclear (also referred to as weak), and gravitational — but only the first three are included in the SM. The gravitational force is the weakest by many orders of magnitude and

although many attempts have been made to include it in the SM, none have been verified experimentally.

Each force in the SM is associated with at least one boson particle. The electromagnetic force is felt by all electrically charged particles, and is mediated by the massless *photon* (γ). The strong nuclear force is mediated by eight massless bosons called *gluons* (g) and is only felt by particles which carry *color charge* (see Chapter 1.2). The weak nuclear force is carried by three massive bosons¹, the W^+ , W^- , and the Z^0 . All fermions are affected by the weak force.

The elementary building blocks of matter are all fermions and can be subdivided into two groups: *leptons* and *quarks*. Leptons can exist in isolation, while quarks cannot due to a property of the strong force (see Chapter 1.2). This property means quarks must bind with other quarks to form composite particles called *hadrons*. The proton (p , composed of $u u d$) is an example of such a particle.

Each subgroup of fermions can be assembled into three sets of doublets, leading to six quarks (referred to as *flavors* of quarks) and six leptons. A quark doublet can be paired with a lepton doublet to form a *generation* of fermions. The Standard Model particle classifications are shown in Figure 1.1. The first generation of fermions, comprised of the *up* quark (u), the *down* quark (d), the *electron* (e), and the *electron neutrino* (ν_e), makes up most of the everyday matter one sees. The other generations of fermions, as well as anti-particles, typically form unstable particles that quickly

¹For the rest of this dissertation, I will refer to these bosons simply as W or Z unless necessary.

decay.

For every particle shown in Figure 1.1, there is a corresponding *anti-particle*, which has the same mass but opposite quantum numbers (e.g., charge). Any particle and anti-particle pair can be pair-produced if there is enough energy available. Anti-particles are denoted by a bar over the symbol name, (e.g., \bar{q} , pronounced “q bar”).

The theories which describe the interactions in the Standard Model are explained in the next sections.

1.1 Quantum Electrodynamics

Quantum Electrodynamics (QED) is the relativistic quantum field theory describing the electromagnetic interaction [1]. The theory applies to interactions involving all charged particles.

Calculations in QED depend on calculating the probability of the interaction happening, $P = |\mathcal{M}|^2$, where \mathcal{M} is called the quantum-mechanical amplitude. This amplitude is determined by examining all of the possible ways the initial and final states “connect” to each other, and summing the contribution from each connection. It turns out, however, that there are an infinite number of ways for the initial state to connect to the final state, and so the amplitude becomes an infinite sum.

Each connection (that is, each term in the infinite sum) can be categorized by the number of vertices it contains. A vertex is the point of interaction between a force-carrying boson and another particle (including another force-carrying boson, if

Three Generations of Matter (Fermions)				
	I	II	III	
mass→	2.4 MeV	1.27 GeV	171.2 GeV	0
charge→	$\frac{2}{3}$	$\frac{2}{3}$	$\frac{2}{3}$	0
spin→	$\frac{1}{2}$	$\frac{1}{2}$	$\frac{1}{2}$	1
name→	u up	c charm	t top	γ photon
Quarks	4.8 MeV $-\frac{1}{3}$ $\frac{1}{2}$ d down	104 MeV $-\frac{1}{3}$ $\frac{1}{2}$ s strange	4.2 GeV $-\frac{1}{3}$ $\frac{1}{2}$ b bottom	0 0 1 g gluon
	<2.2 eV 0 $\frac{1}{2}$ ν_e electron neutrino	<0.17 MeV 0 $\frac{1}{2}$ ν_μ muon neutrino	<15.5 MeV 0 $\frac{1}{2}$ ν_τ tau neutrino	91.2 GeV 0 1 Z weak force
	0.511 MeV -1 $\frac{1}{2}$ e electron	105.7 MeV -1 $\frac{1}{2}$ μ muon	1.777 GeV -1 $\frac{1}{2}$ τ tau	80.4 GeV ± 1 1 W weak force
Leptons				Bosons (Forces)

Figure 1.1: Diagram showing the classifications of the different particles in the Standard Model. The six quarks are shown in purple, leptons in green, and bosons in red. The first generation of fermions is shown in the left-most column, the second in the next column, and the third generation in the column to the left of the bosons. The charge, spin, and approximate masses of each particle are labeled. Note the extremely large mass of the top quark compared to the masses of the other quarks. [Image used with permission from Wikimedia Commons]

allowed). The connection(s) with the fewest vertices needed to describe the process is (are) referred to as the leading-order terms. Those with the next fewest vertices describe the next-to-leading order, et cetera.

Each vertex contributes to the quantum-mechanical amplitude a term proportional to the *coupling constant*, α , which is a measure of the strength of the interaction. Thus, the amplitude can be expanded as a sum in powers of α . Luckily, the coupling constant in QED is small

$$\alpha_{EW} = \frac{ke^2}{\hbar c} \sim \frac{1}{137} \quad (1.1)$$

making it possible to calculate the amplitude perturbatively. The smallness of the coupling constant means that the infinite sum converges rapidly and one only needs to consider the leading-order terms of a process.

Processes in the QED (and, for that matter, in the Standard Model as a whole) can be very complex, involving several initial state particles, multiple interactions, and several final state particles. The complexity is easier to understand by examining a *Feynman diagram* - a visual representation of one term in the infinite sum of the quantum-mechanical amplitude. Figure 1.2 shows an example of such a diagram. Lines represent particles, and each point, or *vertex*, represents an interaction between particles.

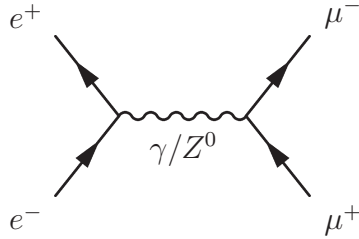


Figure 1.2: Example of a Feynman diagram. Time is on the horizontal axis and flows from left to right. Space is on the vertical axis. Note that these diagrams do not depict the actual scale of the process, but rather the overall evolution in phase space.

1.2 Quantum Chromodynamics

Like QED, Quantum Chromodynamics (QCD) [2] is a relativistic quantum field theory, although QCD possesses an $SU(3)$ symmetry. QCD describes the interaction of particles via the strong nuclear force. Particles that interact via the strong force carry *color* (or *color charge*), similar to the electric charge of the electromagnetic interaction. The discovery of the Δ^{++} baryon [3], which consists of three up quarks with parallel spins, seems to violate the Pauli exclusion principle. However, if each up quark has a different value of a new, “hidden,” quantum number, the exclusion principle remained intact; this new quantum number was called *color*. Quarks can be colored red, green, or blue, while anti-quarks are colored cyan, magenta, and yellow (in other words anti-red, anti-green, or anti-blue). These colors are arbitrary choices, and are not indicators of what one would actually see.

Unlike for QED, the coupling constant for QCD, α_s , is close to unity at low energy, making perturbative calculations impossible. There is no guarantee that the next-to-leading order terms will be smaller than the leading-order ones, allowing them to

be safely ignored, as there was in QED. This makes calculations in QCD extremely difficult at low energy.

Fortunately, the coupling constant decreases with increasing energy, allowing for calculations under certain assumptions and conditions — namely, those with large momentum transfer, $|q^2|$. This behavior of the coupling constant is known as *asymptotic freedom* [4][5].

The coupling constant is described [6] by

$$\alpha_s(|q^2|) = \frac{\alpha_s(\mu^2)}{1 + (\alpha_s(\mu^2)/12\pi)(11n - 2f)\log(|q^2|/\mu^2)} \quad (1.2)$$

where n is the number of colors (three in the Standard Model), f is the number of quark flavors (six in the Standard Model), and μ is an arbitrary cutoff of the integral, which diverges at low energy.

Equation 1.2 is only valid when $|q^2| \gg \mu^2$. One can introduce a parameter Λ_{QCD}

$$\Lambda_{\text{QCD}} = \mu^2 \exp \frac{-12\pi}{(11n - 2f)\alpha_s(\mu^2)} \quad (1.3)$$

such that Equation 1.2 becomes

$$\alpha_s(|q^2|) = \frac{12\pi}{(11n - 2f)\log(|q^2|/\Lambda_{\text{QCD}}^2)}. \quad (1.4)$$

The parameter Λ_{QCD} is the scale at which α_s becomes large, and is also called the *renormalization scale*. For interactions when $|q^2| \gg \Lambda_{\text{QCD}}^2$, the coupling constant is small and a perturbative approach can be used as in QED. The Λ_{QCD} is not predicted by QCD, but experiments find it to be on the order of 100–500 MeV.

The asymptotic freedom of quarks due to the behavior of the strong coupling constant leads to a unique property of quarks called *confinement*. Quarks do not exist in isolation like leptons do; rather, they must be bound with other quarks. Distance is inversely proportional to the energy scale (or momentum transfer), and so as the distance between two quarks increases, the coupling constant increases, keeping the quarks bound together. At small distances, however, the coupling is weak and so the quarks behave as if they were free.

A quark and an anti-quark bind together to form a *meson*, while three quarks form a *baryon*. These two types of bound states are collectively called *hadrons*. A hadron must be “color neutral.” For example, the quark and anti-quark in a meson must be a color/anti-color pair, and the three quarks in a baryon must each carry a different color.

If the quarks in a hadron become too distanced from each other — which requires a lot of energy, due to the coupling constant increasing — a quark and anti-quark can spontaneously pair-produce. This leads to one hadron turning into two hadrons. At sufficiently high energy, this happens many times, in a process called *hadronization*. An exception is the top quark, which decays before it can hadronize (see Chapter 2.1.2).

When a quark of sufficiently high energy hadronizes, the resulting hadrons spray outward in a cone, and are collectively called a *jet*. The higher the energy of the quark (and thus, the sum energy of all the hadrons in the jet), the narrower and more

defined the cone will be. The sum of the energy (momenta) of all the particles in a jet is equal to the initial energy (momentum) of the hadronizing quark. A jet is named by the flavor of the initial quark, e.g., u -jet or b -jet.

The strong coupling of QCD at low energies leads to an effect, when considering an interaction, known as *initial- and final-state radiation* (I/FSR). A particle can radiate a massless boson (gluon or photon) at any time; if this happens before the interaction, it's referred to as initial state radiation (ISR), while if it happens after, it's final state radiation (FSR). Neither ISR nor FSR is a large effect in QED due to the small coupling constant; however, in QCD, the coupling constant is large at low energies, making I/FSR a noticeable effect. The models that describe these radiative processes are not known with a great deal of certainty, and thus must be taken into account as a systematic effect in any analysis.

1.3 The Weak Force and Electroweak Symmetry Breaking

Fermions can interact via the weak force by exchanging massive bosons — that is, the charged W bosons or the neutral Z boson. These bosons interact with varying strengths that depend on a property called *chirality*. Chirality is a measure of whether or not the particle can be superimposed on its mirror image. The wave function of a particle can be written as the sum of left-handed and right-handed chiral parts.

The W bosons couple only to the left-handed chiral component of the fermion's wave function, while the Z couples to both components with different strengths for each.

Flavor change — that is, change from one quark type to another — is possible only through weak interactions. The W generally interacts with two quarks from the same generation, although it is possible to have cross-generation interactions. Indeed, the weak force has quark eigenstates that differ slightly from the mass eigenstates. An *eigenstate* is a state whose solution to the Hamiltonian (or Lagrangian) is a scalar multiple of the state, e.g.,

$$\hat{H}\psi = E\psi \tag{1.5}$$

It is possible to transform from one set of eigenstates to the other; this transformation is described by the complex *Cabibbo-Kobayashi-Maskawa (CKM) matrix* shown below.

$$\begin{pmatrix} d' \\ s' \\ b' \end{pmatrix} = \begin{pmatrix} V_{ud} & V_{us} & V_{ub} \\ V_{cd} & V_{cs} & V_{cb} \\ V_{td} & V_{ts} & V_{tb} \end{pmatrix} \cdot \begin{pmatrix} d \\ s \\ b \end{pmatrix} \tag{1.6}$$

The CKM matrix, by convention, is a complex 3x3 unitary matrix, which operates on the mass eigenstates. Each parameter V_{xy} describes the coupling strength of quark x and quark y to the W boson. Each of these elements of the CKM matrix is a theoretically unconstrained parameter that must be measured experimentally. The current experimental values [3] of the CKM matrix element magnitudes are measured as

$$V_{CKM} = \begin{pmatrix} 0.97419 \pm 0.00022 & 0.2257 \pm 0.0010 & 0.00359 \pm 0.00016 \\ 0.2256 \pm 0.0010 & 0.97334 \pm 0.00023 & 0.0415^{+0.0010}_{-0.0011} \\ 0.00874^{+0.00026}_{-0.00037} & 0.0407 \pm 0.0010 & 0.999133^{+0.000044}_{-0.000043} \end{pmatrix} \quad (1.7)$$

At high energies, the electromagnetic force and the weak nuclear force can be described in the Standard Model as manifestations of the same force, termed the *electroweak force*. However, this “symmetric” description would require the bosons associated with those forces — the photon, W bosons, and the Z boson — to be massless, which is not the case since the W and Z bosons are quite massive. Thus the symmetry between the electromagnetic and the weak force must be broken.

Peter Higgs postulated another boson (later called the *Higgs boson*) which would break electroweak symmetry [7]. Higgs found that the introduction of a complex doublet of gauge bosons, which carries four degrees of freedom, would break the symmetry without disturbing the underlying theory. Three degrees of freedom form the masses of the W and Z bosons, while the fourth gives mass to the Higgs boson itself.

1.3.1 The Higgs Mechanism

As stated above, the Higgs is a mechanism that provides the heavy bosons with mass. This is done through the introduction of a doublet of gauge bosons

$$\phi = \begin{pmatrix} \phi^+ \\ \phi^0 \end{pmatrix} \quad (1.8)$$

with the associated Lagrangian

$$\mathcal{L} = \frac{1}{2}(D_\mu\phi)^\dagger(D^\mu\phi) + \frac{1}{2}\mu^2(\phi^\dagger\phi) - \frac{1}{4}\lambda^2(\phi^\dagger\phi)^2 \quad (1.9)$$

where D_μ is the covariant derivative, and the dagger symbol, \dagger , denotes the Hermitian conjugate.

A visual representation of this potential is shown in Figure 1.3(a). As one can see in Figure 1.3(b), which is a projection of the potential around the z -axis, the minimum of the potential is located at a non-zero value of ϕ . The minimum is referred to as the *vacuum expectation value*, v , and is given by

$$v = \frac{\mu}{\lambda} = 246 \text{ GeV} \quad (1.10)$$

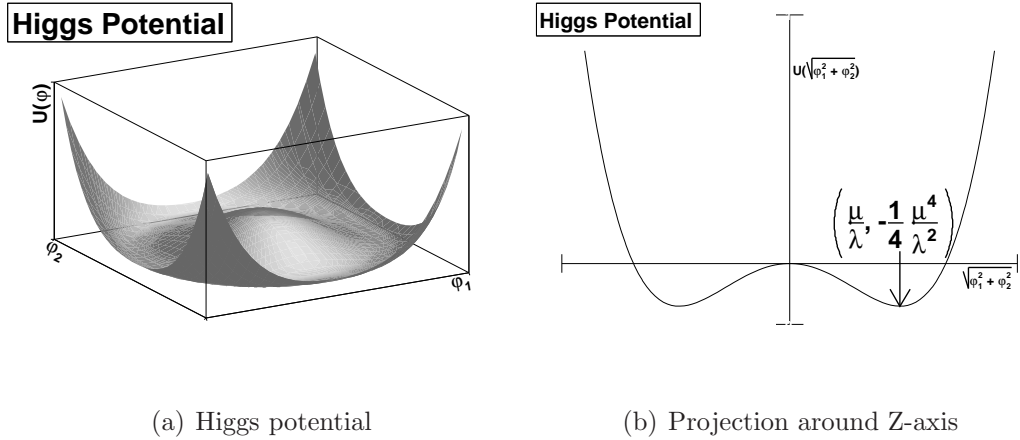


Figure 1.3: Visual representations of the Higgs potential. Note that the minimum value of the potential is located at a non-zero value of ϕ . [Images courtesy of S. Rappoccio]

It turns out it is also necessary to use the Higgs to provide the fermions with mass. Without a Higgs, gauge symmetry requires all fermion masses to be zero, which is

not what is observed. Each fermion, f , has a term added to the Lagrangian

$$\mathcal{L} = -\frac{1}{\sqrt{2}}\lambda_f H f \bar{f} \quad (1.11)$$

where λ_f , called *Yukawa couplings*, are unconstrained. Since the coupling is related to the mass of the fermion, the mass is unconstrained in the theory as well. The top quark has a large Yukawa coupling, and is given by

$$\lambda_t = \frac{v}{\sqrt{2}}m_t \quad (1.12)$$

Assuming a top mass of $175 \text{ GeV}/c^2$, $\lambda_t = 0.99$. This unusually high coupling could indicate that the top quark plays a more important role than the other quarks. The top quark also couples very strongly to the Higgs, and can be used to constrain the Higgs mass. It is thus necessary to understand all of the top quark's properties.

The top quark contributes to the mass of the W and Z bosons via loop diagrams, while the Higgs contributes via radiative corrections; both effects are shown in Figure 1.4. Figures 1.4(a) and 1.4(b) show the loop corrections for the W and Z bosons, respectively, while Figures 1.4(c) and 1.4(d) show the radiative corrections.

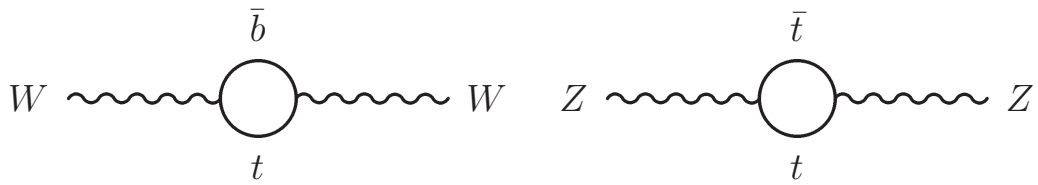
One can define a ratio, ρ , of the W and Z masses as

$$\rho \equiv \frac{m_W^2}{m_Z^2}(1 - \sin^2 \theta_W) = 1 + \Delta r. \quad (1.13)$$

Δr is the radiative correction and is given by

$$\Delta r = \frac{3G_F}{8\pi^2\sqrt{s}}m_t^2 + \frac{\sqrt{2}G_F}{16\pi^2}m_W^2 \left[\frac{11}{3} \log \left(\frac{m_H^2}{m_W^2} \right) \right]. \quad (1.14)$$

where G_F is the Fermi constant and \sqrt{s} is the center-of-mass energy.



(a) Loop correction to the W mass

(b) Loop correction to the Z mass



(c) Radiative correction to the W mass

(d) Radiative correction to the Z mass

Figure 1.4: Feynman diagrams showing the corrections to the W and Z boson masses. Panels (a) and (b) are corrections involving the top quark and Panels (c) and (d) show corrections via the Higgs boson.

Simultaneously measuring $\sin \theta_W$ and the masses of the top quark, W boson, and Z boson thus yields an indirect measurement of the Higgs mass. The uncertainty is dominated by the W and top masses, and so one can consider the other parameters fixed as an approximation. One can then look at the Higgs mass primarily as a function of both the W boson and top quark masses, as shown in Figure 1.5, and indirectly exclude masses of the Higgs boson, providing additional motivation for understanding all of the properties of the top quark.

1.4 Beyond the Standard Model

The Standard Model is one of the most successful theories in physics. It has been tested and verified over the course of half a century with no discrepancies. The charm quark, top quark, gluon, W boson, and Z boson were all predicted by the Standard Model before they were discovered. The measured mass of the W boson agrees with the Standard Model prediction to within 0.01%, and the measured Z mass agreement is almost 100 times better.

Given all of its successes, however, it is important to note its shortcomings. Almost three-quarters of the universe is comprised of dark energy, and another quarter is dark matter — the Standard Model only describes the 4% of visible matter. In the Standard Model, neutrinos are massless, though recent observations of neutrino oscillations require that they have a non-zero mass. The Standard Model prefers a light Higgs boson, but to date, it hasn't been discovered. Even though it is a very

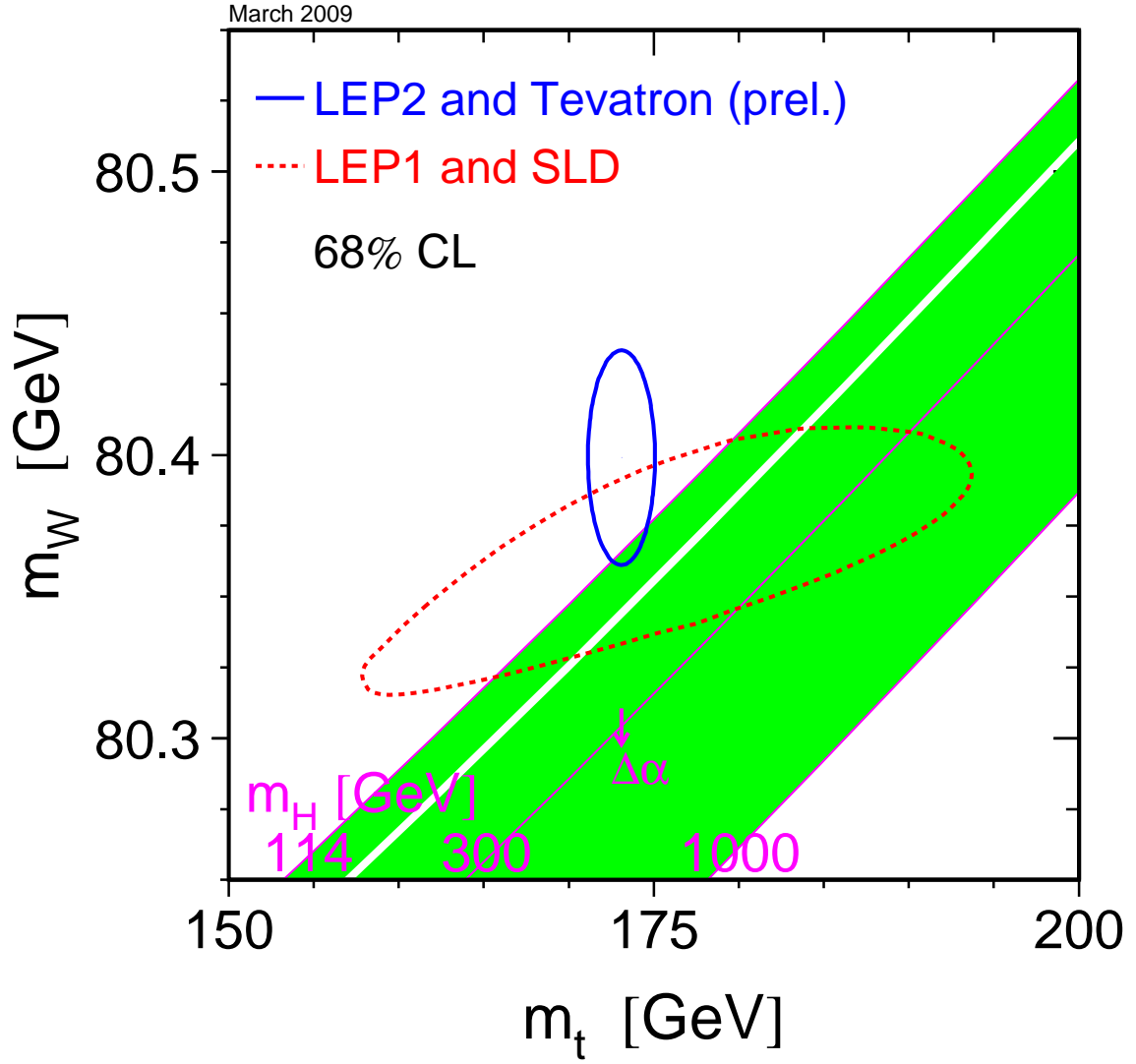


Figure 1.5: Plot showing Higgs boson mass as a function of both the W and t masses. The green bands indicate Higgs masses allowed by the Standard Model (with the masses indicated in purple). The red and blue ovals indicate the measured masses of the W boson and the top quark at the 68% confidence level. LEP excluded $m_H < 114 \text{ GeV}/c^2$ directly, and the Tevatron recently excluded the small white band at $m_H \sim 165 \text{ GeV}/c^2$. [Image courtesy of the LEP Electroweak Working Group]

successful theory, we know the Standard Model is incomplete.

While the top mass has been measured with uncertainties of almost 1%, the top cross section is a comparatively imprecisely-known measurement. The best measurements on the top cross section agree with the theoretical predictions, but have uncertainties of almost 9%. It is therefore imperative to study it further and make sure the measured value agrees with that predicted by the Standard Model, $7.39^{+0.57}_{-0.52}$ pb (using a similar set of PDFs as the ones used in this analysis) [8].

Many models of new physics are preferential to the third generation of fermions, and to the top in particular. While some of these models may not be directly observable with current experiments, they predict enhancements or detractions to the top cross section with respect to the Standard Model. A deviation of the measured cross section would thus be an indirect indication of physics beyond the Standard Model.

Similar measurements at higher energy are being done at the Large Hadron Collider, and so any improvements to the cross section measurement techniques made at CDF will translate directly over.

Chapter 2

$t\bar{t}$ Production at the Tevatron

When the amplitude of a process is known, one can then compute various quantities of interest, including the production cross section (a measure of how often the process occurs) and the decay rate of an unstable particle (a measure of how quickly the particle will transform into two or more different particles). Because of the fact that length is inversely related to energy (see Chapter 1.2), a process with a small cross section requires a large amount of energy to probe. Typical processes in high-energy physics have extremely small cross sections, so it is convenient to introduce a unit called the *barn*, where one barn is equal to 10^{-28} m². Even so, many physics processes of interest have cross sections typically measured in *nanobarns* (nb), *picobarns* (pb), or *femtobarns* (fb).

The cross section, σ , is shown as

$$\sigma = \frac{\text{Process rate}}{\text{Incident flux}} \tag{2.1}$$

where the process rate is the number of times the process occurs per unit time. The incident flux is the number of incoming particles per unit area per unit time, leading the cross section to have units of area, as expected.

Sometimes one wishes to know how the process rate is distributed over a solid angle, Ω . To determine that, one uses the *differential cross section*

$$\frac{d\sigma}{d\Omega}$$

If one integrates over all solid angles, the total cross section is regained as expected.

The differential cross section can be calculated from the quantum-mechanical amplitude (see Chapters 1.1 and 1.2). If one only considers processes of the type

$$1 + 2 \longrightarrow 3 + 4$$

the differential cross section is written, in the center-of-mass frame, as [6]

$$\frac{d\sigma}{d\Omega} = \frac{\mathcal{M}}{64\pi^2 s} \frac{|\vec{p}_f|}{|\vec{p}_i|} \quad (2.2)$$

where \mathcal{M} is the quantum-mechanical amplitude, \vec{p}_f , final momentum of particle 3 or 4, s is the center of mass energy squared, and \vec{p}_i is the initial momentum of particle 1 or 2.

Another common quantity of interest is the decay rate, Γ . The decay rate is also referred to as the *decay width*, and is written as

$$\Gamma = \frac{\text{Number of decays per unit time}}{\text{Number of particles}} \quad (2.3)$$

giving the decay rate units of inverse time, as expected. The *partial decay rate* or *partial decay width* is obtained if one only considers a specific decay chain. The inverse of the decay rate, $\tau = \hbar/\Gamma$, is the lifetime, which is the mean time the particle exists for before decaying.

If one again considers simple processes, this time of the form

$$1 \longrightarrow 2 + 3 \tag{2.4}$$

the decay rate can be calculated from the quantum-mechanical amplitude as [6]

$$\Gamma = \frac{|\vec{p}_f|}{8\pi m_1^2} |\mathcal{M}|^2 \tag{2.5}$$

where \vec{p}_f is the momentum of either of the two final particles, \mathcal{M} is the quantum-mechanical amplitude, and m_1 is the mass of the initial particle. The momentum of the final particles can be determined from conservation of energy and momentum

$$|\vec{p}_f| = \frac{1}{2m_1} \sqrt{m_1^4 + m_2^4 + m_3^4 - 2m_1^2 m_2^2 - 2m_1^2 m_3^2 - 2m_2^2 m_3^2} \tag{2.6}$$

The next sections examine the specific production and decay mechanisms of the top quark at the Tevatron collider (a detailed description of the Tevatron is given in Chapter 3).

2.1 Top Quarks at the Tevatron

In order to measure the top quark cross section, it is necessary to examine its production and decay modes at the Tevatron. There are four dominant production

mechanisms through the strong interaction¹, as shown in Figure 2.1, and three decay modes, as there are three non-zero CKM matrix elements involving the top quark (see Chapter 1.3). However, only one of each is relevant at the Tevatron, and those are to be examined further in the following sections.

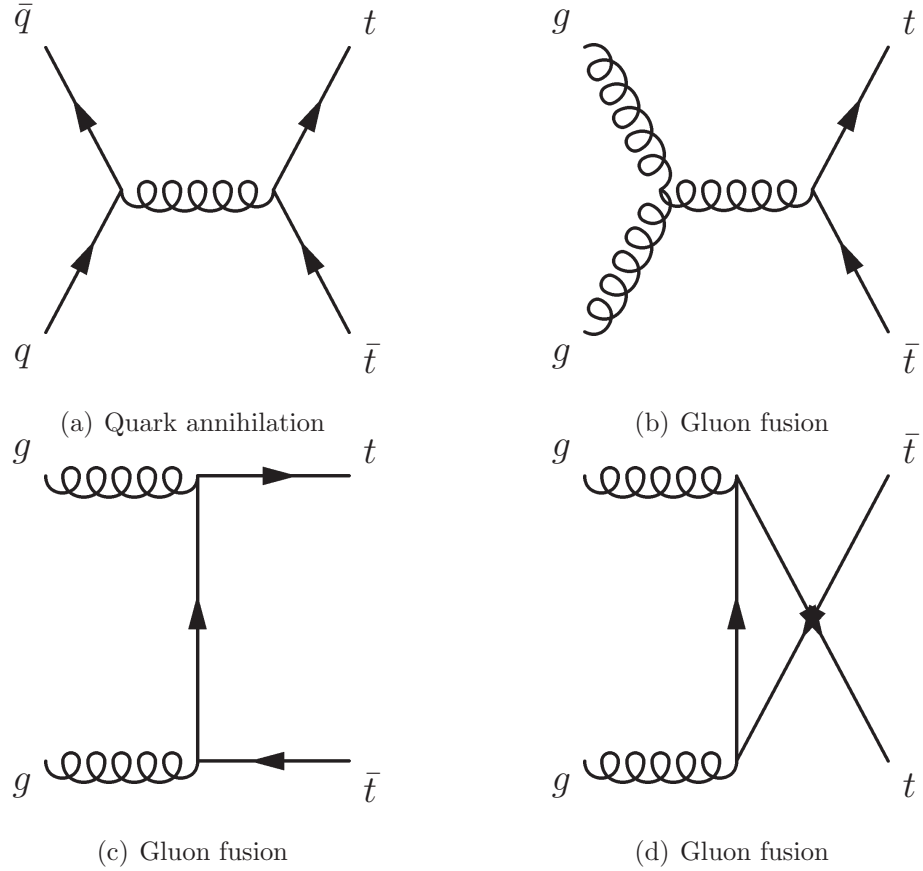


Figure 2.1: Different production methods for pairs of top quarks.

¹There are also production modes through the weak interaction, but they are so rare as to be safely ignored.

2.1.1 Top Production

Protons (as well as anti-protons) are composite particles, comprising three *valence* quarks (anti-quarks) held together by gluons in a *sea* of *virtual* quarks. The valence quarks are the dominant quarks of a hadron, and account for many of its physical properties. When protons (or anti-protons) are collided, it becomes necessary to account for this internal structure. This is done using *parton distribution functions* (*PDFs*) [9], which are models of how the constituent *partons* — the valence quarks, gluons, and sea quarks — behave inside the proton. In other words, PDFs describe what fraction, x_i , of the proton’s total momentum is carried by each parton, i . An example of a PDF for the proton is shown in Figure 2.2.

When protons and anti-protons collide, only one parton from each will hard scatter (i.e., scatter with large momentum transfer); the others are referred to as “spectators.” The scattering from spectators will be much softer, and thus won’t form rare particles, in what is called the *underlying event*. It is necessary to determine how much energy each parton needs to have in order to produce a $t\bar{t}$ pair. If one ignores the proton mass (since it is so much smaller than the top mass), the energy needed to produce a $t\bar{t}$ pair is

$$x_1 x_2 \geq \frac{4m_t^2}{s} \tag{2.7}$$

The minimum energy transfer is given when $x_1 = x_2 = x_{min}$

$$x_{min} = \frac{2m_t}{\sqrt{s}} \tag{2.8}$$

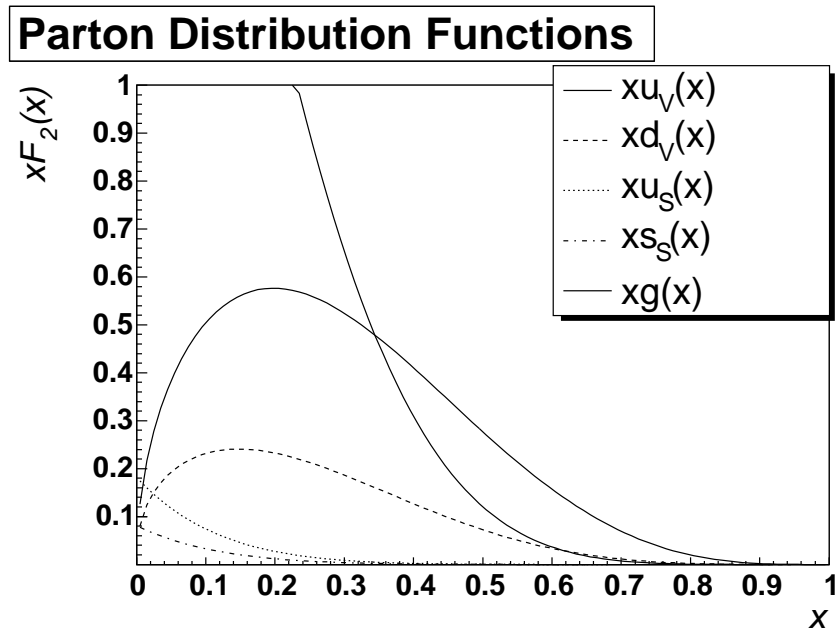


Figure 2.2: The parton distribution functions for valence quarks ($xu_v(x)$ and $xd_v(x)$), gluons ($xg(x)$), and sea quarks ($xu_s(x)$ and $xs_s(x)$) in the proton. The height of the curve is akin to the probability that the parton carries the fraction, x , of the total proton momentum. Note that above $x = 0.18$, the majority of the proton momentum is carried by the u and d valence quarks (shown by the $xu_v(x)$ and $xd_v(x)$ curves, respectively), leading quark annihilation to be the dominant top quark production mechanism at the Tevatron. [Image courtesy of S. Rappoccio]

At the Tevatron, $\sqrt{s} = 1.96$ TeV, so the minimum fraction of momentum needed by at least one parton, assuming a top mass of $175 \text{ GeV}/c^2$, is $x_{min} = 0.18$. In contrast, at the Large Hadron Collider, $\sqrt{s} = 14$ TeV, making $x_{min} = 0.025$. In Figure 2.2, the u and d quarks have a combined fraction of the proton momentum higher than that of the gluon at $x = 0.18$. Thus, at the Tevatron, the leading production mode is quark annihilation, $q\bar{q} \rightarrow t\bar{t}$, while at the Large Hadron Collider, where the gluon component is much larger at $x = 0.025$, the leading production mode is gluon fusion, $gg \rightarrow t\bar{t}$.

2.1.2 Top Decay

Unlike the less massive quarks, the top quark has a very short lifetime. So short, in fact, that it decays before it can hadronize. For example, the partial decay width of the top quark decaying to a W boson and a bottom (b) quark is given by [10]

$$\Gamma(t \rightarrow Wb) \approx 180 \text{ MeV} |V_{tb}|^2 \left(\frac{m_t}{m_W} \right)^3. \quad (2.9)$$

Assuming a top mass of $m_t = 175 \text{ GeV}/c^2$, the partial width is approximately 2 GeV, leading to a lifetime of $\tau \sim 4 \times 10^{-25}$ s. As this lifetime is much less than the estimated 10^{-23} s time-scale for hadronization, the top decays before it can hadronize.

The decay of the top quark is governed by the elements V_{tb} , V_{ts} , and V_{td} of the CKM matrix (Equation 1.7). Given that V_{ts} and V_{td} are much smaller than V_{tb} , the top quark decays almost exclusively via the weak force to a W boson and a b quark.

It is thus useful to categorize top events based on how the W decays. W decay is described in great detail elsewhere [11], so I focus here only on the basic elements.

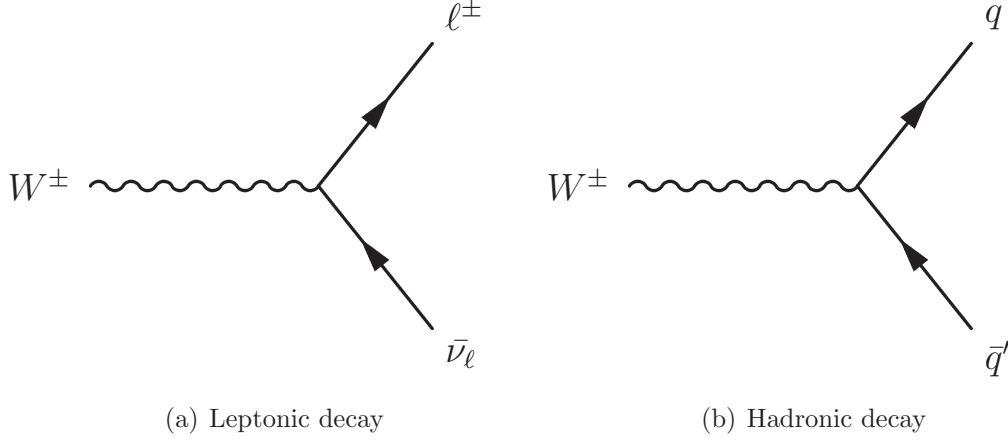


Figure 2.3: Different decay modes for W bosons.

The W has two decay modes, shown in Figure 2.3: $W^\pm \rightarrow \ell^\pm \nu$ (Figure 2.3(a)) and $W^\pm \rightarrow q\bar{q}$ (Figure 2.3(b)), with branching ratios of approximately 33% and 67%, respectively. Because there are two W s in the event, there are three possible final states. Approximately 10% of the time, both W s will decay to leptons and neutrinos; this is called the *di-lepton* channel. Approximately 45% of the time, both decay to quarks, which hadronize into jets, leading to the *multi-jet* or *all-hadronic* channel. The remaining 45% of the time, one W decays leptonically and the other hadronically, leading to the *lepton-plus-jets*, or *semi-leptonic*, channel as shown in Figure 2.4. Leptons, with the exception of taus, in the final state offer a cleaner signal, but jets offer more statistics. The lepton-plus-jets channel offers a good compromise, and is the focus of this dissertation.

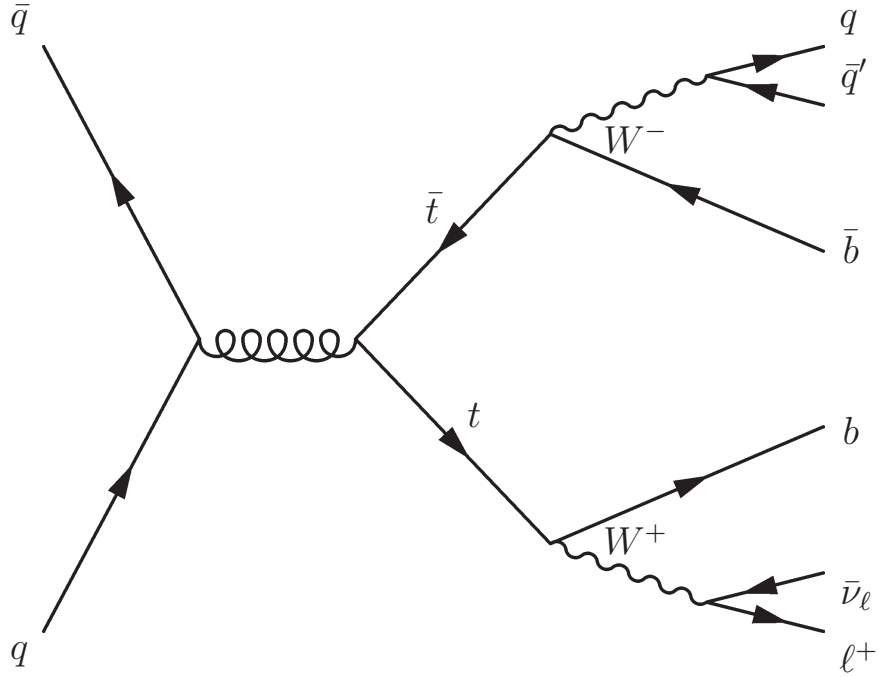


Figure 2.4: A sample lepton-plus-jets event in $p\bar{p} \rightarrow t\bar{t}$.

2.2 Measuring the Cross Section

In order to actually measure the $t\bar{t}$ cross section, one first needs to know how many such events are in the data-set. From there, one obtains the cross section

$$\sigma = \frac{N_{\text{events}}}{L} \quad (2.10)$$

where L is called the *integrated luminosity* and is a measure of the size of the data-set (see Chapter 3.2.6 for a detailed discussion).

Unfortunately, counting the number of top events is not simple, due to *backgrounds*. Backgrounds are other processes which look like top events in the detector, and there are two types. Some background events have the exact same *signature* — the particles in the final state — as a top decay, while others don't have exactly the

same signature but rather a similar one, and detector effects make it seem the same.

A lepton-plus-jets top event has a relatively complicated signature: two light-flavor jets (from one W decay), missing transverse energy and a muon or electron (from the other W decay), and two b -jets. If the two light-flavor jets are not reconstructed properly in the detector, for example, the resulting event has the same signature as s -channel single top production [12].

The necessary background processes to consider in the lepton-plus-jets channel are classified into several main groups: $W + \text{jets}$, which includes $Wb\bar{b} + \text{jets}$, $Wc\bar{c} + \text{jets}$, $Wc + \text{jets}$, and $Wq\bar{q} + \text{jets}$; other electroweak processes including single top, di-boson (WW , WZ , or ZZ), and $Z + \text{jets}$; and QCD processes.

One then uses simulations to estimate how many background events are expected and subtracts that from the number of observed events in the data to obtain the number of expected top events. From there, the cross section is calculable as

$$\sigma_{t\bar{t}} = \frac{N_{\text{data}} - N_{\text{bkg}}}{\mathcal{A} \cdot L} \quad (2.11)$$

where \mathcal{A} is called an *acceptance* and is a measure of the efficiency of the event selection criteria. This will be explained in Chapter 5.

Chapter 3

Experimental Apparatus

The Collider Detector at Fermilab (CDF) and D-Zero (DØ) are multi-purpose experiments in operation at the Tevatron collider, located at Fermi National Accelerator Laboratory (FNAL or Fermilab) in Batavia, Illinois, USA. CDF collected all of the data used in this analysis. This chapter gives an overview of the accelerator and CDF, focusing on the parts of the detector most used in the analysis.

3.1 The Tevatron

The Tevatron was built at FNAL in the early 1980s to accelerate beams of protons and anti-protons each to an energy of 1 TeV and collide them. In 1985, the Tevatron achieved collisions at a center-of-mass energy $\sqrt{s} = 1.8$ TeV and continued running until 1996 when it shut down and underwent a major upgrade. During this initial operating period, called Run I, the top quark was discovered in 1995 [13][14].



Figure 3.1: Aerial view of the Tevatron accelerator. The Tevatron ring is the large circle in the center of photograph. At the top of the circle is CDF, and to the right is DØ. At the left is part of the Main Injector. [Image courtesy of M. Prewitt]

After an upgrade period of almost 5 years, the Tevatron resumed operations in early 2001, at a higher energy of $\sqrt{s} = 1.96$ TeV and higher intensities. The Tevatron has continued to operate at this higher capacity during what is called Run II, and currently is scheduled to be turned off at the end of 2011. Achieving an energy of 980 GeV in each beam requires several acceleration steps, which can be seen in Figure 3.2, and these steps are described in the following sections. Much more detailed descriptions of the components of the accelerator are available from the Fermilab webpage [15].

3.1.1 Proton Source, Preacceleration, and the Linac

The acceleration chain starts in a Cockcroft-Walton preaccelerator, where hydrogen ions, H^+ , are accelerated to 750 keV. These ions come from the Proton Source, which

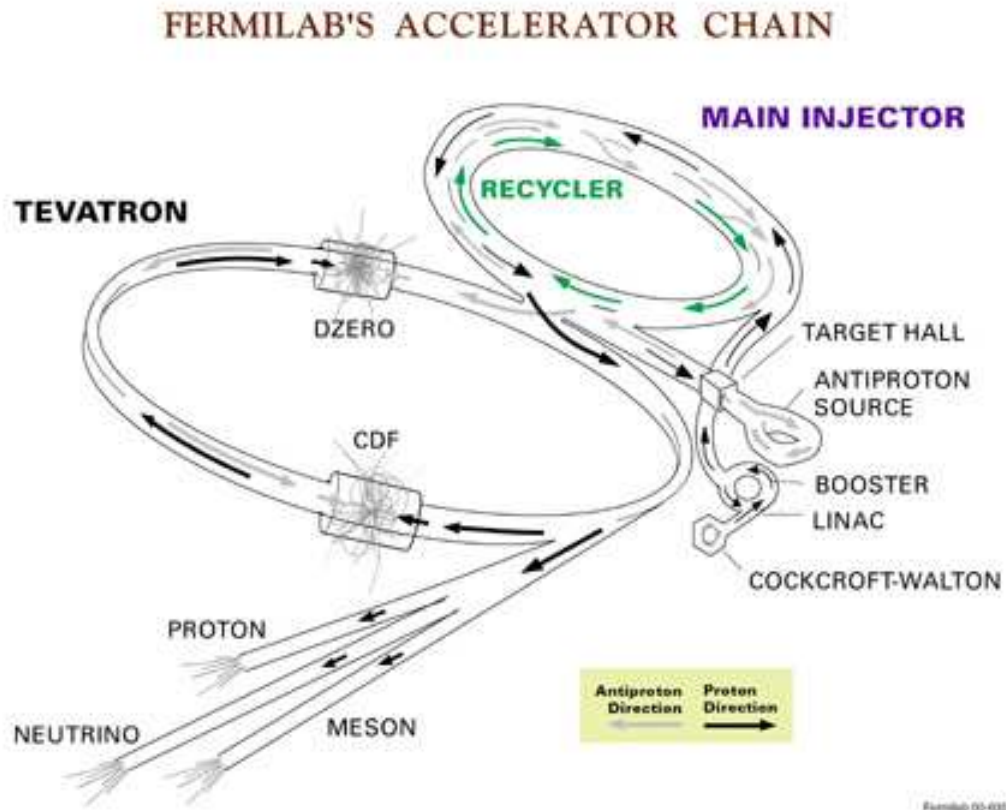


Figure 3.2: Schematic of the Tevatron collider chain. Acceleration starts in the Cockcroft-Walton towers, and proceeds through the Linac, Booster, and Main Injector before protons and antiprotons collide in the Tevatron. Note that not all components in the acceleration chain are shown in this image. [Image courtesy of Fermi National Accelerator Laboratory]

contains pure hydrogen gas that ionizes the hydrogen through the generation of a dense plasma.

Once at an energy of 750 keV, the ions are passed into the Linear Accelerator (Linac), which consists of two sets of radio frequency cavities. The first set brings the ions to an energy of 116 MeV and the second to an energy of 400 MeV. The Linac's AC electric field breaks the continuous stream of H^- ions into bunches. This bunch structure is necessary later in the acceleration chain for mechanical reasons as well as to increase the likelihood of collisions. The 400 MeV ions are passed through a carbon foil to strip off the electrons on their way to the Booster.

3.1.2 Booster, Main Injector, Accumulator, and Recycler

The Booster is a synchrotron accelerator 475 m in circumference, and accelerates the 400 MeV protons to 8 GeV in less than one second. The Booster then sends the protons to the Main Injector.

The Main Injector is another synchrotron, with a circumference of approximately 3 km, and serves multiple purposes in the accelerator chain. It accelerates 8 GeV protons and anti-protons to 150 GeV for injection into the Tevatron ring. The Main Injector also accelerates 8 GeV protons to 120 GeV, after which they are sent to and collided with a nickel alloy target producing antiprotons through the interaction $p + Ni \longrightarrow p + \bar{p} + p + Ni$, with an efficiency of $\sim 20 \times 10^{-6}$. Thus, it takes about 1 million protons to produce 20 antiprotons, due to the low efficiency, which must

be selected among the resultant particles. This is done using a lithium lens and pulsed dipole magnet; only negatively charged particles with the mass of a proton will be bent at the angle necessary to continue in the accelerator. The antiprotons are stochastically cooled before they are sent to the Accumulator where they are stored and cooled further. Once enough antiprotons have been accumulated to exceed the storage capacity of the Accumulator, they are sent to the Recycler which is housed in the same ring as the Main Injector. Here they are cooled even further and stored at 8 GeV until they are moved into the Main Injector, accelerated, and sent to the Tevatron.

3.1.3 Tevatron Collider

The Tevatron is a superconducting synchrotron with a circumference of 6.3 km that accelerates both protons and antiprotons from 150 GeV to their final energy of 980 GeV. The two beams are steered in opposite directions in the same beam-pipe by a set of niobium-titanium superconducting magnets; these 774 dipole magnets, 240 quadrupole magnets, and dozens of other types of magnets are maintained at a temperature of 4 K by liquid helium. Electrostatic separators keep the beams from colliding except at two points along the ring – these points are where the CDF and DØ detectors are located.

Within these detectors, the beams are focused using quadrupole magnets; the width of each bunch is reduced to approximately $35\text{ }\mu\text{m}$, although the length increases

to 30 cm during the focusing. The beams are then crossed to induce collisions at the center of each detector, at a collision rate of approximately 1.7 MHz.

3.2 The Collider Detector at Fermilab

The Collider Detector at Fermilab (CDF) [16][17] is a general multi-purpose detector situated in the Tevatron collider. CDF has several subcomponents that collectively provide excellent tracking, particle identification, and momentum and energy measurement. The detector is azimuthally and forward-backward symmetric, making a cylindrical coordinate system a logical choice for reference, though Cartesian coordinates are used in some situations. The proton beam direction is chosen to be the positive z direction, with the positive y direction pointing upward, and the positive x direction points to the center of the Tevatron, forming a right-handed coordinate system. Many times only the portion of the momentum, p , or energy, E , perpendicular to the beam direction is desired — these are referred to as *transverse* quantities, and are denoted with a subscript T : p_T or E_T . Another useful coordinate is the pseudorapidity, defined as

$$\eta \equiv -\tan\left(\frac{\theta}{2}\right) \quad (3.1)$$

where θ is the angle from the positive y -axis.

The specific components of CDF are shown in Figure 3.3 and are explained in detail in the following sections. Figure 3.4 shows the tracking volume of CDF.

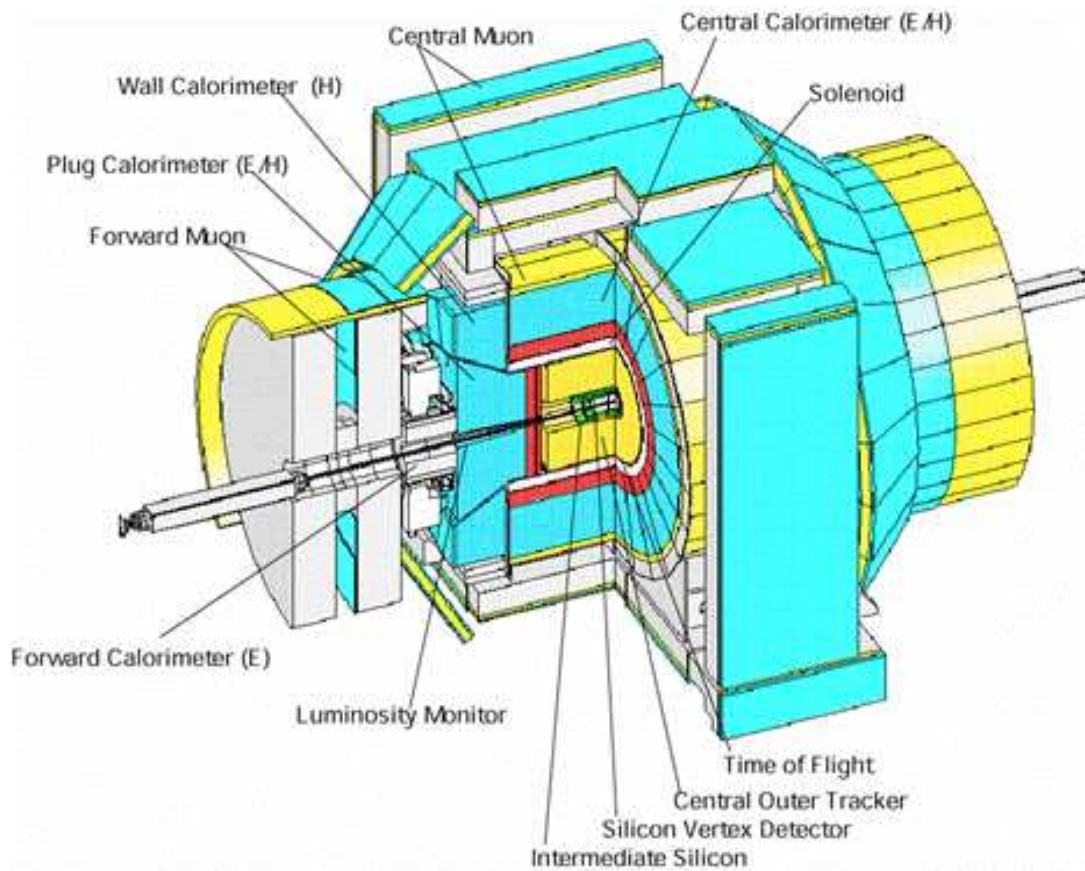


Figure 3.3: Schematic of the CDF detector. At the center sits the silicon systems, highlighted in green, with the Central Outer Tracker (the inner yellow component) outside them. Beyond that are the hadronic (H) and electromagnetic (E) calorimeters (the inner components highlighted in light blue). Situated at the outside of the detector are the muon chambers, in light blue. Also shown are the Time of Flight system (white), Cerenkov Luminosity Counters (labeled as the Luminosity Monitor), and the solenoid, marked in red. The outer yellow components are steel shielding. [Image courtesy of CDF]

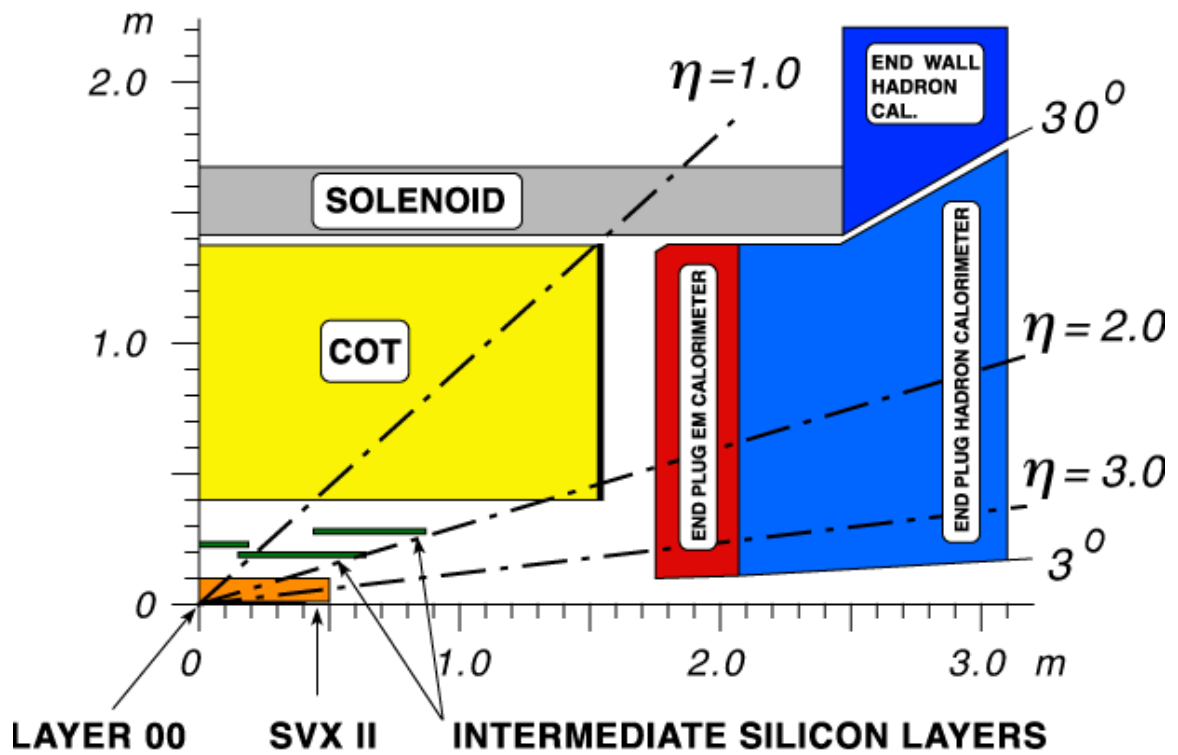


Figure 3.4: Schematic of the inner tracking components of CDF. At the center sits the Silicon Vertex Detector in orange and the Intermediate Silicon Layers in green. Beyond that is the Central Outer Tracker in yellow. The solenoid is shown in grey, and the Plug Electromagnetic calorimeter in red. At the very outside of the tracking area is the Plug Hadronic calorimeter in blue. [Image courtesy of CDF]

3.2.1 Silicon System

The silicon system, shown in Figure 3.5, is situated at the center of CDF, and is comprised of three subcomponents: the Silicon Vertex Detector (SVX) [18], which is the bulk of the system; the Intermediate Silicon Layers (ISL) [19]; and Layer 00 (L00) [20]. Together, they provide very precise tracking resolution, allowing not only the reconstruction of secondary vertices in an event, but also real-time triggering of events using the *impact parameter*, d_0 , of reconstructed tracks (see Chapter 3.2.7.2). The impact parameter is the shortest transverse distance between the interaction point and the reconstructed track. Both of these features are important for identifying the b -jets in the top decays.

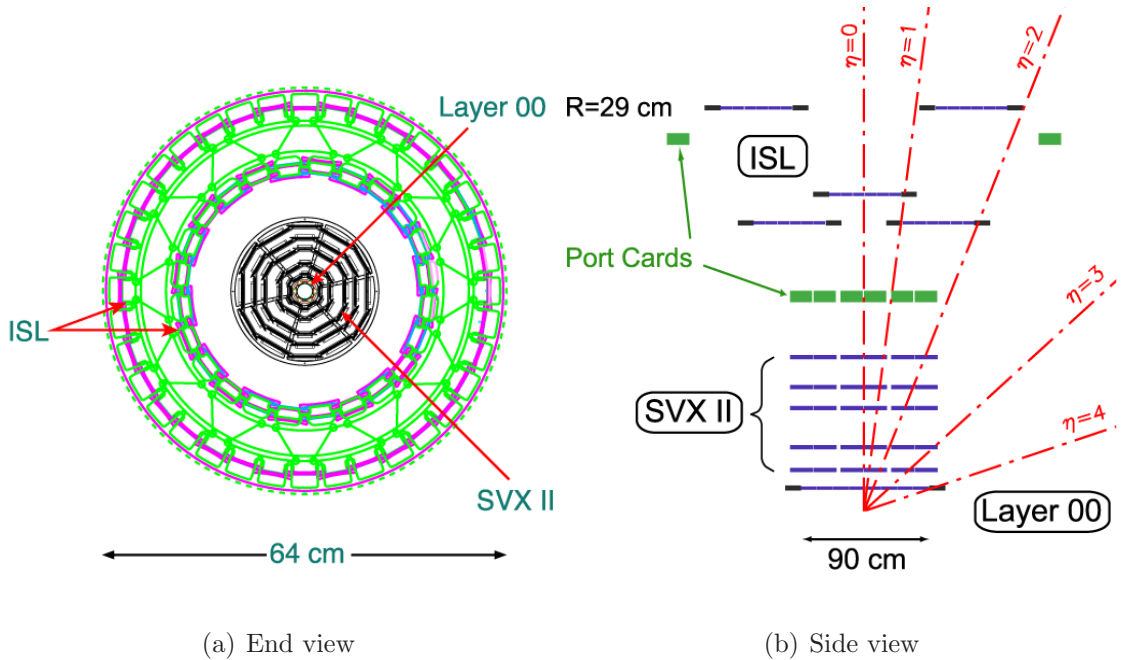


Figure 3.5: Two views of the silicon system at CDF. Panel (a) shows an end view, and Panel (b) shows a side view. Note the z scale on the side view is highly compressed. [Images courtesy of CDF]

All three subcomponents are silicon micro-strip detectors. Silicon makes for an excellent tracking material choice due to its electrical and ionization properties, as well as its commercial availability, although its cost prohibits its use throughout the entire tracking volume of CDF. The semiconductor silicon is “doped” with another element, creating *p-doped* (if the additional element has fewer electrons than silicon) or *n-doped* (if it has more electrons) silicon. A *pn junction* forms when p-doped silicon is brought into contact with n-doped silicon. Free charge carriers recombine at the contact area creating a depleted region at the junction. A voltage applied across the silicon will deplete the entire region, allowing for its use as a tracking medium.

The silicon sensors at CDF consist of n-doped silicon, with strips of p-doped silicon applied on top, aligned axially with the beam-pipe, to provide tracking in the $r - \phi$ plane. As a charged particle enters a piece of silicon it ionizes, creating electron-hole pairs which flow towards the strip on top due to the applied voltage. L00 utilizes single-sided strips since it is mounted directly on the beam-pipe, whereas SVX and ISL use double-sided strips for enhanced tracking resolution in the $r - z$ plane. These double-sided strips have a second strip of n-doped silicon bonded to the opposite side of the silicon wafer than the p-doped strip. Some of these strips are mounted at a small stereo angle, 1.2° , relative to the p-doped strips, while the rest are mounted at a 90° angle.

The silicon system consists of many strips, arranged into *layers*. The number of strips in a given layer increases with the distance from the beam-pipe, simply because

there is more room. The charge collected by each strip is read out using chips mounted on each end. Basic specifications of the silicon detector are shown in Table 3.1

Table 3.1: Summary of basic specifications for L00, SVX, and ISL subsystems.

Name	Radius (cm)
SVX Layer 0	2.54
SVX Layer 1	4.12
SVX Layer 2	6.52
SVX Layer 3	8.22
SVX Layer 4	10.10
ISL Central	22.00
ISL Layer 6 Fwd/Bwd	20.00
ISL Layer 7 Fwd/Bwd	28.00
L00 (narrow)	1.35
L00 (wide)	1.62

Layer 00 was installed as an upgrade in 2003, and is designed to enhance the resolution of the track impact parameter. It uses the same radiation-hard silicon used in the Large Hadron Collider detectors. A secondary benefit is to compensate for the expected gradual failure of the inner layer(s) of SVX due to radiation damage.

3.2.2 Central Outer Tracker

The Central Outer Tracker (COT) [21], located between a radius of 40 cm and 138 cm within the magnetic field, is a wire-strip tracking chamber filled with a roughly equal mixture of argon and ethane gases. The wires are arranged into eight *superlayers*, with four positioned axially and four positioned at a small stereo angle. There are two types of wires in the COT: anode wires, which produce an electric field, and

sense wires, which do the tracking.

As a charged particle passes through the COT, it ionizes the gas, producing electrons. The electric field from the anode wires causes the electrons to drift toward the sense wires. Measurement of the arrival time of the drifting electrons yields a position of the passing particle; the charged particle produces many of these drifting electrons as it passes through, allowing for the reconstruction of its entire trajectory.

3.2.3 Calorimeters

CDF uses two sets of calorimeters to measure the energy of the particles passing through it: a set of electromagnetic calorimeters and a set of hadronic calorimeters, which measure the energy of electrons and photons, and hadrons, respectively. Each set of calorimeters is composed of several separate structures, so as to fully envelop the rest of the CDF detector. The *central electromagnetic* (*CEM*) [22] and *central hadronic* (*CHA*) calorimeters are located in the central region of the detector, $|\eta| < 1$, outside the COT. The *plug electromagnetic* (*PEM*) [23] and *plug hadronic* (*PHA*) calorimeters are located on the end-caps of the detector, in the forward regions, $|\eta| > 1$, of the detector. The hadronic calorimeters are positioned directly behind the electromagnetic ones.

The calorimeters are composed of alternating layers of plastic scintillators and an absorbers. The electromagnetic calorimeters use lead as the absorber, while the hadronic calorimeters use steel. As the particle interacts with the scintillator it pro-

duces multiple lower-energy particles; those new particles produce additional particles with even lower energy. This process is called *showering*.

As particles interact in the scintillator, they create light that is detected by photomultiplier tubes located at the end of each piece of scintillator, losing some energy in the process. The particles then pass through the absorber layer, losing more energy, and the process is repeated. The total energy of the initial particle is related to the number of layers it interacts with before losing all of its energy, as well as to the amount of light captured by the photomultiplier tubes. There is enough absorber in each calorimeter to prevent most of the particles from passing completely through, although some still manage to “punch through” to the muon chambers.

3.2.4 Muon Chambers and Scintillators

At the very outside of the detector sit the muon chambers (CMU, CMP, CMX, BMU) and muon scintillators (CSP, CSX, BSU). These are designed to detect muons that pass through the rest of the detector.

The muon chambers are four-layer drift cells that operate in a similar manner as the COT. Directly outside of the central calorimeters is the *Central Muon Chamber* (CMU) [24], which detects muons with $p_T > 1.4 \text{ GeV}/c$. Beyond that, behind 60 cm of steel, sits the *Central Muon Upgrade* (CMP) [25], which detects muons with $p_T > 2.0 \text{ GeV}/c$. Both the CMU and CMP sit in the very central region, $|\eta| < 0.6$. The rest of the COT fiducial region, $0.6 < |\eta| < 1.0$ is covered by the *Central Muon Extension*

(*CMX*) [25] arches. Additional forward coverage, $1.0 < |\eta| < 1.5$, is provided by the *Barrel Muon Chamber (BMU)*.

The muon scintillators are located to the outside of the respective muon chambers (e.g., the CSP sits outside the CMP), with the exception of the CSX. The CSX scintillators are located both inside and outside of the CMX chambers. The scintillators provide the same coverage as the muon chambers.

Unlike the drift cells of the muon chambers, the scintillators work quickly. They do not give an accurate measure of the position, however, like the muon chambers do. Together, the drift cells and scintillators can provide accurate information about where and when a muon passed through.

Muons that pass through the chambers or scintillators will be reconstructed as a “stub” by the triggers (see Chapter 3.2.7.1) or the offline event reconstruction software. Reconstructed tracks in the COT and silicon system are extrapolated to this stub to form a muon “candidate.” A track which is linked to the CMX is called a *CMX muon*, while a track linked to both the CMU and CMP is called a *CMUP muon*.

3.2.5 Time of Flight

The Time of Flight system (TOF) [26] sits above the COT just inside the solenoid at $|\eta| < 1$ and provides a measurement of the time each particle has traveled. The TOF consists of more than two hundred bar-shaped scintillators, and is located in

the central region, $|\eta| < 1$, between the COT and the superconducting magnet at a radius of approximately 138 cm. As particles pass through and interact with the scintillator, light is created and read out by photomultiplier tubes attached at each end.

This timing information is used — together with information on the energy, momentum, and charge — for particle identification. It enhances the identification of b -jets, and is also used to filter out particles resulting from cosmic rays. These cosmic particles do not originate from the collisions and are thus not relevant to this analysis.

3.2.6 Cerenkov Luminosity Counters

Most analyses require a measurement of how many collisions, or *events*, have occurred. This is done using a measurement called the beam *luminosity*.

The Cerenkov Luminosity Counters (CLC) [27] sit directly on the beam-pipe in the very forward regions, $3.7 < |\eta| < 4.7$, and are filled with isobutane. Photomultiplier tubes measure the Cerenkov light produced when charged particles interact with the isobutane. This interaction rate is converted to a measure of the instantaneous beam luminosity, which is also shown by

$$\mathcal{L} = \frac{fnN_pN_{\bar{p}}}{A} \quad (3.2)$$

where f is the revolution frequency, n is the number of bunches (36), N_p is the number of protons per bunch, $N_{\bar{p}}$ is the number of anti-protons per bunch, and A is the overlapping area of the beams. As the beams are collided, the luminosity

decreases (following an exponential decay function) as protons and anti-protons are lost to collisions and orbit instabilities.

Uncertainty in the measured luminosity arises from two sources. The first is due to the theoretical uncertainty on the inelastic $p\bar{p}$ cross section, and the second is due to the measurement resolution of the CLC. Each source has an approximate 4% uncorrelated uncertainty, leading to a total uncertainty on the measured luminosity of 5.9% [28].

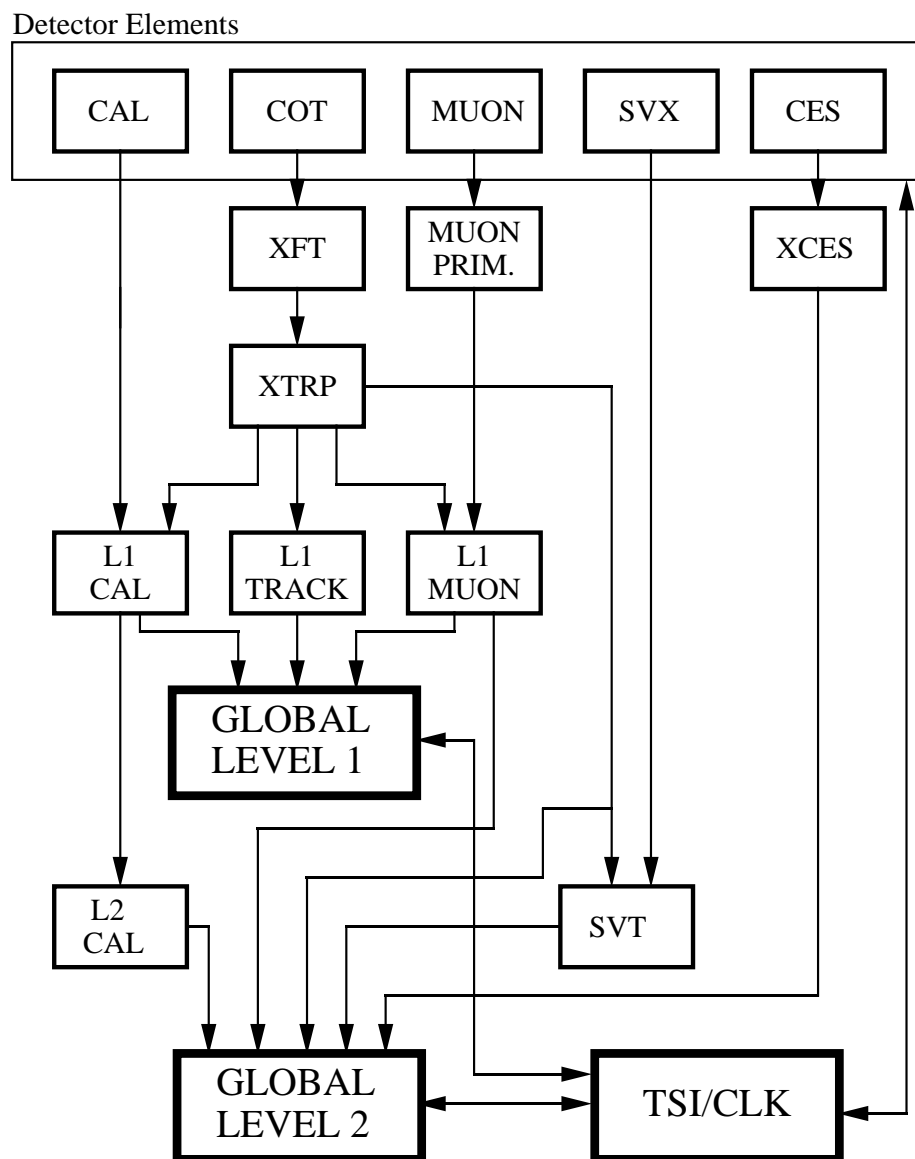
3.2.7 Trigger System

The collision rate at the Tevatron is approximately 1.7 MHz but CDF is only able to record events at a rate of about 200 Hz, and so a three-level trigger system is used to capture only the most interesting events. Each level in the system makes a decision with more information and with more time than the previous level. A block diagram of the first two levels of the trigger system is shown in Figure 3.6 and each level is described in more detail in the following sections.

3.2.7.1 Level 1

The Level 1 (L1) trigger is the first subsystem and uses very basic information about the collision to form a decision. This accept (L1A) or reject (L1R) decision is always rendered approximately 5 μ s after the collision and as such is implemented in hardware. Limitations on the next level of the triggering system limit the maximum

RUN II TRIGGER SYSTEM



PIW 9/23/96

Figure 3.6: Block diagram of the first two levels of the trigger system at CDF. [Image courtesy of CDF]

L1A rate to 45 kHz (although in practice L1A rates are closer to 25 kHz).

Level 1 takes information from the COT, calorimeters, and muon chambers only and performs very basic event reconstruction. A piece of hardware called the *eXtremely Fast Tracker* (*XFT*) [29] was installed as an upgrade in 2003, and takes information from the four axial layers of the COT and reconstructs tracks after each collision; the reconstructed tracks are then passed to the *Extrapolation Unit* (*XTRP*) [30] which projects those XFT tracks out to the calorimeters and muon chambers.

These extrapolated tracks are passed to three individual triggers: L1CAL, which additionally uses clusters of energy in the calorimeters to identify calorimeter objects¹ such as jets, photons, electrons, and missing transverse energy and uses those objects to make a decision to keep or reject the event; L1TRACK, which simply uses the XTRP information to make the decision; and L1MUON, which uses hits in the muon chambers to reconstruct muon objects and decide. These three decisions are then passed to the Global L1 and combined with AND/OR logic to come up with the L1A or L1R.

The L1 consists of several different *trigger paths*, each of which has different acceptance requirements; events can be accepted by more than one L1 path. These trigger paths are independent of the three individual triggers mentioned above, and typically mimic the selections used in various analyses (e.g., one path requires at

¹Objects are combinations of energy in the calorimeters and tracks in the COT

least 28 GeV of missing transverse energy, while another requires a CMU muon with transverse momentum of at least 6 GeV/ c). Events that are accepted by any of the trigger paths are then buffered for the Level 2 trigger system, while events which are not accepted are simply discarded.

3.2.7.2 Level 2

The Level 2 (L2) trigger is a combination of hardware and software triggers, and is asynchronous with an average processing time of $\sim 30 \mu\text{s}$. Limitations on Level 3 limit the L2A rate to approximately 800 Hz.

Level 2 uses the same information as Level 1 but with a higher resolution. It also incorporates two additional subcomponents: the Central Showermax (CES) calorimeter and the Silicon Vertex Trigger (SVT), which uses hit information from SVX (but not ISL or L00). The CES is a strip chamber placed in the CEM at a depth equal to the average maximum depth of an electromagnetic shower, and provides additional information about photons and electrons that makes identification of these particles easier. Because of the large number of channels in the silicon system, the SVX cannot be fully read out in time for Level 1, so each event is held in an onboard circular buffer; it is not read out unless the event passes the Level 1 trigger.

The SVT combines data from SVX and the XTRP to reconstruct tracks in real time with an accuracy close to that of a full-fledged offline analysis. This is necessary to precisely measure the impact parameter of the track, d_0 (see Chapter 3.2.1). This

allows the trigger to quickly choose events which have b -jets, such as $t\bar{t}$ events, as they will be displaced from the primary vertex. The SVT is the first trigger in a hadronic collider capable of using the impact parameter of tracks to filter events.

Like the L1 trigger, the L2 consists of several trigger paths. Events that are accepted by any of them are buffered for the Level 3 trigger system, while those that aren't are discarded.

3.2.7.3 Level 3

The Level 3 (L3) trigger is solely a software-based system, and is implemented as a large farm of about 150 Linux computers. Each event that passes L2 is first sent to the Event Builder (EVB), which is a small farm of Scanner CPUs, before being sent to the L3. The L1 and L2 triggers only use a small subset of the event data while making a decision in order to reduce the time needed, while the rest of the event data is stored in several buffers. The EVB reads out all of the event data only after an L2A and assembles it into a form readable by the L3 farm.

The L3 uses all of the event data to fully reconstruct the event and analyze the full event topology before making a final decision to accept or reject the event. As with L1 and L2, events that are rejected are simply discarded; events that are accepted are sent to the Consumer Server Logger, where they are stored temporarily before being written to tape for permanent storage. The Consumer Server Logger also copies a small fraction of events for immediate online data quality monitoring in the CDF

control room.

3.2.7.4 Prescales

The L1 and L2 trigger systems can apply a *prescale* to each trigger path, which reduces the accept rate of that path. This is necessary, especially at higher instantaneous luminosities, to keep overall accept rates within specified limits. When a prescale is applied to a trigger path, only every n^{th} event is kept. Thus, the higher the prescale, the lower the accept rate from that trigger path. CDF's trigger prescales can be applied dynamically; that is, they can be changed during the run. At high instantaneous luminosities, many prescales are large. As the luminosity decreases, the accept rates decrease as well, and so prescales are lowered to the overall accept rates.

Chapter 4

Introduction to the Measurement

As described in Chapter 3, the Tevatron collides proton and anti-proton beams inside CDF, and particles spray out in all different directions. Muons almost make it outside the detector without a trace, while electrons shower in the electromagnetic calorimeters. Both leave tracks of their passage in the silicon system and Central Outer Tracker. Bare quarks hadronize forming jets which shower in the hadronic calorimeters. Neutrinos escape CDF completely unscathed and show up as missing transverse energy (see Chapter 6.3).

Measuring the top cross section in the lepton-plus-jets channel requires assembling information from all of the above components to reconstruct each event. Once the events are reconstructed, the signal (the top events) must be separated from the backgrounds (all of the other events).

The Simultaneous Heavy Flavor Fraction and Top Cross Section Measurement

(SHyFT, though generally referred to as METHOD III) is a procedure to calculate both the signal and backgrounds in a lepton-plus-jets data sample, and is similar to METHOD II in that both techniques assume that all potential processes that can contribute to the sample are accounted for.

No single variable is able to distinguish between the three main samples in this analysis - the $t\bar{t}$ signal, the W + heavy flavor background and the W + light flavor background. $t\bar{t}$ and W + heavy flavor both contain heavy flavor; W + heavy flavor and W + light flavor both have few jets in the event. But the combination of the number of jets and jet flavor is able to separate these three samples (as well as $Wc/Wc\bar{c}$ + jets). W + heavy flavor has few jets while $t\bar{t}$ has several; $W_{b\bar{b}}$ contains jets with heavy flavor whereas W + light flavor does not. This can be seen in the cartoon shown in Figure 4.1.

A flavor separator is an algorithm that provides a single output to determine the flavor of a jet. There are two flavor separators in use at CDF, and both require the jet to be *b-tagged* with a SECVTX tag, which is a set of requirements on the tracks and secondary vertex of the jet that is designed to identify the jet as containing a b quark [31]. There are three “tunings” to the SECVTX tagging algorithm — loose, tight, and ultratight — each with a much lower mistag rate but also a lower tagging rate than the previous [32].

Of the two flavor separators in use at CDF — the mass of the secondary vertex in

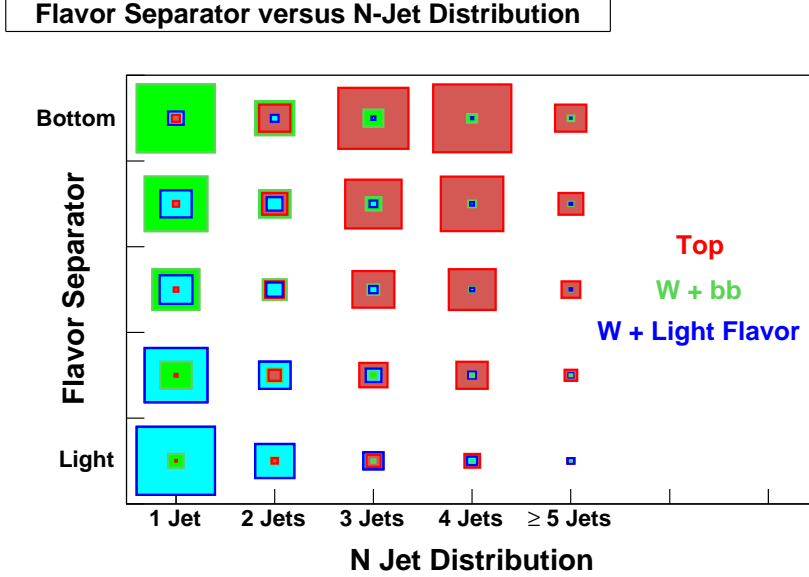


Figure 4.1: Cartoon of jet flavor versus n_{jet} for different samples. The size of each box indicates the contribution of the sample to the bin. Each variable on its own is not enough to separate the three samples, but together it is easy to distinguish them.

a b -tagged jet¹ and the Karlsruhe Institute of Technology (KIT) Flavor Separator [33] — KIT is a more powerful flavor separator since it is a trained neural net combining multiple inputs. We use KIT as the flavor separator with tight SECVTX tags, because those are what the neural net was initially trained on.

The KIT flavor separator uses more than twenty inputs, such as the mass of the secondary vertex in the jet and the two-dimensional distance from the primary vertex to the secondary vertex, to compute a “ b -ness” to each jet. The output, a number between -1 (non b -like) and 1 (b -like), allows for discrimination between bottom jets versus other jets, and even allows for some discrimination between charm and light flavor jets, as seen in Figure 4.2.

¹The SecVtxMass variable from the SECVTX object representing the jet.

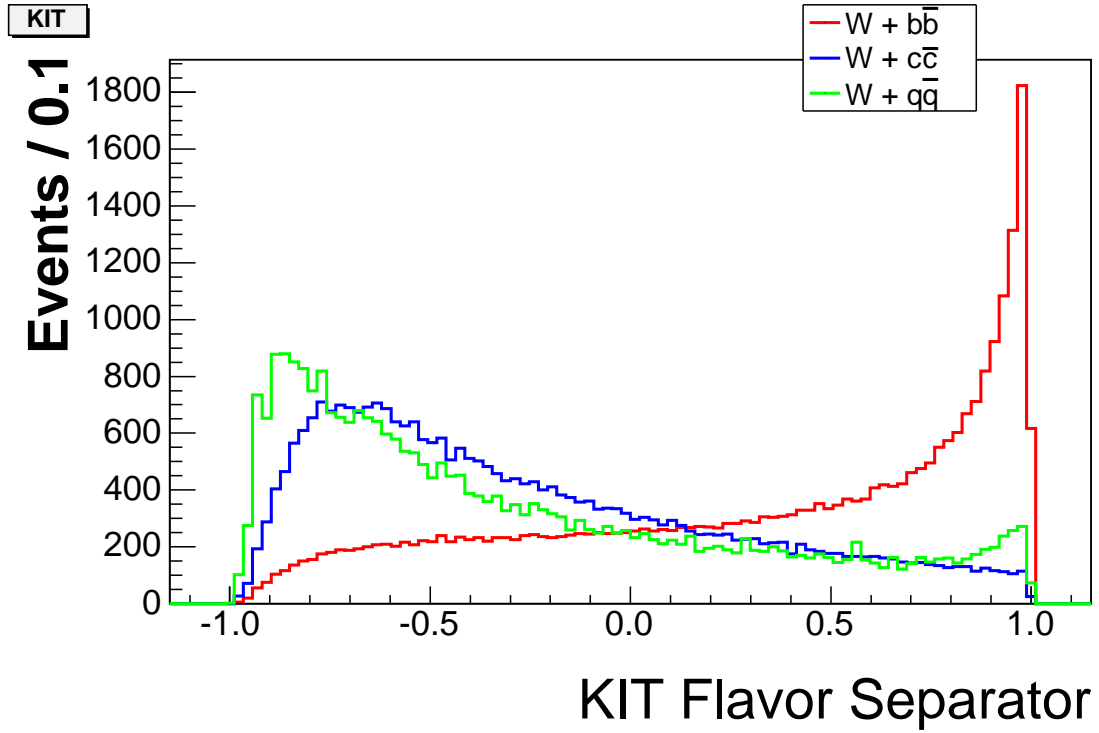


Figure 4.2: Sample output of the KIT Flavor Separator, showing how different flavors are distinguished from each other. In green is light flavor (u, d jets), in blue is charm flavor, and in red is bottom flavor. Light flavor peaks around -0.9, charm peaks around -0.6, and bottom flavor peaks at 1, providing a good method to distinguish the flavor of a jet.

While both the n_{jet} spectrum and a flavor separator together distinguish the different samples, they are not enough to distinguish parameters that affect those samples. Namely, a change in the top event yield can be due to a different production cross section, or it can be due to a change in the b -tagging efficiency. A change in the b -tagging efficiency affects events with one b -tag differently than those with two tags; a change in the Top cross section affects both identically, as seen in Figure 4.3. To help isolate this differential effect, we use the number of tags as another discriminating factor in the fit.

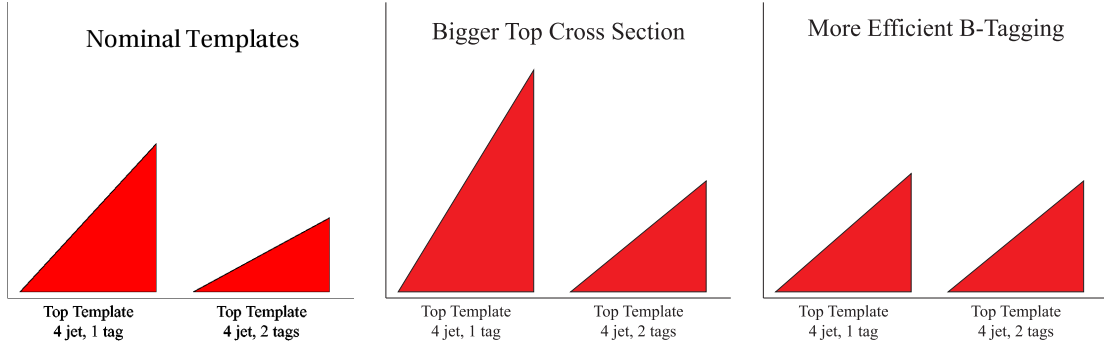


Figure 4.3: Cartoon illustrating how increasing the b -tag scale factor or the top cross section affects single and double tags differently. As the top cross section is increased, both 1-tag 2-tag templates get larger. However, if the b -tagging becomes more efficient, some 1-tag events become 2-tag events, leading to fewer events in the single-tag template and more in the double-tag template.

The flavor-separator distribution of each sample for a given number of jets and b -tags, i.e., a given bin in n_{jet} and n_{tag} (a *jet-tag bin*), is called a *template*. Templates are obtained from the Monte Carlo simulation; they are used (and stored) as histograms normalized to the expected yield corresponding to 1 fb^{-1} .

We make templates using the KIT Flavor Separator for signal and background

samples after passing them through our event selection (see Chapter 5). The sample used to model QCD is made from data, while all other background samples were generated using Monte Carlo simulation by the Top Group (see Chapter 6). Sample templates are shown in Figs 4.4 - 4.6.

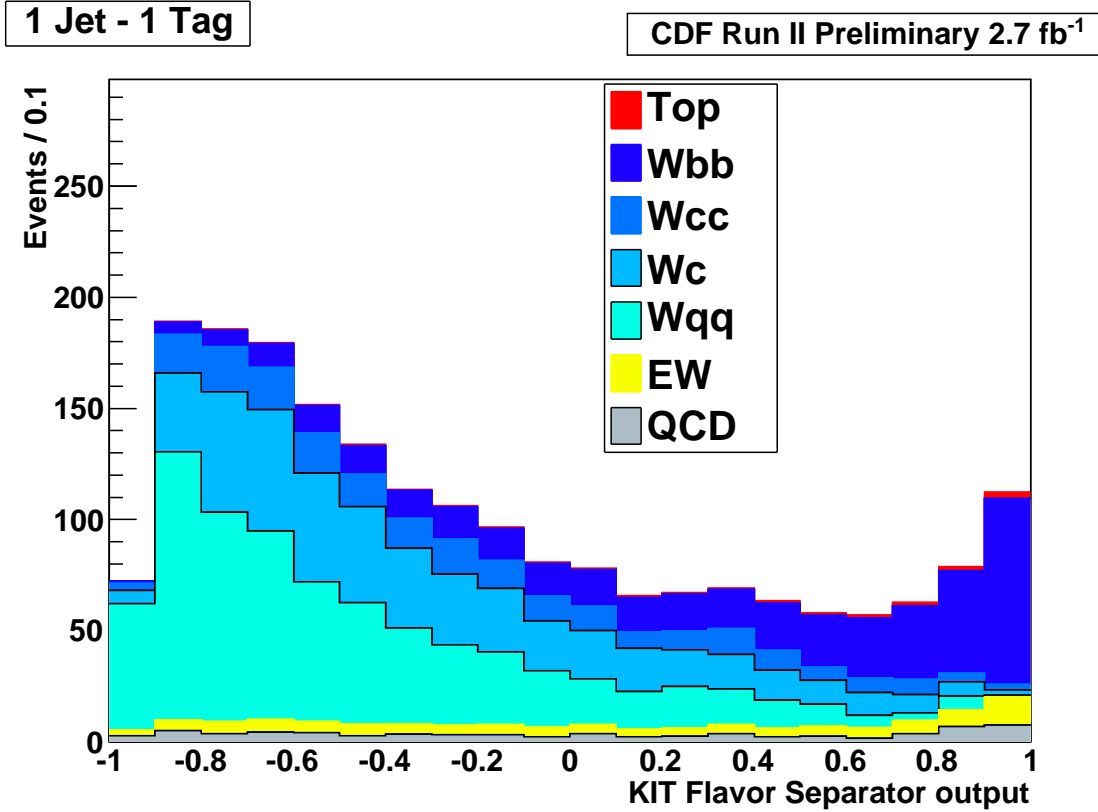


Figure 4.4: KIT Flavor Separator distribution in the 1-jet 1-tag bin.

The complete set of templates is shown in Figures 4.7 and 4.8. Figure 4.7 shows the KIT Flavor Separator templates, split by n_{jet} and n_{tag} bins and scaled to the expected yield corresponding to 2.7 fb⁻¹ of data. Figure 4.8 shows the projection of the templates on the n_{jet} distribution.

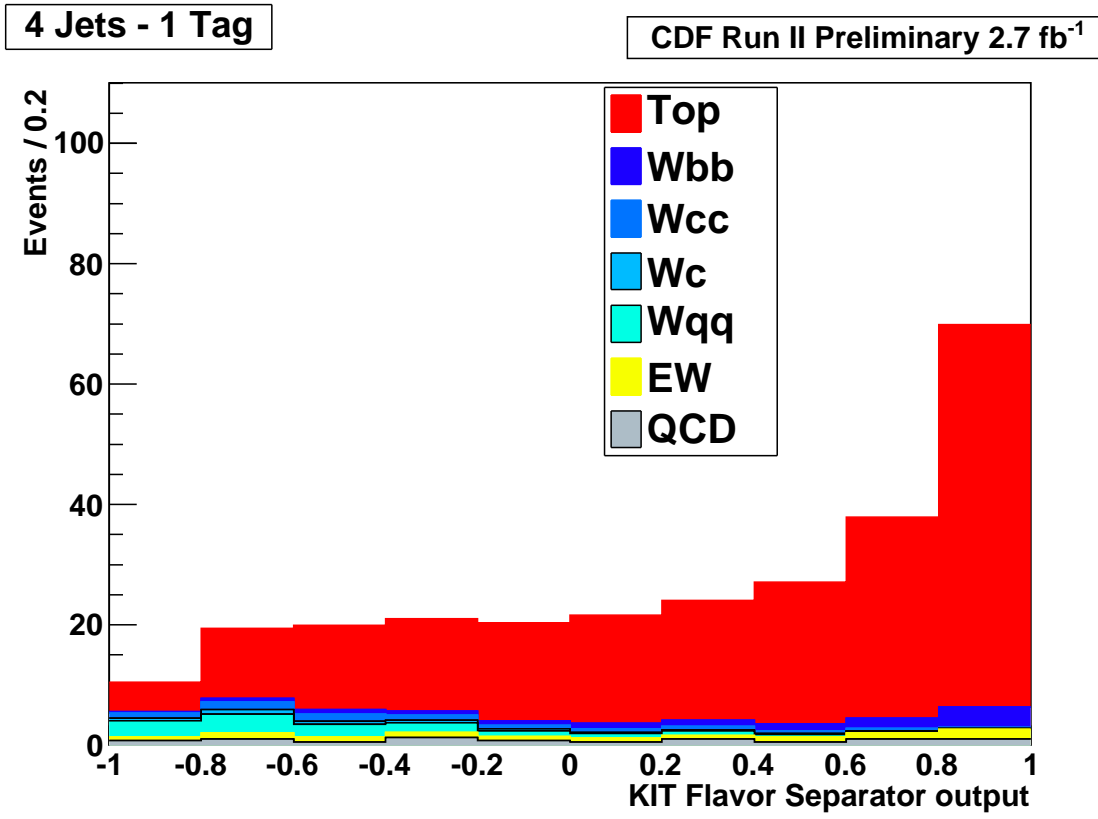


Figure 4.5: KIT Flavor Separator distribution in the 4-jet 1-tag bin.

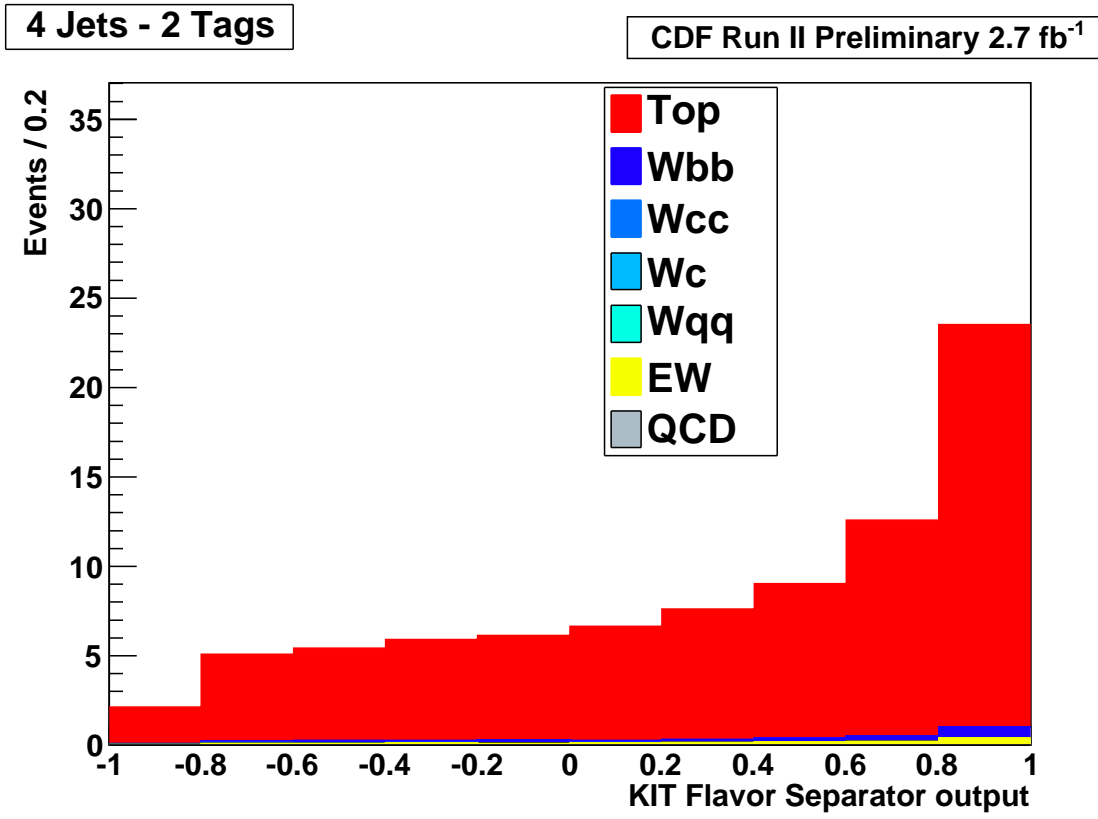


Figure 4.6: KIT Flavor Separator distribution in the 4-jet 2-tag bin.

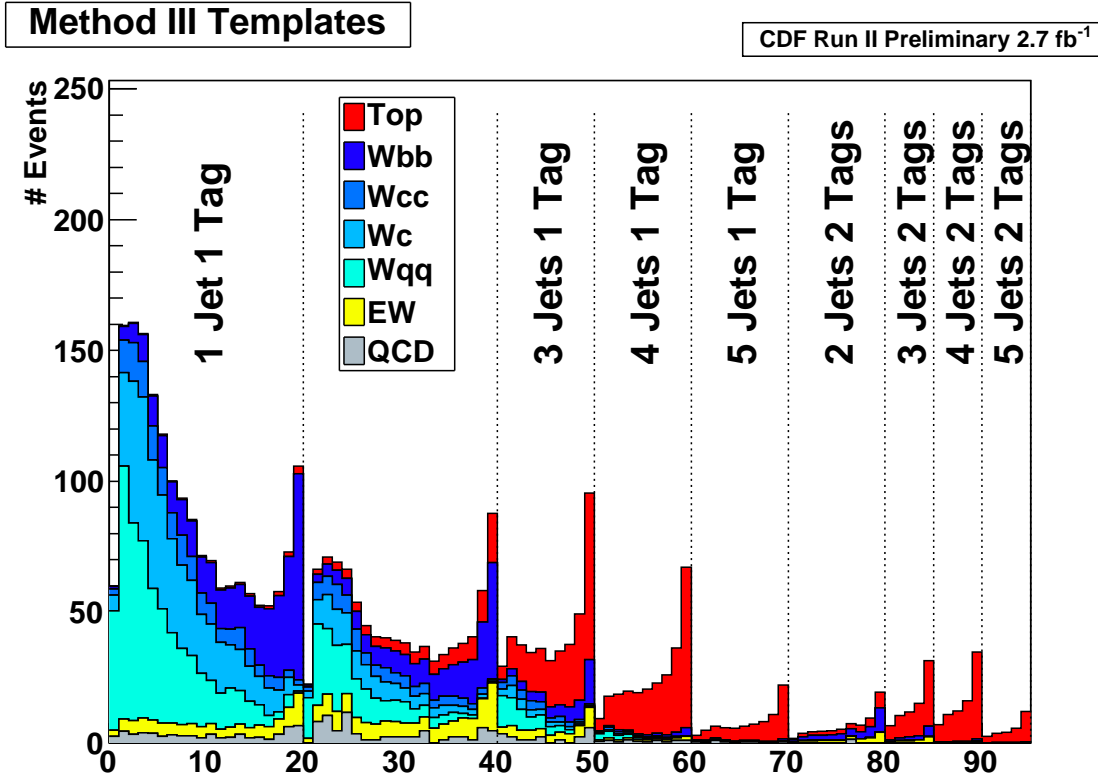


Figure 4.7: The complete set of all templates, split by n_{jet} and n_{tag} bins, normalized to the expected yield corresponding to 2.7 fb^{-1} of data.

Method III Templates N Jet Distribution

CDF Run II Preliminary 2.7 fb⁻¹

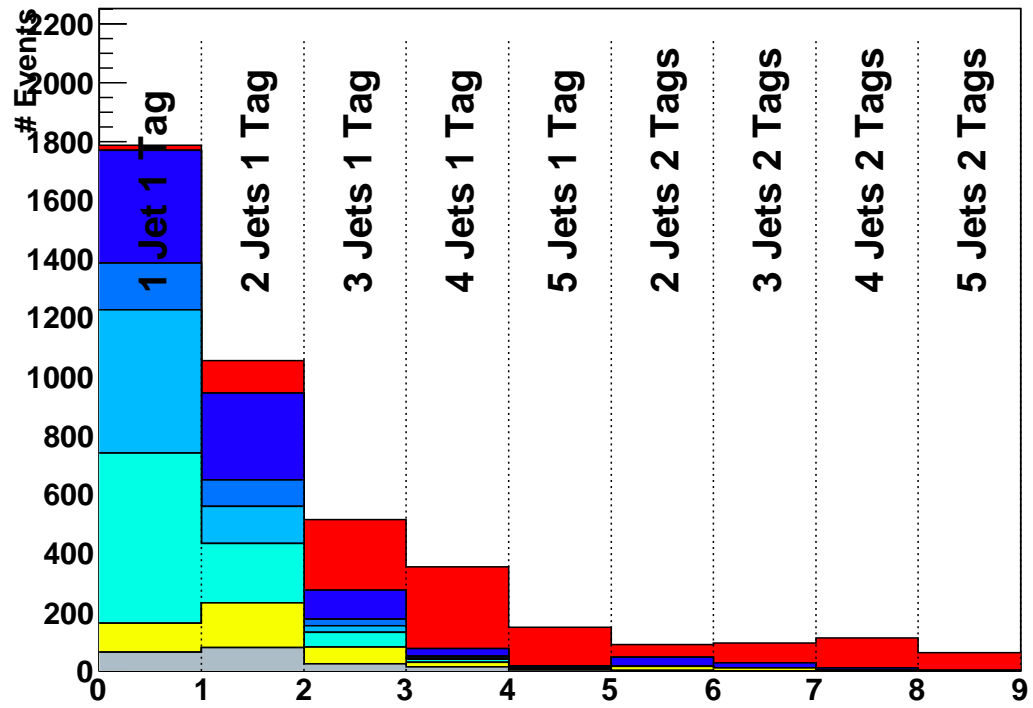


Figure 4.8: The complete set of all templates, scaled to the expected yield corresponding to 2.7 fb⁻¹ of data, projected onto the n_{jet} distribution.

Chapter 5

Event Selection

We use data collected from February 4, 2002 to April 16, 2008, obtained using two high- p_T lepton triggers: the electron trigger, `ELECTRON_CENTRAL_18_V`, and the muon-trigger, `MUON_CMUP18_V`. Full details about these two triggers can be found in Appendix A. The specific runs used are contained in the Good Run List v23 as defined by CDF’s Data Quality Monitoring group [34], based on availability of detector components. A full summary of the data used is shown in Table 5.1. This corresponds to 2.7 fb^{-1} of data.

The criteria required in order for an event to be considered “good” is designed so that only top events are analyzed. Ordinarily, these event selection criteria would be optimized for that effect; that is, the specific cuts applied and the order in which they’re applied would be confirmed to ensure that as much backgrounds have been removed as possible while retaining as many top events as possible. In this analysis,

Table 5.1: Information about the data used in this analysis. The electron-triggered data-sets, BHELXX, are shown; muon-triggered data-sets, BHMUX, were also used and have the same properties as the electron-triggered ones. Integrated luminosities are given in pb^{-1} .

Data-set	Date collected	Runs	Int. lumi
BHELMK	28 Feb 2008 – 16 Apr 2008	258880 – 261005	183.56
BHELMK	27 Jan 2008 – 27 Feb 2008	256840 – 258787	101.81
BHELMK	05 Dec 2007 – 27 Jan 2008	254800 – 256824	161.87
BHELMK	28 Oct 2007 – 03 Dec 2007	252836 – 254683	32.01
BHELMJ	13 May 2007 – 04 Aug 2007	241665 – 246231	280.86
BHELMJ	01 Apr 2007 – 13 May 2007	237845 – 241664	162.01
BHELMJ	31 Jan 2007 – 31 Mar 2007	233133 – 237795	234.99
BHELMJ	24 Nov 2006 – 30 Jan 2007	228664 – 233111	243.19
BHELMI	01 Sep 2006 – 22 Nov 2006	222529 – 228596	156.76
BHELMI	09 Jun 2006 – 01 Sep 2006	217990 – 222426	166.29
BHELKI	05 Sep 2005 – 22 Feb 2006	203819 – 212133	258.37
BHELKH	07 Dec 2004 – 04 Sep 2005	190697 – 203799	362.94
BHELKD	04 Feb 2002 – 22 Aug 2004	138425 – 186598	331.47

however, we start with the standard lepton-plus-jets selection (as shown in Table 5.2) and add a QCD veto cut but do not make any further optimization. This is because we fit for the backgrounds in the non-signal region and to estimate them in the signal region.

Table 5.2: Selection criteria for the lepton-plus-jets channel.

Variable	Selection Criteria
n_{jet}	≥ 1
Jet E_T	$\geq 20 \text{ GeV}/c^2$
Jet $ \eta $	< 2.0
Lepton	1 CEM electron, or CMUP or CMX muon
Lepton E_T	$\geq 20 \text{ GeV}/c^2$
n_{tag}	≥ 1 Tight SECVTX tag

The QCD backgrounds are extremely difficult to model, so it is advantageous to simply remove as much of the QCD contribution as possible. The missing transverse energy distribution for QCD peaks toward zero (see Chapter 6.3 for a detailed discussion); therefore, we require $\cancel{E}_T > 20$ GeV to eliminate much of the QCD contribution. Further elimination is possible by applying a combination of cuts called the Single Top QCD Veto [35]. The first cut in the veto exploits the fact that in top decays the lepton and the neutrino (which is the cause of the \cancel{E}_T ; indeed $p_T^\nu = \cancel{E}_T$) are decay products of a W boson, whereas in QCD background events the \cancel{E}_T comes from mis-measured jets, and so the invariant transverse mass of the W , m_T^W , makes a useful quantity. This is defined as

$$m_T^W = \sqrt{2(p_T^\ell p_T^\nu - p_x^\ell p_x^\nu - p_y^\ell p_y^\nu)} \quad (5.1)$$

and peaks near $80 \text{ GeV}/c^2$ for actual W events. In Equation 5.1 p_x^ν and p_y^ν are the x and y components of the \cancel{E}_T , respectively.

Further discrimination for electron samples is required as well, and is provided by both a tighter cut on m_T^W ($20 \text{ GeV}/c^2$) as well as a quantity called the *Missing Transverse Energy Significance* (*MET Significance* or *MetSig*). For QCD events, \cancel{E}_T can only show up as lost or mis-measured jets; one would thus expect the \cancel{E}_T to be small and in a similar direction as those mis-measured jets. The *MetSig* is defined as

$$MetSig = \frac{\cancel{E}_T}{\sqrt{\vec{E}_T^{\text{uncl}} \cdot \hat{\cancel{E}}_T}} \quad (5.2)$$

where the denominator is the amount of unclustered energy (that is, energy not

included in reconstructed jets) in the direction of the \cancel{E}_T , and acts as a measure of the uncertainty on the \cancel{E}_T .

The QCD elimination cuts and final selection criteria are shown in Table 5.3.

Table 5.3: Event selection criteria. The last three cuts together form the Single Top QCD Veto.

Variable	Selection Criteria
\cancel{E}_T	≥ 20 GeV
n_{tag}	1 or 2
Run	Good silicon
m_T^W	> 10 GeV/ c^2 for muons
m_T^W	> 20 GeV/ c^2 for electrons
$MetSig$	$> (-0.05m_T^W + 3.5)$ for electrons

It is useful to know how efficient the event selection criteria is at selecting top events while rejecting background events. This is done by calculating the acceptances for each sample. Event acceptances, \mathcal{A} , for all of our samples are shown in Tables 5.4. One- and two-tag acceptances are shown separately. The acceptance is defined as

$$\mathcal{A} = N_{\text{tagged}}/N_{\text{generated}} \quad (5.3)$$

Table 5.4: Event acceptances of each sample.

Sample	$N_{\text{generated}}$	N_{1-tag}	\mathcal{A}_{1-tag} (%)	N_{2-tag}	\mathcal{A}_{2-tag} (%)
Top	556,871	261,674	47.00	197,979	35.55
QCD	593,507	5,299	8.93	39	0.00
EW	3,873,284	180,800	4.67	74,899	1.93
$W + b\bar{b}$	2,143,278	233,001	10.87	120,379	5.62
$W + c\bar{c}$	2,736,006	69,050	2.53	32,496	1.19
$W + c$	4,015,745	125,446	3.13	80,224	2.00
$W + \text{LF}$	5,130,330	52,046	1.01	267	0.00

Chapter 6

Signal and Background Modeling

We estimate our signal contribution and most of the background contributions using Monte Carlo simulation. The signal Monte Carlo simulation sample was generated using PYTHIA v6.216, assuming a top mass of $m_t = 175 \text{ GeV}/c^2$. The sample was generated corresponding to the data yield of 2.7 fb^{-1} , but is stored as 1 fb^{-1} statistics for convenience. Indeed, all of our signal and background samples are stored in this manner.

As described in Chapter 2.2, the backgrounds for this study consist of $W + \text{jets}$ ($Wb\bar{b}$, $Wc\bar{c}$, Wc , $W + \text{light flavor}$), di-boson, single top, $Z + \text{jets}$ and QCD (the last of which is modeled by data). All non-QCD Monte Carlo simulation samples were generated by the Top Group using PYTHIA v6.216; MadGraph; or ALPGEN v2.10' with MLM matching and PYTHIA v6.326 for showering (see Chapter 3.2.3) [36]. When an event is simulated with two different generators (e.g., ALPGEN, with showering

done by PYTHIA), it’s possible for the same signature to be produced two different ways. MLM matching [37][38] is an algorithm which removes this double-counting of events.

Many Monte Carlo simulation samples have extra scale factors applied after the simulation, to account for effects which are not modeled properly in the simulation. Many of these factors are obtained through comparisons to data. It is important to note that the fit results we obtain will be on top of these extra factors.

All Monte Carlo simulation-based samples have a scale factor, ϵ_{lep} , to account for the trigger and lepton identification efficiencies that differ between data and Monte Carlo simulation [39] [40]. These efficiencies are averaged over all data periods, vary by lepton type, and are shown in Table 6.1.

Table 6.1: The values of ϵ_{lep} used for both electrons and muons.

Data Period	Lepton Type	ϵ_{lep}
0	CEM	0.9533
0	CMUP	0.8438
0	CMX	0.9760
1–17	CEM	0.9440
1–17	CMUP	0.8129
1–17	CMX	0.8534

Each of these processes is described in more detail in the following sections. See Appendix B.1 for the full list of generation parameters, and Appendix B.2 for details about all of the datasets used for both signal and background estimations.

6.1 $W + \text{Heavy Flavor}$

$W + \text{heavy flavor}$ backgrounds consist of $Wb\bar{b} + \text{jets}$, $Wc\bar{c} + \text{jets}$, and $Wc + \text{jets}$, as well as $Wq\bar{q} + \text{jets}$ that contains any heavy flavor. All $W + \text{jets}$ samples are normalized by a fixed scale factor, S_{σ_W} , to compensate for the difference between the true (‘all orders’) $W + \text{jets}$ production cross section and the cross section from ALPGEN (which is leading-order with some corrections), and is given by

$$S_{\sigma_W} = \frac{\sigma_{W_{true}}}{\sigma_{W_{ALPGEN}}} = 1.35 \quad (6.1)$$

Full details of these samples can be found in Table B.5 in Appendix B.2.

6.2 $W + \text{Light Flavor}$

$W + \text{light flavor}$ backgrounds consist of $W + \text{jets}$ events with no heavy flavor. As with the $W + \text{heavy flavor}$ backgrounds, these light flavor backgrounds also have the same scale factor, S_{σ_W} , given by Equation 6.1.

The Monte Carlo simulation samples for the $W + \text{light flavor}$ backgrounds have some heavy flavor contributions, due to the appearance of $b\bar{b}$ and $c\bar{c}$ pairs in the modeling of hadronization (via gluon splitting). These must be taken care of by a heavy flavor overlap algorithm. In our case, we move any event with heavy flavor to the appropriate $W + \text{heavy flavor}$ template.

Full details of these samples can be found in Table B.6 in Appendix B.2.

6.3 QCD

While much of the QCD background was eliminated with the Single Top QCD Veto (see Chapter 5), some remains and must be estimated. Anti-electrons¹ are particles that pass the same kinematic electron cuts as our signal sample but fail two of the electron ID cuts [41]. This ensures the particles are not identified as electrons, and thus do not come from W decays; as QCD is the only other process which can produce something with that signature, it must be the source of the anti-electrons. The anti-electron sample is a skim of the High p_T Central Electron sample in each period of data, and is created by the CDF Top Group [42]. It does a good job modeling the shape of the QCD background distribution, but its normalization is different due to changes in the electron ID cuts.

In order to get the proper normalization, we re-normalize the flavor-separator distribution by applying a scale factor, S_{QCD} . The S_{QCD} is calculated by fitting the \cancel{E}_T distributions from anti-electrons and $W + \text{jets}$ to the data. Applying the full selection criteria to the anti-electron sample would yield too few events for a proper fit; instead, the n_{tag} requirement is not applied (the \cancel{E}_T is also excluded). Because the fit is made to data with the n_{tag} requirement, however, the resulting scale factor is applied to the QCD template for that particular jet-tag bin. Figure 6.1 shows the \cancel{E}_T distribution for the 1-jet 1-tag bin from which the S_{QCD} is obtained. Table 6.2 shows the fixed scale factors used in this analysis for each jet- and tag-bin.

¹These are different than the anti-matter equivalent of electrons.

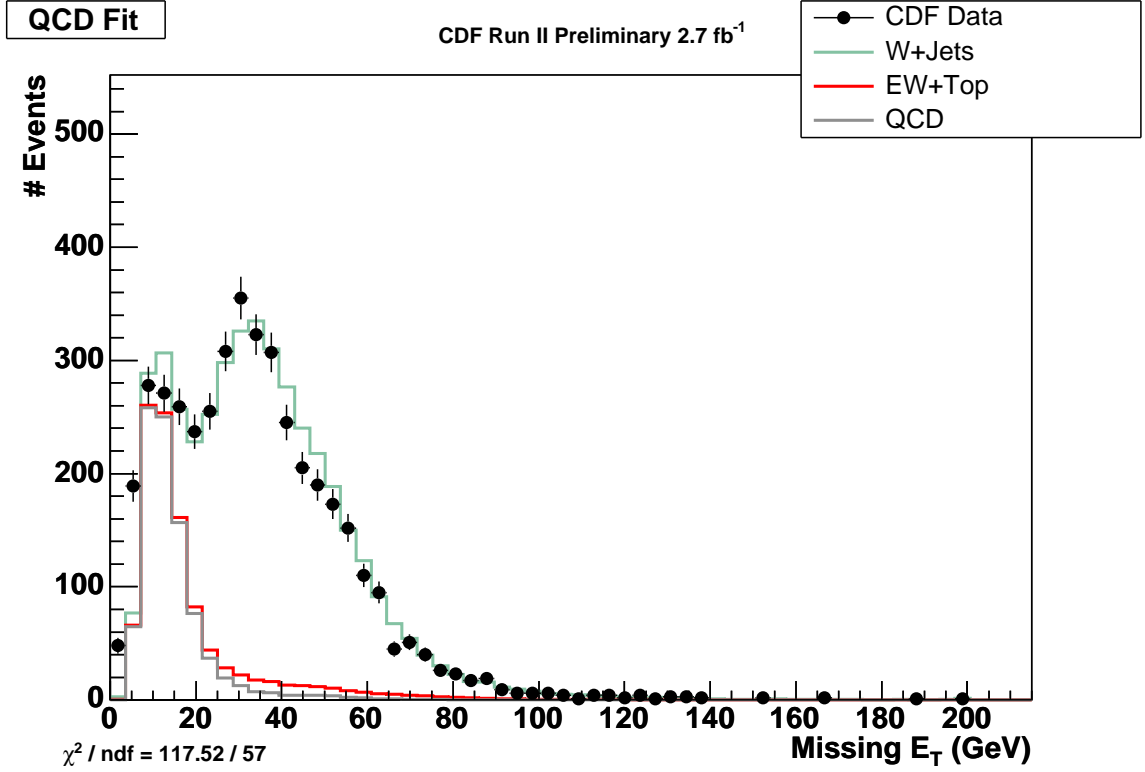


Figure 6.1: \cancel{E}_T fit of QCD and $W + \text{jets}$ to the data for the 1-jet 1-tag bin. From this, the S_{QCD} for that jet and tag bin is obtained. Note that a large fraction of the QCD distribution lies below the $\cancel{E}_T \leq 20$ GeV cut we apply.

Table 6.2: The values of S_{QCD} used in each jet- and tag-bin, for tight tags.

Jet- and Tag-Bin	S_{QCD}
1 jet, 1 tag	0.0707343
2 jets, 1 tag	0.285361
3 jets, 1 tag	0.287186
4 jets, 1 tag	0.14526
5 jets, 1 tag	0.139088
2 jets, 2 tags	0.00562856
3 jets, 2 tags	1.21568×10^{-07}
4 jets, 2 tags	6.81147×10^{-10}
5 jets, 2 tags	3.52158×10^{-10}

6.4 Other Electroweak Processes

The other electroweak processes we consider as backgrounds for this analysis include single top (both s - and t -channel), di-boson (WW , WZ , ZZ), and Z + jets. Similar to the W + jets events above, the Z + jets samples need to be rescaled by a K -factor to take into account contributions from higher-order processes that are not included in ALPGEN. We use $K = 2.0$ for the Z + heavy flavor samples and $K = 1.4$ for Z + light flavor samples [43], and these are not allowed to float in the fit.

Full details of these samples can be found in Table B.3 in Appendix B.2.

6.5 Mistags

All of the Monte Carlo simulation samples, including our top signal sample, have the potential of one or more light flavor jets being mistakenly tagged as a b -jet (a *mistag*). Unfortunately, the tagging algorithm applied during the simulation does a poor job of modeling the observed mistag rate. We apply a separate algorithm called the *mistag parameterization* or *mistag matrix* [44] to re-normalize the shape produced by the simulation so that it agrees with the observed mistag rate.

Chapter 7

Fitter

The fitter is a binned Poisson likelihood fitter, based on the MINUIT package [45] of the ROOT analysis software [46], that combines the templates according to the normalizations and fits them to data.

The set of templates for all samples are combined by normalizing them to the predicted yield for 2.7 fb^{-1} , where the normalization factors are functions of other physical quantities (cross sections and various scale factors), which are all parameters in the fit. The individual normalizations of the templates are allowed to float freely in the fit, except the QCD and Electroweak templates whose normalizations are constrained by Gaussian penalty terms. However, the normalization of a given sample does not float by jet- and tag-bins. For example, the size of the Top 4-jet, 1-tag bin is tied directly to the size of the Top 2-jet, 2-tag bin.

In addition to the template normalizations, several scale factors and systematic

uncertainties are included in the fit. The systematic uncertainty “shifts” (see Chapter 8) also float within Gaussian constraints, which are derived from a separate set of templates as described below. All parameters of the fit are initialized to yield the theoretical cross sections of the samples; all systematic shifts are initialized to zero.

7.1 Treatment of Systematic Effects

There are several physical variables that link the templates, including the $t\bar{t}$ production cross section, $W + \text{jets}$ K-factors, and K-factors for Electroweak and QCD samples. These float in the fit and are ultimately determined by the data. Other effects are known externally within some errors, and still more effects are based on some modeling assumptions. The former set of effects includes the b -tag scale factor, the Jet Energy Scale, the mistag rate, the amount of initial- and final-state radiation in the decay, and the energy scale (Q^2) of the interaction, while the latter set includes the shape of the QCD distribution, the parton showering model, the parton distribution functions, and the KIT Flavor Separator correction. These two sets of effects are all included as systematics in the analysis (see Chapter 8 for descriptions of each of these effects). Each of these externally-known effects is applied as a multiplicative factor to a subset of the templates by parameterizing their effect. When the effect does not deviate from its nominal value, the multiplicative factor is 1.0.

Parameterizing the systematic factors is done with functions¹, $P_N^x(i, j, R_x)$ that

¹We call these functions *PolyNoids*

depend on the jet-bin j , tag-bin i and the relative shift, R_x , of the factor. We require that $P_N^x(i, j, 0) \equiv 1$; that is, with no systematic shift the function returns the nominal yields. The parameterization function for a given (systematic) effect (e.g., I/FSR) is obtained by first remaking templates with the desired effect changed. Together with the nominal template, this yields three values of template normalization (five for JES). The points — of normalization versus deviation from the nominal value — are then interpolated with a polynomial. The resulting polynomial function describes, in terms of the shifted variable, the effect of the relative change, R_x , of the parameter in question, x , on the normalization. This "shift" parameter becomes another floating factor in the fit. See Figure 7.1 for examples of the fitted functions, and see Appendix B.4 for full details about all of the functions used.

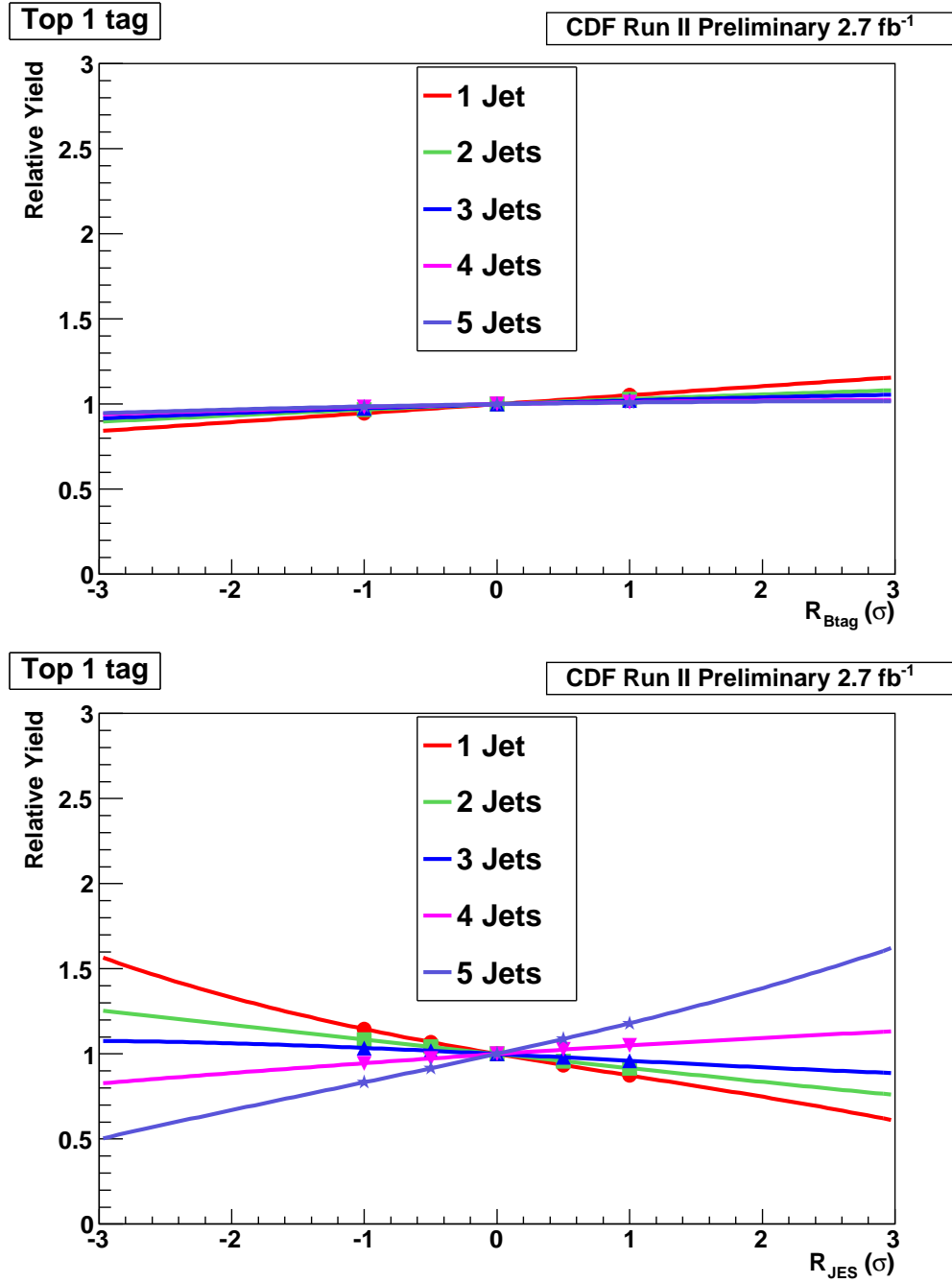


Figure 7.1: Examples of the functional forms of the template normalization as systematic effects are shifted. Shown at the top are the Top 1-tag event yields as the b -tag scale factor is shifted. Shown at the bottom are the Top 1-tag event yields as the Jet Energy Scale is shifted.

7.2 Preparing for the Fit

The total expected yield for each template in a given jet-bin j and tag-bin i is a function of several different quantities, as mentioned previously. These include the normalization factors for each sample, $\sigma_{t\bar{t}}$ and K_A ; the event yield from Monte Carlo simulations $N_x^{MC}(i, j)$; w_{ALP} , a weighting factor to account for the different sizes of the Monte Carlo simulation samples; the scale factor for trigger and lepton ID efficiencies, ϵ_{lep} , as shown in Table 6.1 in Chapter 6; the integrated luminosity, $L = \int \mathcal{L} dt$; the probability that i out of j jets are b -tagged, $\mathcal{B}(i, j)$; S_{σ_W} , given by Equation 6.1 in Chapter 6.1; and the parameterized functions for systematic effect, x , $P_N^x(i, j, R_x)$. The expected event yields in jet-bin j and tag-bin i are given in Equations 7.1 – 7.7.

$$N_{t\bar{t}}^{pred}(i, j) = \sigma_{t\bar{t}} \cdot N_{t\bar{t}}^{MC}(i, j) \cdot w_{ALP} \cdot \epsilon_{lep} \cdot L \cdot \mathcal{B}(i, j) \cdot P_N^{I/FSR}(i, j, R_{I/FSR}) \cdot P_N^{Btag}(i, j, R_{Btag}) \cdot P_N^{Mistag}(i, j, R_{Mistag}) \cdot P_N^{JES}(i, j, R_{JES}) \quad (7.1)$$

$$N_{Wbb}^{pred}(i, j) = K_{Wbb} \cdot N_{Wbb}^{MC}(i, j) \cdot w_{ALP} \cdot \epsilon_{lep} \cdot L \cdot S_{\sigma_W} \cdot \mathcal{B}(i, j) \cdot P_N^{Btag}(i, j, R_{Btag}) \cdot P_N^{Mistag}(i, j, R_{Mistag}) \cdot P_N^{JES}(i, j, R_{JES}) \cdot P_N^{Q^2}(i, j, R_{Q^2}) \quad (7.2)$$

$$N_{Wc\bar{c}}^{pred}(i, j) = K_{Wc\bar{c}} \cdot N_{Wc\bar{c}}^{MC}(i, j) \cdot w_{ALP} \cdot \epsilon_{lep} \cdot L \cdot S_{\sigma_W} \cdot \mathcal{B}(i, j) \cdot P_N^{Btag}(i, j, R_{Btag}) \cdot P_N^{Mistag}(i, j, R_{Mistag}) \cdot P_N^{JES}(i, j, R_{JES}) \cdot P_N^{Q^2}(i, j, R_{Q^2}) \quad (7.3)$$

$$N_{Wc}^{pred}(i, j) = K_{Wc} \cdot N_{Wc}^{MC}(i, j) \cdot w_{ALP} \cdot \epsilon_{lep} \cdot L \cdot S_{\sigma_W} \cdot \mathcal{B}(i, j) \cdot P_N^{Btag}(i, j, R_{Btag}) \cdot P_N^{Mistag}(i, j, R_{Mistag}) \cdot P_N^{JES}(i, j, R_{JES}) \cdot P_N^{Q^2}(i, j, R_{Q^2}) \quad (7.4)$$

$$N_{Wq\bar{q}}^{pred}(i, j) = K_{Wq\bar{q}} \cdot N_{Wq\bar{q}}^{MC}(i, j) \cdot w_{ALP} \cdot \epsilon_{lep} \cdot L \cdot S_{\sigma_W} \cdot \mathcal{B}(i, j) \cdot P_N^{Mistag}(i, j, R_{Mistag}) \cdot P_N^{JES}(i, j, R_{JES}) \cdot P_N^{Q^2}(i, j, R_{Q^2}) \quad (7.5)$$

$$N_{EW}^{pred}(i, j) = K_{EW} \cdot N_{EW}^{MC}(i, j) \cdot w_{ALP} \cdot \epsilon_{lep} \cdot L \cdot \mathcal{B}(i, j) \cdot P_N^{Btag}(i, j, R_{Btag}) \cdot P_N^{Mistag}(i, j, R_{Mistag}) \cdot P_N^{JES}(i, j, R_{JES}) \quad (7.6)$$

$$N_{QCD}^{pred}(i, j) = K_{QCD} \cdot N_{QCD}^{MC}(i, j) \cdot S_{QCD}(i, j) \quad (7.7)$$

The total event tagging probability, $\mathcal{B}(i, j)$, is calculated by figuring all permutations of how i b -tags can be selected among j jets. The probability of a single jet being

b -tagged is dependent upon the flavor of the jet as well as whether it is tagged during the simulation (as explained in Chapter 6.5, however, we do not trust the tagging algorithm in the simulation completely). This probability, \mathcal{P} , of a single jet being tagged is shown in Equation 7.8, where S_{btag} is the b -tagging scale factor, and S_{mis} is given by the mistag parameterization.

$$\mathcal{P} = \begin{cases} S_{btag} & \text{heavy flavor jet tagged during simulation} \\ 0 & \text{heavy flavor jet not tagged during simulation} \\ S_{mis} & \text{light flavor jet} \end{cases} \quad (7.8)$$

The fitter minimizes the negative log likelihood given by Equation 7.9 where the sum over k is over histogram bins, j over n_{jet} , i over n_{tag} , x is over the sample types (e.g., Top, Wbb, QCD), and the constraints l are listed in Table 7.1

$$\begin{aligned} -2 \ln L = -2 \left\{ \sum_{i,j}^{tag,jet \text{ bins}} \sum_k (\ln \mathcal{P}(N^{data}(i,j)_k, \sum_x^{samples} N_x^{pred}(i,j)_k)) - \right. \\ \left. \frac{1}{2} \sum_l^{constraints} \frac{(z_l - \bar{z}_l)^2}{\sigma_l^2} \right\} \end{aligned} \quad (7.9)$$

where \mathcal{P} is a Poisson probability that the predicted yield given by the templates statistically overlaps with the data. This probability is given by

$$\ln \mathcal{P}(x, y) = x \ln y - y - \ln \Gamma(x + 1) \quad (7.10)$$

where $\Gamma(x)$ is the mathematical Gamma function.

The normalizations of each sample ($\sigma_{t\bar{t}}$ and the K_A factors) are free to float in the fit. These normalizations are initialized to the yield for 2.7 fb^{-1} based on the theoretical cross sections, except for the $t\bar{t}$ template, which is initialized to a cross section of 1 pb so that an additional normalization factor is the $t\bar{t}$ cross section in picobarns.

Because of the theoretical cross section, the electroweak normalization is Gaussian constrained to within 10%. The QCD normalization is similarly constrained to 30%, due to comparisons between E_T fits in the anti-electron and jet-electron samples (see Chapter 6.3). These initial normalizations, as well as the systematic shifts and any applicable constraints, are shown in Table 7.1.

Table 7.1: The various parameters included in the fit.

Parameter	Initial Value	Constraint
$\sigma_{t\bar{t}}$ (pb)	1.0	none
$K_{Wb\bar{b}}$	1.0	none
$K_{Wc\bar{c}}$	1.0	none
K_{Wc}	1.0	none
$K_{Wq\bar{q}}$	1.0	none
K_{EW}	1.0	0.1
K_{QCD}	1.0	0.3
R_{Btag}	0.0	1.0
R_{Mistag}	0.0	1.0
R_{JES}	0.0	1.0
R_{Q^2}	0.0	1.0
$R_{I/FSR}$	0.0	1.0

7.3 Pseudoexperiments

We ran 16,000 pseudoexperiments to ensure that the fitter works correctly. Values are chosen (thrown) for each of our samples and uncertainties. The values chosen are based on theoretical cross sections or K-factors measured using other procedures, and are shown in Figures 7.2 – 7.8. These form pseudotemplates from which random values are chosen to be “data” points. The fitter is run on these “fake data” templates, and

the fit results compared to the thrown values.

As the pseudoexperiments mimic what will happen with actual data, they provide an estimate of the total uncertainties on each parameter. These expected errors are shown in Figures 7.9 – 7.15.

Since the data points are generated by throwing random numbers off of the templates, the pull distributions, shown in Figures 7.16 – 7.22, should be unit Gaussians with a mean of zero. The pull is calculated as

$$\text{Pull} = \frac{\text{Measured} - \text{Generated}}{\text{Error}}. \quad (7.11)$$

Any bias in the samples will show up as a deviation of the pull from a unit Gaussian. The $Wc + \text{jets}$ pull (in Figure 7.17) shows a bias of approximately -13% , which we discovered was due to the Q^2 systematic effect. By excluding the Q^2 systematic, the pull becomes a zero-mean unit Gaussian, as desired. As the pull for the top sample is unaffected by this and remains a zero-mean unit Gaussian, it does not affect the cross section measurement.

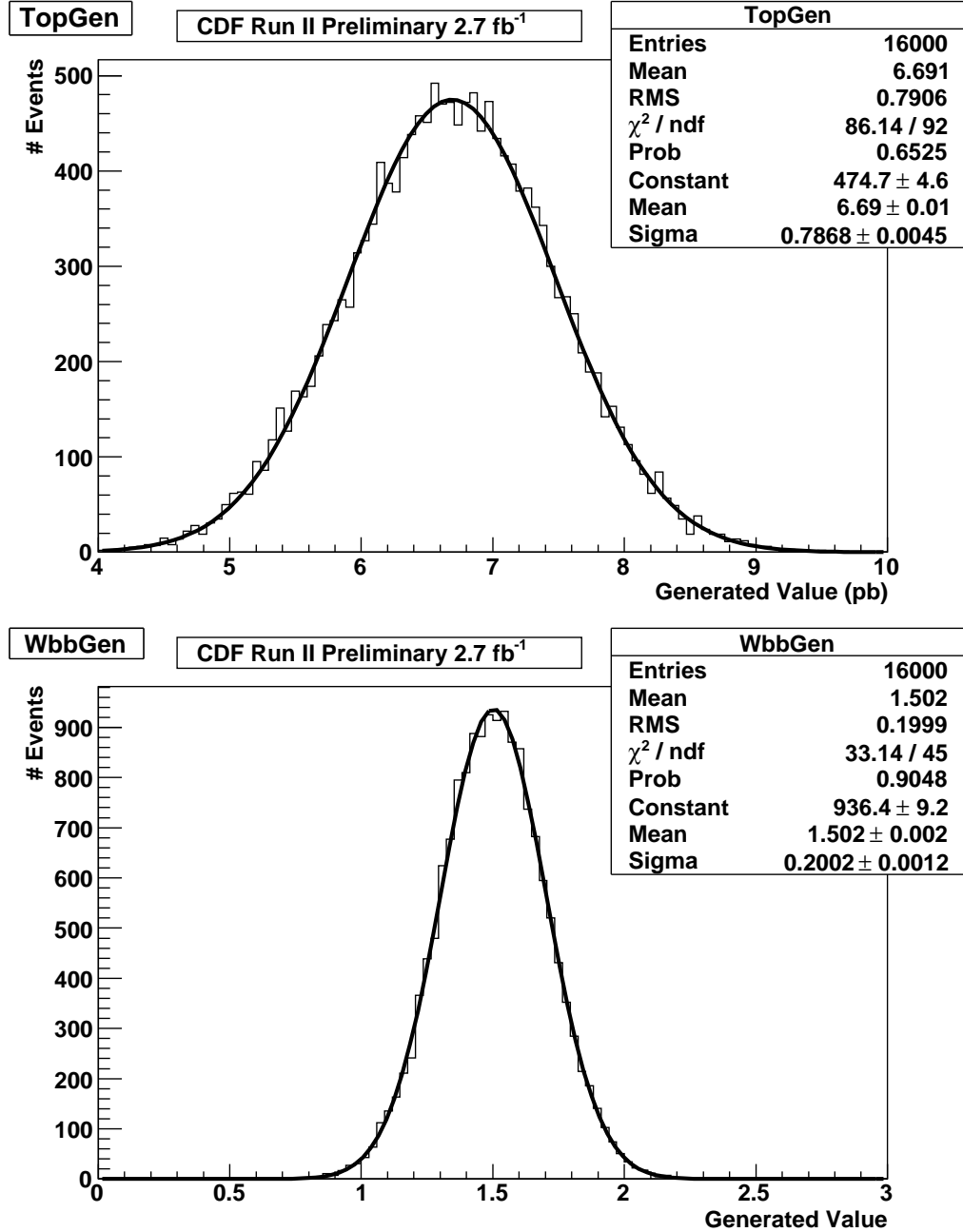


Figure 7.2: Generated values in the pseudoexperiments for Top and $Wb\bar{b} + \text{jets}$ samples. The Top pseudotemplates are generated at the theoretical cross section, while the $Wb\bar{b} + \text{jets}$ ones are generated at 1.5 times the rate predicted by ALPGEN.

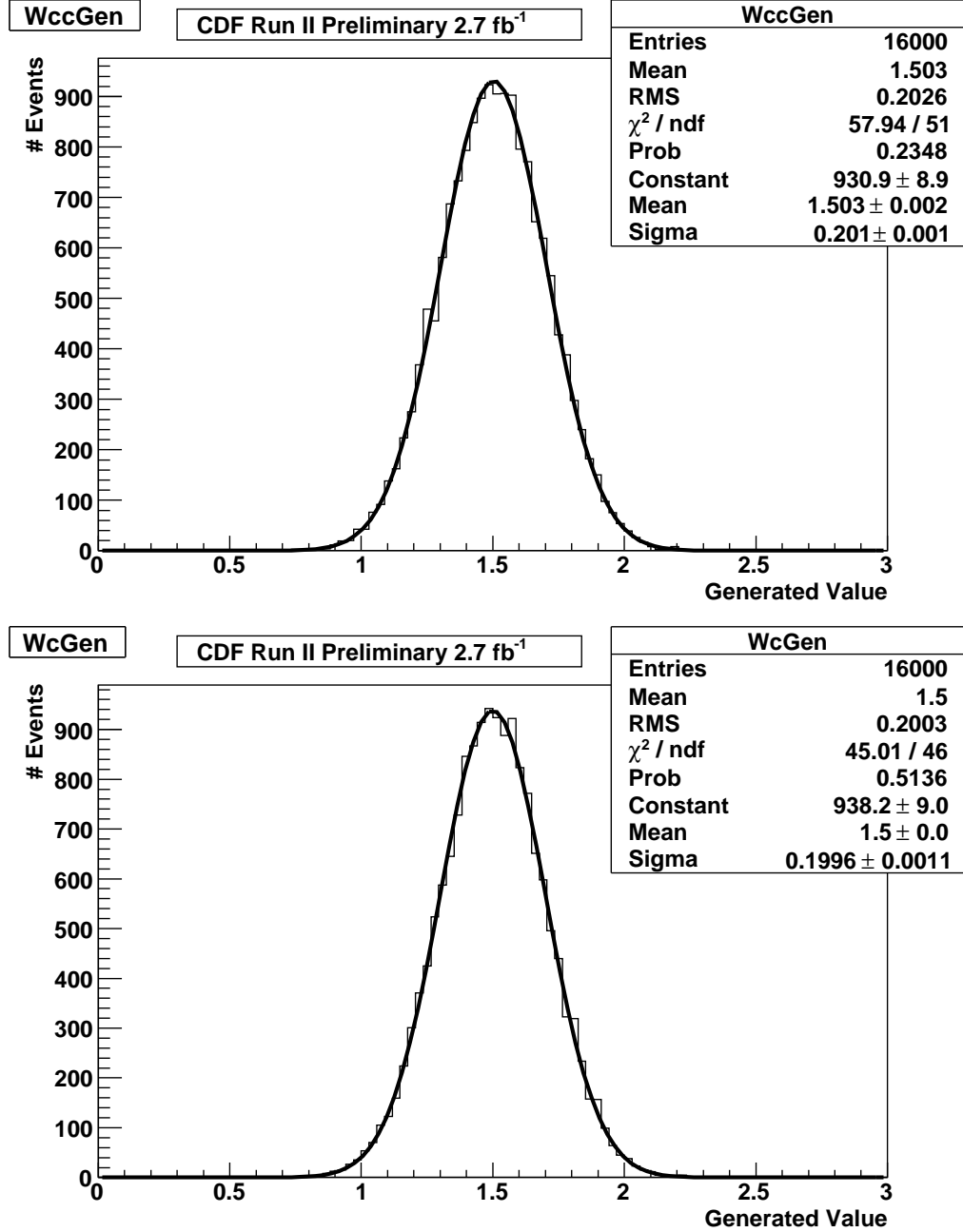


Figure 7.3: Generated values in the pseudoexperiments for $Wc\bar{c} + \text{jets}$ and $Wc + \text{jets}$ samples. Both are generated at 1.5 times the rate predicted by ALPGEN.

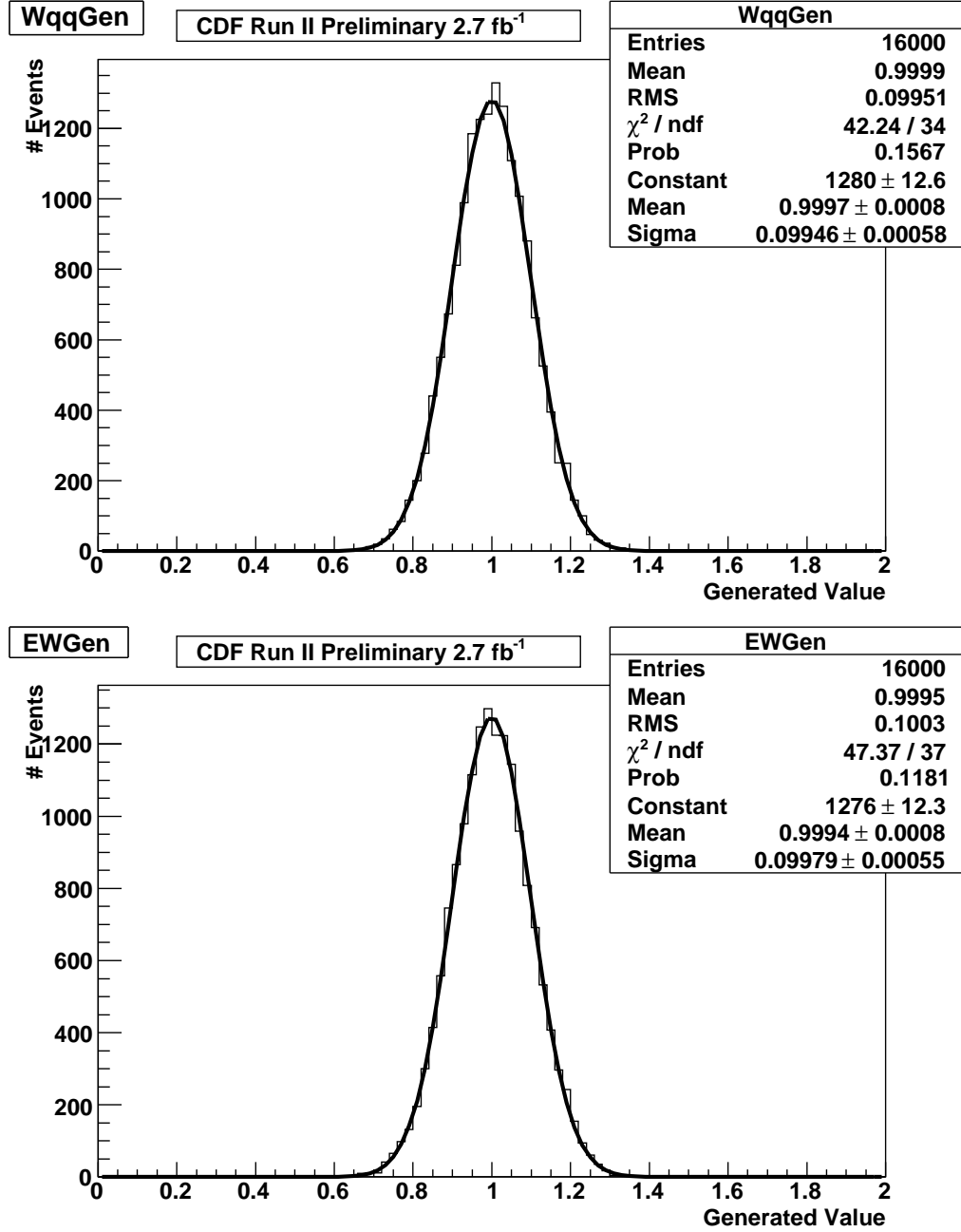


Figure 7.4: Generated values in the pseudoexperiments for $W \rightarrow q\bar{q}'$ and Electroweak samples. Both are generated at the rate predicted by ALPGEN.

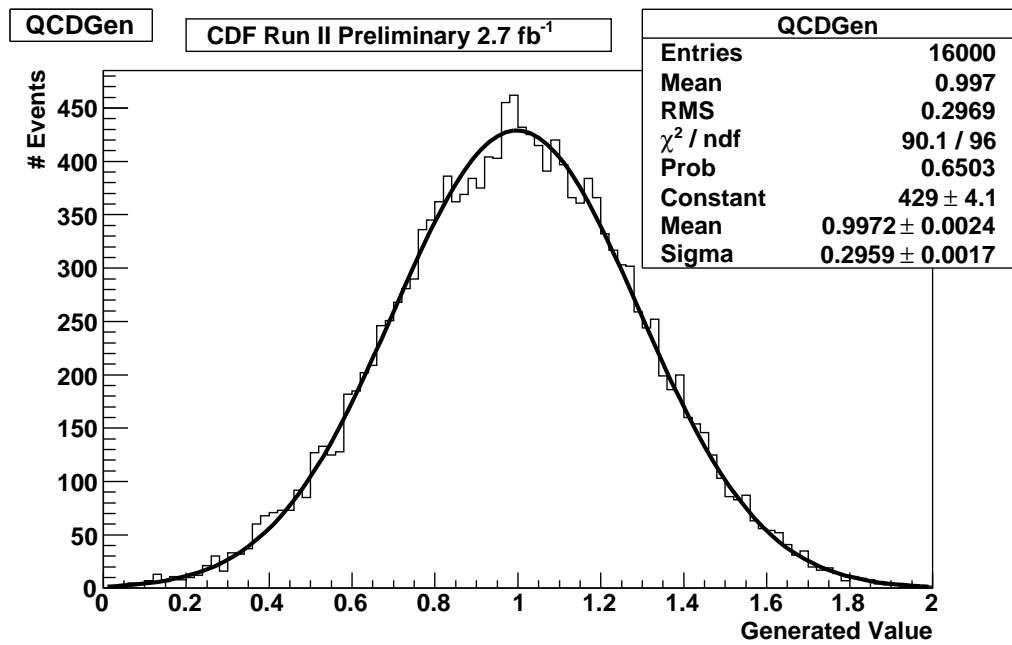


Figure 7.5: Generated values in the pseudoexperiments for the QCD sample. The pseudotemplates are generated at the theoretical cross section.

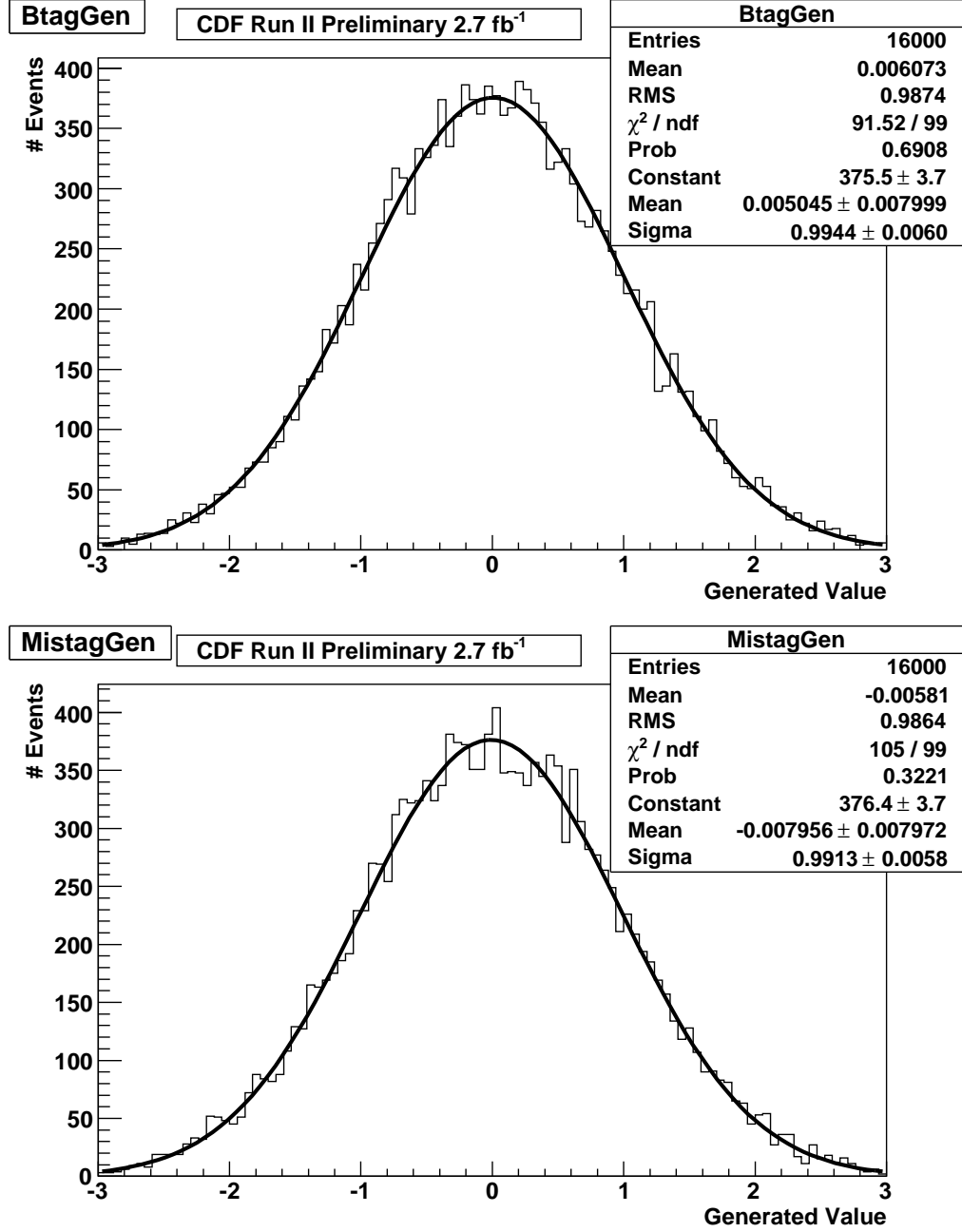


Figure 7.6: Generated values in the pseudoexperiments for the Btag and Mistag systematic uncertainties. They are generated at an initial shift of zero, with a one sigma Gaussian constraint.

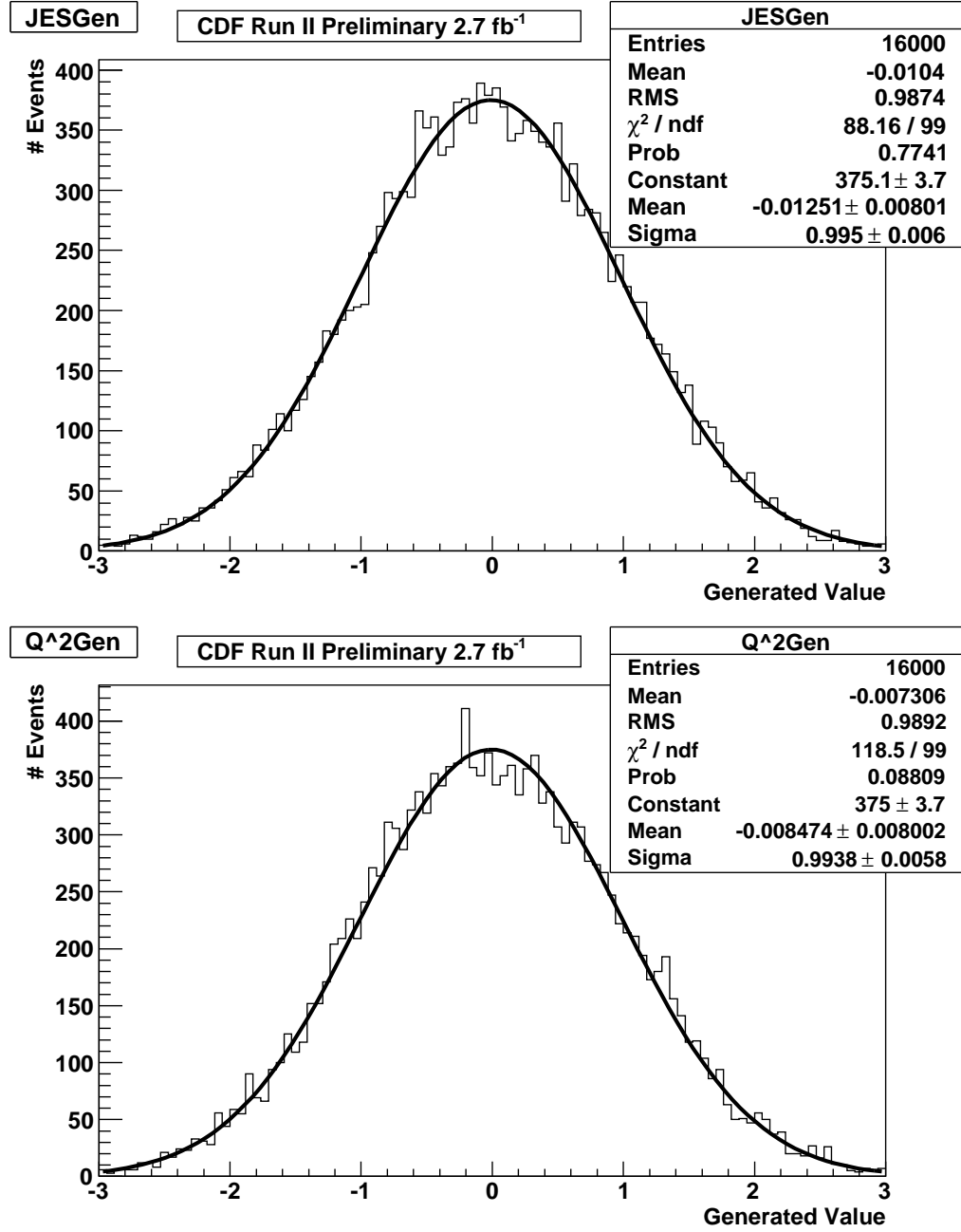


Figure 7.7: Generated values in the pseudoexperiments for the Jet Energy Scale and Q^2 systematic uncertainties. They are generated at an initial shift of zero, with a one sigma Gaussian constraint.

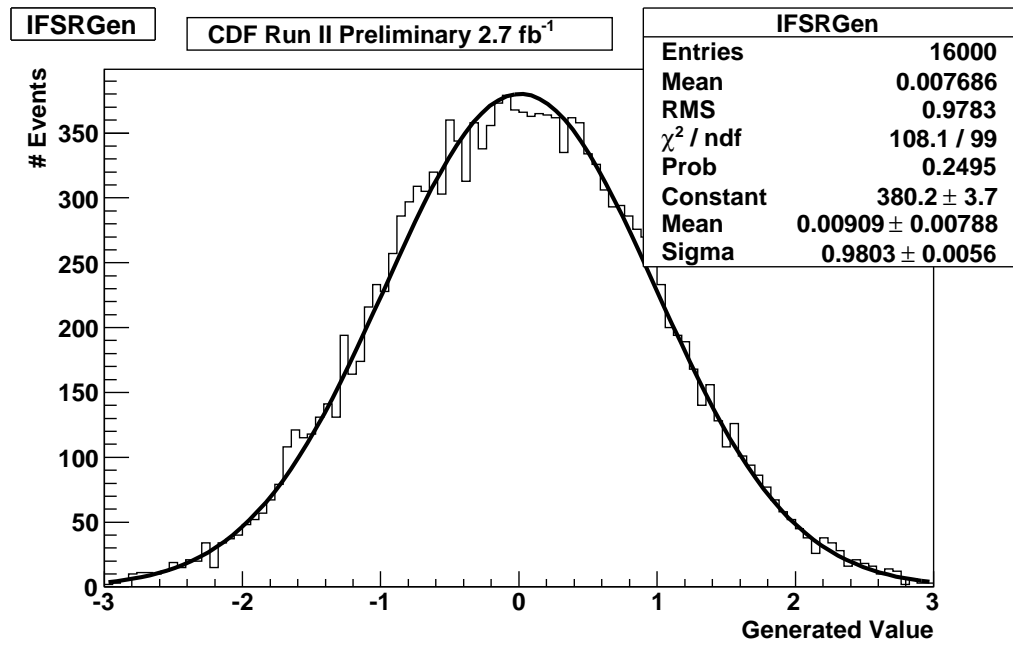


Figure 7.8: Generated values in the pseudoexperiments for the I/FSR systematic uncertainty. They are generated at an initial shift of zero, with a one sigma Gaussian constraint.

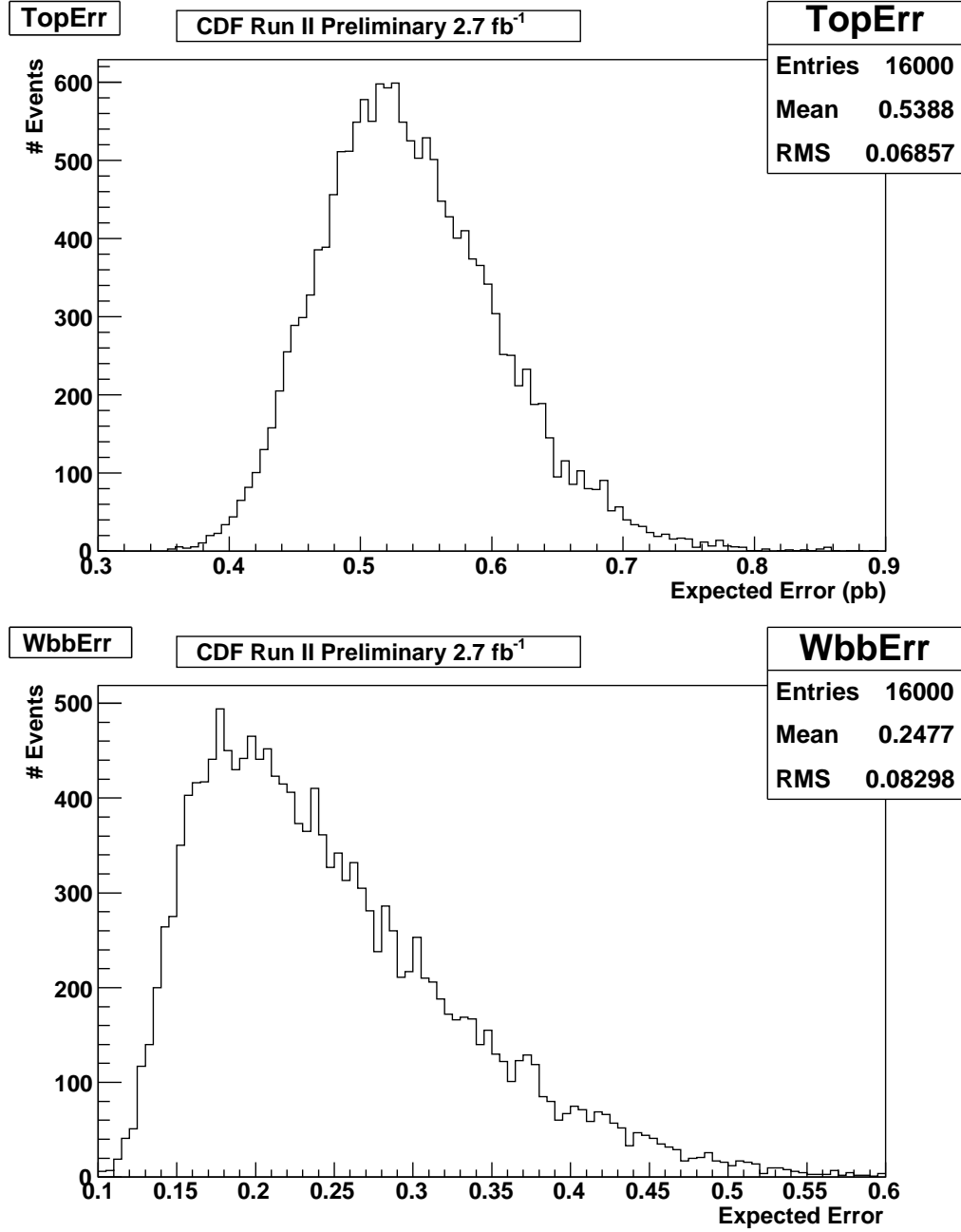


Figure 7.9: Expected errors for the Top and $Wb\bar{b} + \text{jets}$ samples.

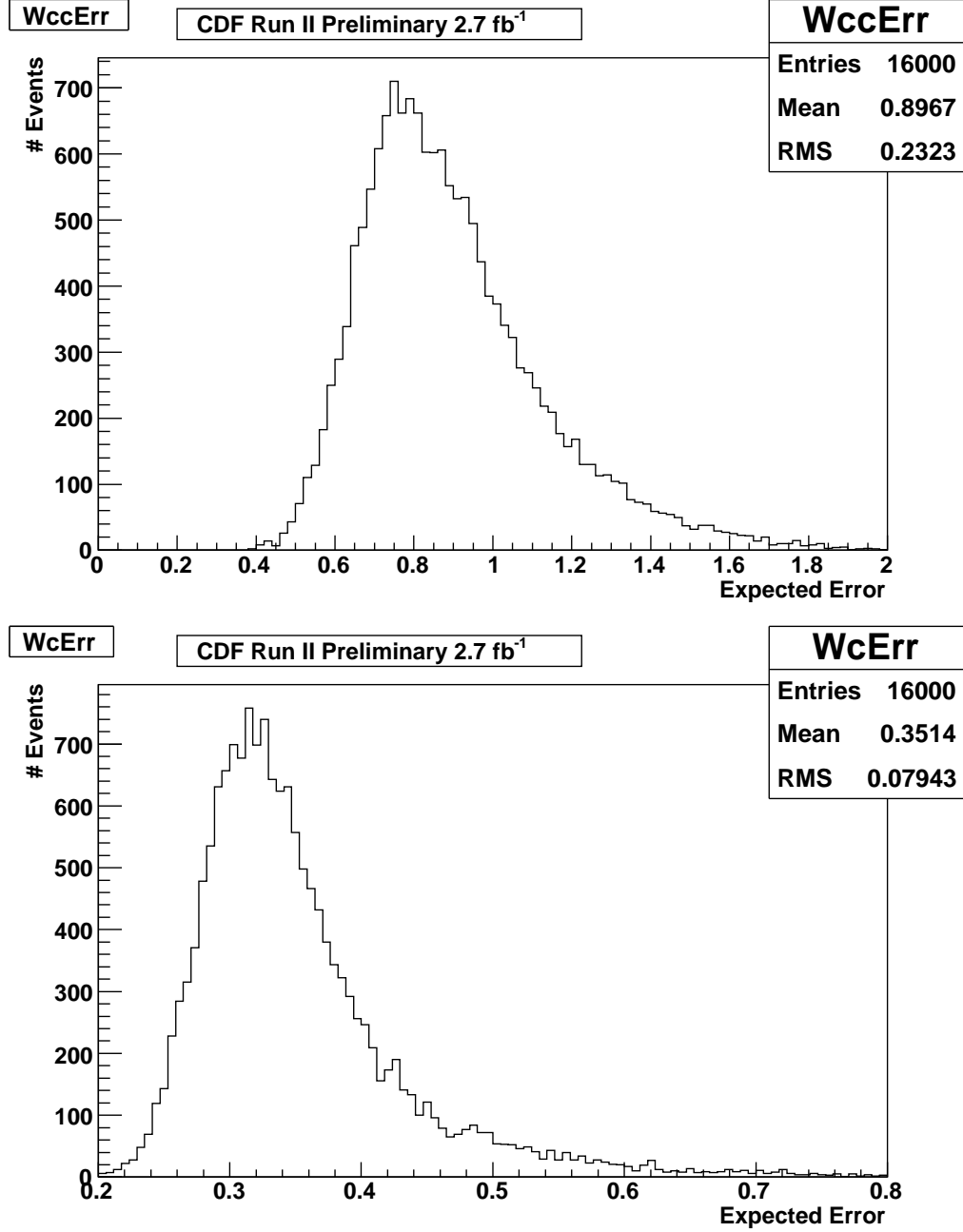


Figure 7.10: Expected errors for $Wc\bar{c} + \text{jets}$ and $Wc + \text{jets}$ samples.

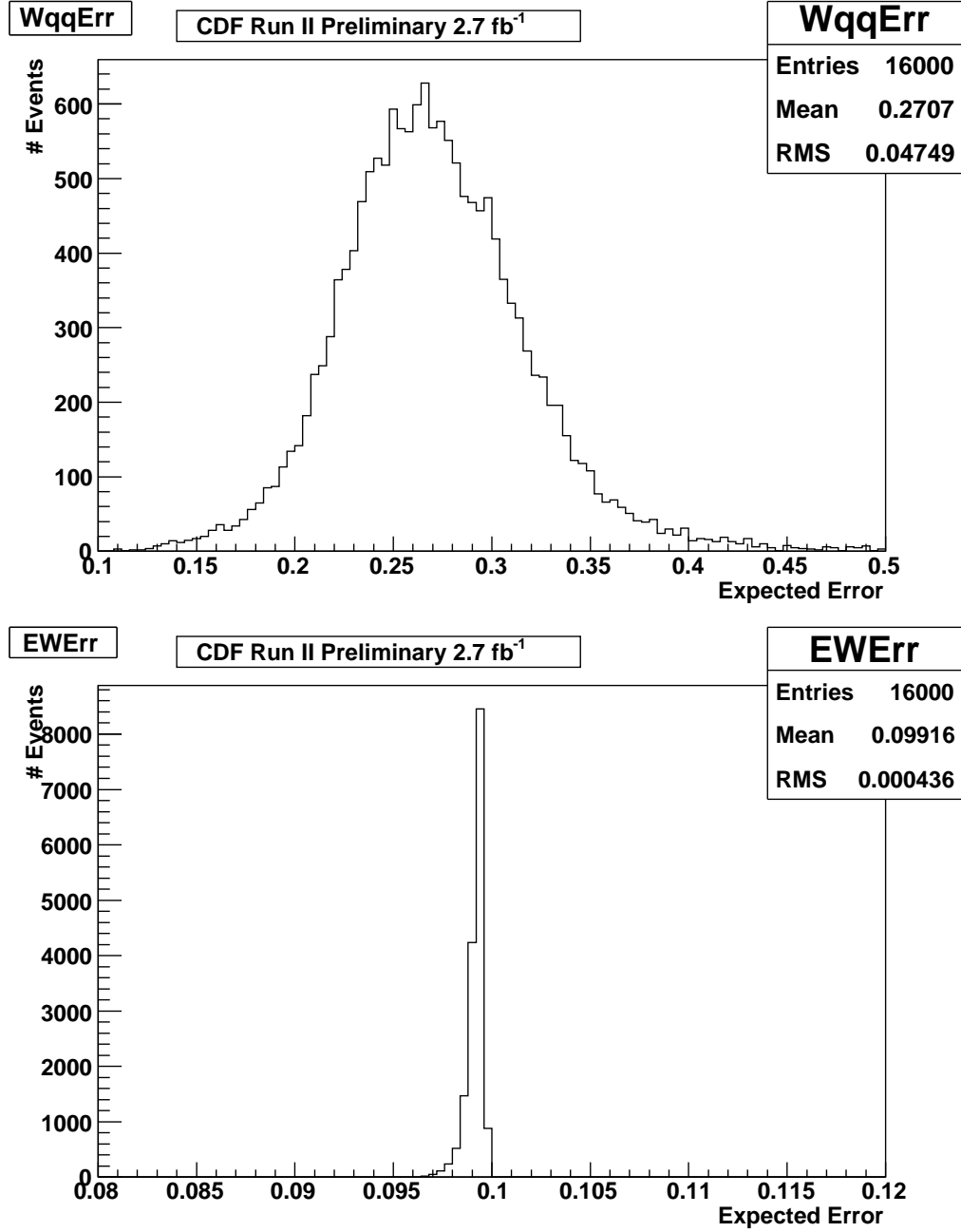


Figure 7.11: Expected errors for the $W \rightarrow q\bar{q}'$ and electroweak samples.

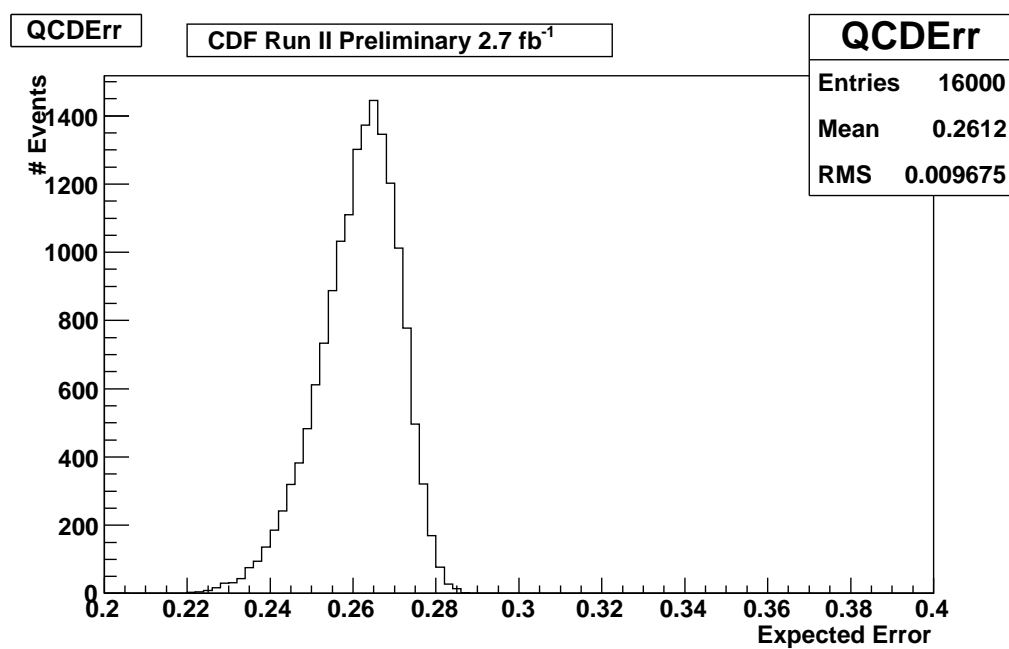


Figure 7.12: Expected errors for the QCD sample.

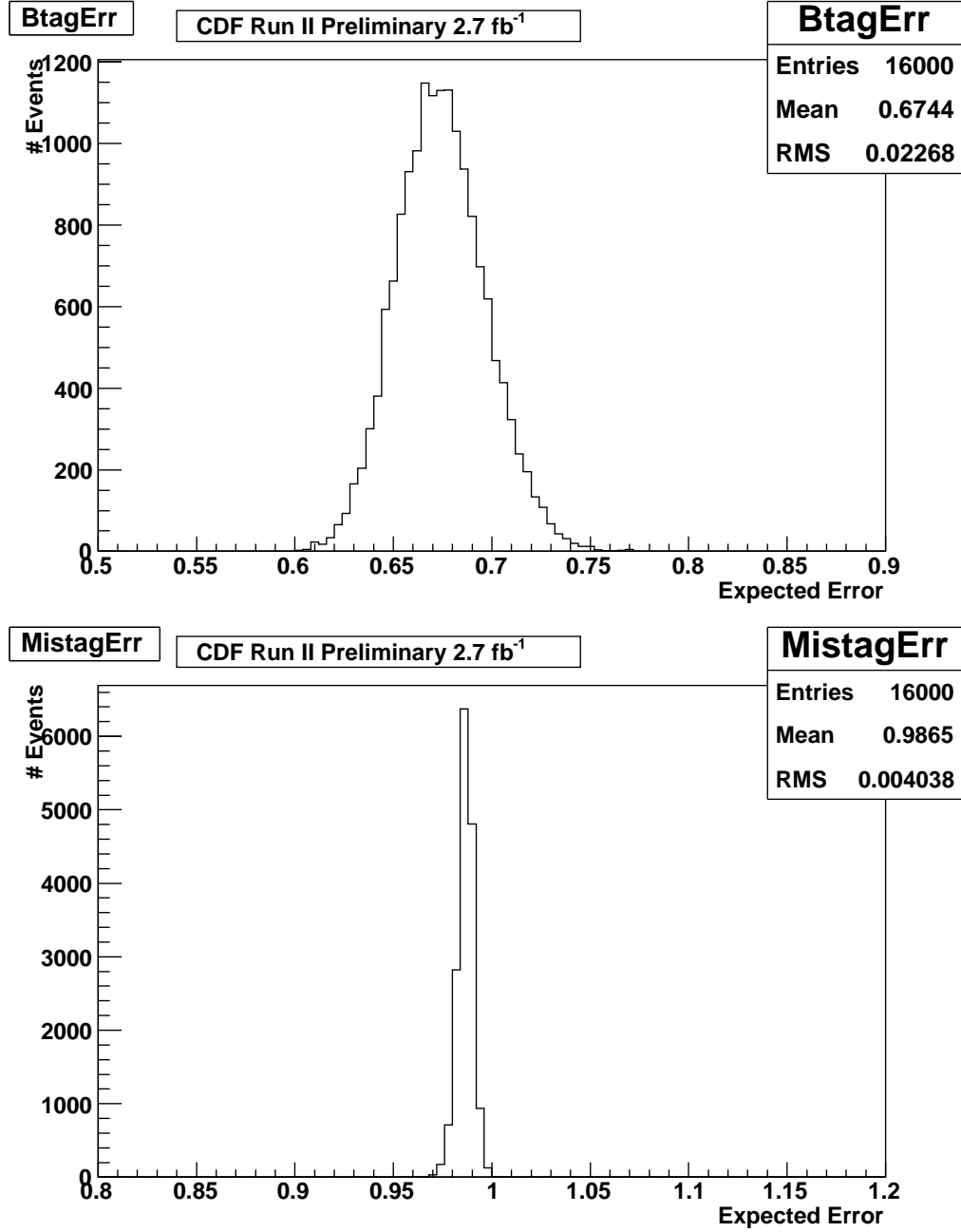


Figure 7.13: Expected errors for the Btag and Mistag systematic uncertainties.

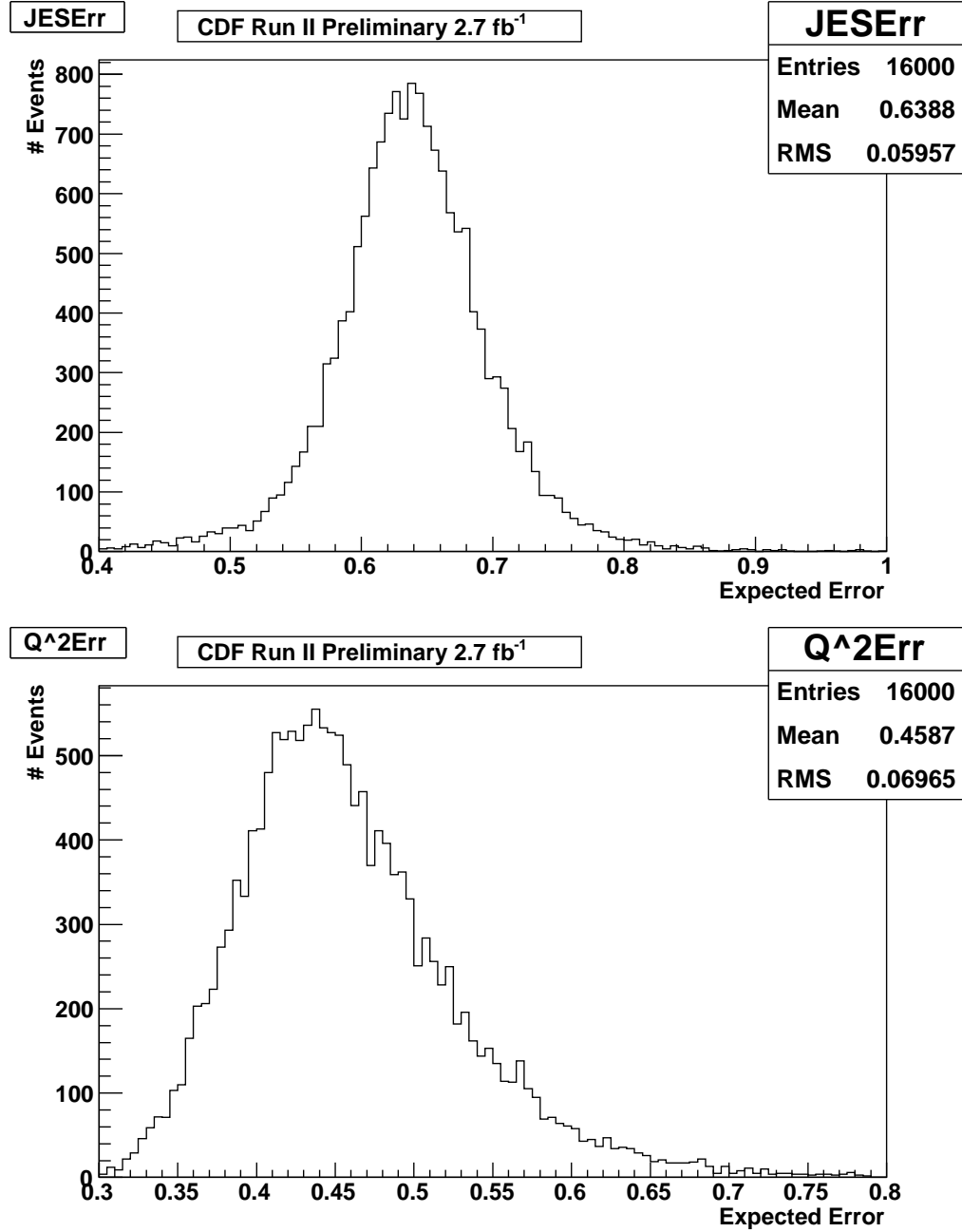


Figure 7.14: Expected errors for the Jet Energy Scale and Q^2 systematic uncertainties.

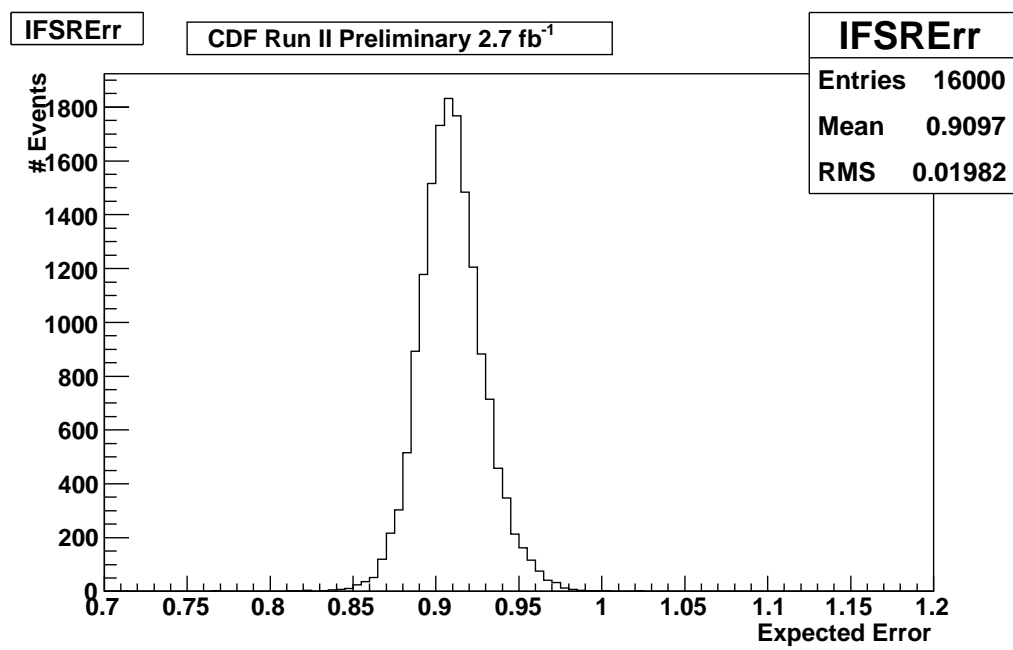


Figure 7.15: Expected errors for the I/FSR systematic uncertainty.

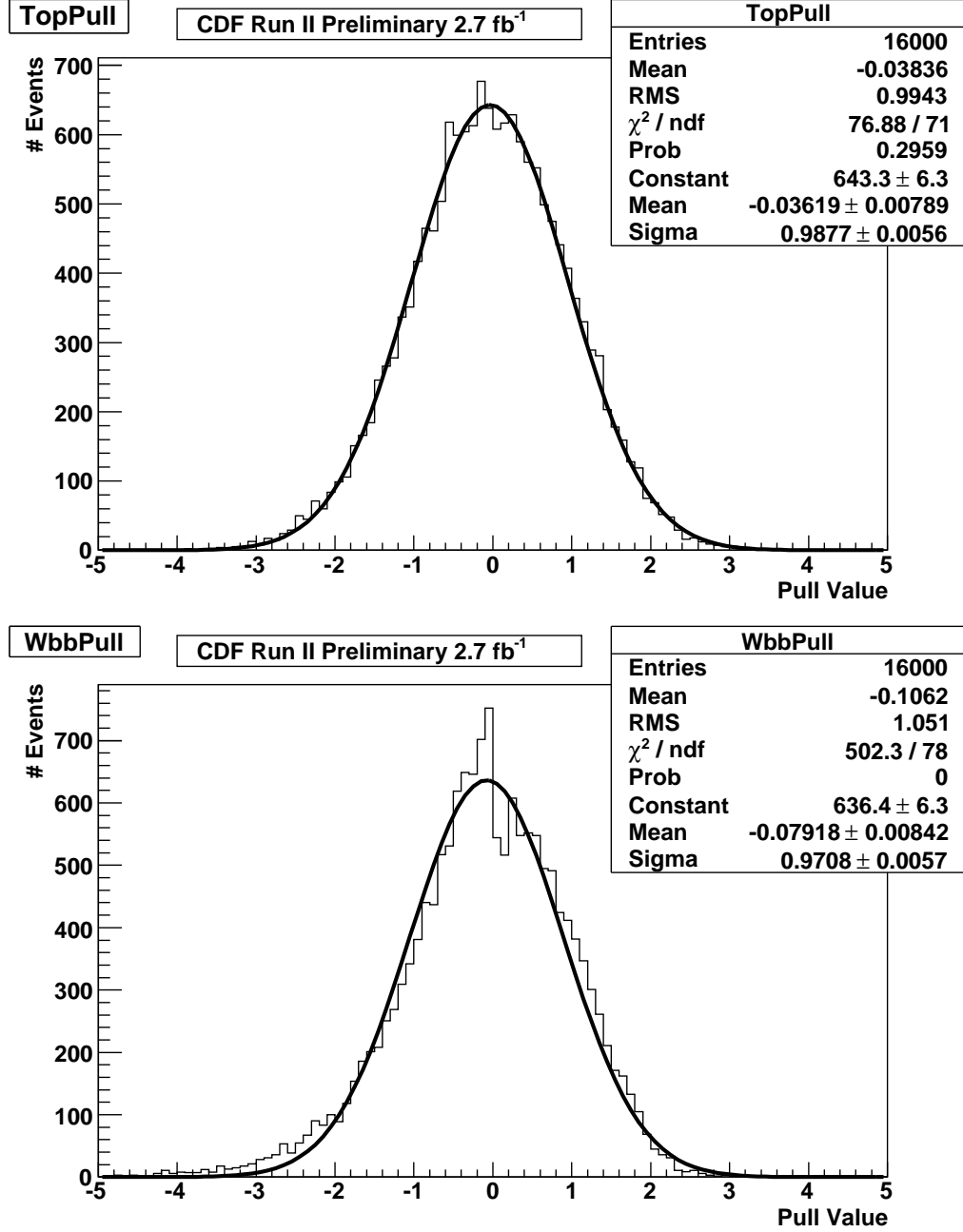


Figure 7.16: Pseudoexperiment pull distributions the Top and $Wb\bar{b} + \text{jets}$ samples.

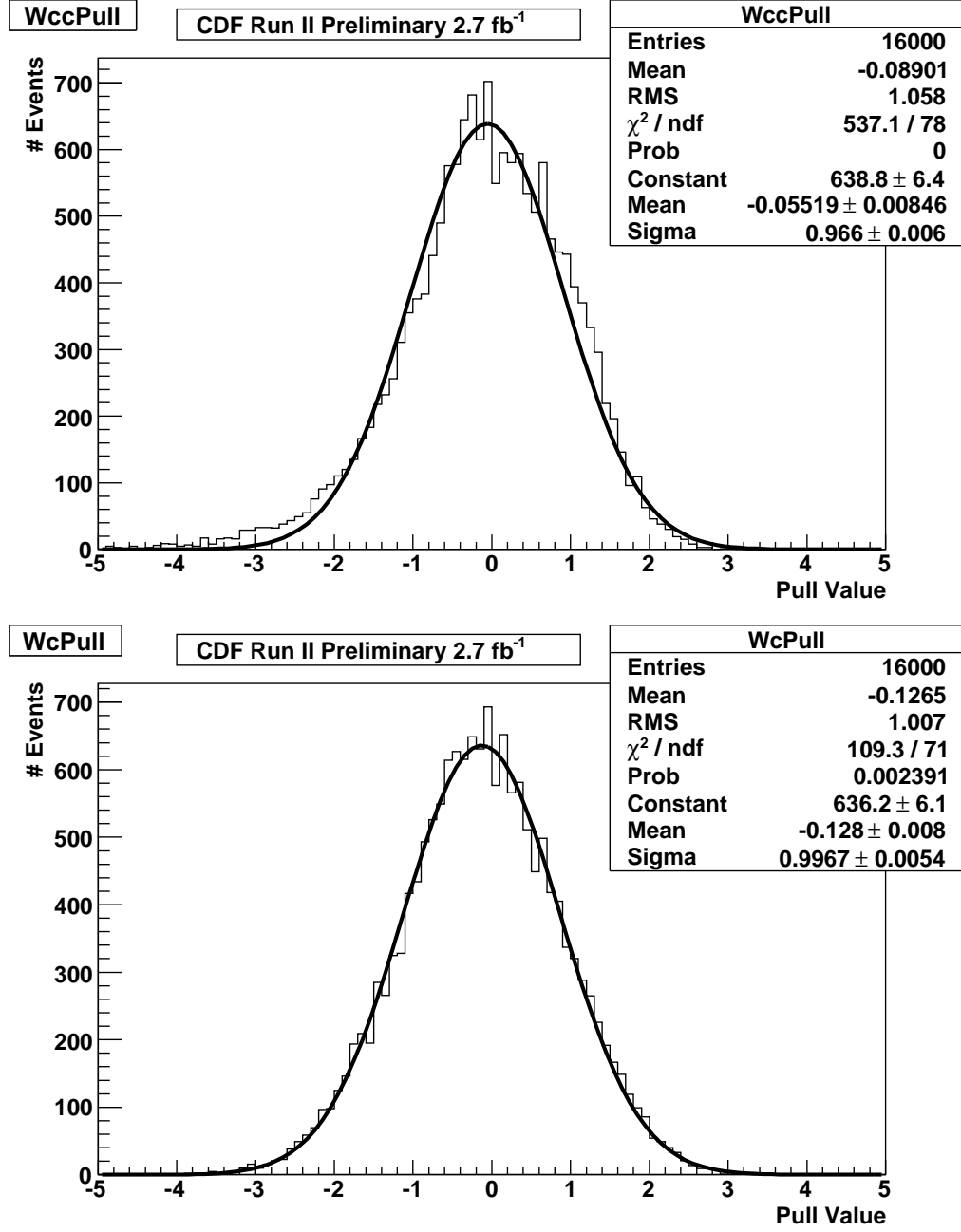


Figure 7.17: Pseudoexperiment pull distributions the $Wc\bar{c} + \text{jets}$ and $Wc + \text{jets}$ samples.

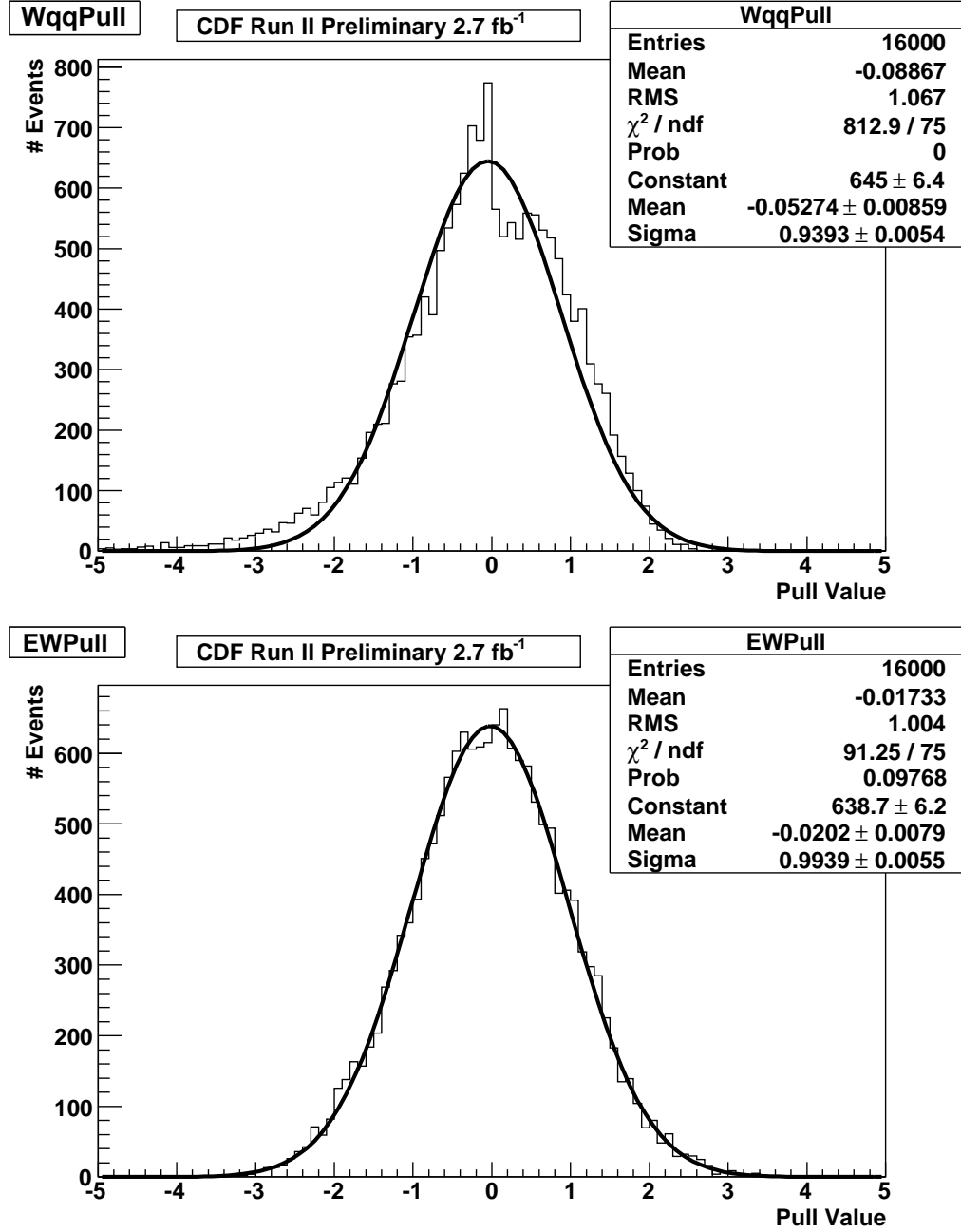


Figure 7.18: Pseudoexperiment pull distributions the $W \rightarrow q\bar{q}'$ and electroweak samples.

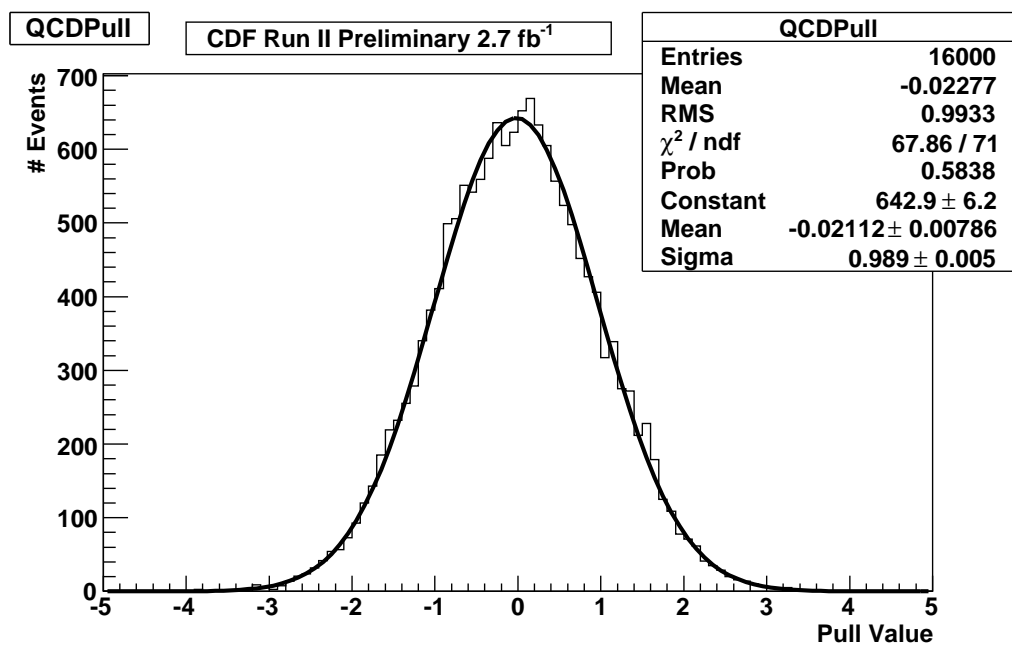


Figure 7.19: Pseudoexperiment pull distribution for the QCD samples.

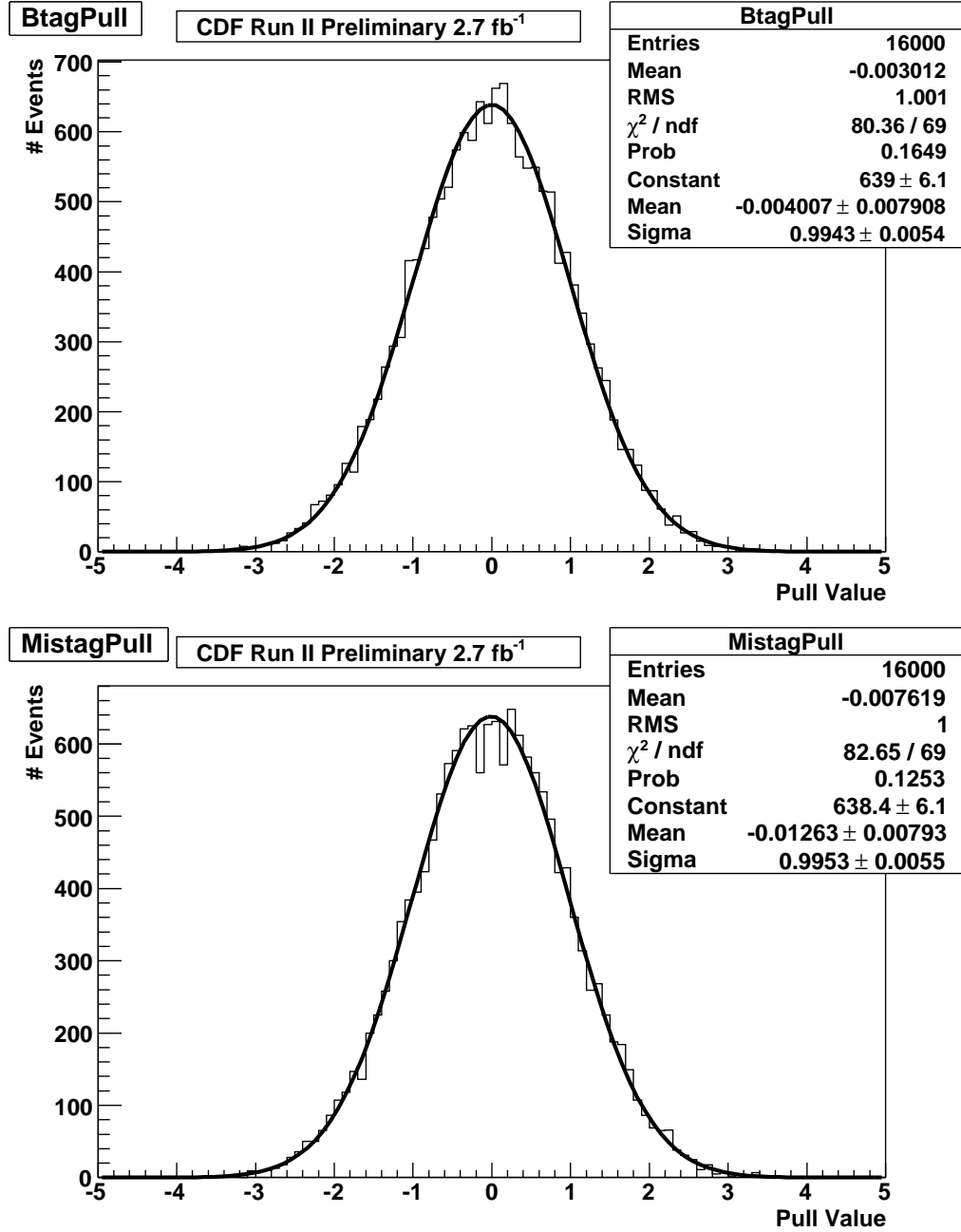


Figure 7.20: Pseudoexperiment pull distributions for the Btag and Mistag systematic uncertainties.

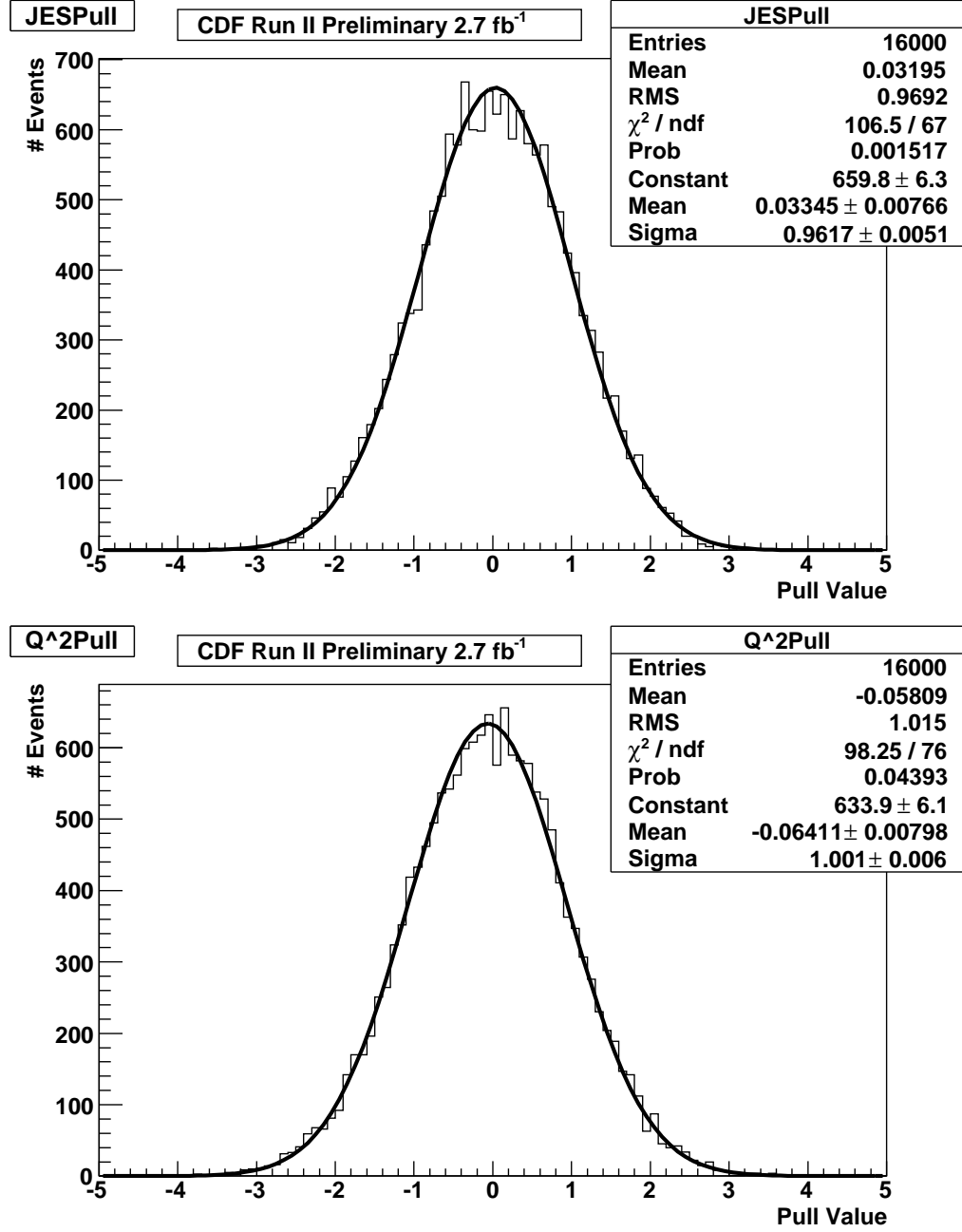


Figure 7.21: Pseudoexperiment pull distributions for the Jet Energy Scale and Q^2 systematic uncertainties.

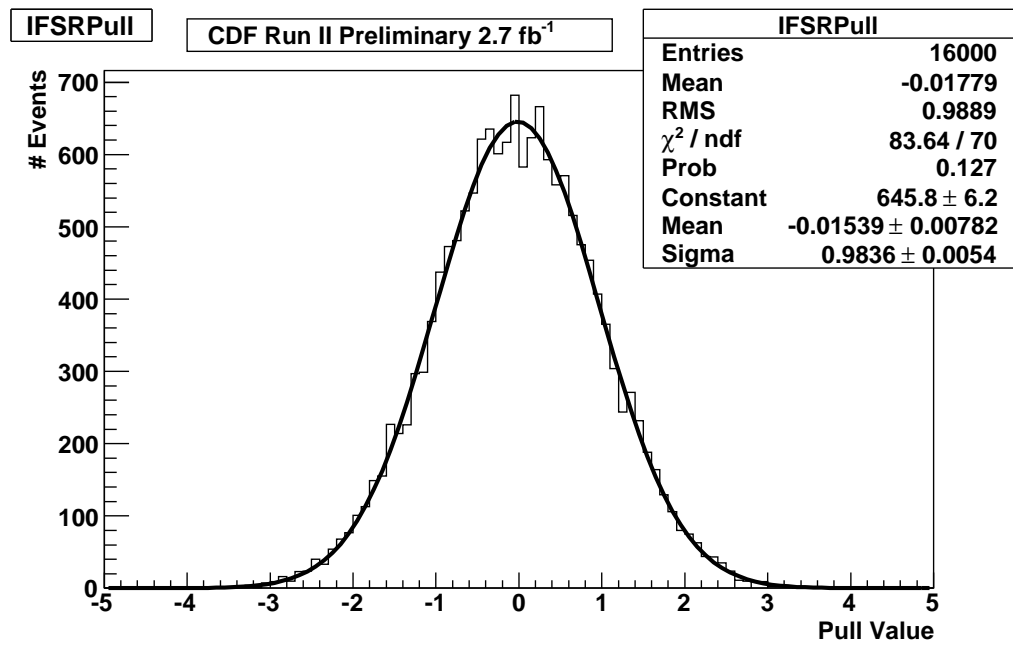


Figure 7.22: Pseudoexperiment pull distributions for the I/FSR systematic uncertainty.

Chapter 8

Systematic Uncertainties

Systematic uncertainties in this measurement can affect both the normalizations as well as the shapes of the templates. These are manifested through the fitter. There are other uncertainties that affect the measurement by a set percentage. They are dealt with in different manners.

For the rate uncertainties, we generate additional sets of templates with the variable in question shifted up and down, as described in Chapter 7.1. To estimate an individual rate uncertainty, the fit is run twice. This is done first with all parameters floating and second with all uncertainties but the one in question fixed to the values obtained in the first pass. The uncertainties from the two fit results are subtracted in quadrature to yield the single systematic uncertainty. This is only an estimate of an individual uncertainty due to the correlations between fit parameters, and only calculated for comparison purposes.

For shape uncertainties, we again generate an additional set of templates with the variable in question shifted, and then re-run the fit with those templates in place of the nominal ones. We take the difference in the result as the uncertainty.

We account for five rate uncertainties, three shape uncertainties, and two other uncertainties, as described in the following sections.

8.1 Initial- and Final-State Radiation

Recall from Chapter 1.2 that Initial- and Final-State Radiation (I/FSR) are processes in which gluons are radiated before or after the collision, respectively. Regardless of when they are radiated, the uncertainty arises due to I/FSR leading to a larger or smaller number of jets in the event. Two parameters in the CDF modeling control the amount of ISR and FSR present in the event simulation. The first is Λ_{QCD} , which is the scale at which perturbative QCD is no longer possible. The second is used as a scale in the calculation of the strong coupling constant as well as a scale in the PDFs [47].

Since this is a rate uncertainty only, we make additional sets of templates with more or less ISR and FSR as compared to the normal settings (see Table B.7 in Appendix B.2 for details of the data-sets). We then parameterize the change in the event yield as a function of the amount of I/FSR, $R_{I/FSR}$, and include it as another input, $P_N^{I/FSR}(i, j, R_{I/FSR})$, to the final fit.

8.2 Jet Energy Scale

The *Jet Energy Scale* (*JES*) is a series of corrections applied to the raw energy measured from the calorimeters (see Chapter 3.2.3) in order to estimate the true energy of the jet [48]. These corrections are necessary to account for various detector effects, such as calibration, η and ϕ dependence, et cetera. The uncertainties of each correction are convoluted together to yield an overall uncertainty, σ , on the energy of the jet. More details about these corrections and their associated uncertainties are available in CDF JES webpage [49].

When the JES varies according to this uncertainty, σ , it is possible for the energy of a jet to be pushed above the minimum jet threshold energy. Thus, zero-jet events could become one-jet events, one-jet events could become two-jet events, et cetera. Conversely, the energy of a jet may be pushed below the threshold energy and so one-jet events become zero-jet events, two-jet events become one-jet events, et cetera. Thus, it is also possible for events which previously failed (or passed) our event selection criteria to subsequently pass (or fail) when the JES is shifted up (or down).

We account for this uncertainty by varying the JES on all Monte Carlo simulation-based samples to four different points: $\pm 0.5 \sigma$ and $\pm 1 \sigma$. We build new templates from these four samples, and parameterize the change in the event yield as a function of the shift, R_{JES} , in the JES. This is included as an additional input, $P_N^{JES}(i, j, R_{JES})$, to the final fit.

8.3 Q^2 Energy Scale

What is commonly referred to as the Q^2 energy scale is actually two energy scales: the vertex energy scale, Q_v ; and the renormalization and factorization scale, Q_r . The vertex energy scale, or the scale at which the QCD coupling, α_s , is evaluated for a particular vertex, is given by $Q_v = \text{ktfac} \cdot p_T$. The renormalization and factorization scale is given by $Q_r = \text{qfac} \cdot \sqrt{M_Z^2 + \sum p_T^2(p)}$. The default values of both qfac and ktfac are set to 1.0. Despite the usual reference to these energy scales as Q^2 , they are not combined analytically in any way.

Decreasing the values of qfac and ktfac effectively increases the value of α_s (α_s : see Chapter 1.2 for a full discussion), which is inversely proportional to these energy scales, leading to an enhanced radiative production of additional partons. This increased production in turn leads to more jets.

The CDF Top Group has generated $W + \text{jets}$ samples with both qfac and ktfac varied simultaneously to values of 0.5 and 2.0. The full details of these samples are available in Tables B.8 – B.11 in Appendix B.2. We used these samples to generate new $W + \text{jets}$ templates and parameterize the event yield as a function of the Q^2 shift, R_{Q^2} . This parameterization becomes an input, $P_N^{Q^2}(i, j, R_{Q^2})$, to the fit.

8.4 b -tag Scale Factor

Monte Carlo simulation does a reasonably good job of modeling the b -tagging rate; the measure of the agreement between Monte Carlo simulation and data is called the b -tag scale factor. The b -tag scale factor was previously calculated as $S_{btag} = 0.95 \pm 0.05$ [50], indicating no evidence for disagreement. In order to take into account the uncertainty on this scale factor, however, we generate new templates with the b -tag scale factor shifted by $\pm 1\sigma$. With a higher b -tag scale factor, events can migrate from the single-tag bin to the double-tag bin (and vice versa for a lower scale factor), as seen in Figure 4.3. We parameterize the change in event yield as a function of the shift, R_{Btag} , of the b -tag scale factor and use that as an additional input, $P_N^{Btag}(i, j, R_{Btag})$, to the fit.

8.5 Mistag Rate

In stark contrast to the b -tagging efficiency, Monte Carlo simulation does a poor job of modeling the mistag rate, or the rate at which a non b -jet is identified as one. The mistag rate used in this analysis (see Chapter 6.5) was calculated separately using a data-driven mistag matrix (or mistag parameterization). This mistag matrix comes with a roughly 20% uncertainty, largely due to $\alpha\beta$ corrections [51]. The mistag parameterization includes two correction factors, α and β , to make the predicted mistag rate agree with the observed rate, and they have uncertainties associated with

them. Varying the mistag rate can shift some zero-tag events to single-tag events, and single-tag events to double-tag events (and vice versa). To account for this possibility, additional templates of Monte Carlo simulation-based backgrounds are made with the mistag rate varied up and down by 20%. These templates are used to parameterize the event yield as a function of the shift, R_{Mistag} , in the mistag rate and the parameterization becomes an additional input, $R_N^{Mistag}(i, j, R_{Mistag})$, to the final fit.

8.6 Parton Showering

Monte Carlo simulation generators need to make modeling assumptions about several things, including how partons are showered — that is, how the simulation models the hadronization of quarks and showering of jets. Different parton showering models can change the shape of the flavor-separator distribution. In order to account for the uncertainty in these modeling assumptions, we make additional templates of the top sample, which was generated using a different parton showering model. The default sample was generated using PYTHIA, and the additional templates were generated using HERWIG. The fit is run once with the default top sample and once with the HERWIG sample. The two results are subtracted to yield the uncertainty due to the parton showering model.

8.7 QCD Shape

Modeling of the QCD shape is done using anti-electrons (see Chapter 6.3). In order to account for potential differences, we make additional QCD templates using jet-electrons to model the shape instead. Jet-electrons are jets which “fake” electrons — that is, the jets appear to be electrons. In order to account for this shape uncertainty, we run the fit a second time, replacing the anti-electron QCD templates with the jet-electron ones. The difference in the top cross section result is taken to be the systematic uncertainty due to the QCD shape.

8.8 KIT Flavor Separator

The KIT Flavor Separator does not model the observed mistag rates in data perfectly, and so a correction function is applied within the neural net. This correction function changes the shape of the output distribution, and to account for that, we make additional templates without the correction. As with the other shape uncertainties, the fit is re-run with these uncorrected templates, and the results compared. The difference in the top cross section result becomes the uncertainty due to the KIT Flavor Separator correction.

8.9 Parton Distribution Functions

As explained in Chapter 1.2, the exact parton distribution functions for protons and anti-protons are not known, and there are several models used to describe them. It is thus necessary to examine the effects of using a different parton distribution function. The top sample for this analysis was generated using CTEQ5L.

As we use the same event selection as in METHOD II analyses, which re-weighted the top sample using the CTEQ6L parton distribution function [52], we simply take the same fractional uncertainty of 4% on the top cross section.

8.10 Luminosity

Recall from Chapter 3.2.6 that measured luminosity has an uncertainty of 5.9%. This is the largest uncertainty in the analysis. In order to account for this, we take an uncertainty equal to 5.9% of the top cross section result.

Chapter 9

Results

The results we obtain from the fitter are twofold: a set of normalizations for the templates and a set of relative shifts for the systematic uncertainties that together minimize the negative log likelihood when those templates are fit to the data; and a visual representation of that fit to the data.

The fit to the data is shown in Figures 9.1 and 9.2. The normalizations from the fit are shown in Table 9.1. The top cross section result is given in picobarns, whereas the $W + \text{jets}$, EW, and QCD results are given as K-factors, relative to the default normalizations used in this analysis. The results for the systematic uncertainties are shown as shifts relative to the default values used. The normalizations we obtain are similar to those obtained from other procedures.

The correlation matrix of the fit parameters is shown in Table 9.2. There are several things to note about these correlations. The strong anti-correlation between

the Mistag shift and the $W \rightarrow q\bar{q}'$ sample, and lack of strong correlations to any other samples, is likely the cause of the large uncertainty on the Mistag shift result. The $W + \text{jets}$ samples are highly correlated with the Q^2 shift, which likely caused the problems seen in the pseudoexperiments from Chapter 7.3.

Shown in Table 9.3 is a comparison of the uncertainties from this analysis to a METHOD II analysis using the same amount of data and assumed top mass [52]. METHOD III has improved on almost every uncertainty. The only exception is the uncertainty due to the Jet Energy Scale, which remained the same. Note that some uncertainties were estimated concurrently in METHOD III, whereas they were determined separately in METHOD II; we provide an individual estimate as best we can. These are denoted with asterisks and are included only for comparison purposes.

Table 9.1: Normalizations for each sample as determined by the fit. The top cross section is quoted in picobarns, whereas the $W + \text{jets}$, electroweak, and QCD results are given as k -factors. The systematic uncertainty results are given as relative shifts.

Sample	Fit Value
$\sigma_{t\bar{t}}$	$7.64^{+0.57}_{-0.54}$
$K_{Wb\bar{b}}$	$1.57^{+0.28}_{-0.22}$
$K_{Wc\bar{c}}$	$0.9^{+0.9}_{-0.7}$
K_{Wc}	$1.90^{+0.34}_{-0.32}$
$K_{Wq\bar{q}}$	$1.10^{+0.34}_{-0.25}$
K_{EW}	$1.0^{+0.1}_{-0.1}$
K_{QCD}	$0.82^{+0.26}_{-0.26}$
R_{Btag}	$0.31^{+0.64}_{-0.64}$
R_{Mistag}	$-0.05^{+0.98}_{-0.98}$
R_{JES}	$0.47^{+0.63}_{-0.61}$
R_{Q^2}	$0.07^{+0.44}_{-0.44}$
R_{IFSR}	$0.1^{+0.9}_{-0.9}$

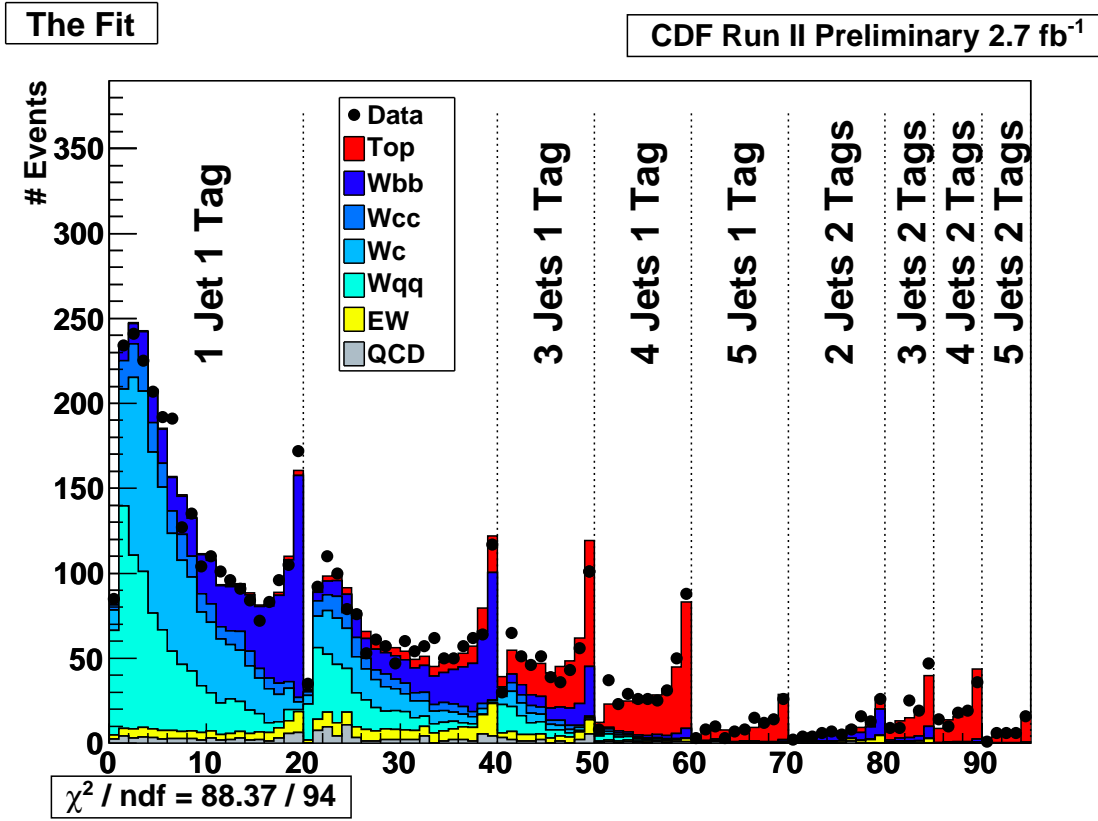


Figure 9.1: The templates after being fit to the data, split by n_{jet} and n_{tag} bins.

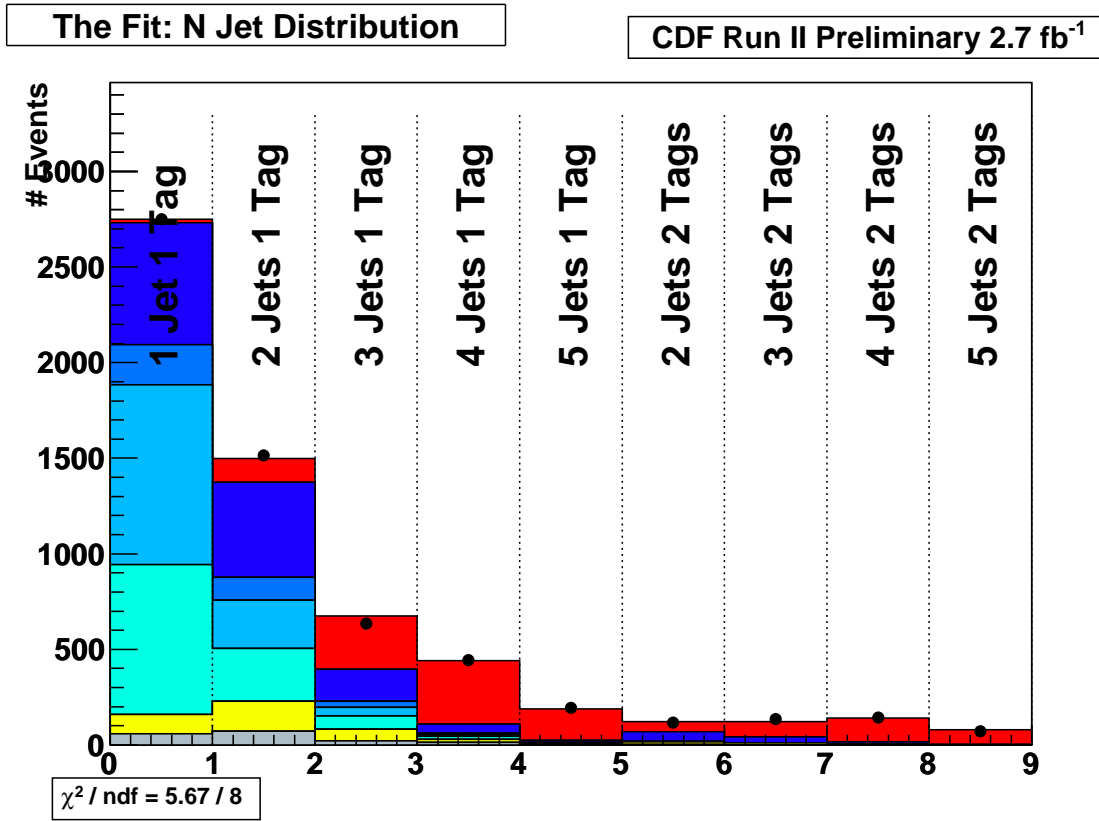


Figure 9.2: The templates after being fit to the data, projected onto the n_{jet} distribution

Table 9.2: Correlation matrix showing the correlations between all of the parameters in the fit. Note the very strong correlations between the Q^2 shift and the $W + \text{jets}$ samples, as well as the high anti-correlation between $Wc\bar{c} + \text{jets}$ and Wc samples.

Parameter	$\sigma_{t\bar{t}}$	$K_{Wb\bar{b}}$	$K_{Wc\bar{c}}$	K_{Wc}	$K_{Wq\bar{q}}$	K_{EW}	K_{QCD}	R_{Btag}	R_{IFSR}	R_{JES}	R_{Mistag}	R_{Q^2}
$\sigma_{t\bar{t}}$	1.00	0.10	0.21	0.13	0.23	0.00	0.01	-0.50	0.20	-0.61	-0.19	0.03
$K_{Wb\bar{b}}$	0.10	1.00	0.53	0.17	0.57	0.02	-0.02	-0.31	-0.24	0.37	-0.10	0.87
$K_{Wc\bar{c}}$	0.21	0.53	1.00	-0.34	0.41	0.01	-0.06	-0.10	-0.01	-0.06	-0.09	0.70
K_{Wc}	0.13	0.17	-0.34	1.00	0.02	0.09	0.12	-0.44	-0.22	0.29	-0.24	0.05
$K_{Wq\bar{q}}$	0.23	0.57	0.41	0.02	1.00	0.05	0.00	-0.19	-0.07	0.10	-0.73	0.48
K_{EW}	0.00	0.02	0.01	0.09	0.05	1.00	0.00	-0.03	0.00	0.00	0.00	0.12
K_{QCD}	0.01	-0.02	-0.06	0.12	0.00	0.00	1.00	0.05	-0.01	-0.05	-0.01	0.09
R_{Btag}	-0.51	-0.31	-0.10	-0.44	-0.19	-0.03	0.05	1.00	0.10	0.10	0.18	-0.05
R_{IFSR}	0.20	-0.24	-0.01	-0.22	-0.07	0.00	-0.01	0.10	1.00	-0.45	-0.01	-0.23
R_{JES}	-0.61	0.37	-0.06	0.29	0.10	0.00	-0.05	0.09	-0.45	1.00	-0.01	0.36
R_{Mistag}	-0.19	-0.08	-0.09	-0.24	-0.73	0.00	-0.01	0.18	-0.01	-0.01	1.00	0.07
R_{Q^2}	0.03	0.87	0.70	0.05	0.48	0.12	0.09	-0.05	-0.23	0.36	0.07	1.00

Table 9.3: Comparison of uncertainties from this analysis and a previous one using METHOD II with the same amount of data. Values are given in picobarns. The uncertainties marked with an asterisk are included for comparison only. Note that this analysis includes the Heavy Flavor Correction as part of the statistical uncertainty. The METHOD II analysis did not use the KIT Flavor Separator, and so does not have an uncertainty associated with its correction. Finally, the METHOD II analysis did not estimate an uncertainty due to the Q^2 energy scale.

Uncertainty	Method III	Method II
Statistical	0.33	0.36
Heavy Flavor Correction	—	0.27
Jet Energy Scale*	0.29	0.29
Tagging*	0.23	0.39
Mistags*	0.08	0.17
Q^2 *	0.21	—
ISR/FSR*	0.01	0.06
Luminosity	0.45	0.43
QCD Shape	0.01	0.06
Monte Carlo Generator	0.11	0.21
KIT Correction	0.10	—
Lepton ID	0.05	0.04
Z_0	0.02	0.02
PDF	0.05	0.04
Total	0.73	0.84

9.1 Kinematic Validation Plots

Using the normalizations returned from the fitter, we made several kinematic plots to show agreement between the data obtained and our Monte Carlo simulations. These are shown in Figures 9.3 – 9.69. The kinematic plots provide a cross check, to verify that this method of measuring the cross section and background contributions simultaneously does a good job of modeling both the signal and background distributions.

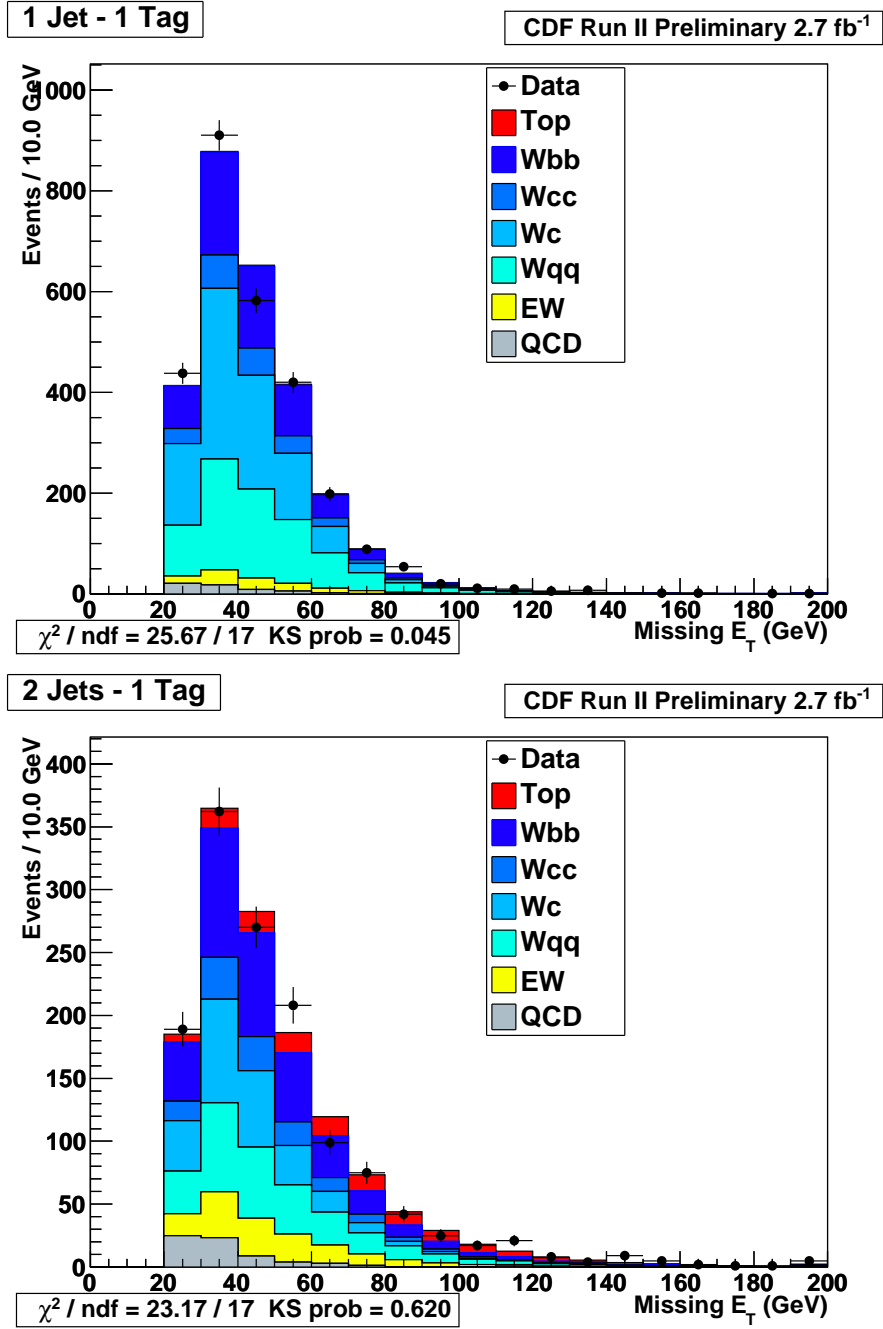


Figure 9.3: Validation plots of the missing transverse energy for single tags.

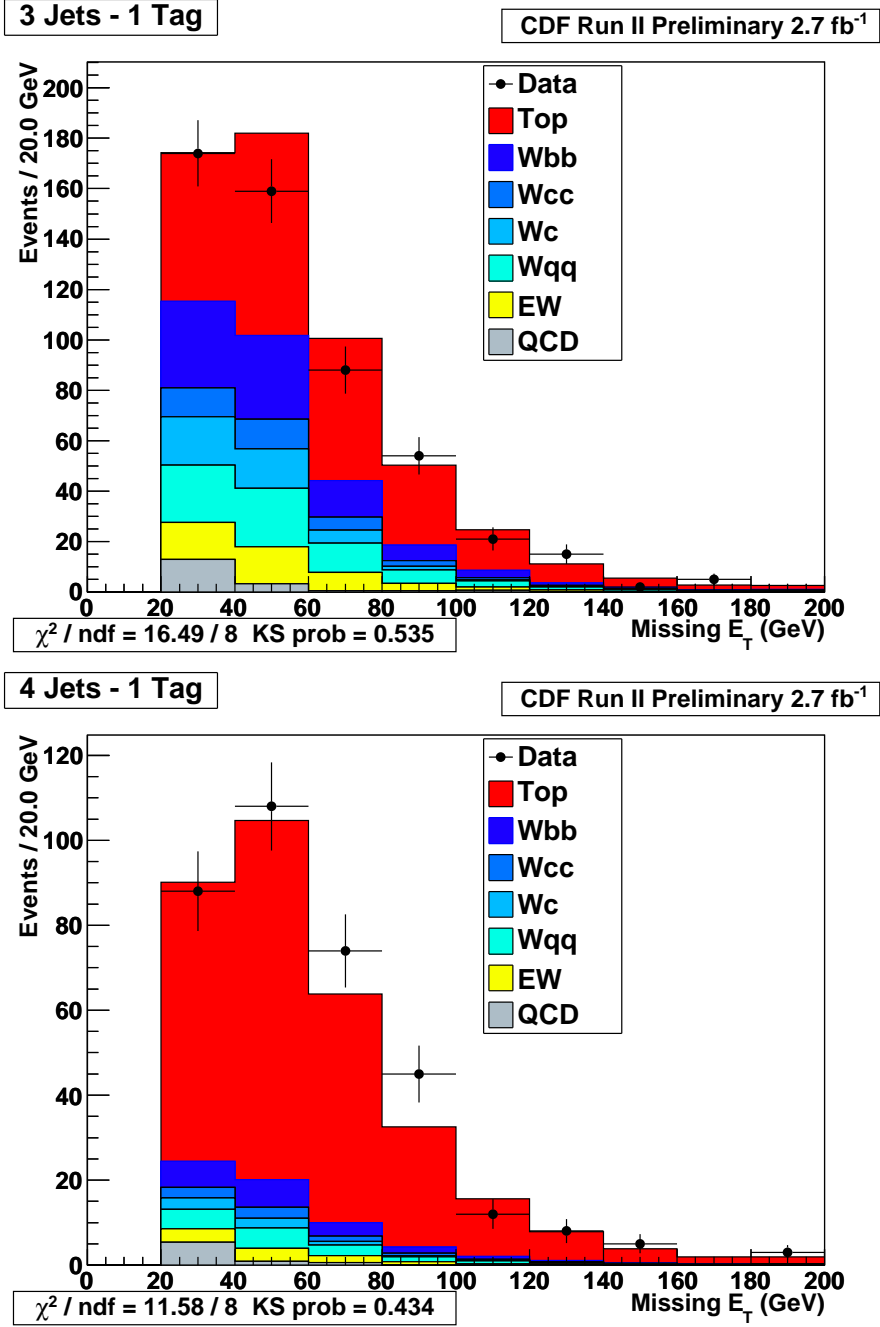


Figure 9.4: Validation plots of the missing transverse energy for single tags.

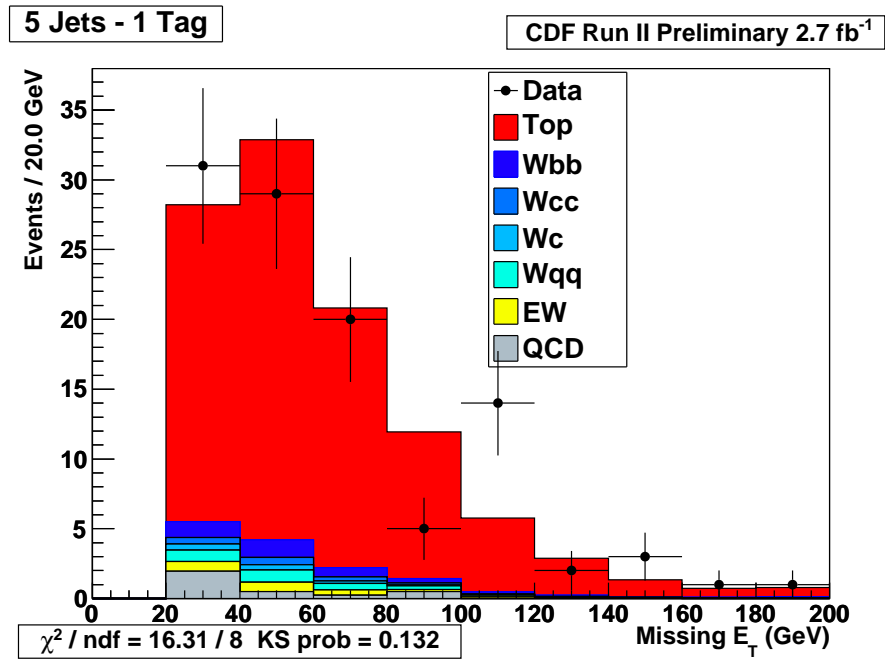


Figure 9.5: Validation plots of the missing transverse energy for single tags.

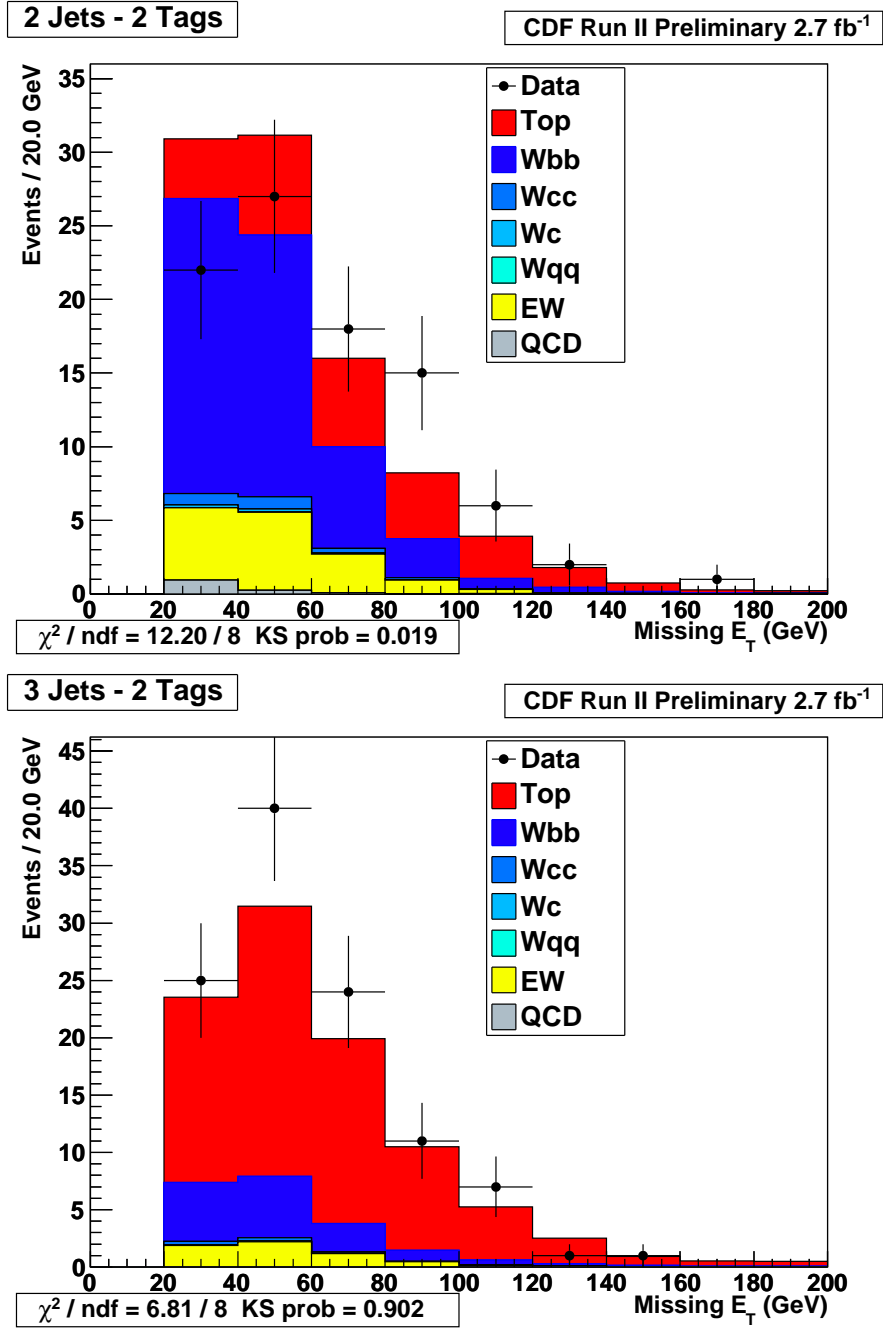


Figure 9.6: Validation plots of the missing transverse energy for double tags.

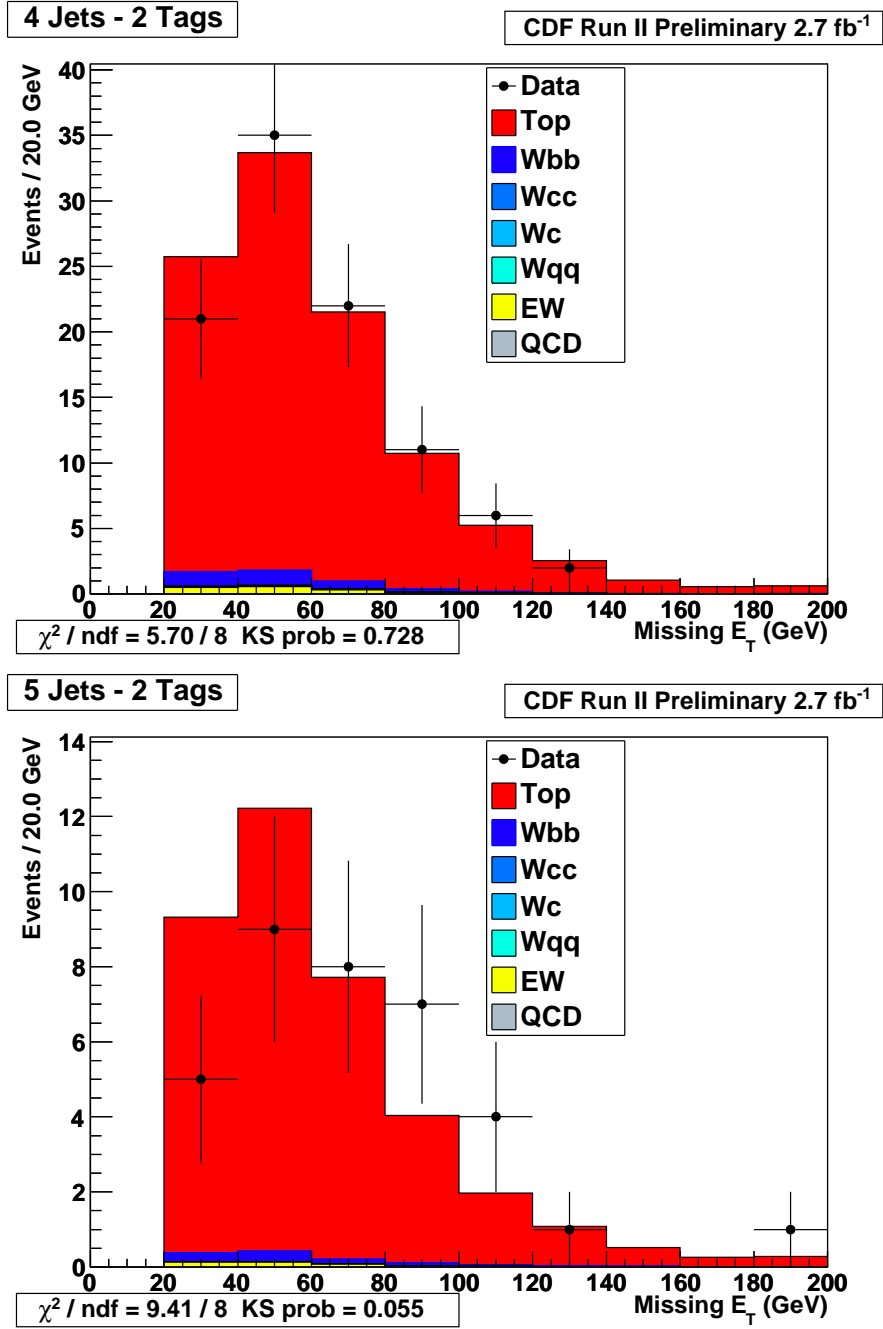


Figure 9.7: Validation plots of the missing transverse energy for double tags.

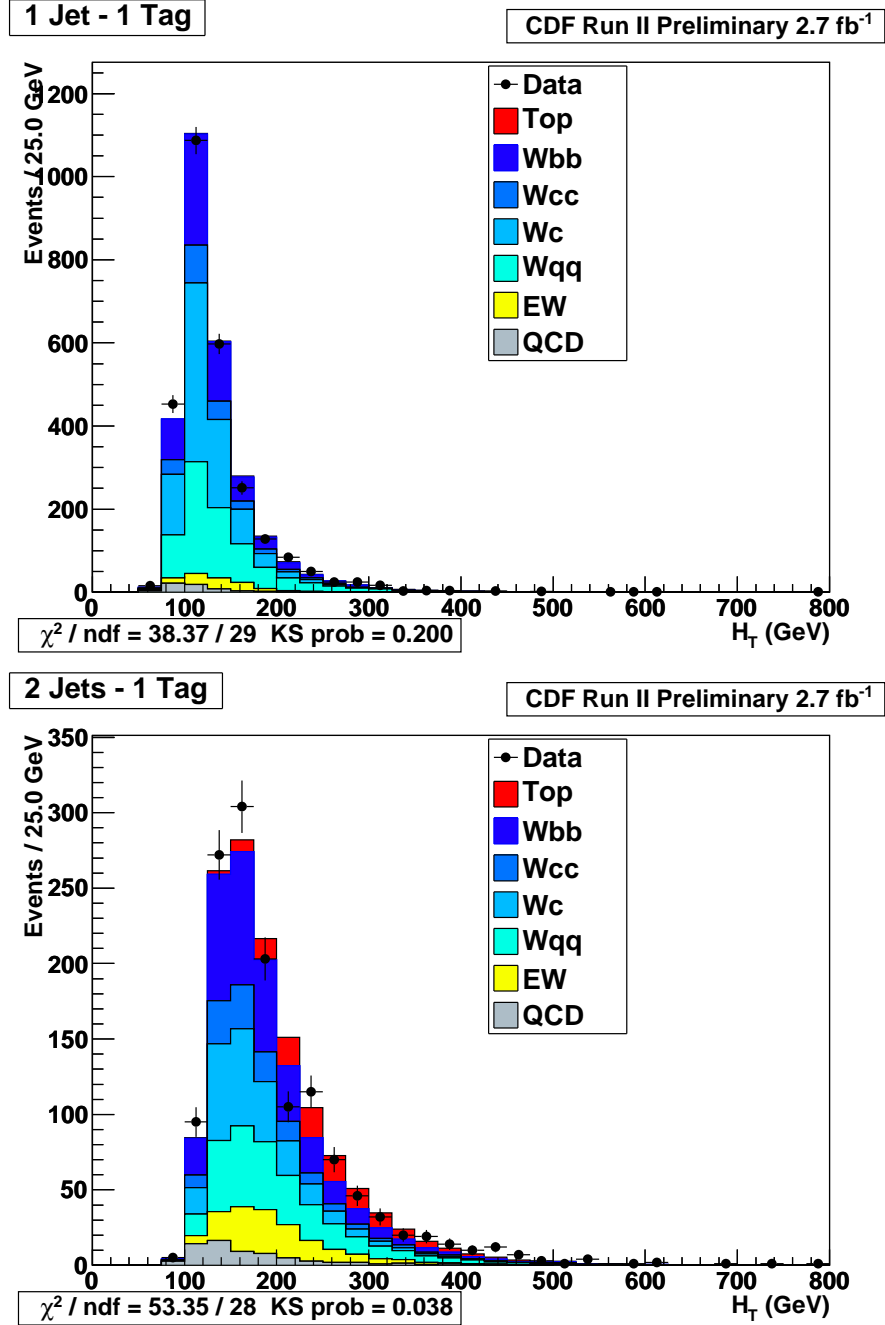


Figure 9.8: Validation plots of the total transverse energy in the event for single tags.

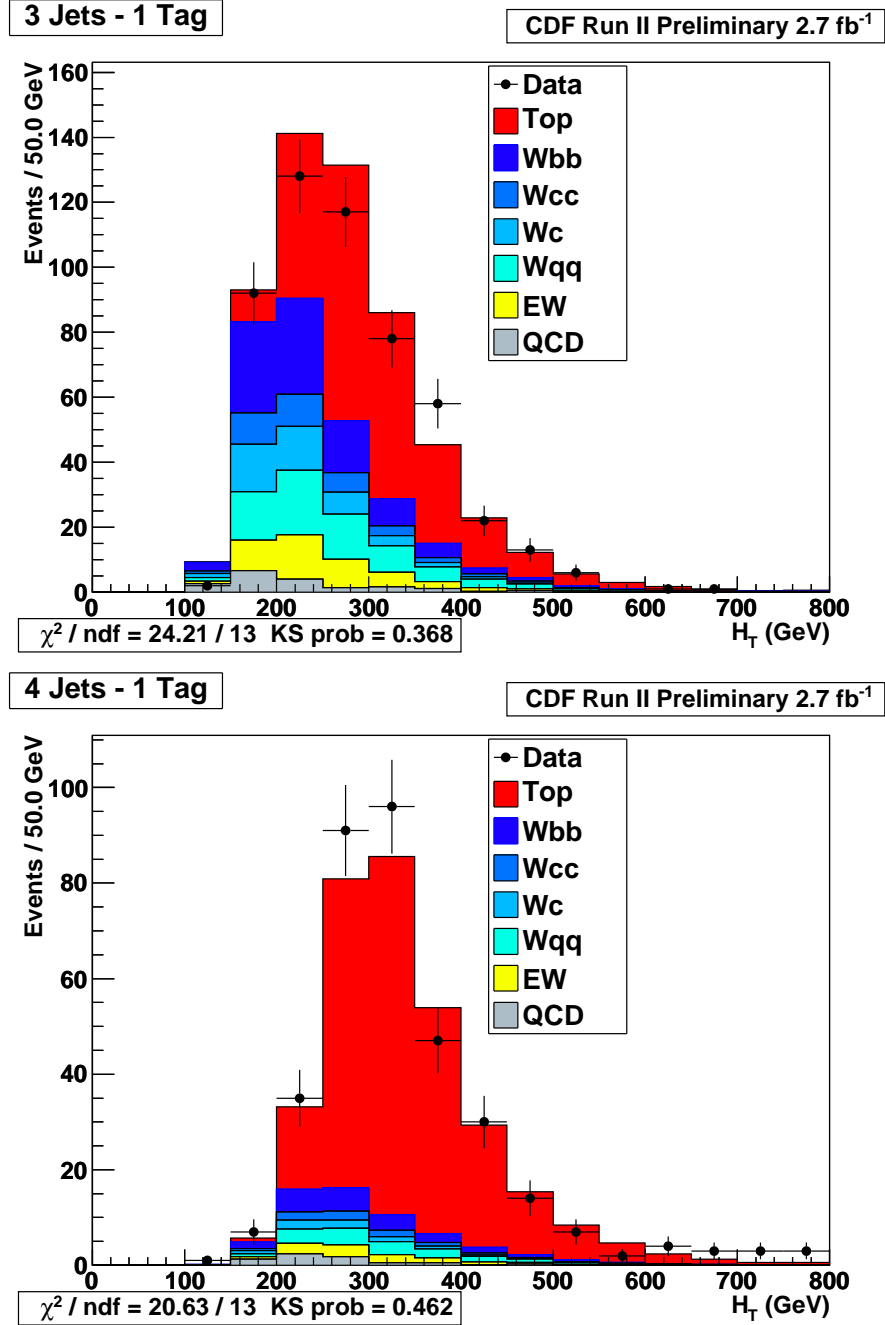


Figure 9.9: Validation plots of the total transverse energy in the event for single tags.

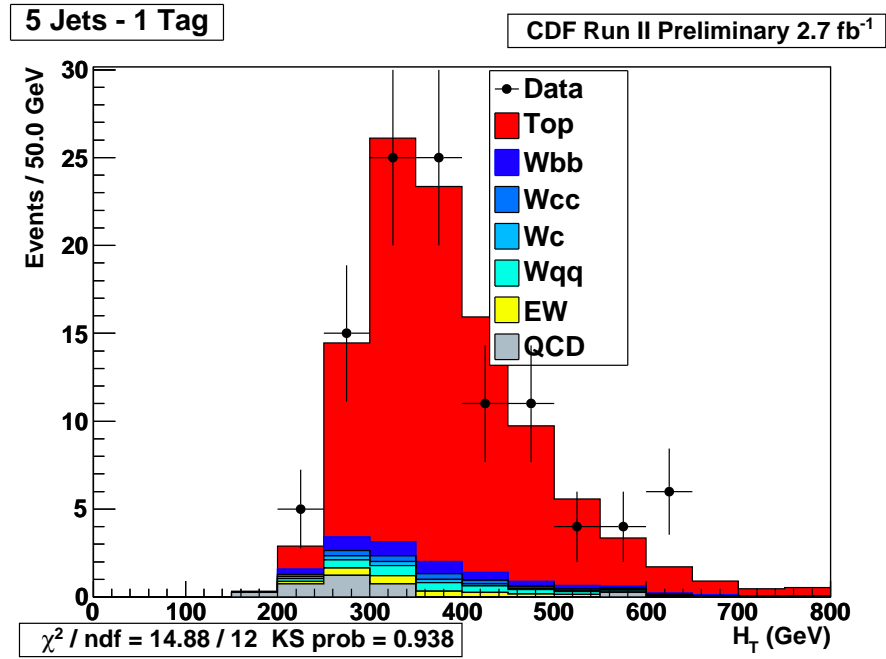


Figure 9.10: Validation plots of the total transverse energy in the event for single tags.

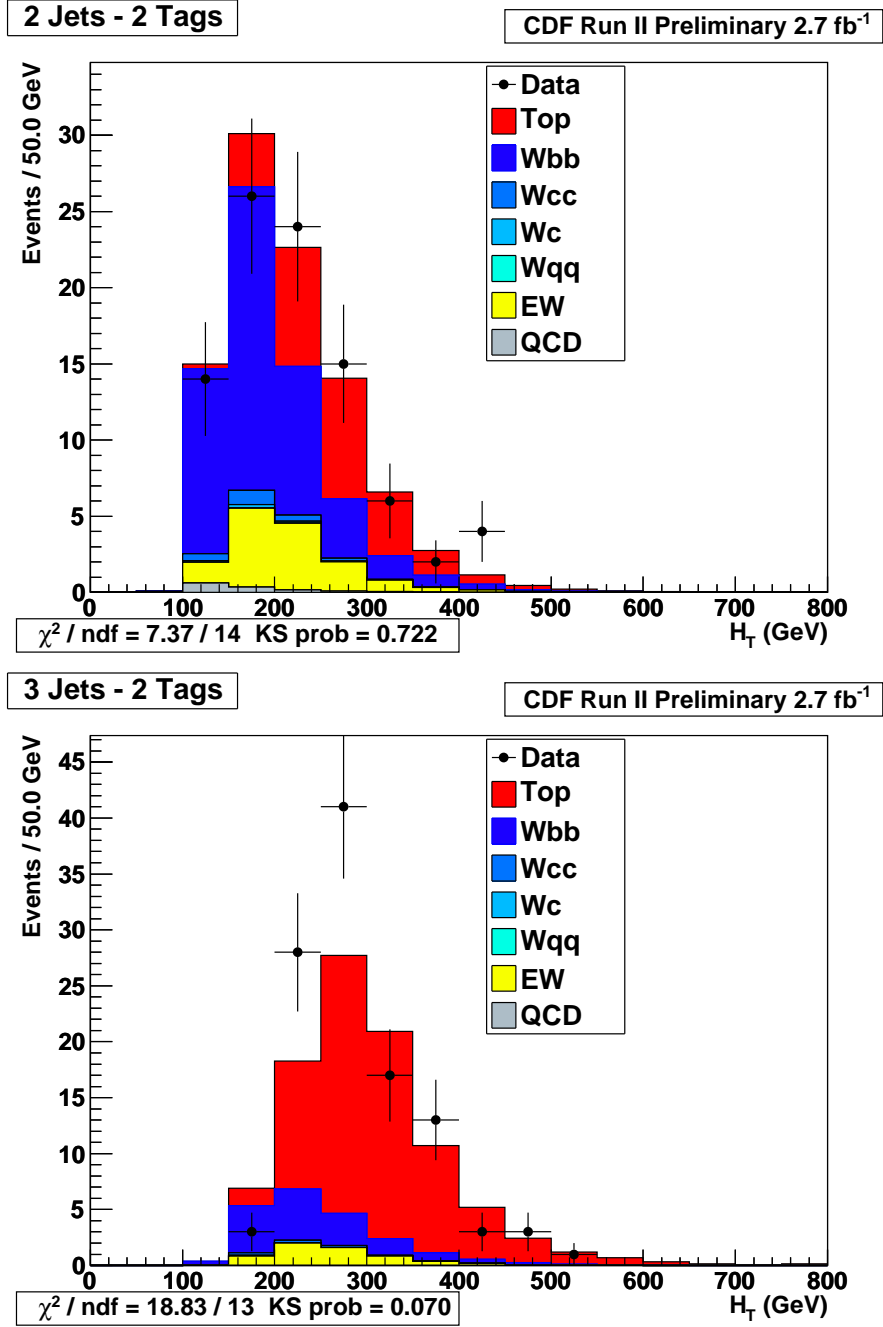


Figure 9.11: Validation plots of the total transverse energy in the event for double tags.

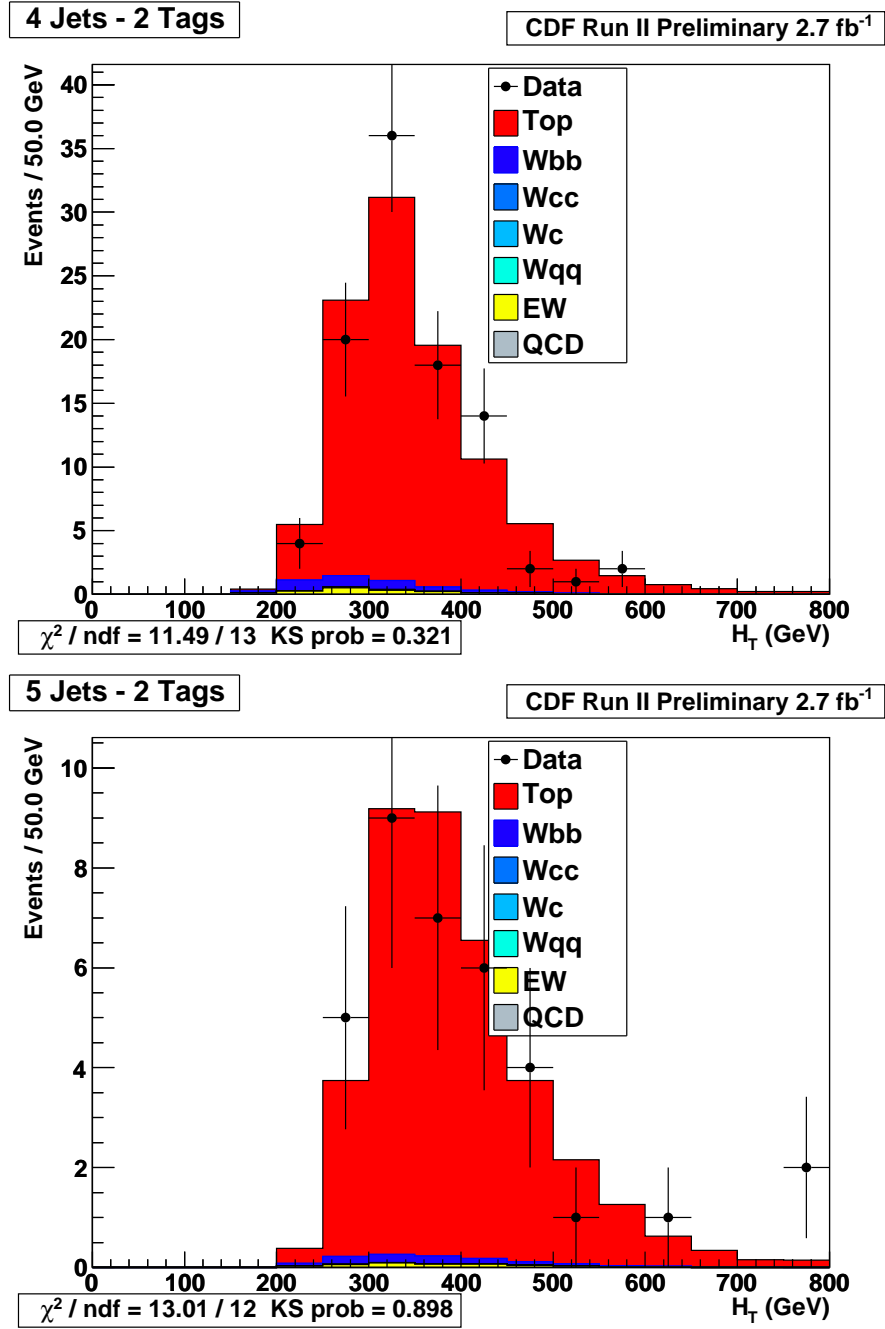


Figure 9.12: Validation plots of the total transverse energy in the event for double tags.

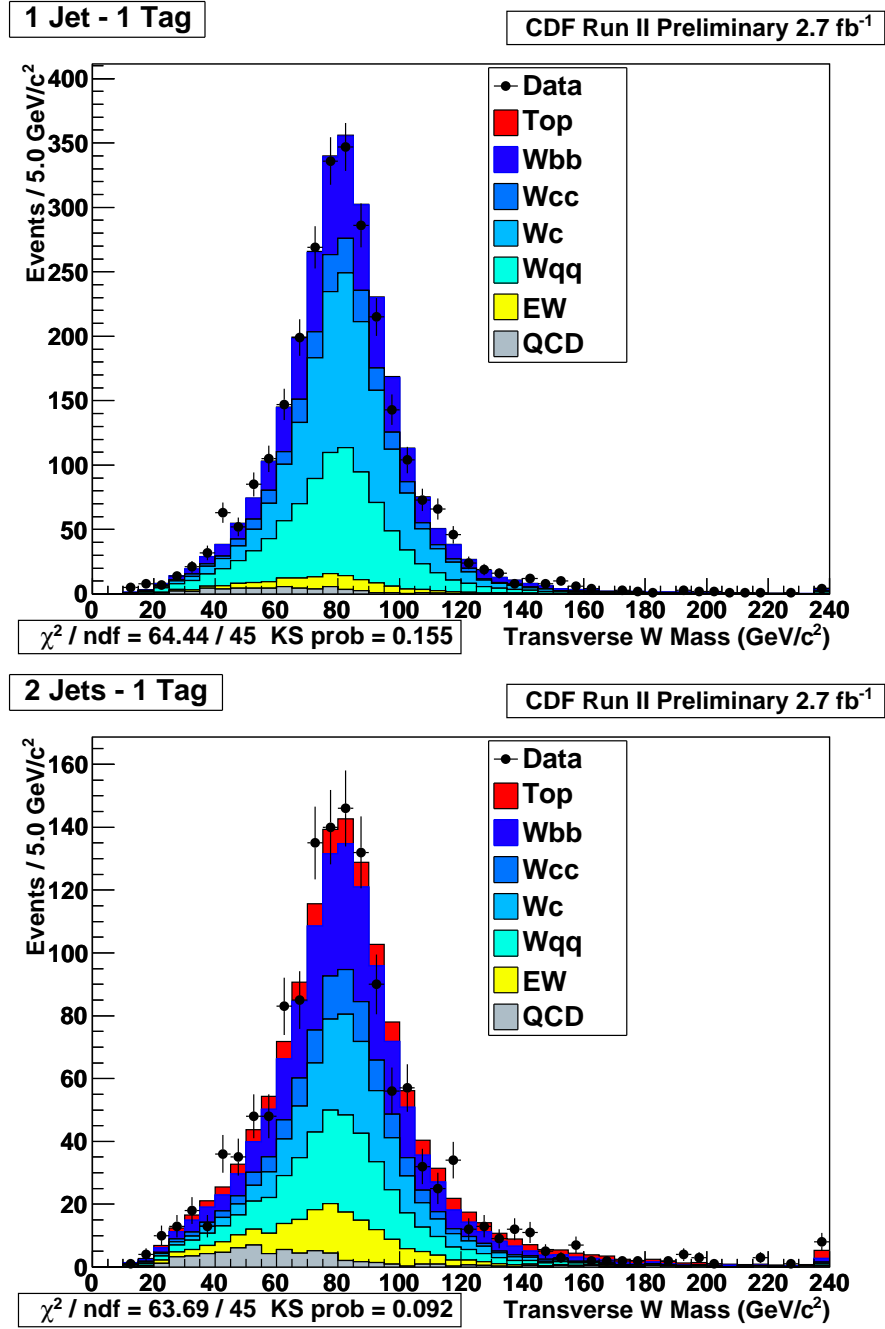


Figure 9.13: Validation plots of the transverse mass of the W for single tags.

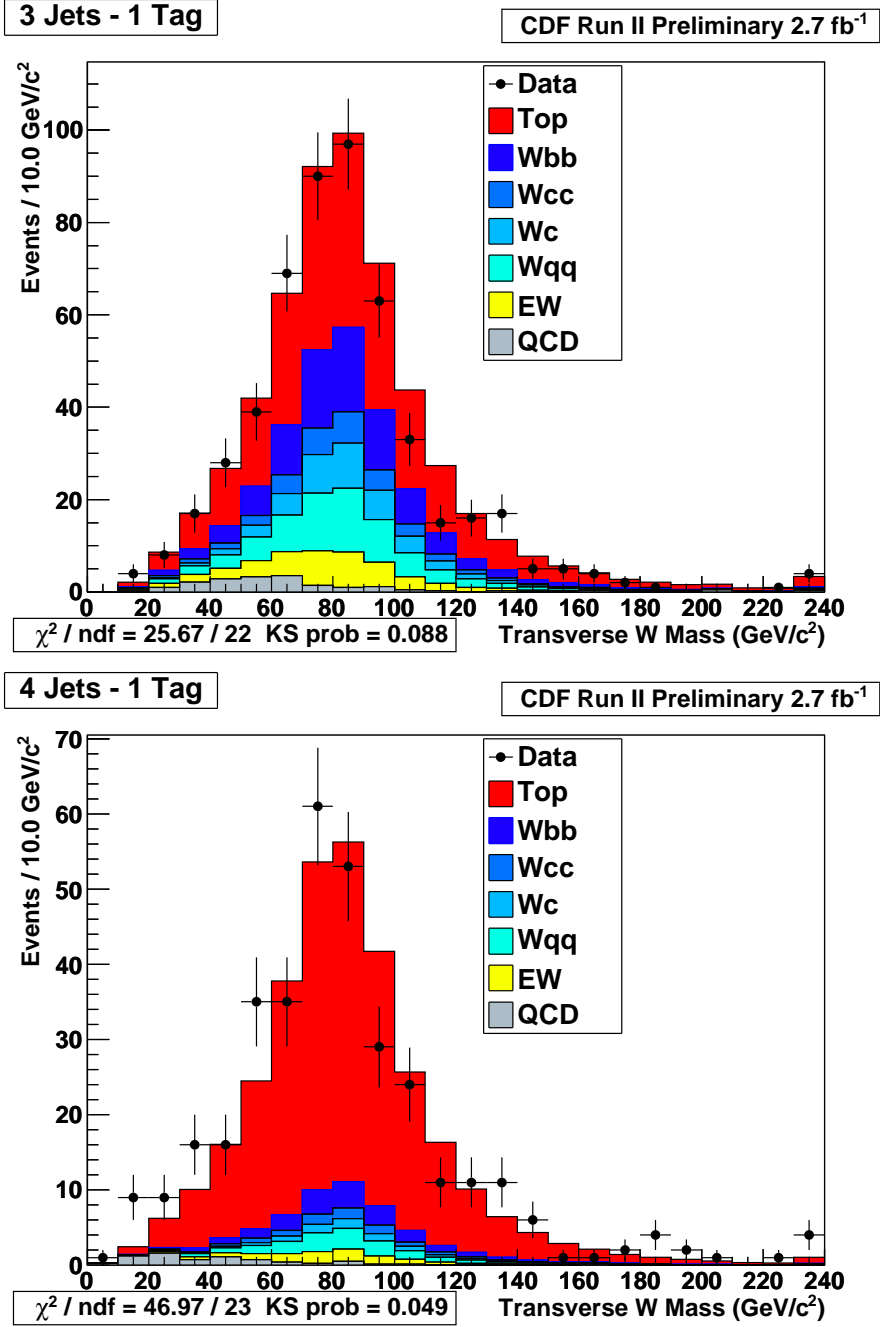


Figure 9.14: Validation plots of the transverse mass of the W for single tags.

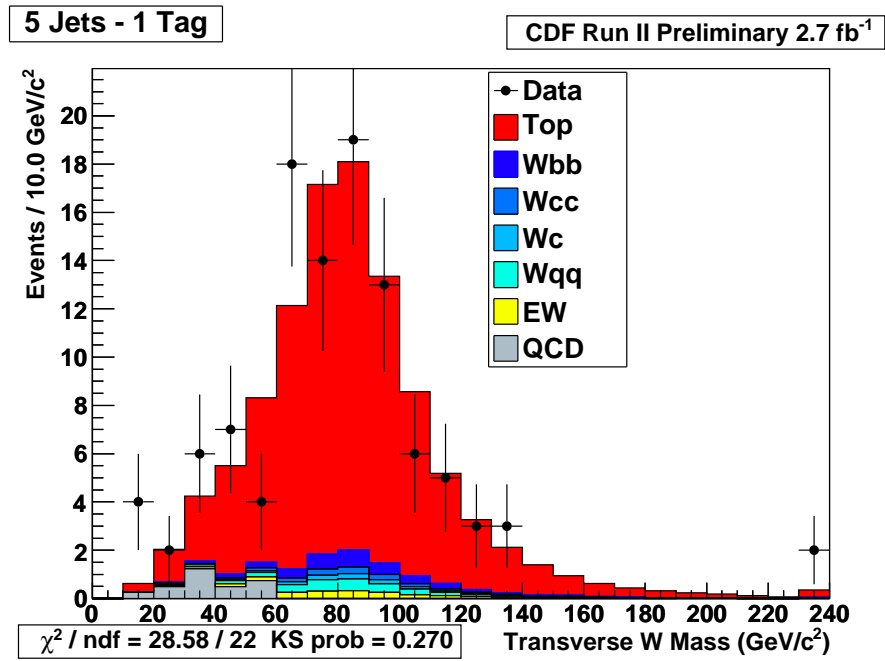


Figure 9.15: Validation plots of the transverse mass of the W for single tags.

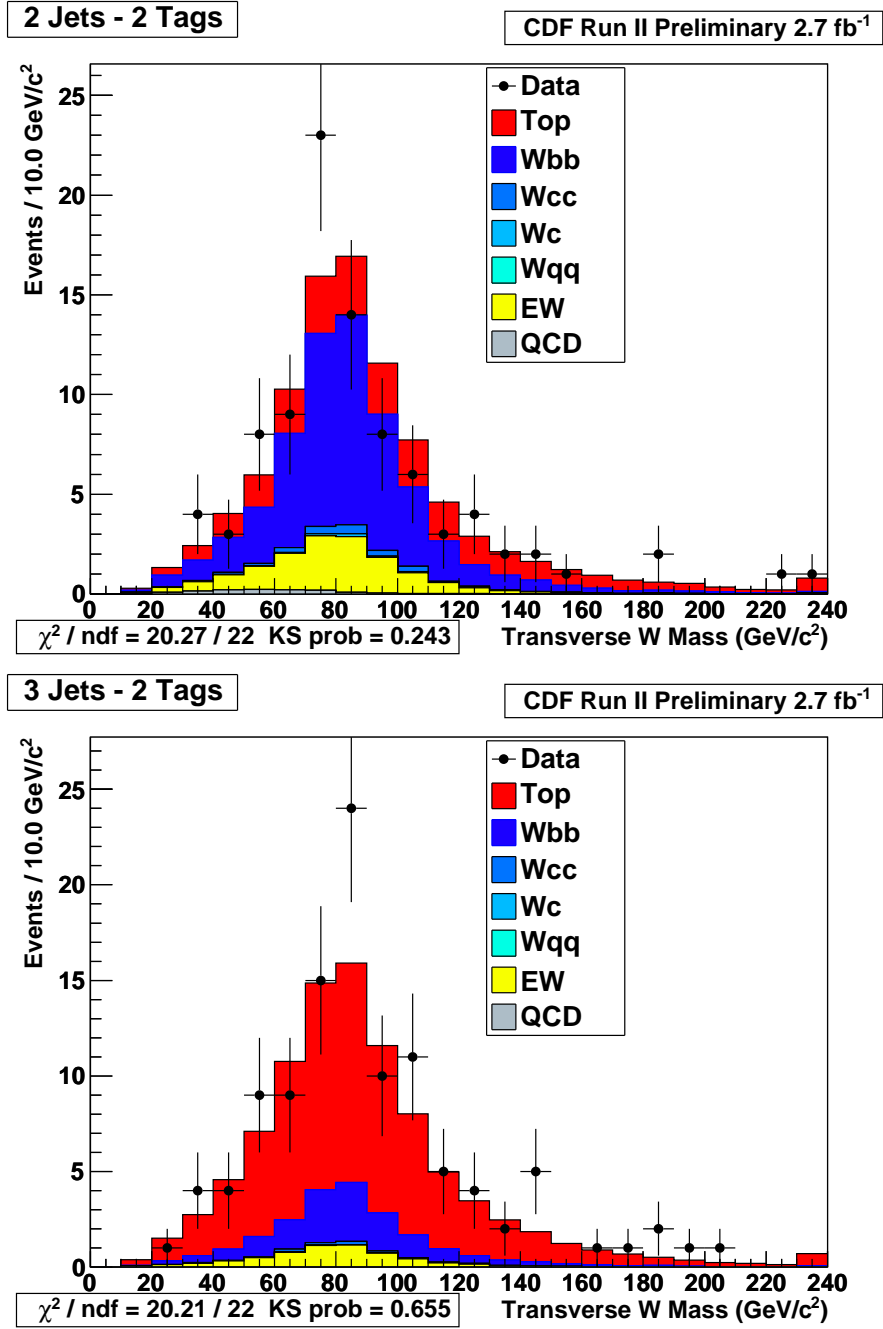


Figure 9.16: Validation plots of the transverse mass of the W for double tags.

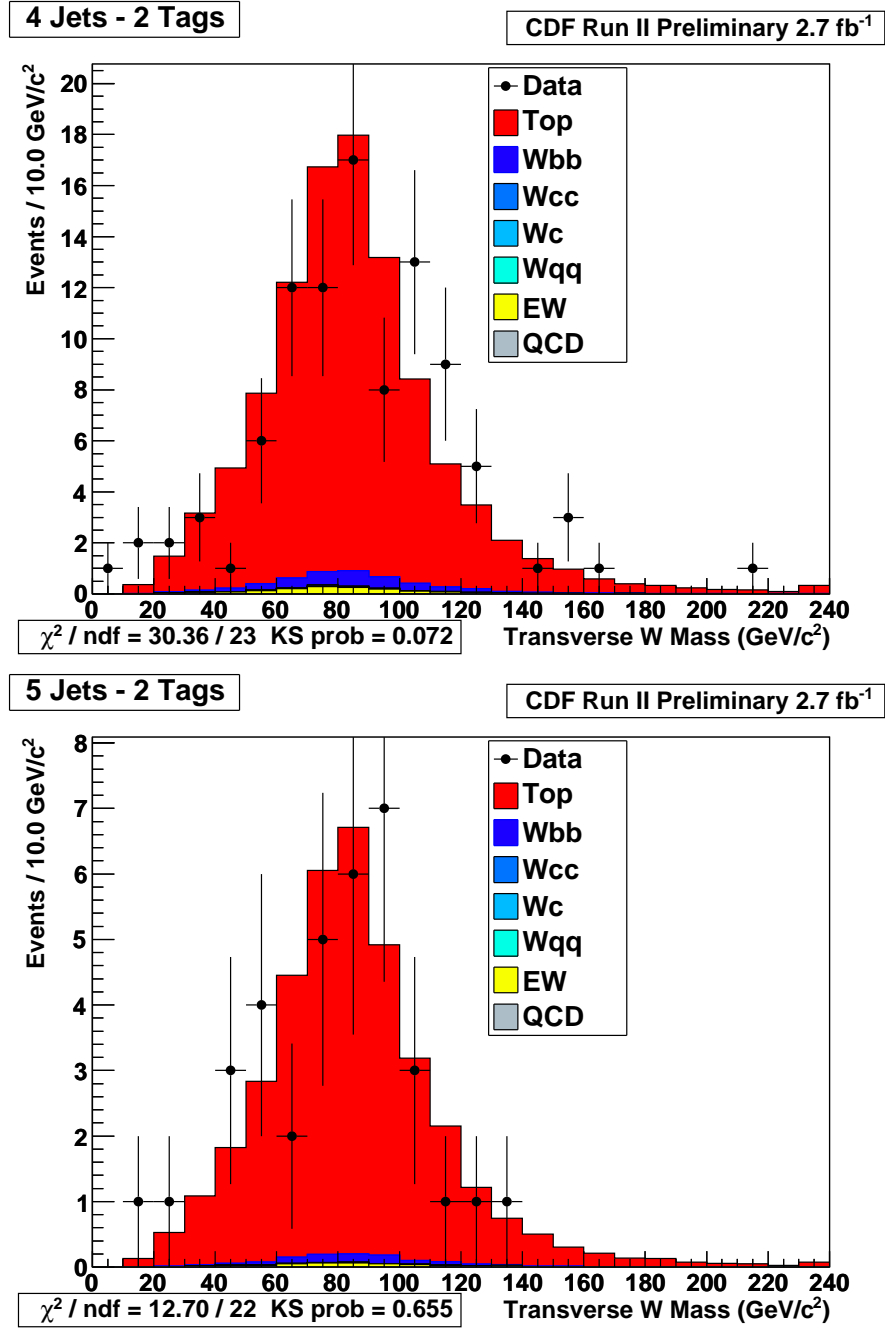


Figure 9.17: Validation plots of the transverse mass of the W for double tags.

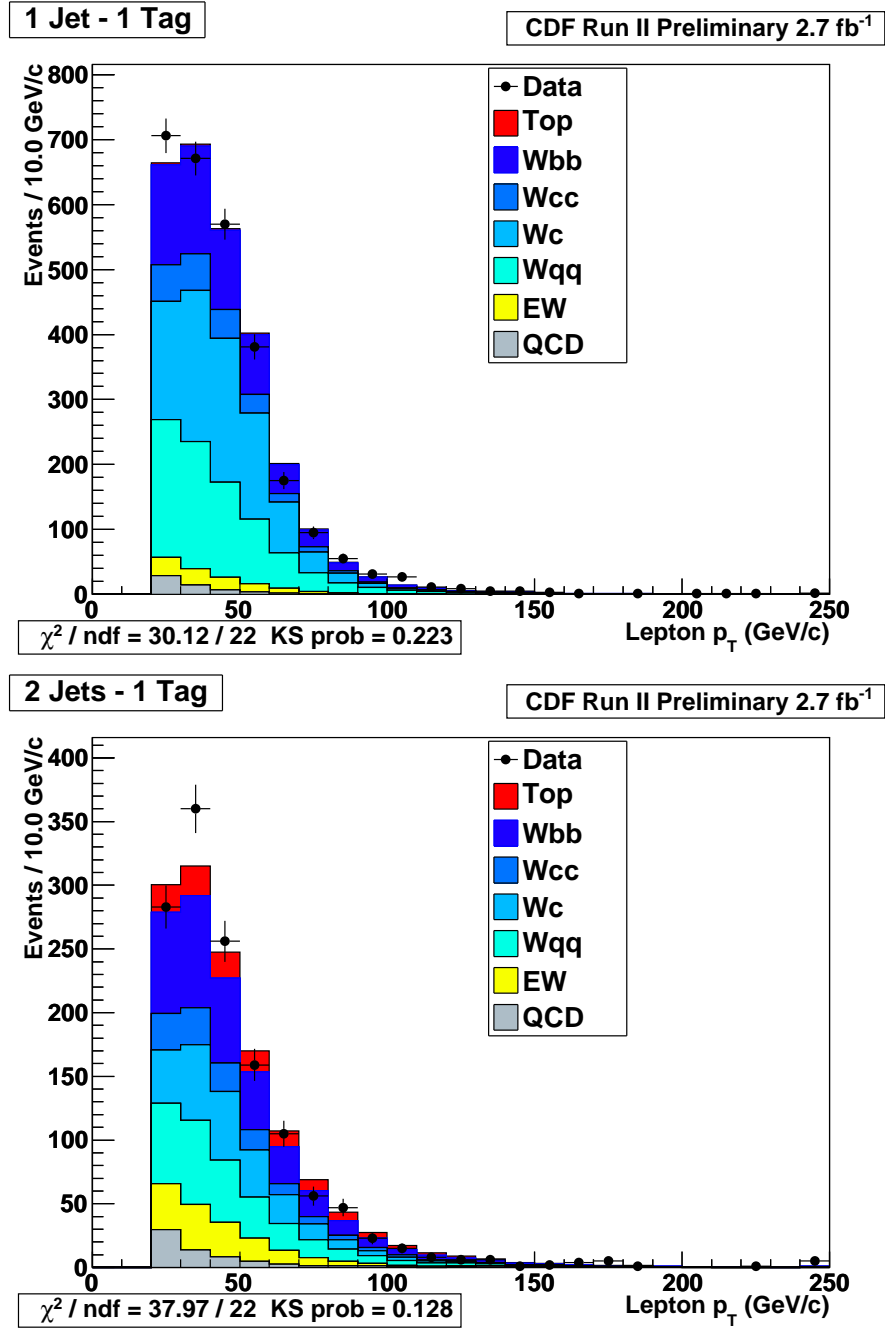


Figure 9.18: Validation plots of the transverse momentum of the lepton for single tags.

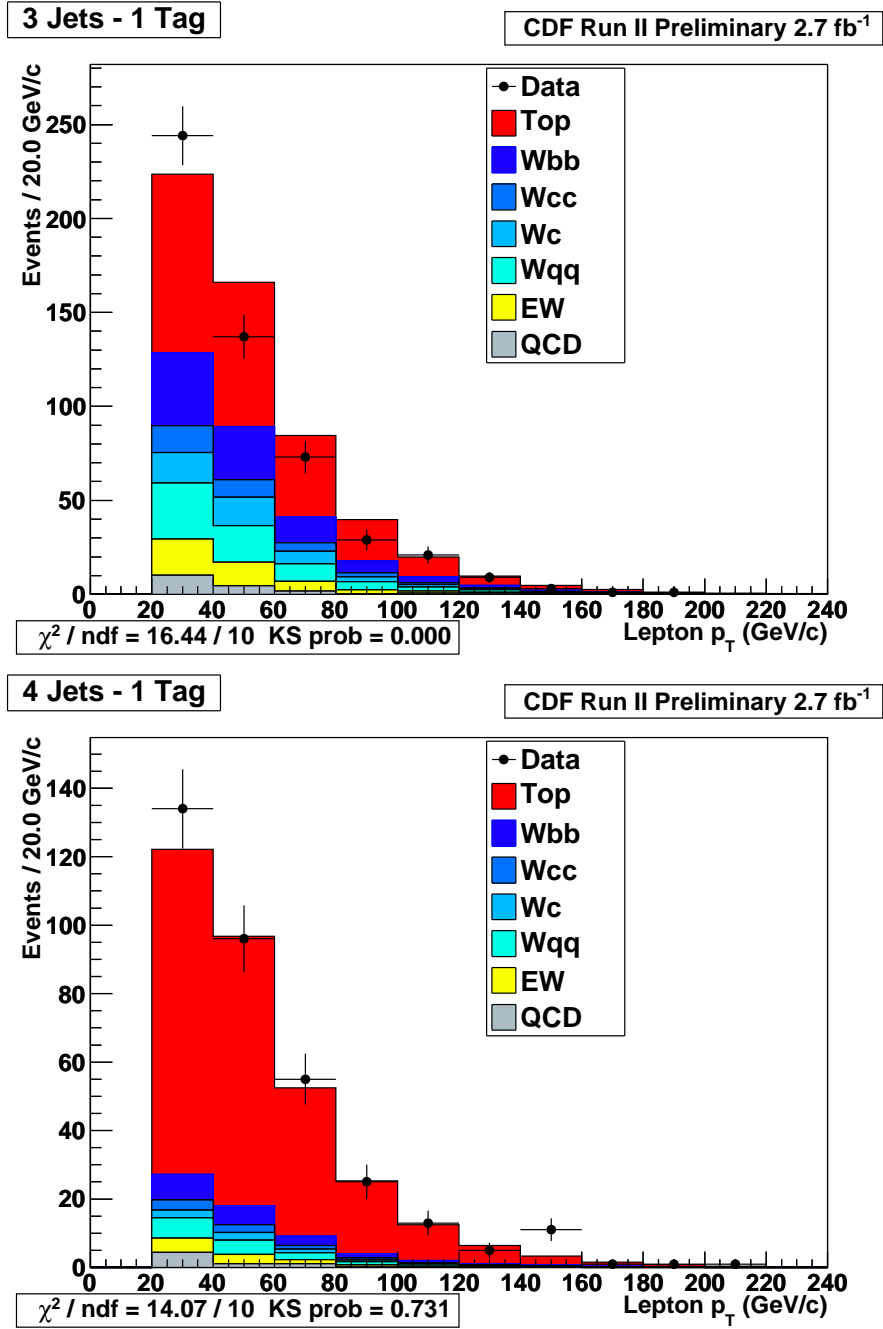


Figure 9.19: Validation plots of the transverse momentum of the lepton for single tags.

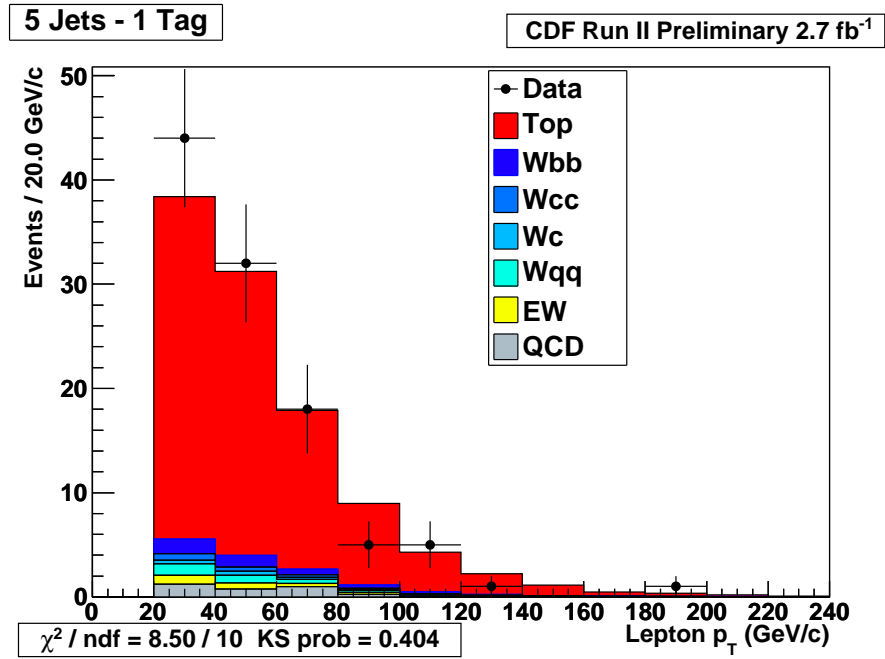


Figure 9.20: Validation plots of the transverse momentum of the lepton for single tags.

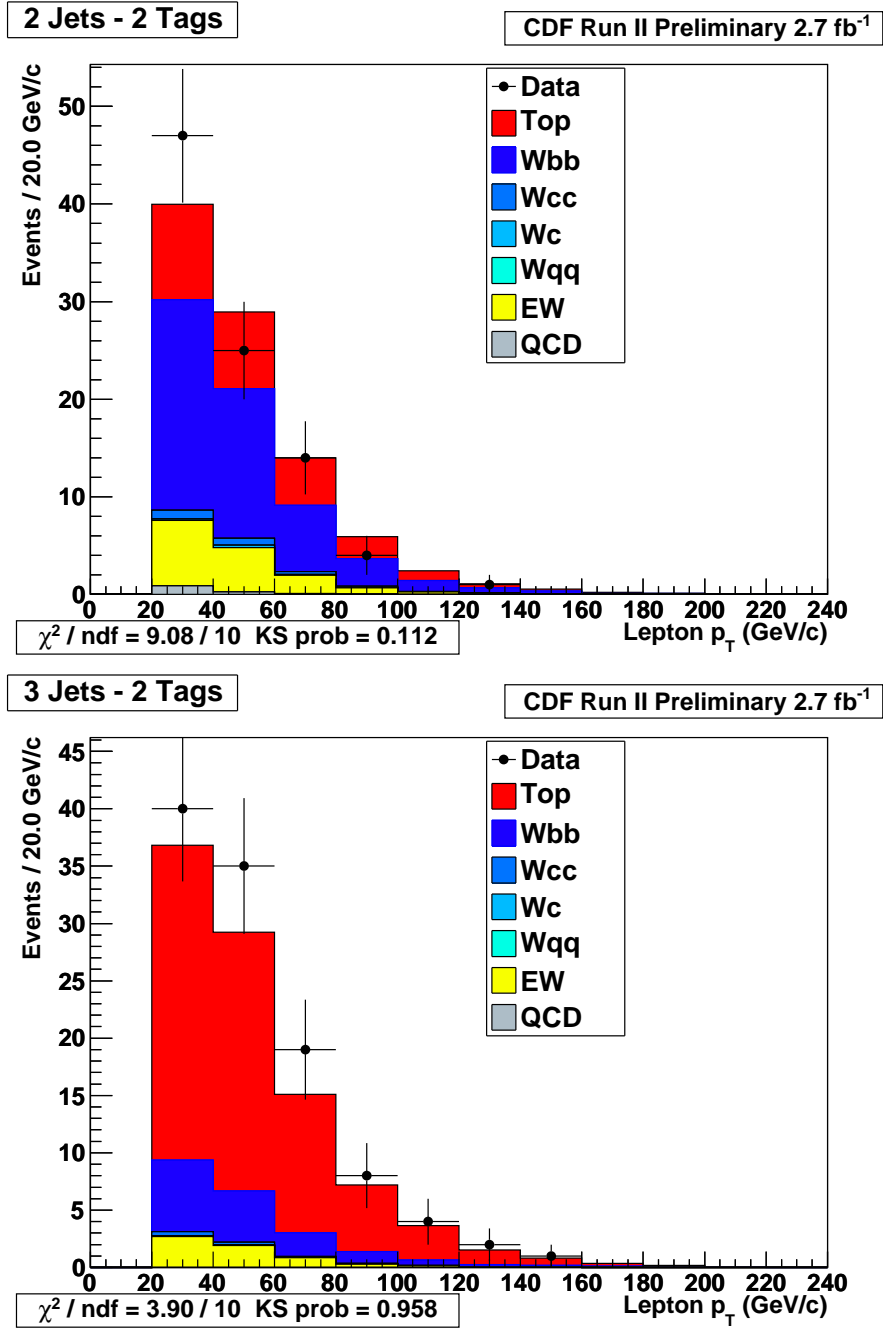


Figure 9.21: Validation plots of the transverse momentum of the lepton for double tags.

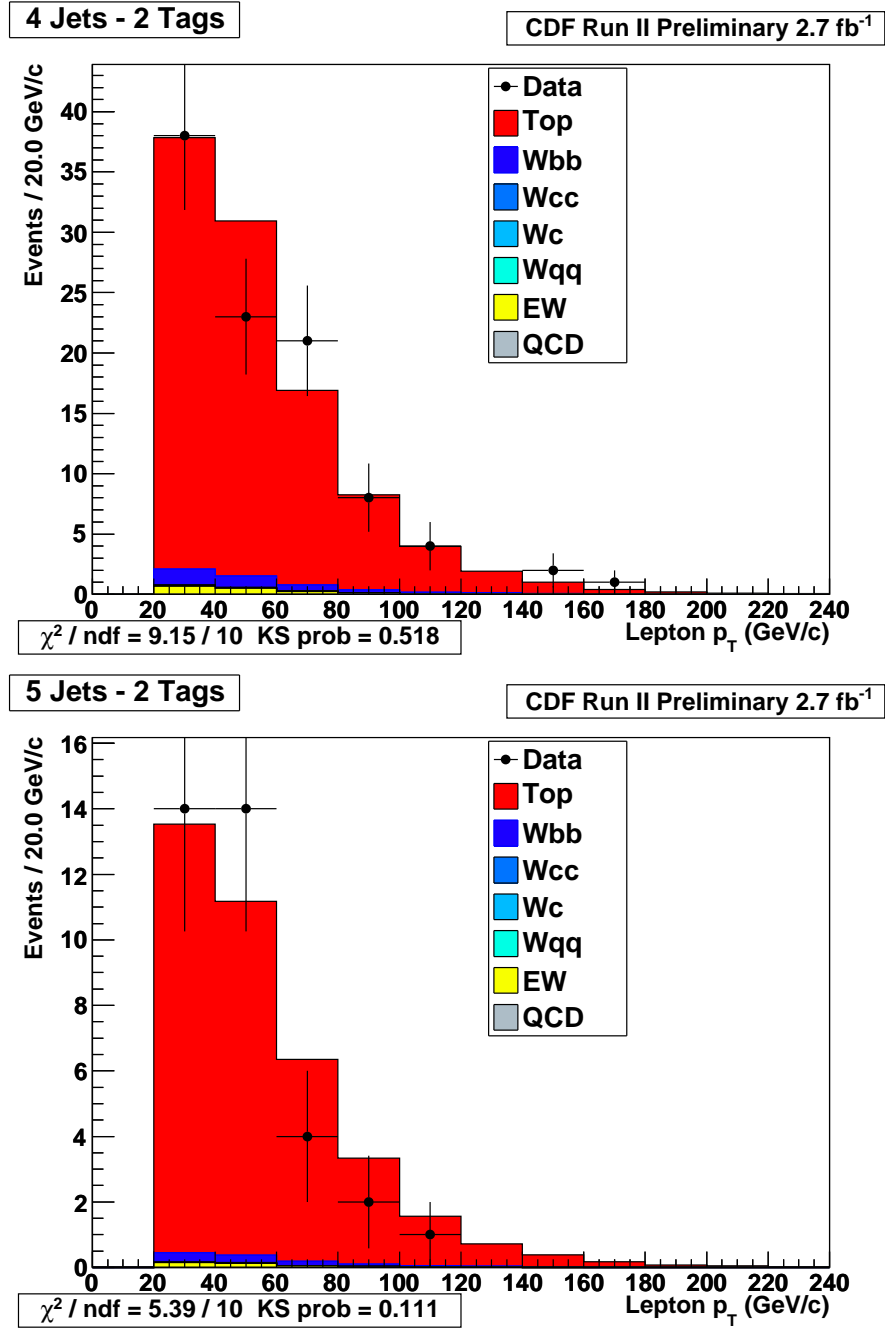


Figure 9.22: Validation plots of the transverse momentum of the lepton for double tags.

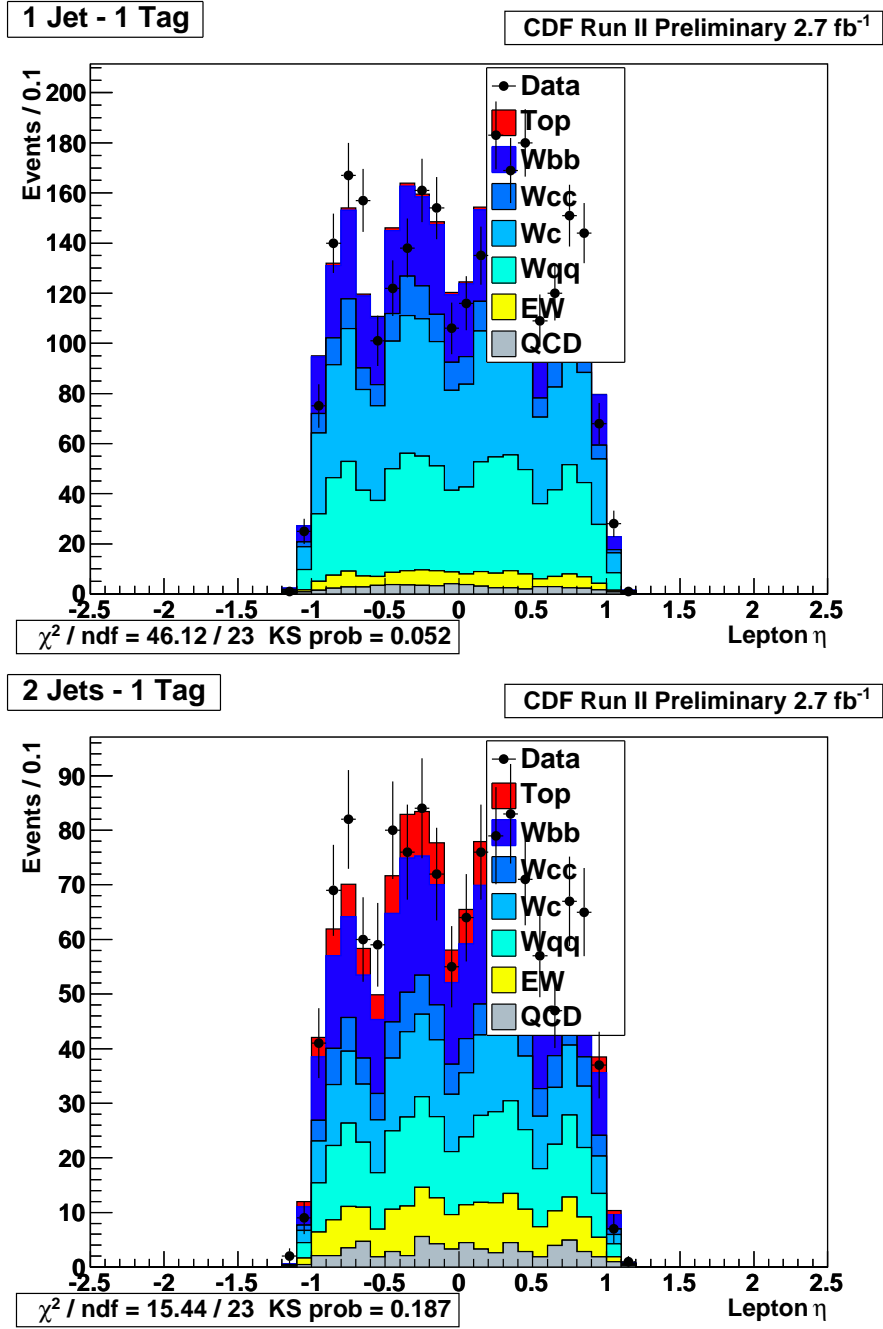


Figure 9.23: Validation plots of the pseudorapidity, η , of the lepton for single tags.

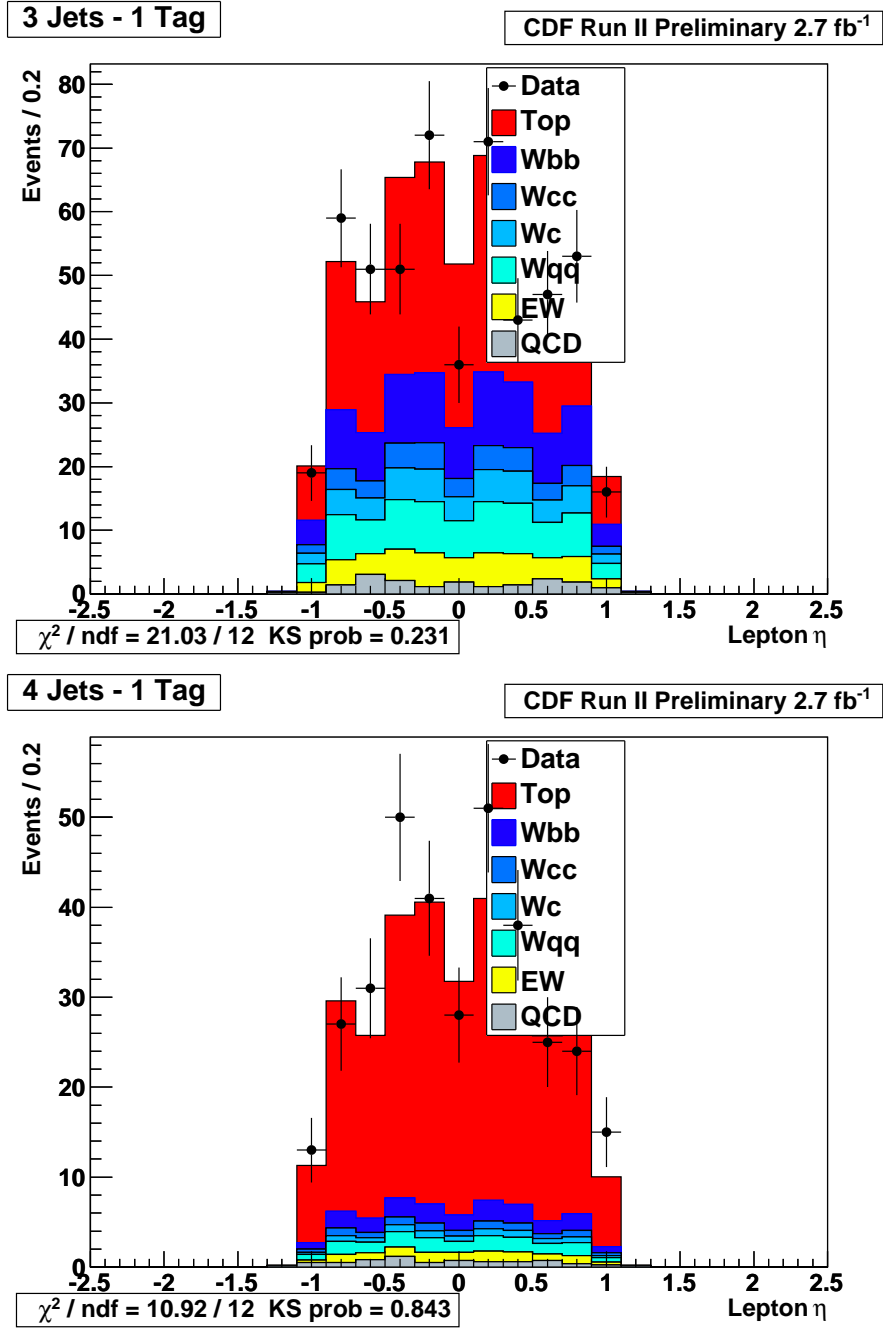


Figure 9.24: Validation plots of the pseudorapidity, η , of the lepton for single tags.

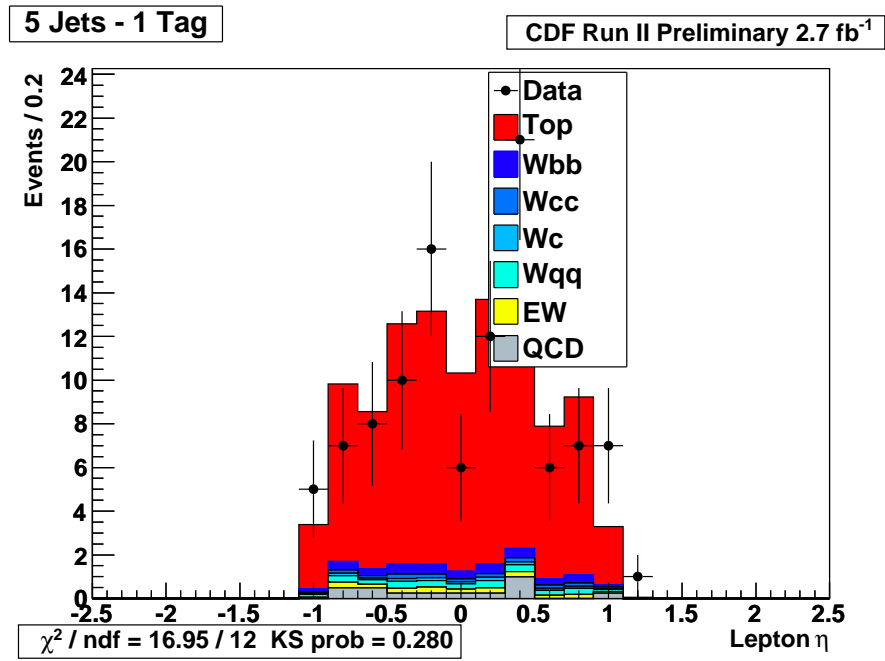


Figure 9.25: Validation plots of the pseudorapidity, η , of the lepton for single tags.

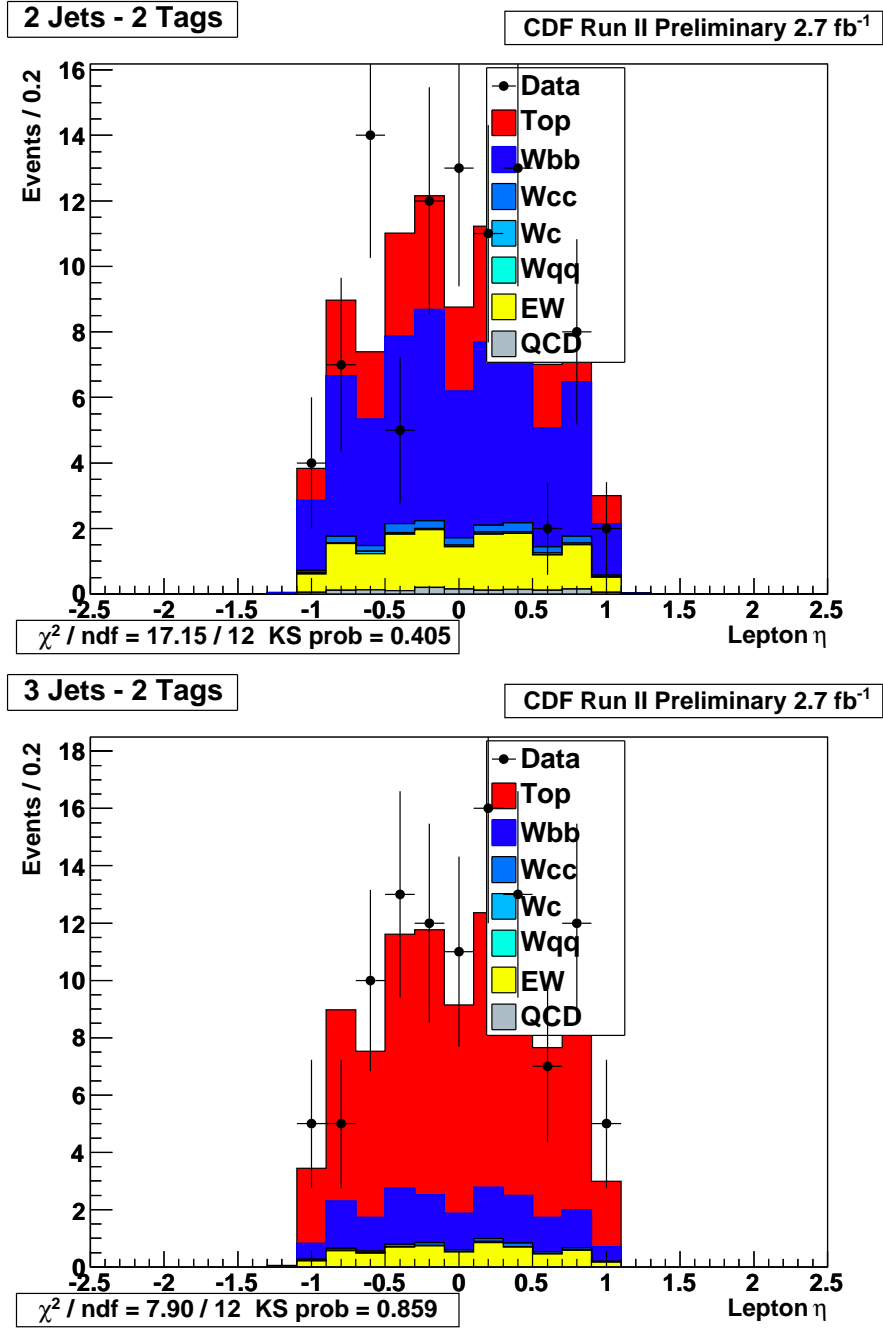


Figure 9.26: Validation plots of the pseudorapidity, η , of the lepton for double tags.

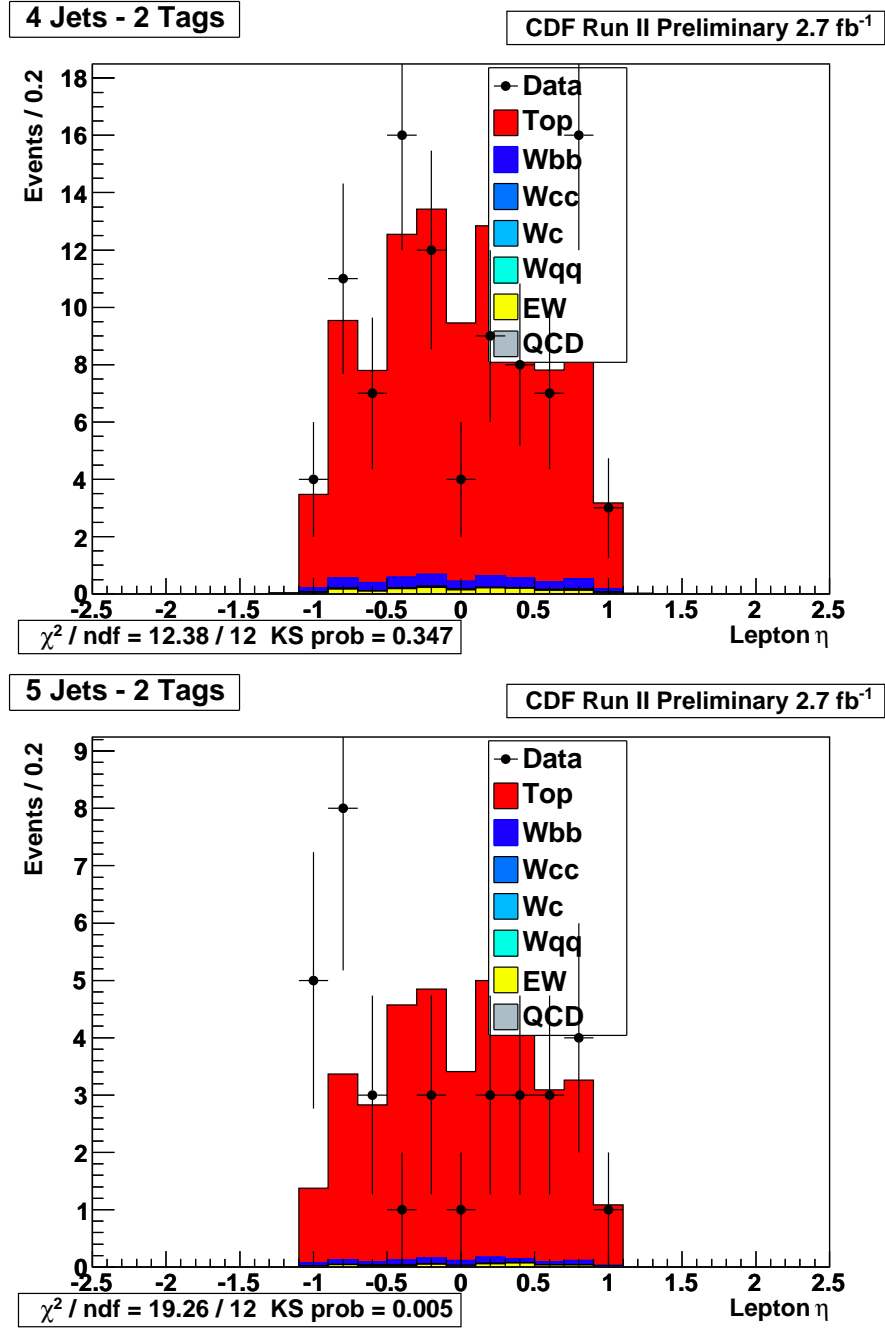


Figure 9.27: Validation plots of the pseudorapidity, η , of the lepton for double tags.

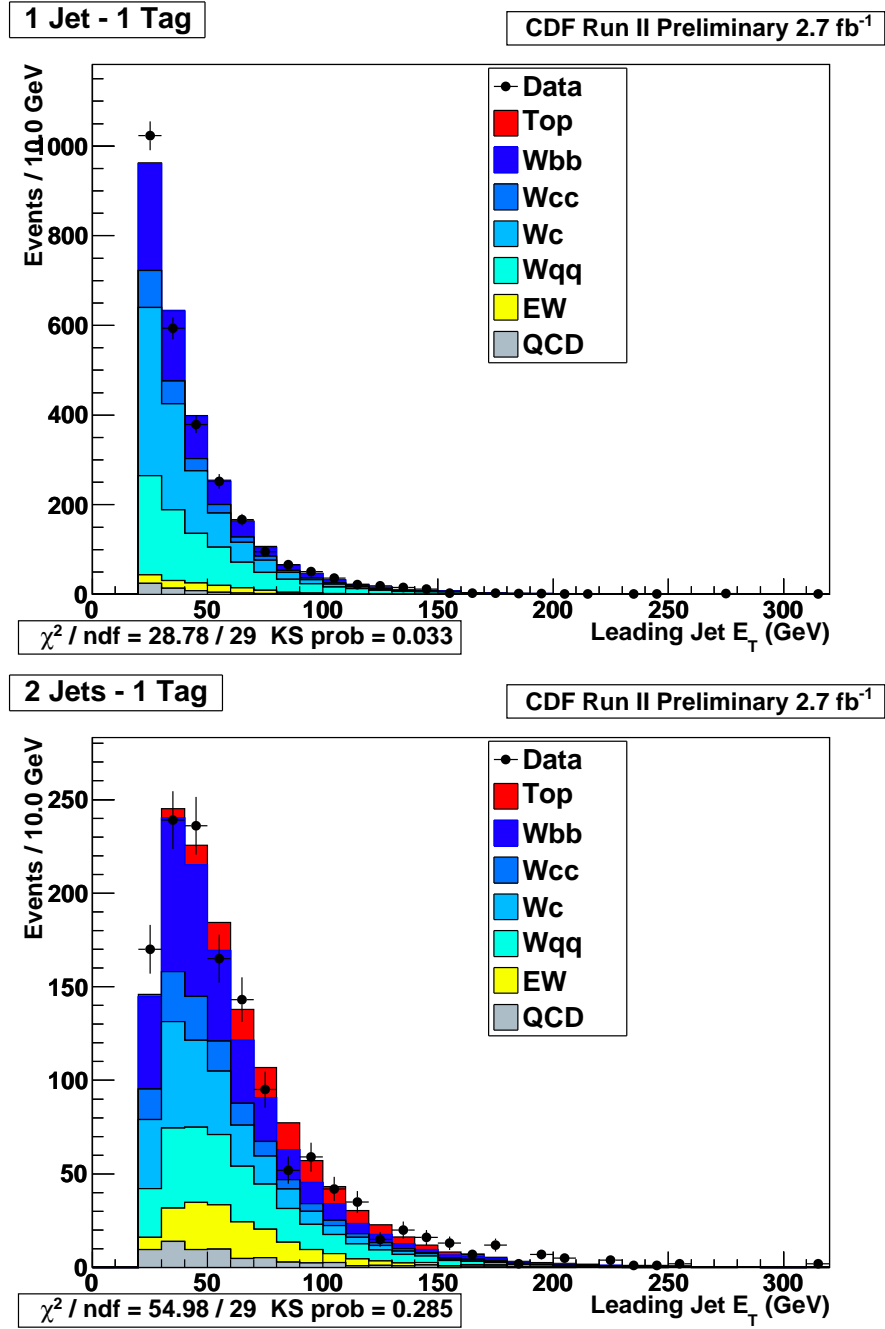


Figure 9.28: Validation plots of the transverse energy, E_T , of the leading jet for single tags.

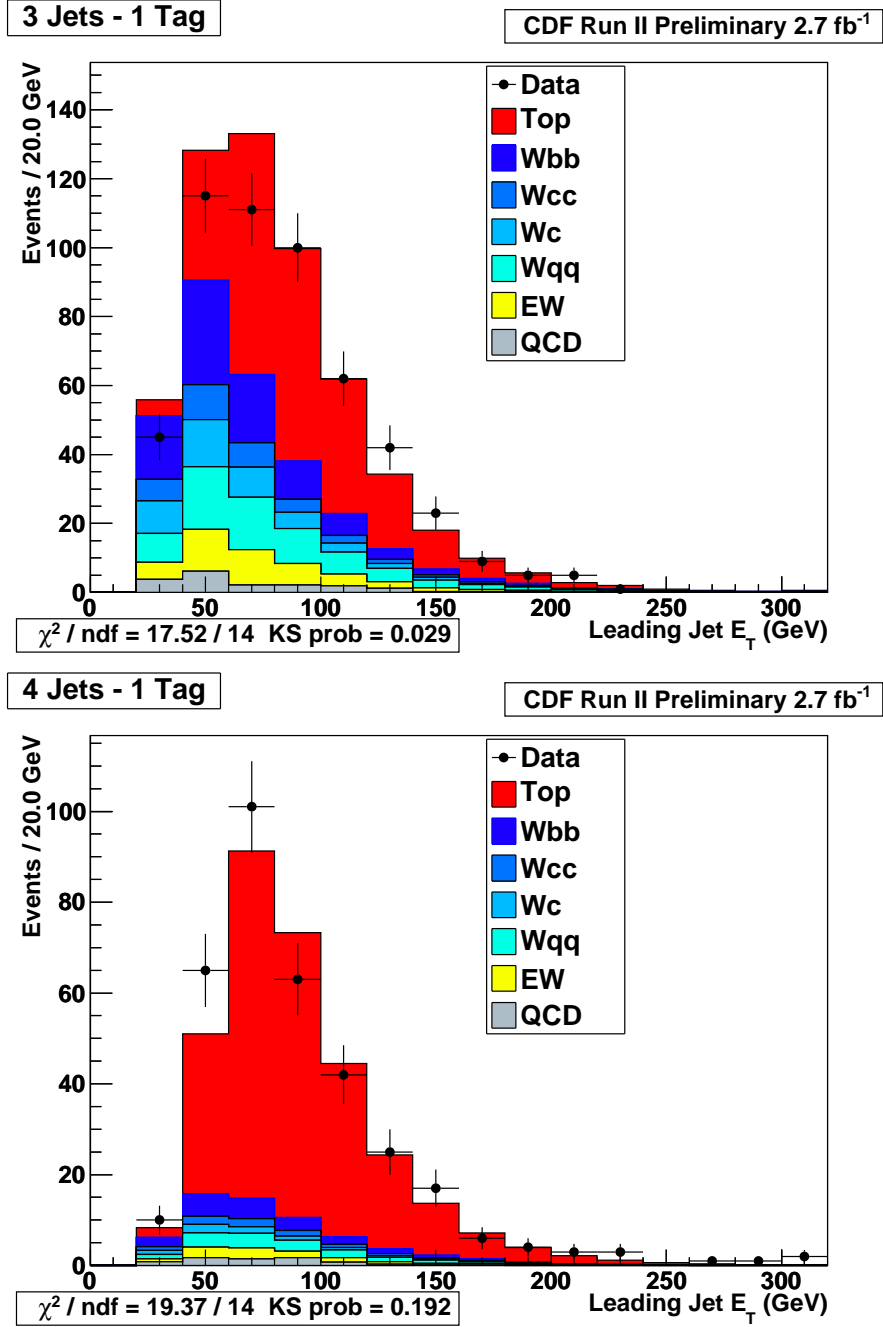


Figure 9.29: Validation plots of the transverse energy, E_T , of the leading jet for single tags.

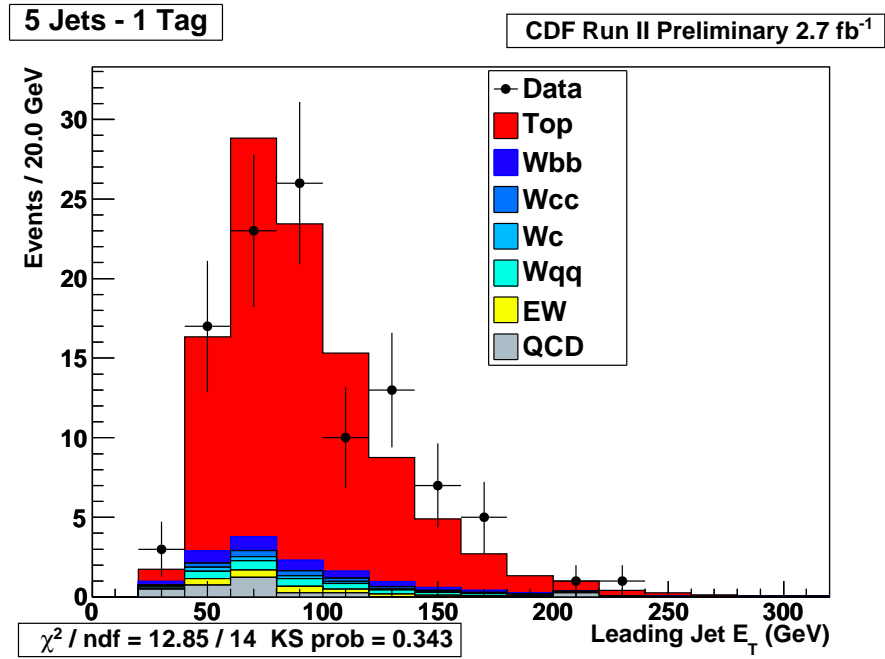


Figure 9.30: Validation plots of the transverse energy, E_T , of the leading jet for single tags.

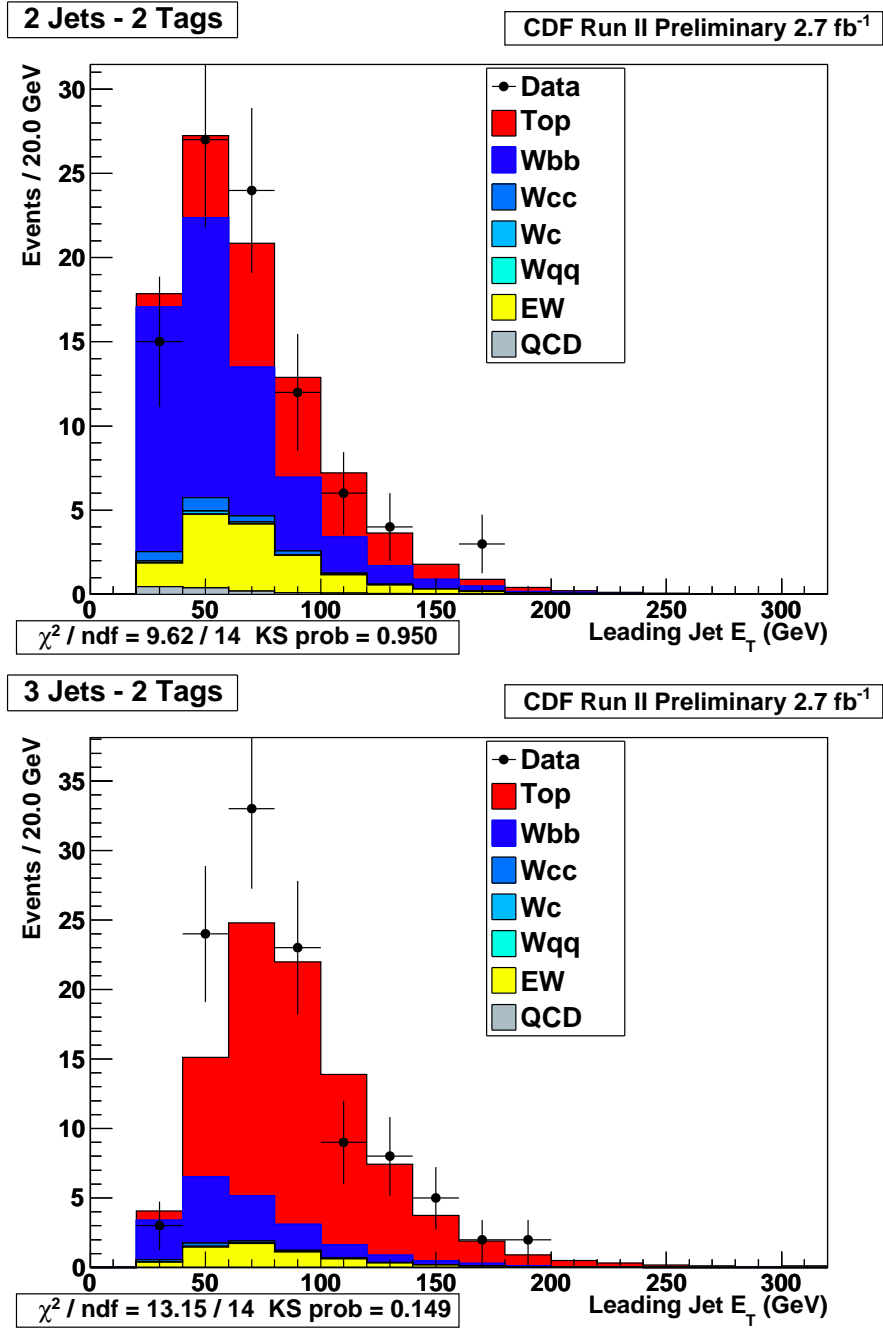


Figure 9.31: Validation plots of the transverse energy, E_T , of the leading jet for double tags.

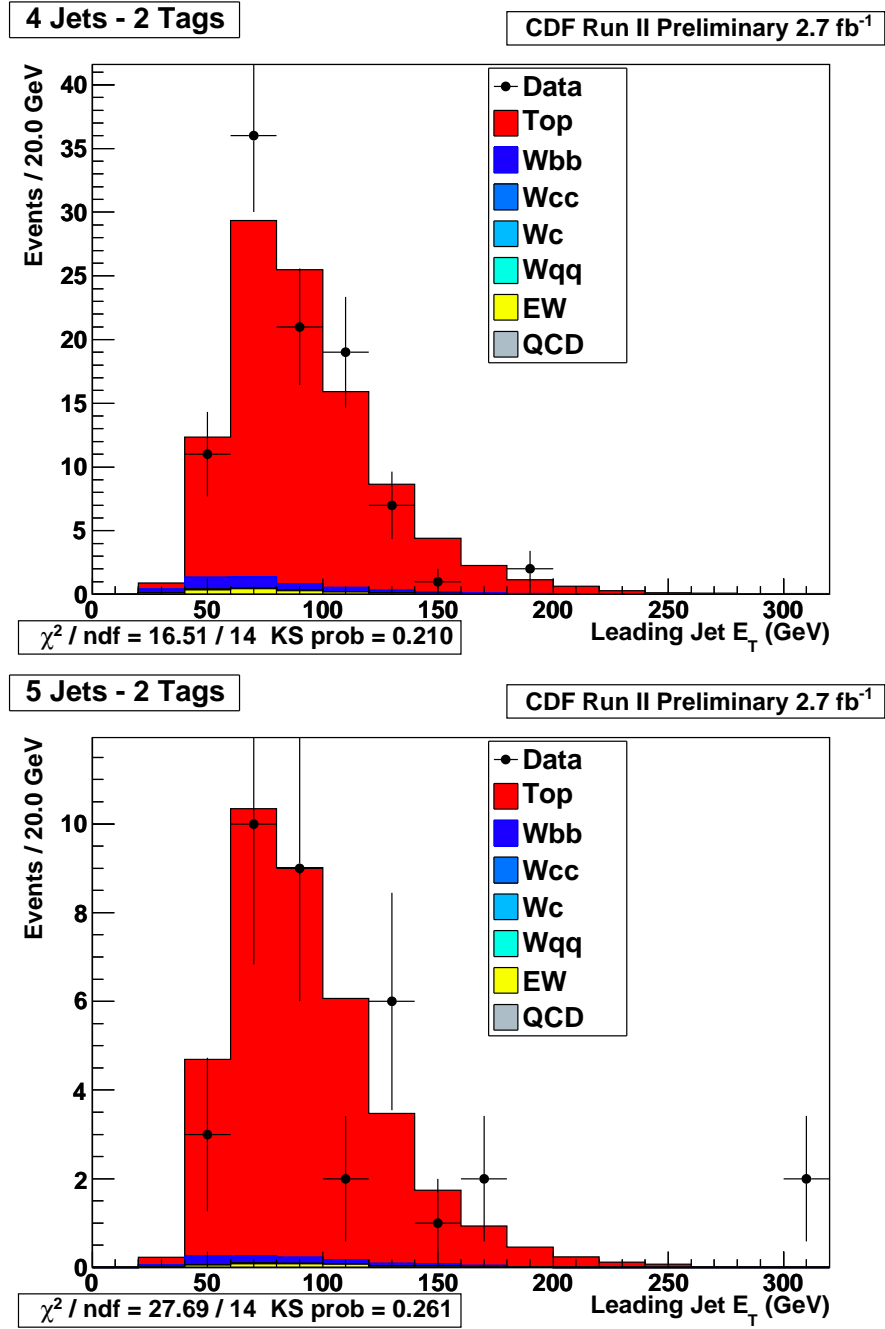


Figure 9.32: Validation plots of the transverse energy, E_T , of the leading jet for double tags.

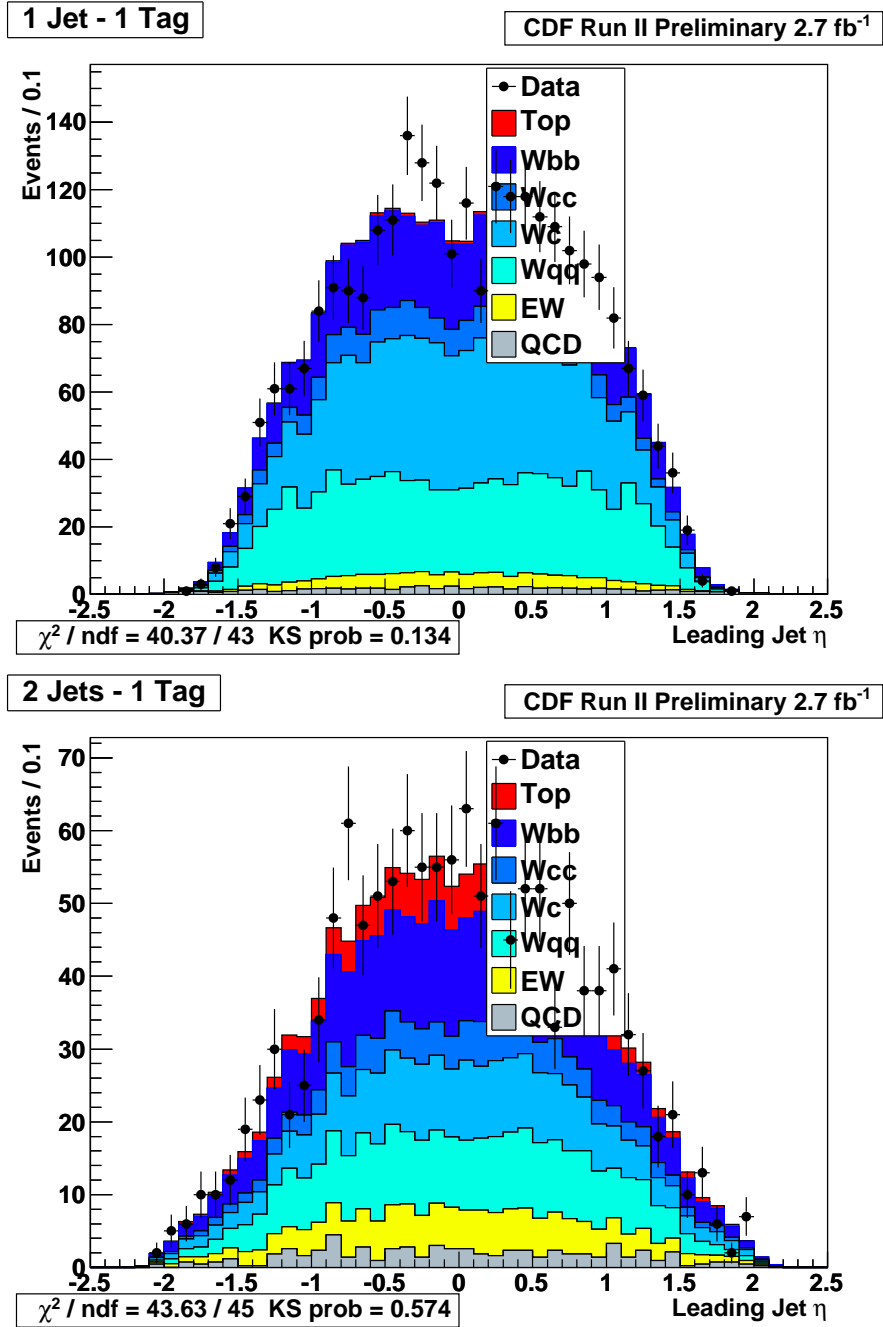


Figure 9.33: Validation plots of the pseudorapidity, η , of the leading jet for single tags.

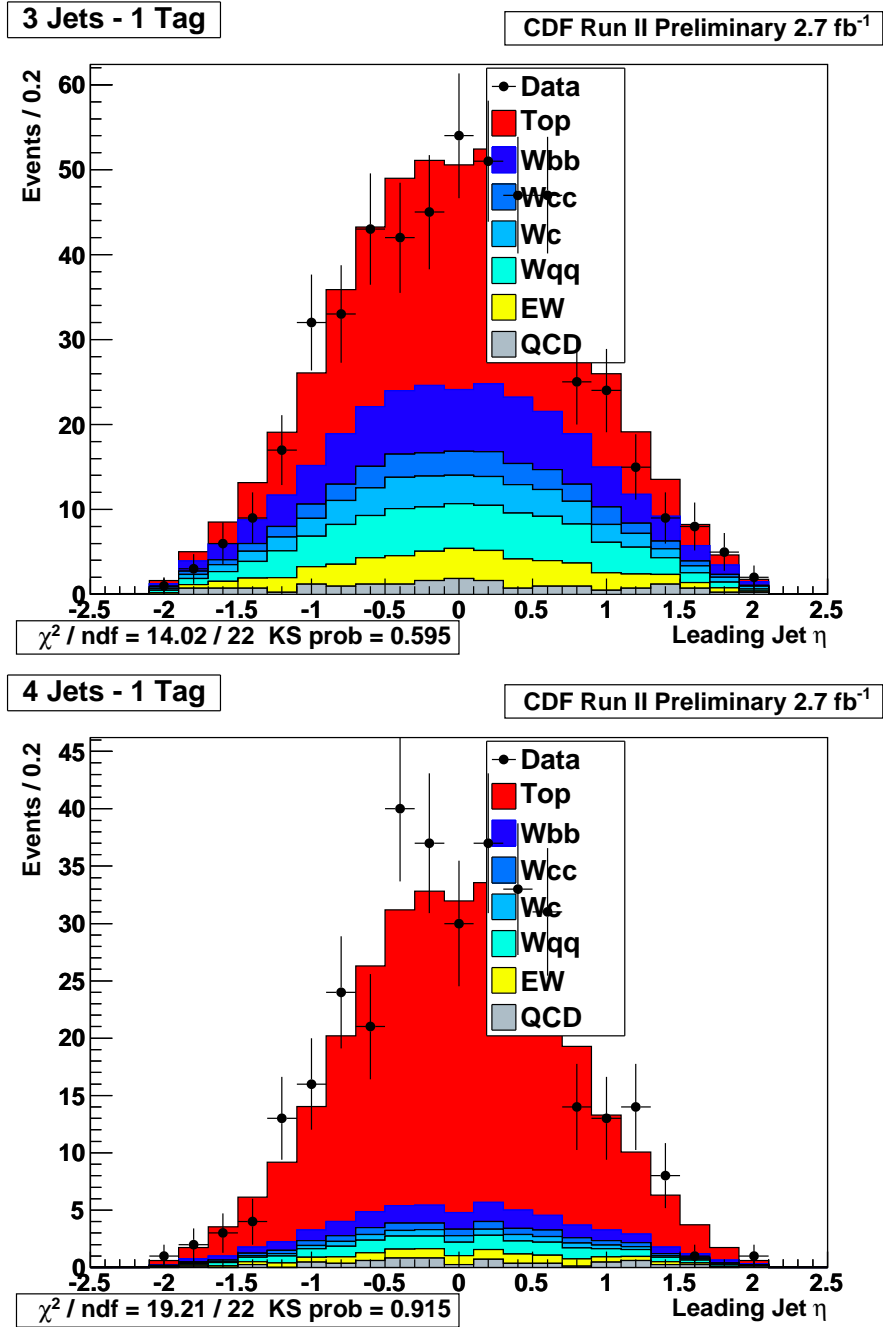


Figure 9.34: Validation plots of the pseudorapidity, η , of the leading jet for single tags.

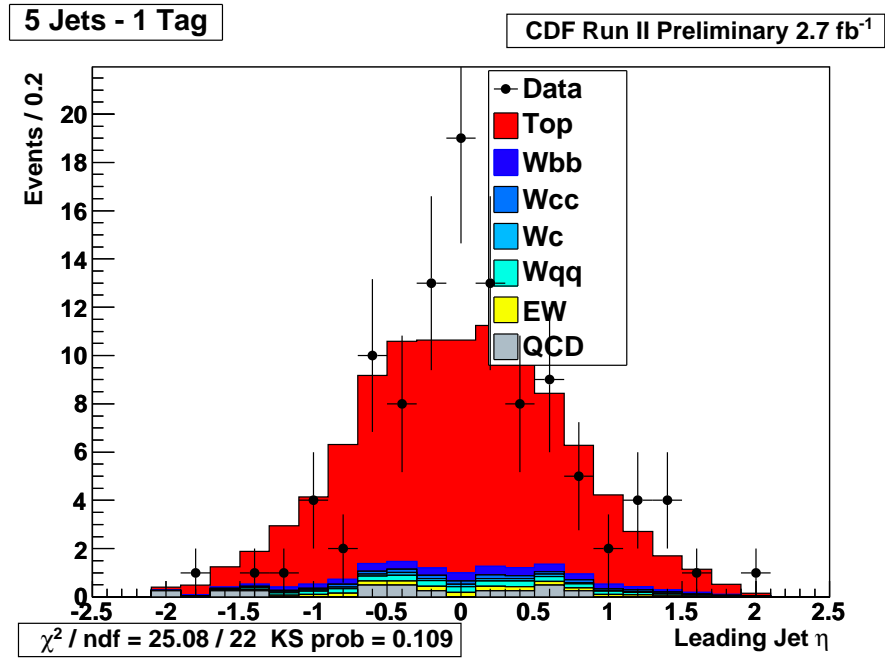


Figure 9.35: Validation plots of the pseudorapidity, η , of the leading jet for single tags.

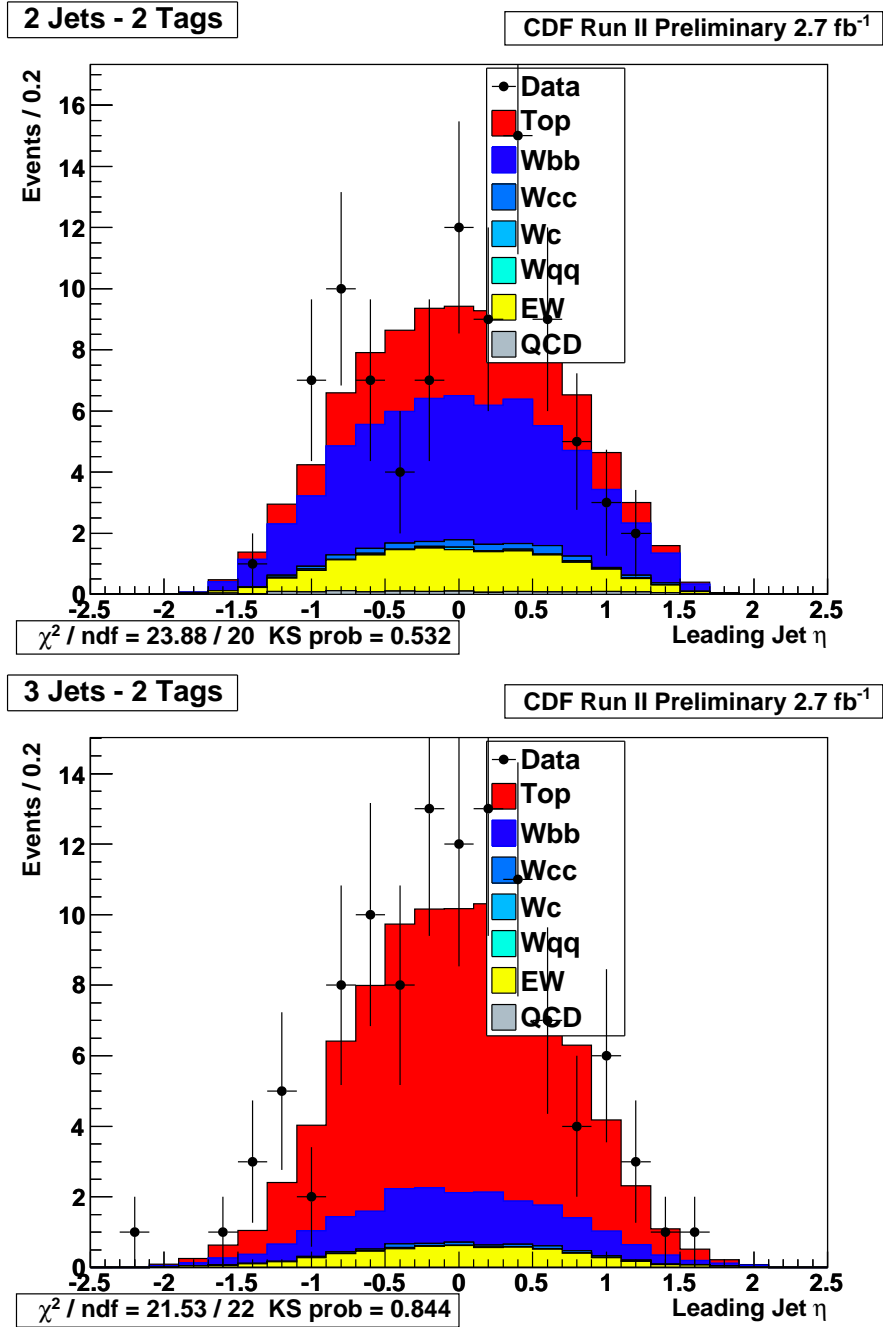


Figure 9.36: Validation plots of the pseudorapidity, η , of the leading jet for double tags.

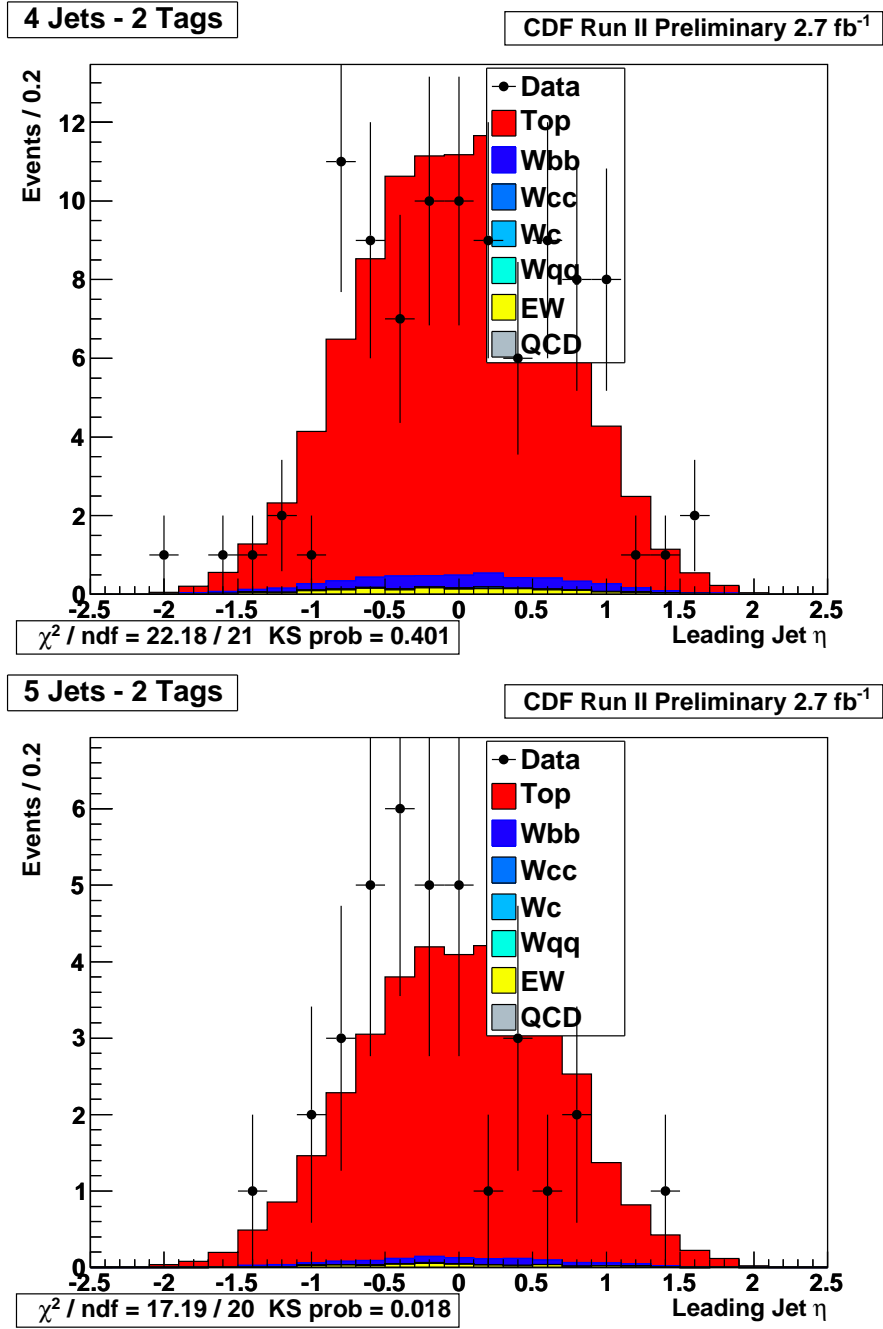


Figure 9.37: Validation plots of the pseudorapidity, η , of the leading jet for double tags.

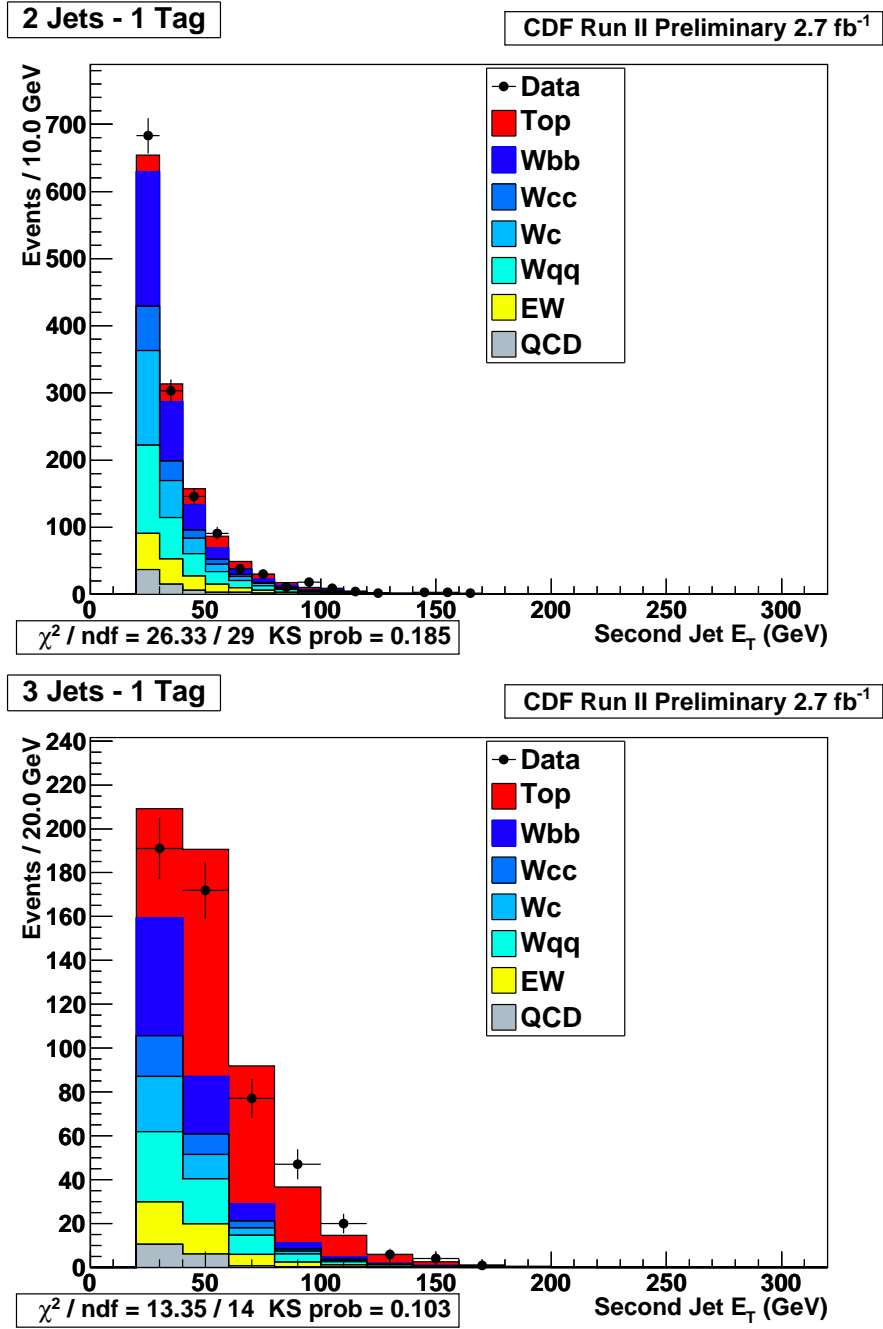


Figure 9.38: Validation plots of the transverse energy, E_T , of the secondary jet for single tags.

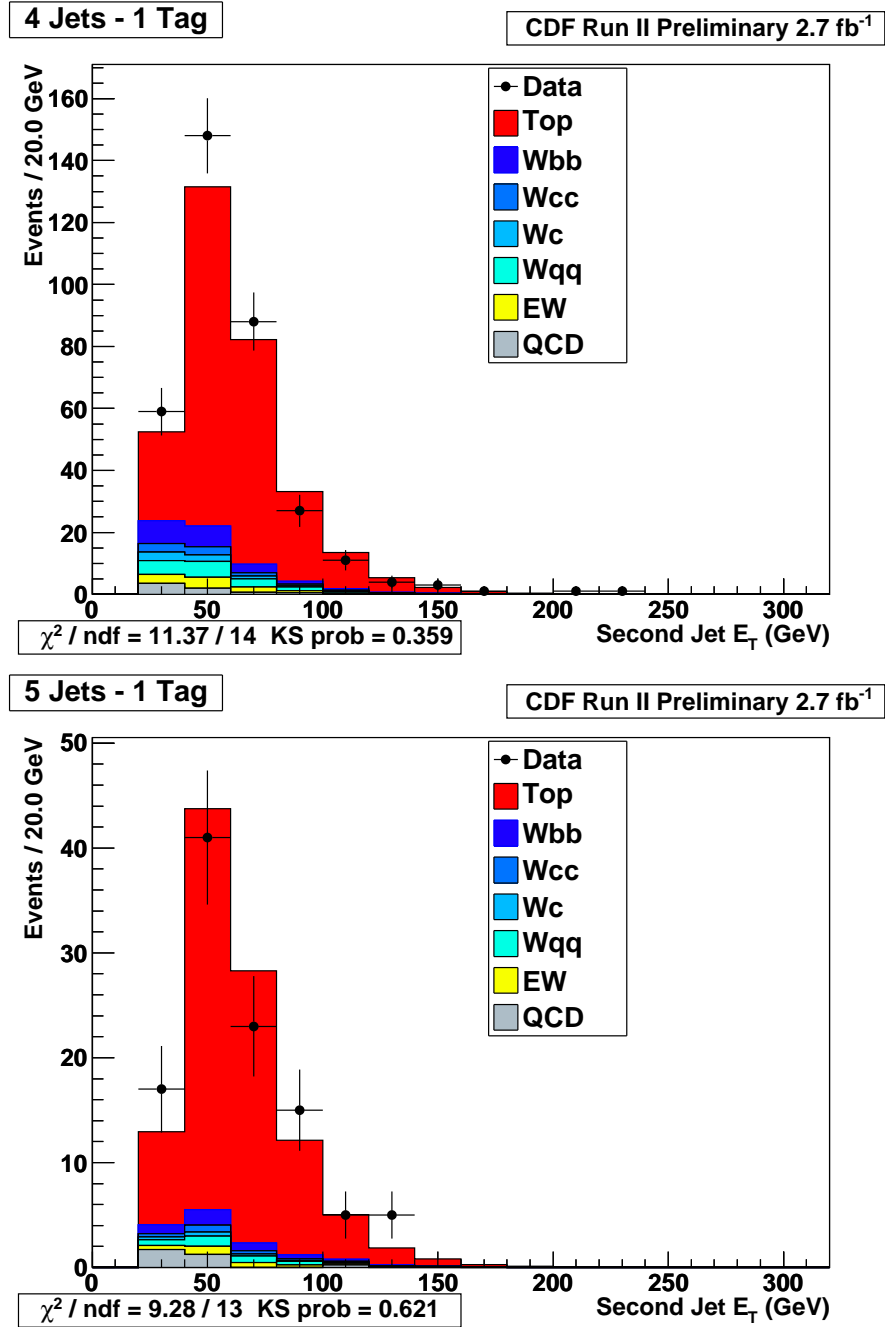


Figure 9.39: Validation plots of the transverse energy, E_T , of the secondary jet for single tags.

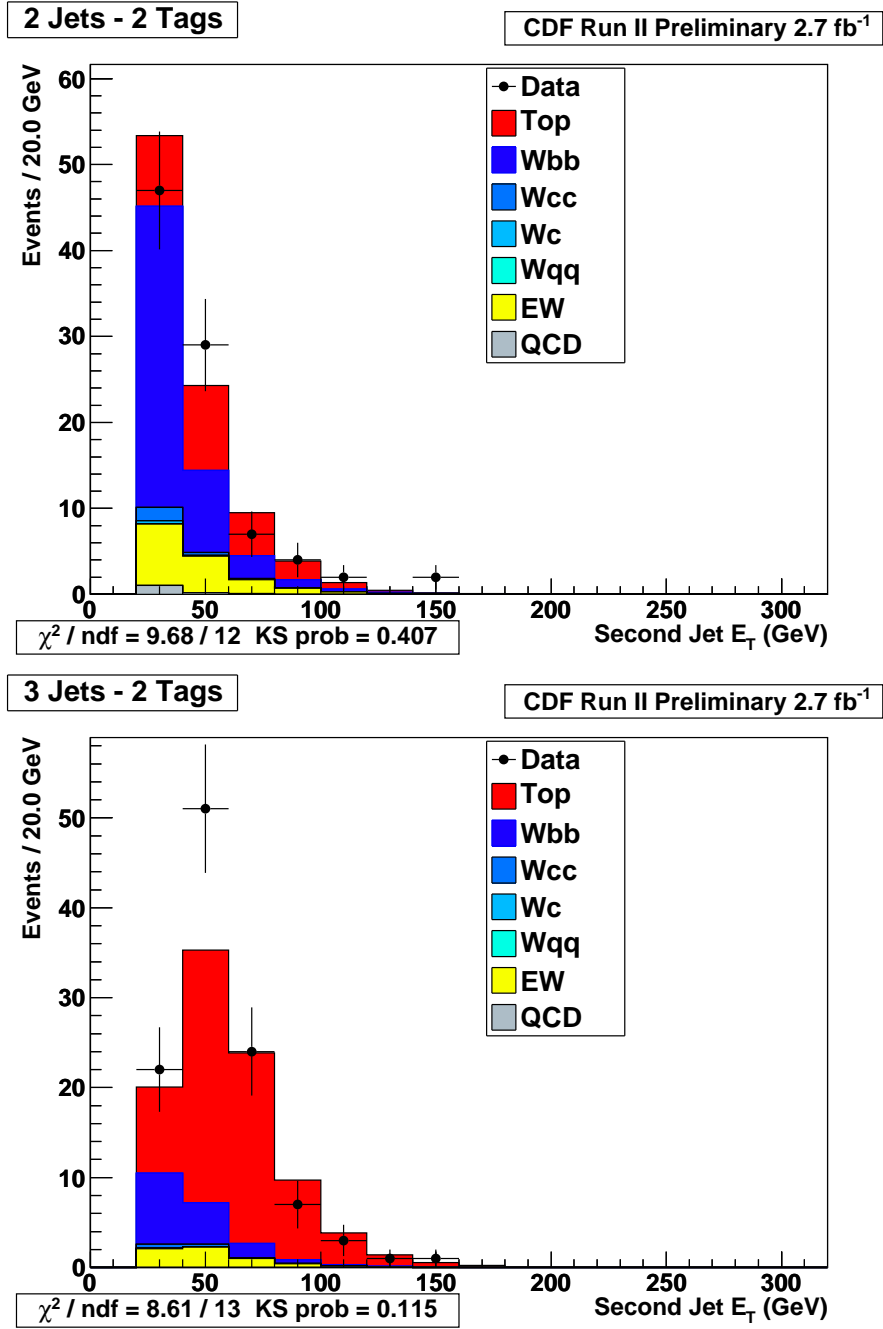


Figure 9.40: Validation plots of the transverse energy, E_T , of the secondary jet for double tags.

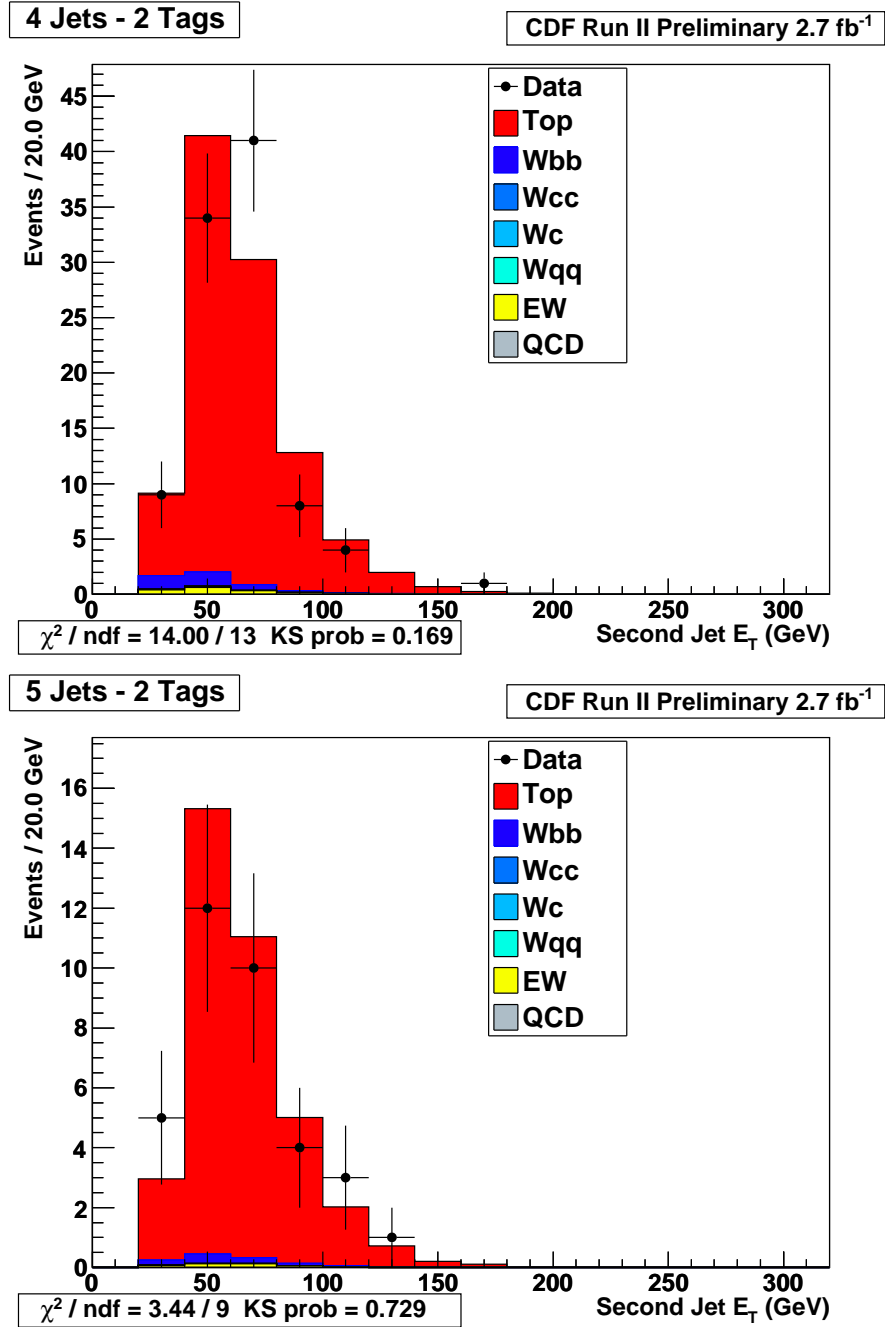


Figure 9.41: Validation plots of the transverse energy, E_T , of the secondary jet for double tags.

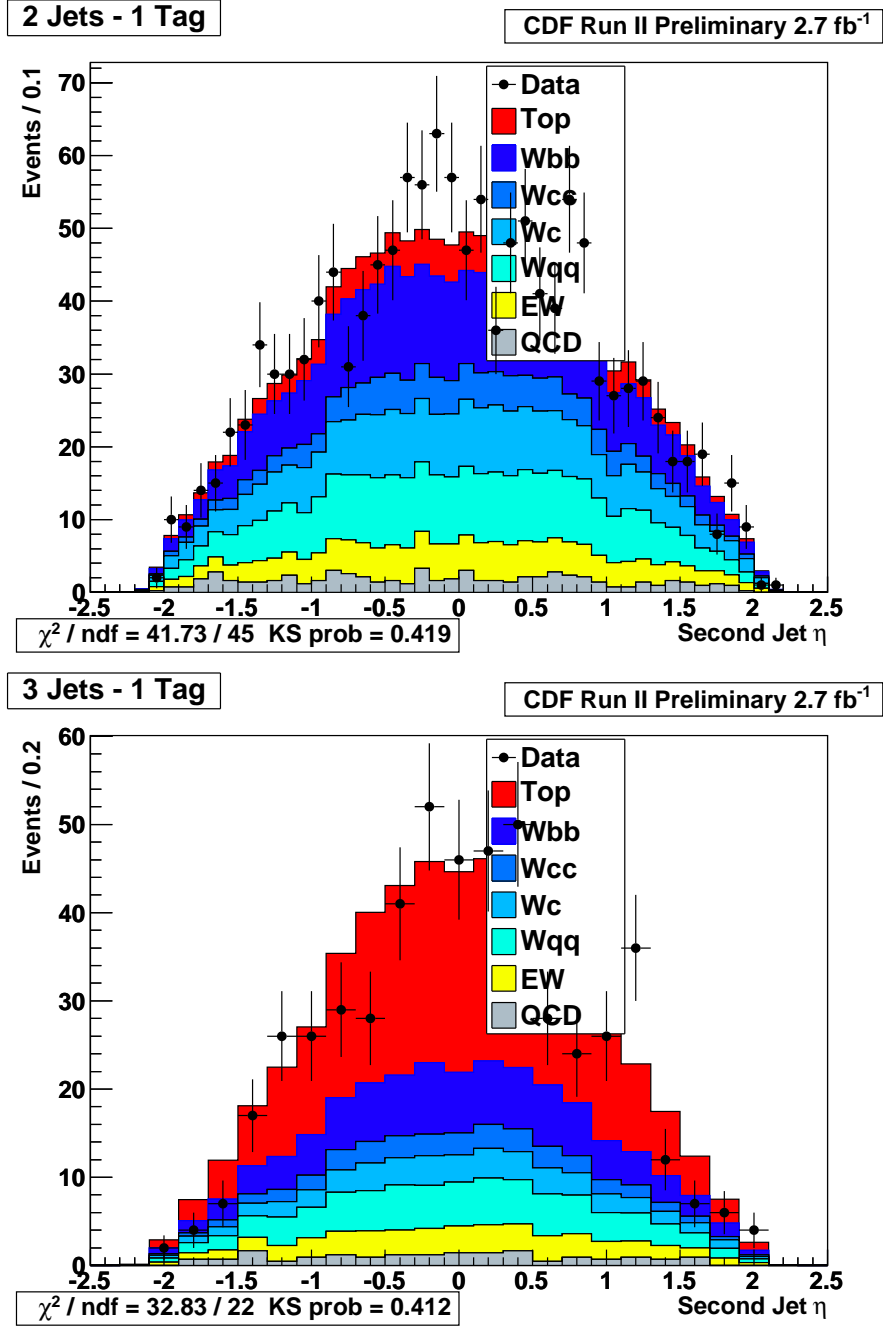


Figure 9.42: Validation plots of the pseudorapidity, η , of the secondary jet for single tags.

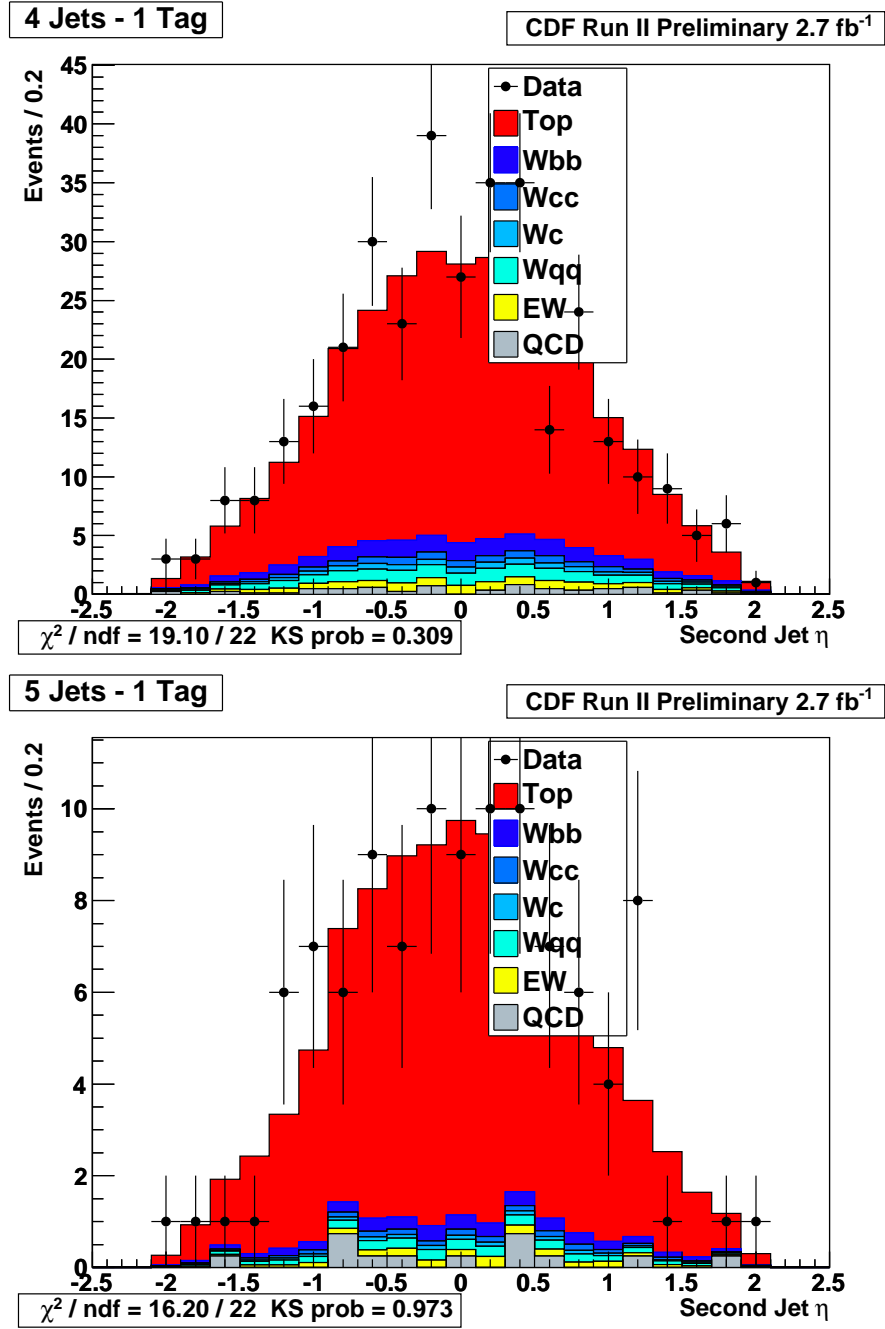


Figure 9.43: Validation plots of the pseudorapidity, η , of the secondary jet for single tags.

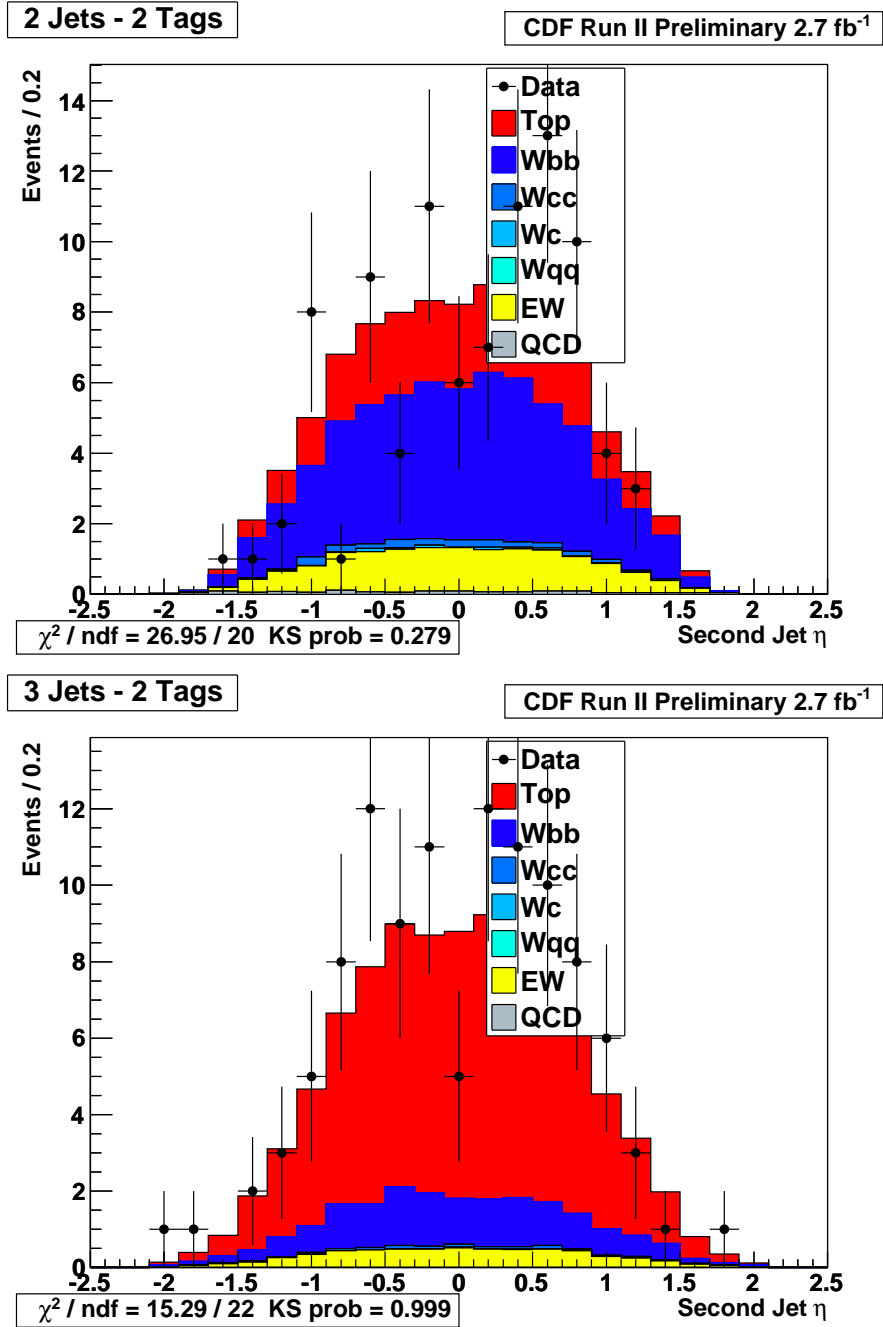


Figure 9.44: Validation plots of the pseudorapidity, η , of the secondary jet for double tags.

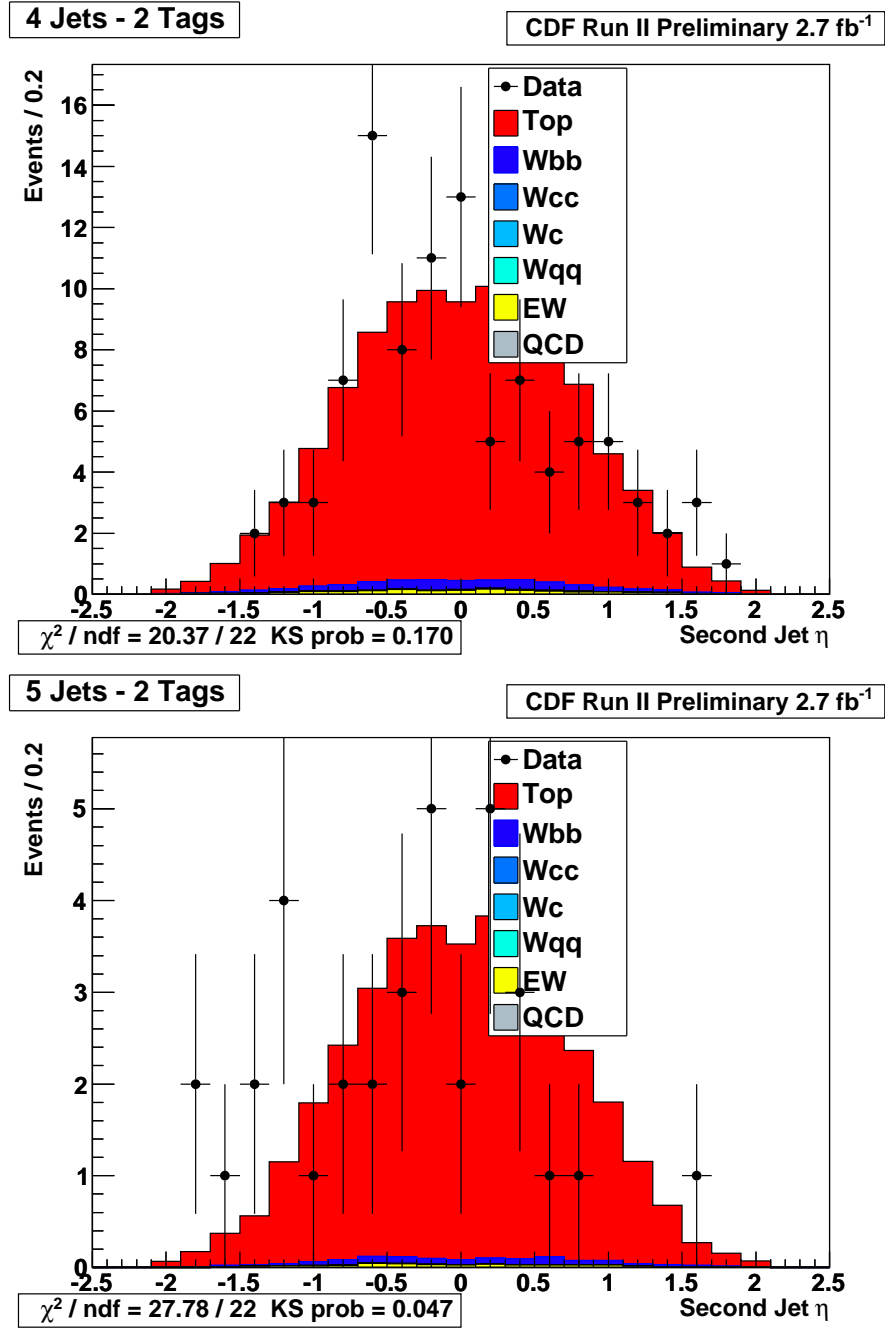


Figure 9.45: Validation plots of the pseudorapidity, η , of the secondary jet for double tags.

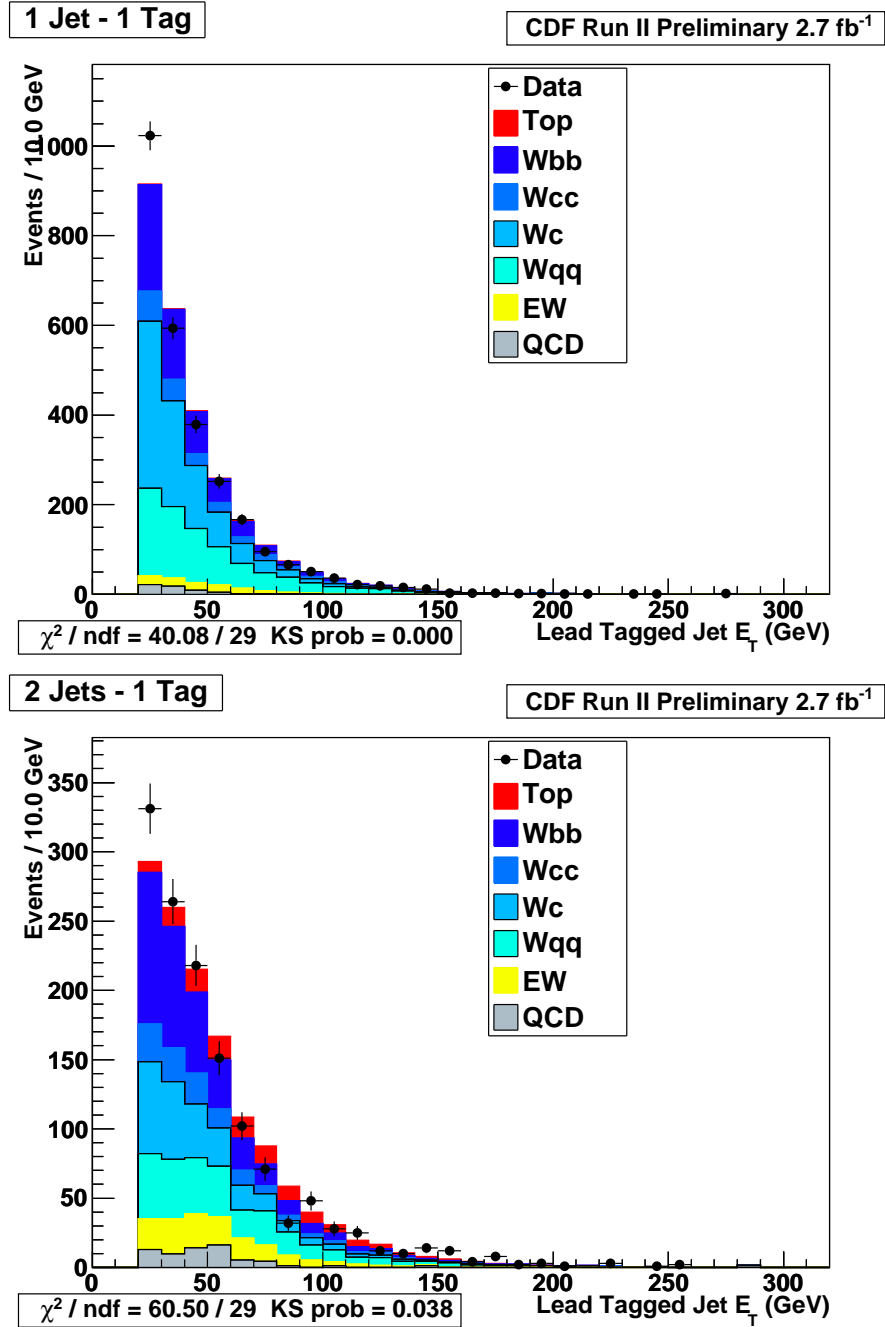


Figure 9.46: Validation plots of the transverse energy, E_T , of the leading tagged jet for single tags.

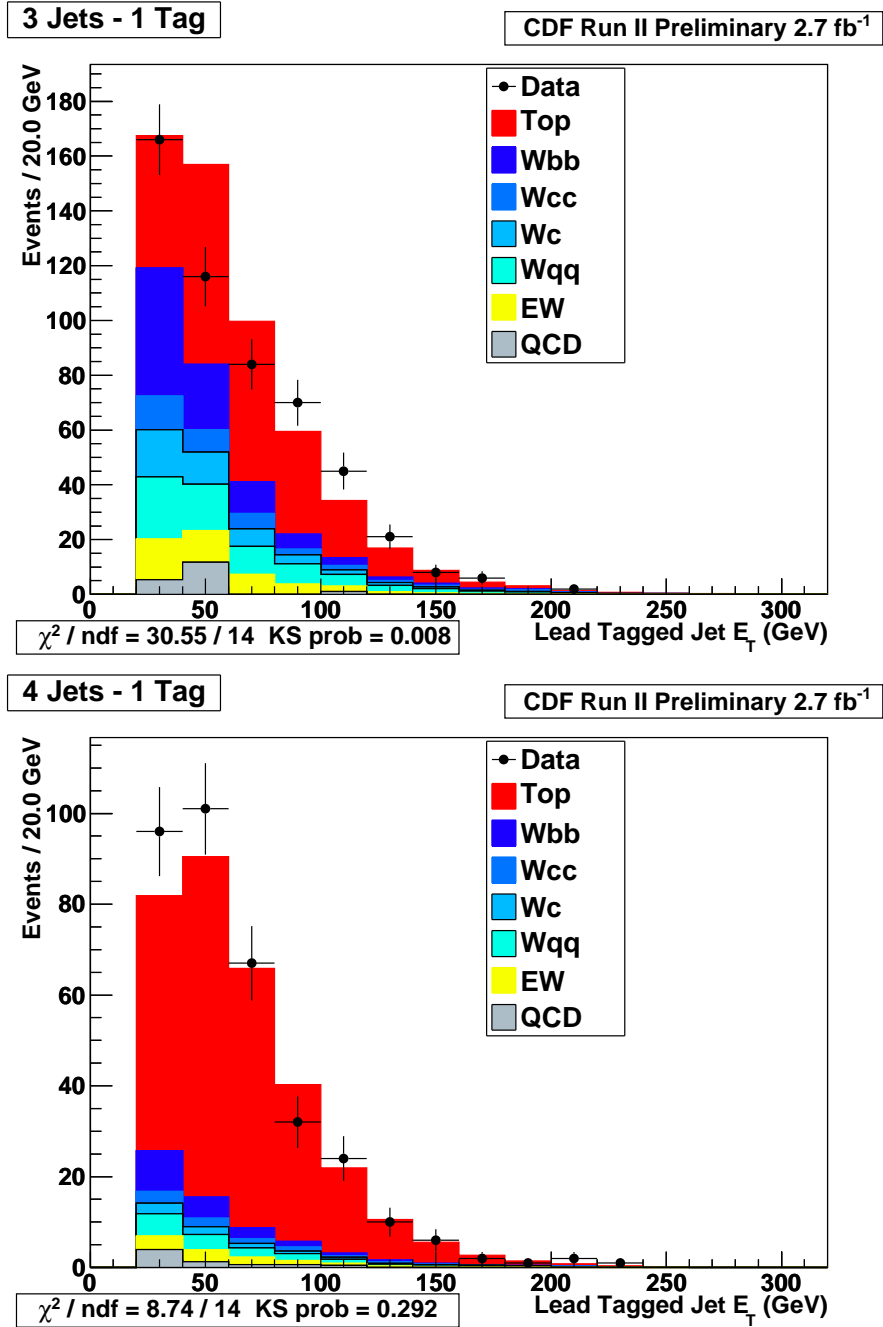


Figure 9.47: Validation plots of the transverse energy, E_T , of the leading tagged jet for single tags.

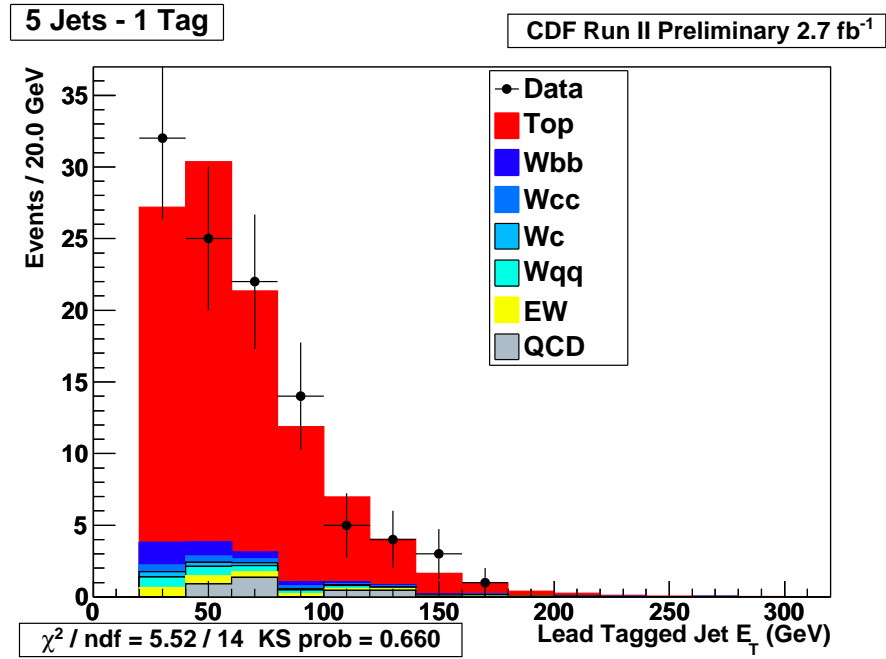


Figure 9.48: Validation plots of the transverse energy, E_T , of the leading tagged jet for single tags.

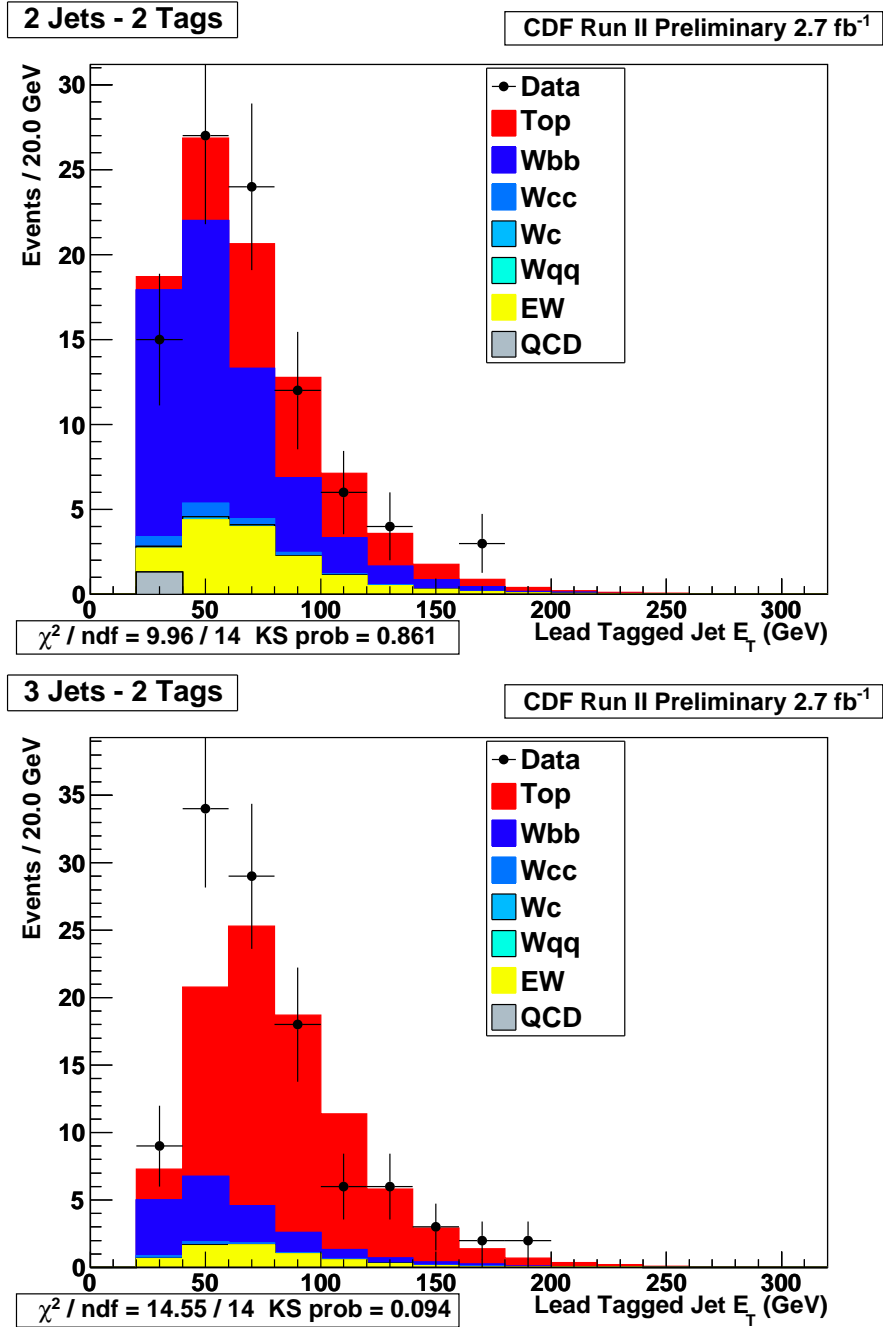


Figure 9.49: Validation plots of the transverse energy, E_T , of the leading tagged jet for double tags.

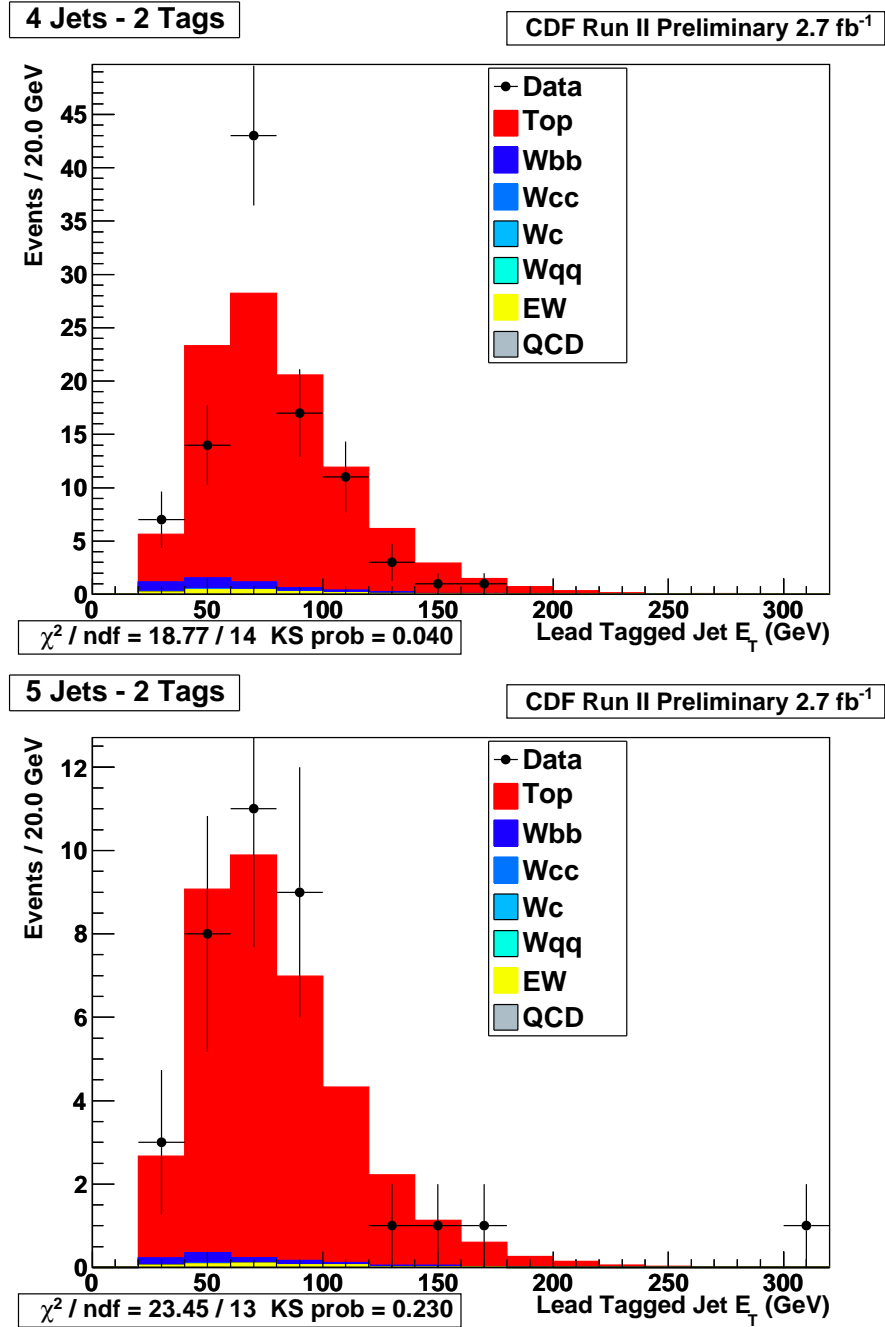


Figure 9.50: Validation plots of the transverse energy, E_T , of the leading tagged jet for double tags.

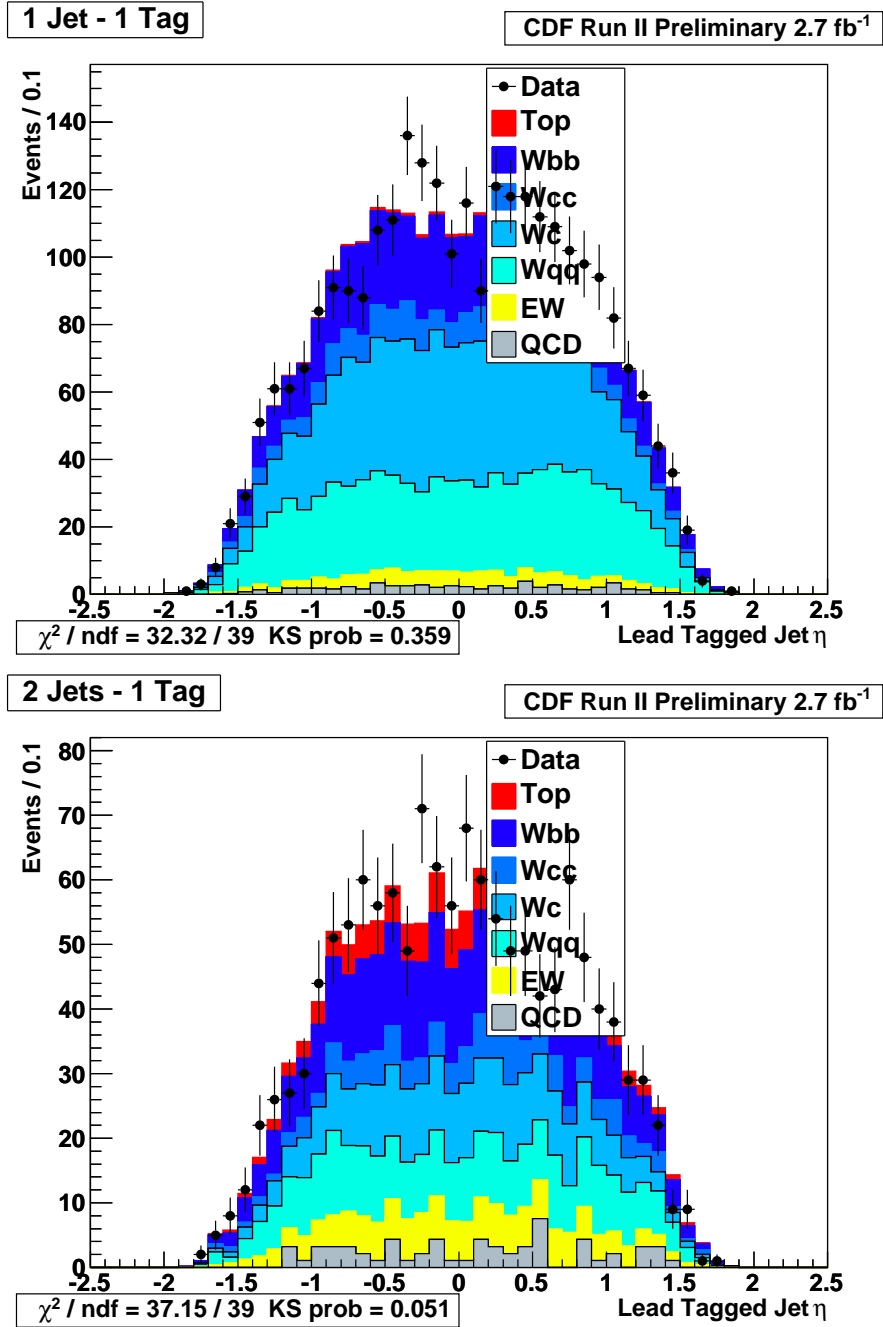


Figure 9.51: Validation plots of the pseudorapidity, η , of the leading tagged jet for single tags.

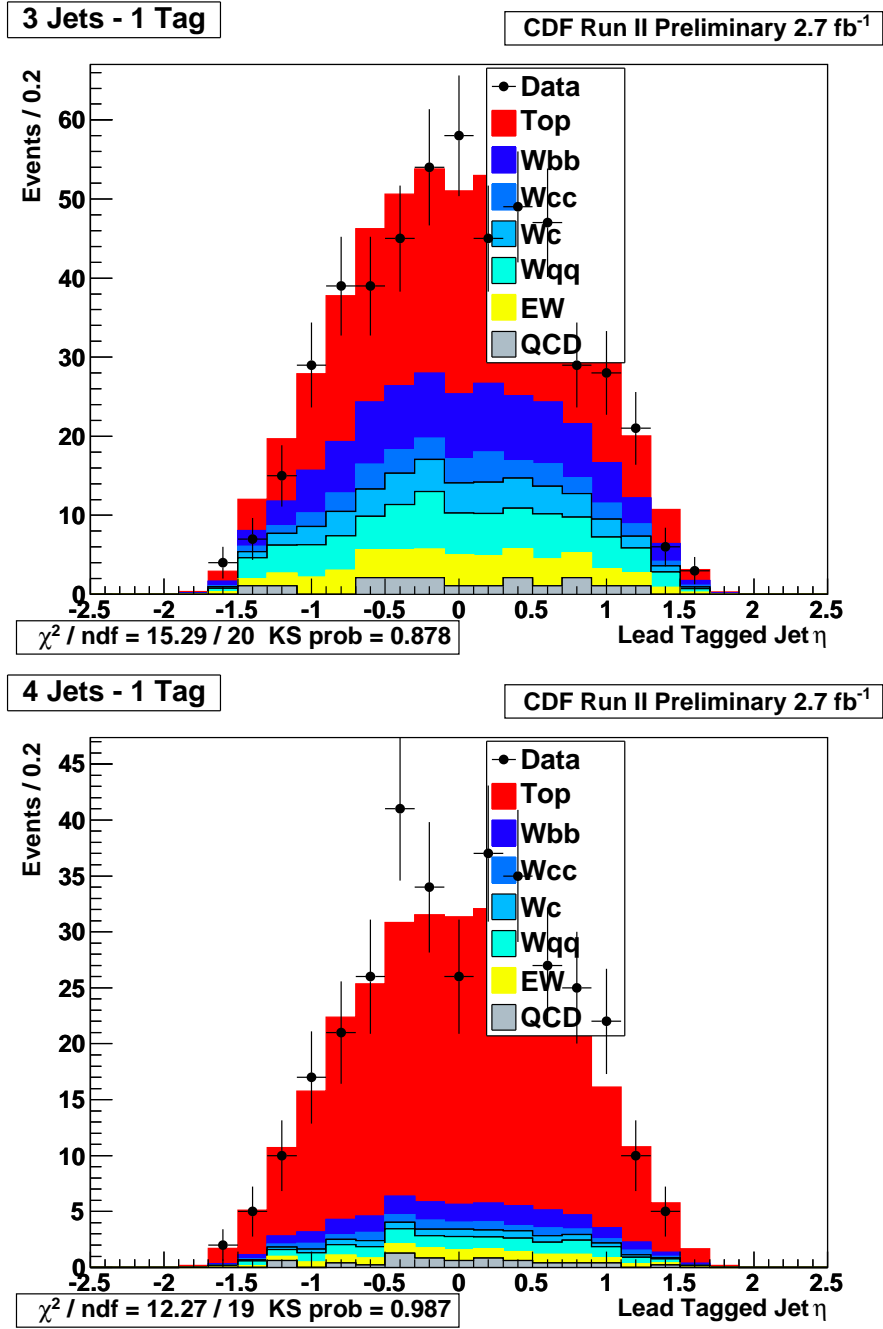


Figure 9.52: Validation plots of the pseudorapidity, η , of the leading tagged jet for single tags.

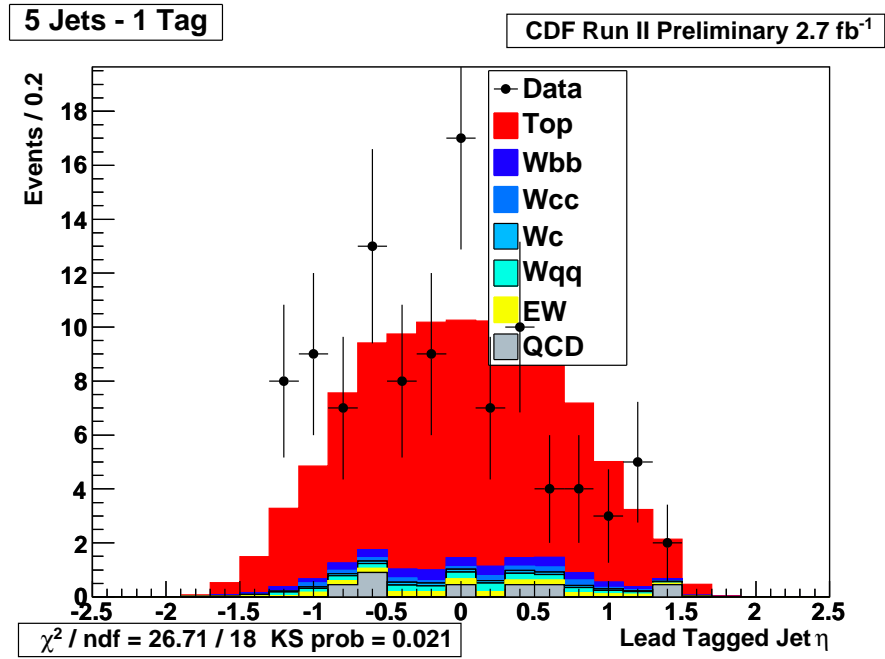


Figure 9.53: Validation plots of the pseudorapidity, η , of the leading tagged jet for single tags.

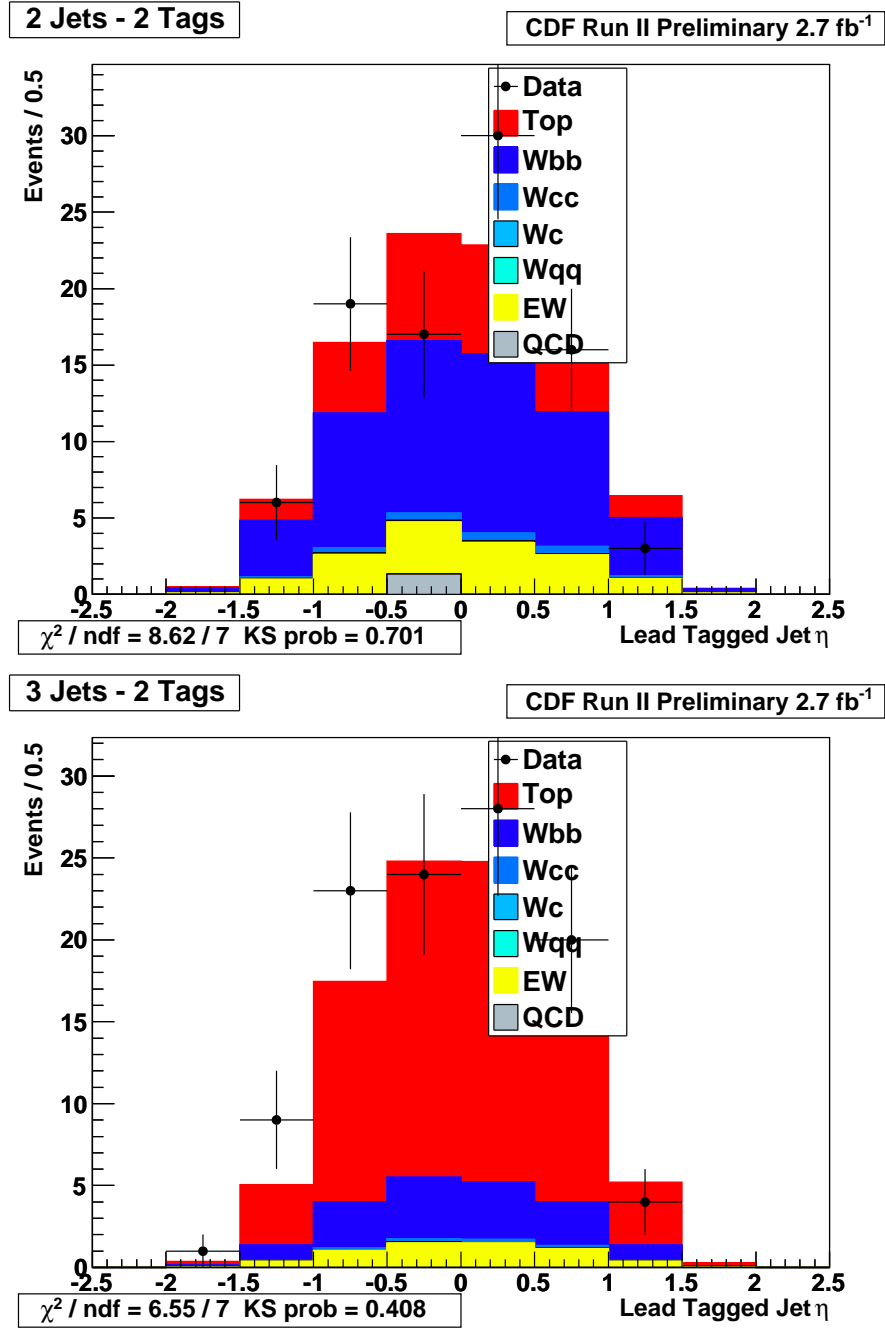


Figure 9.54: Validation plots of the pseudorapidity, η , of the leading tagged jet for double tags.

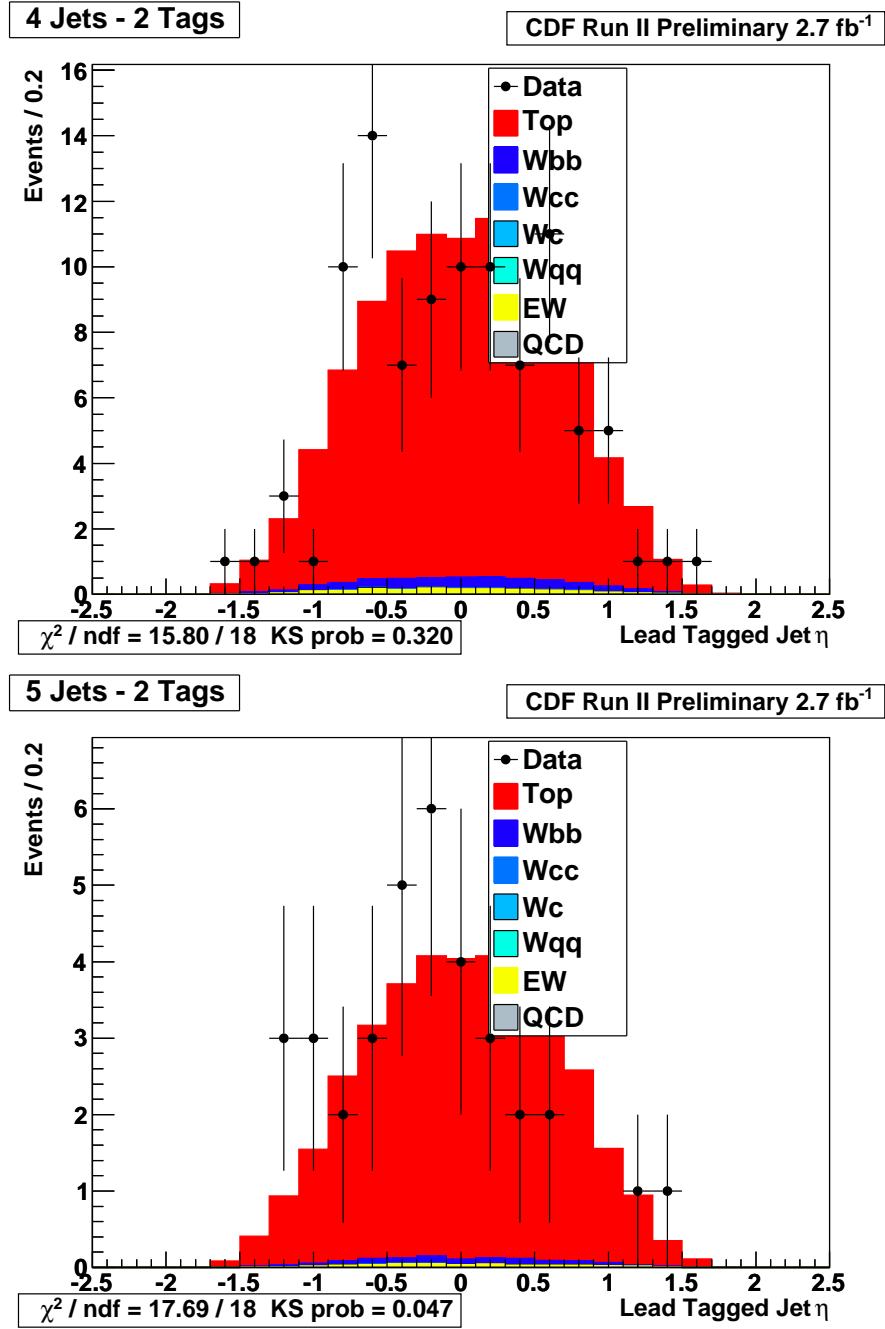


Figure 9.55: Validation plots of the pseudorapidity, η , of the leading tagged jet for double tags.

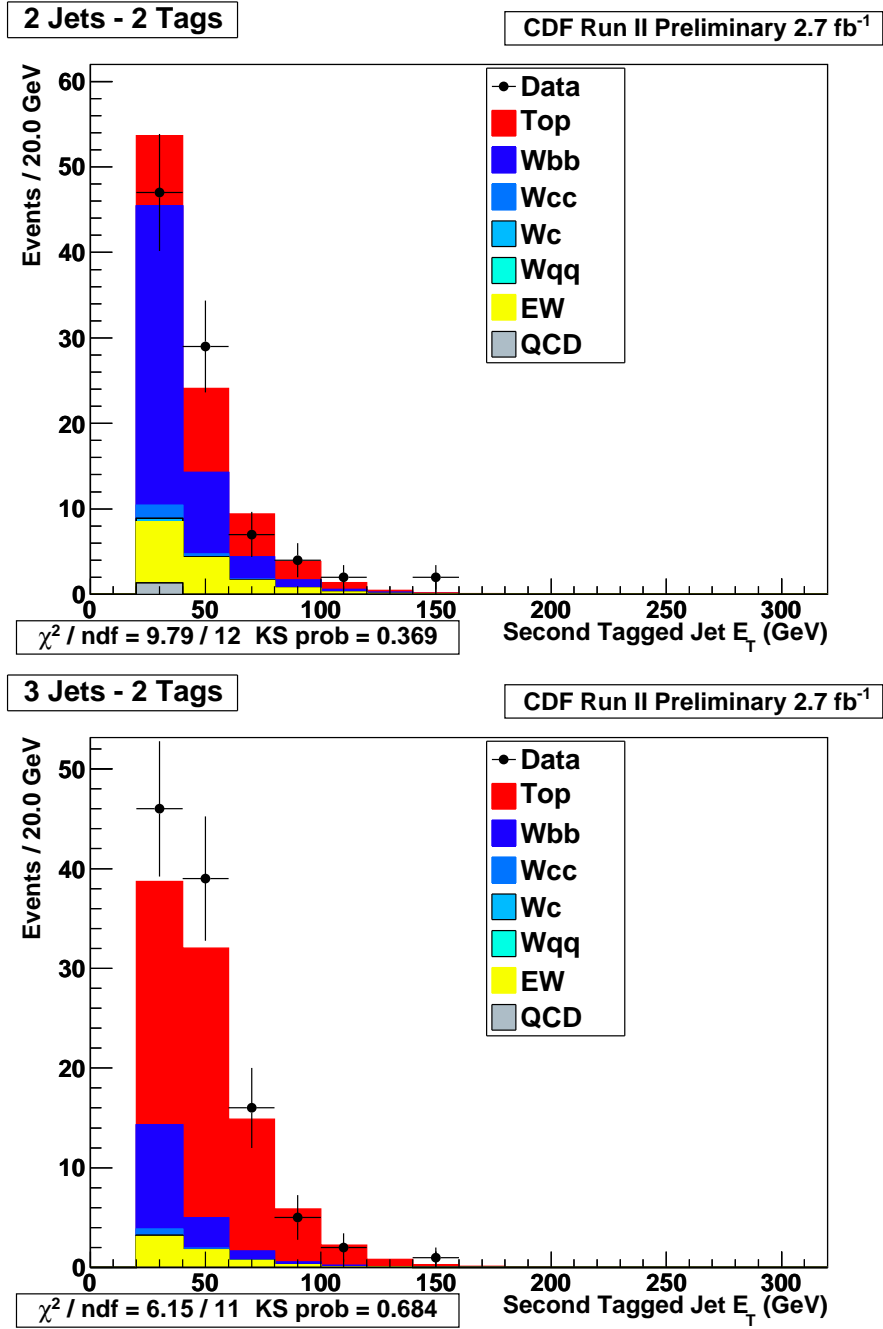


Figure 9.56: Validation plots of the transverse energy, E_T , of the secondary tagged jet for double tags.

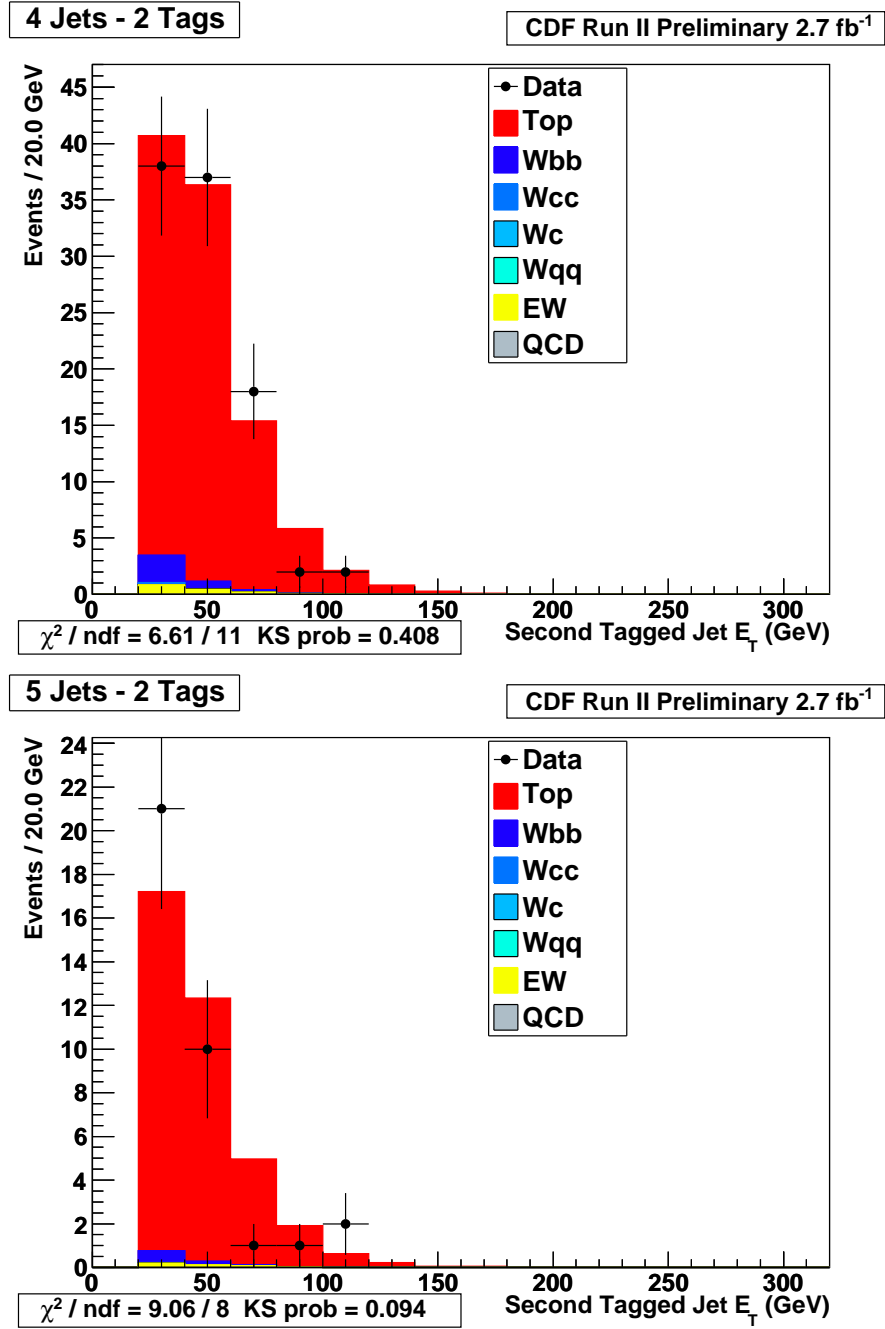


Figure 9.57: Validation plots of the transverse energy, E_T , of the secondary tagged jet for double tags.

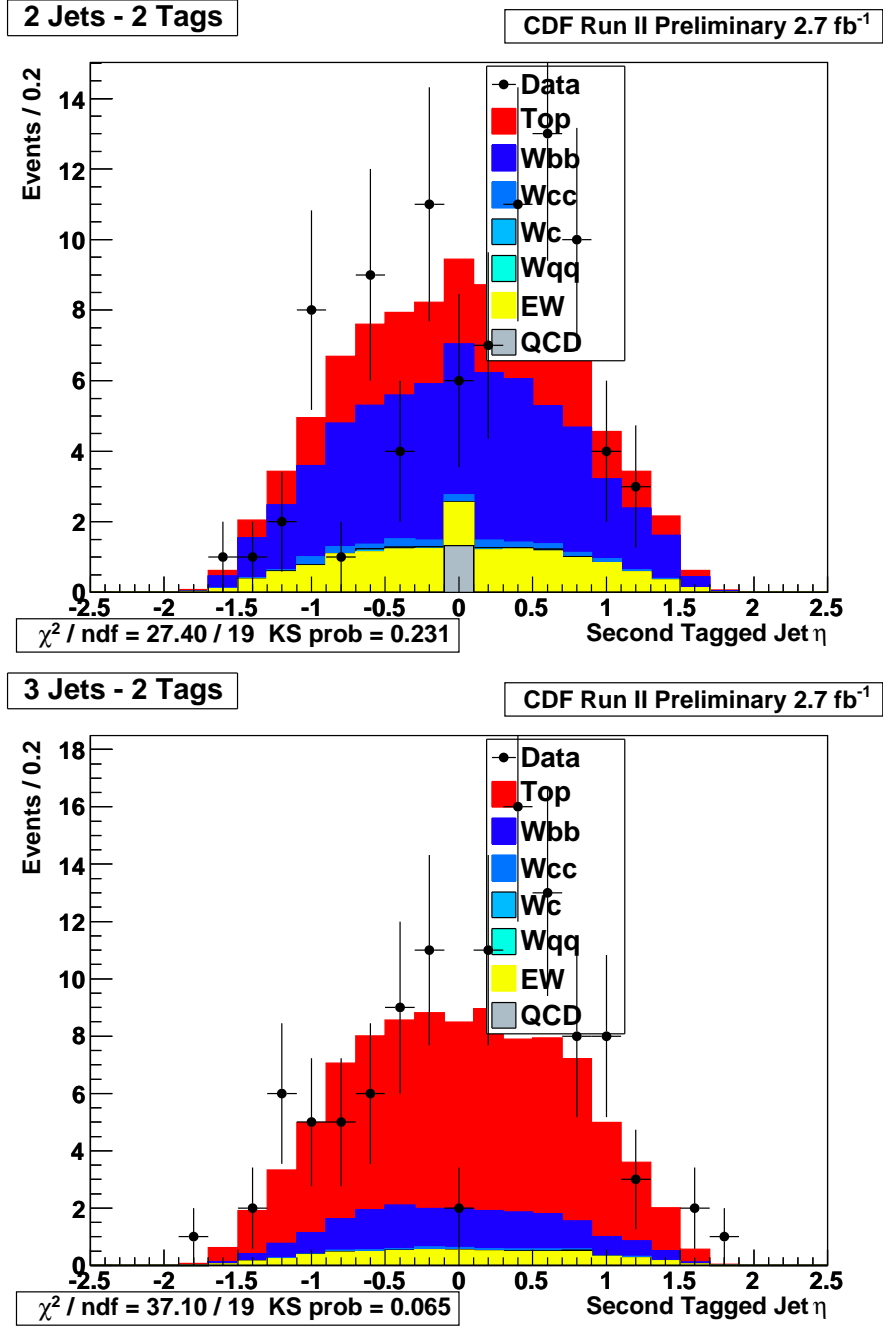


Figure 9.58: Validation plots of the pseudorapidity, η , of the secondary tagged jet for double tags.

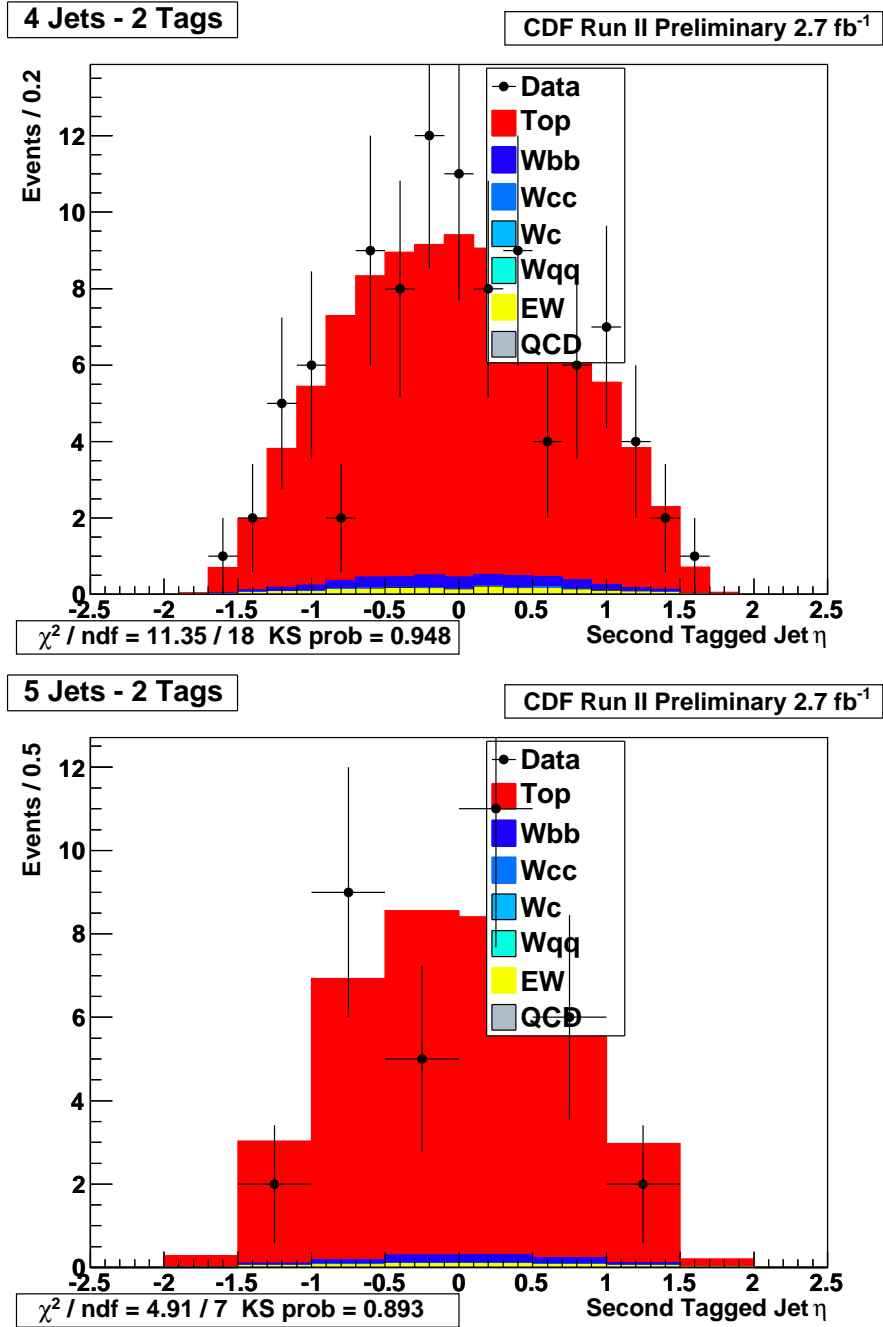


Figure 9.59: Validation plots of the pseudorapidity, η , of the secondary tagged jet for double tags.

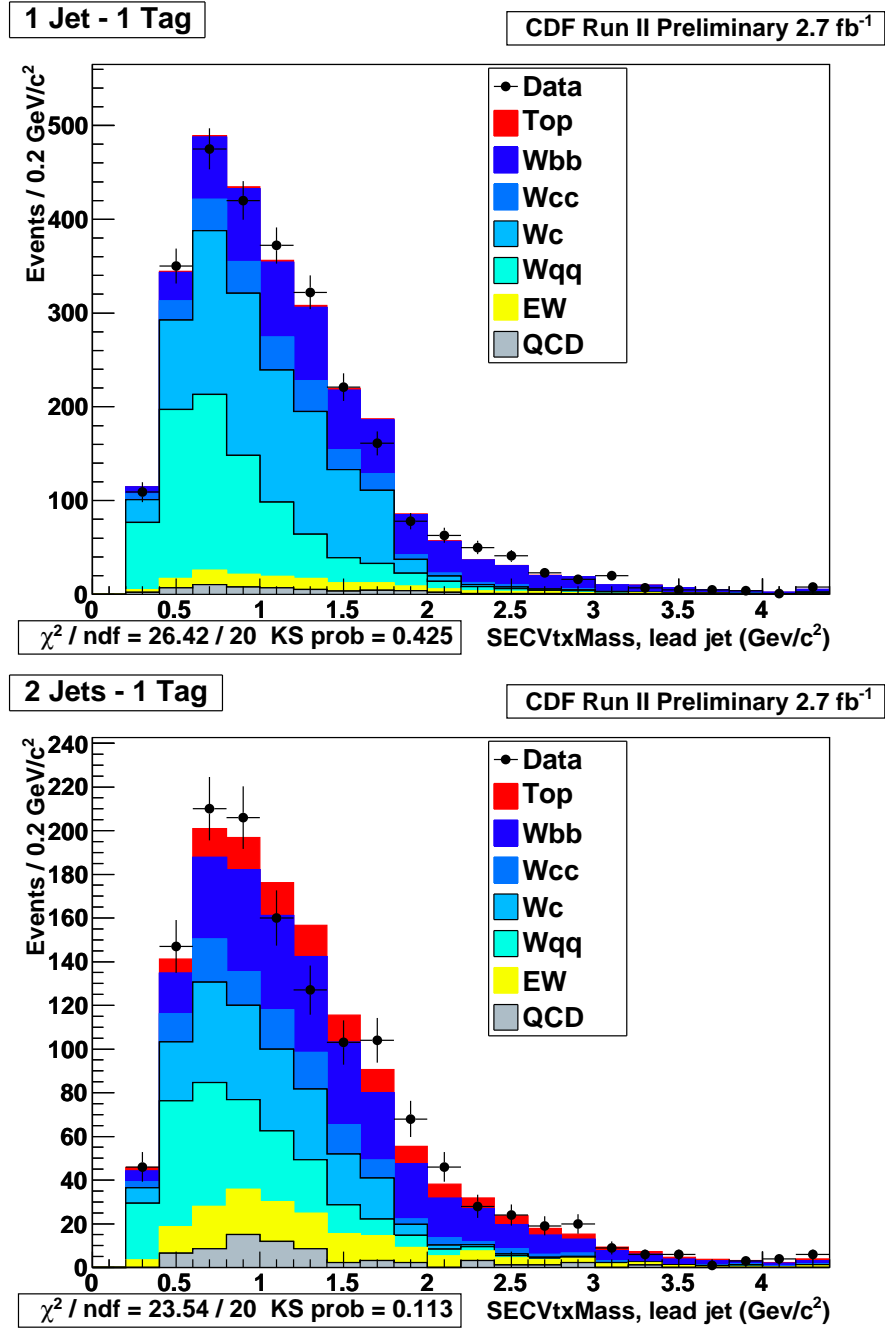


Figure 9.60: Validation plots of the secondary vertex mass, SecVtxMass, of the leading tagged jet for single tags.

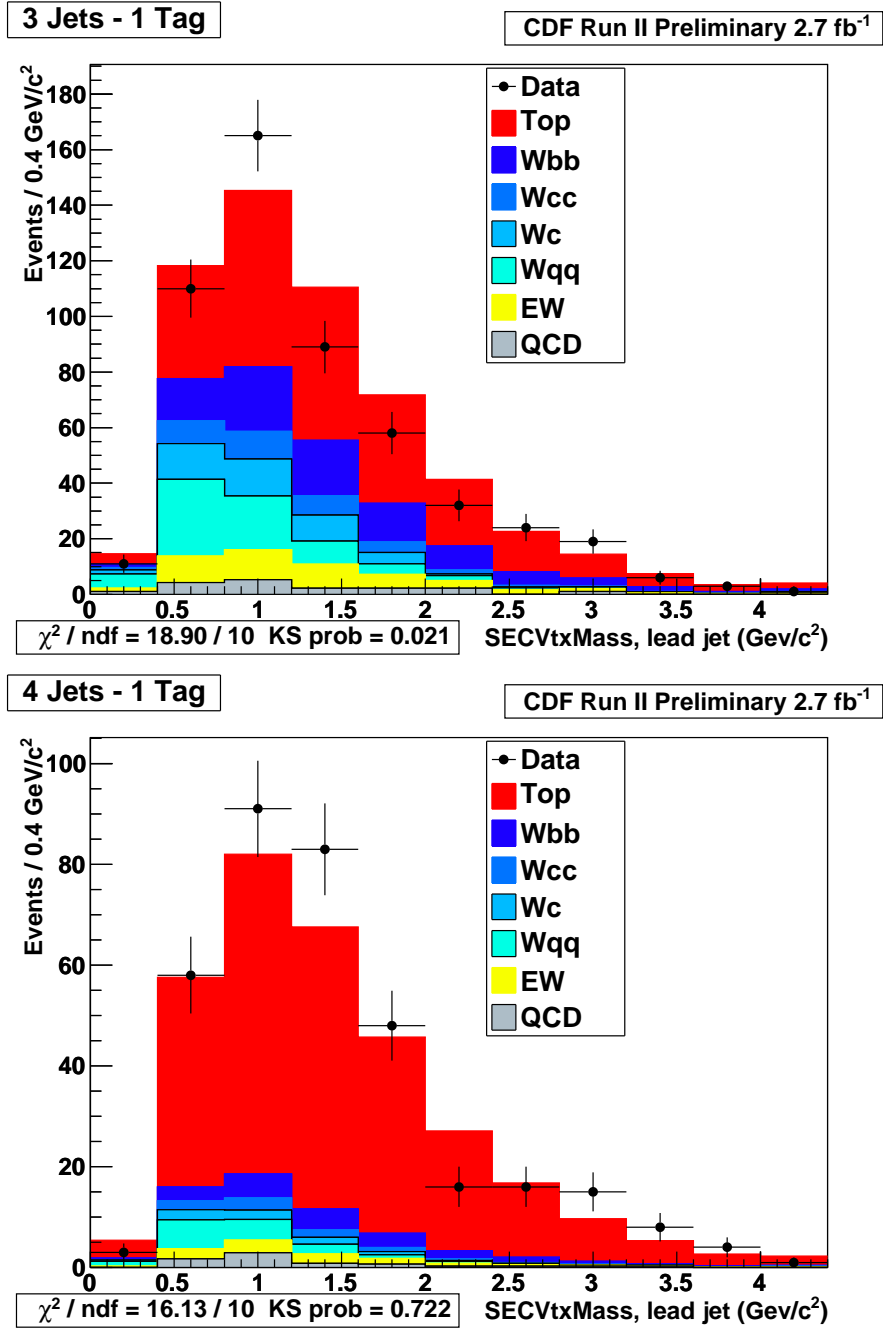


Figure 9.61: Validation plots of the secondary vertex mass, SecVtxMass, of the leading tagged jet for single tags.

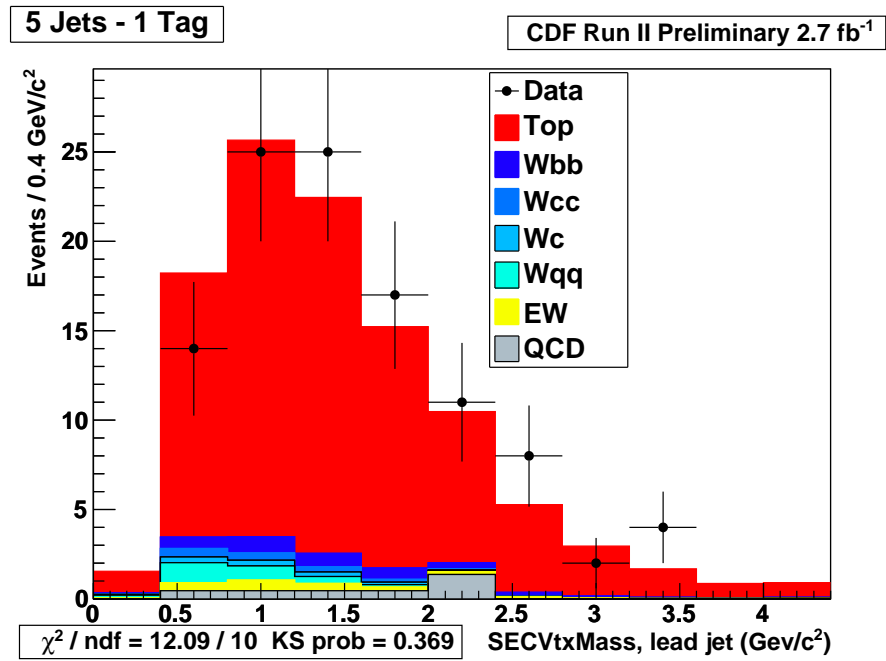


Figure 9.62: Validation plots of the secondary vertex mass, SecVtxMass, of the leading tagged jet for single tags.

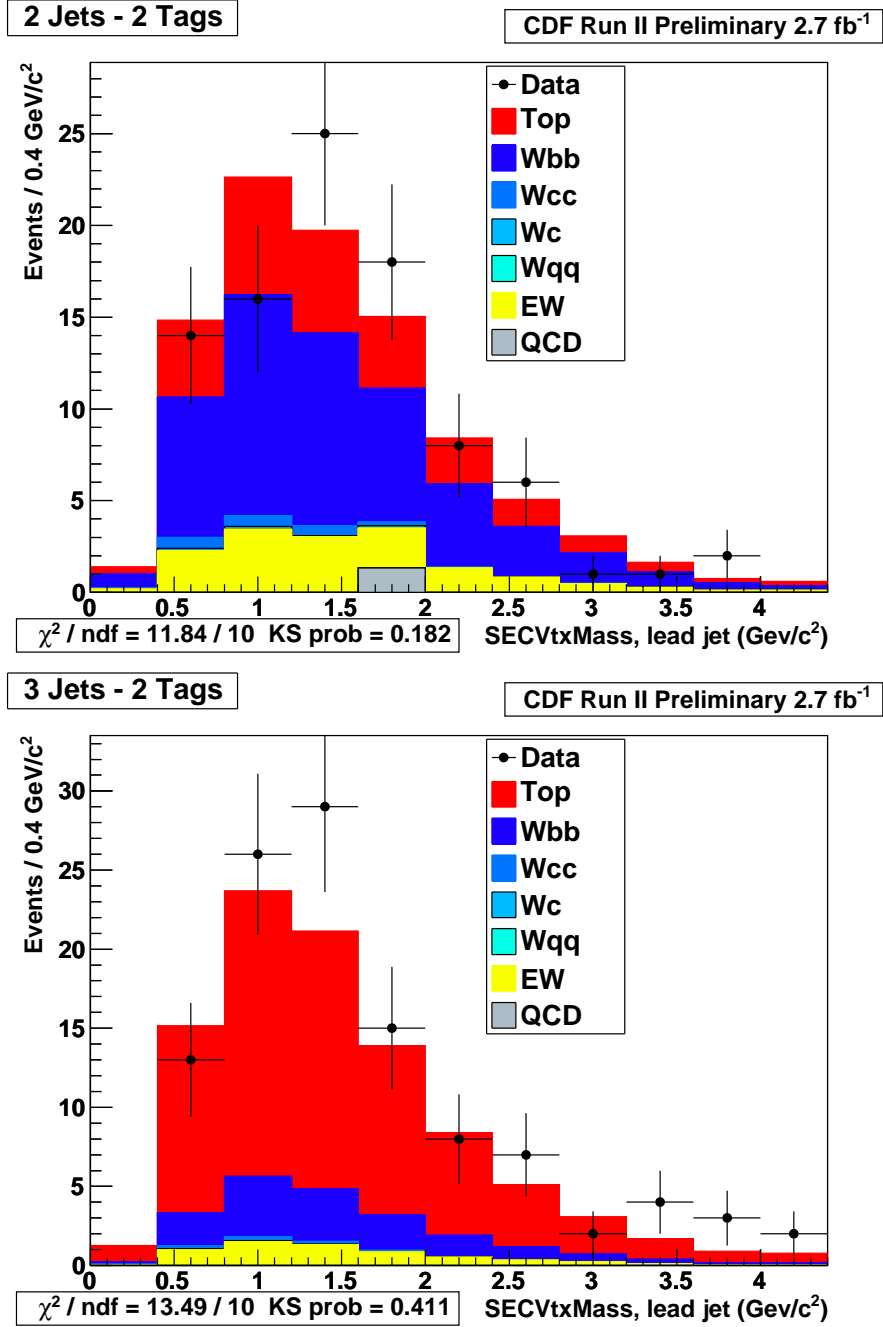


Figure 9.63: Validation plots of the secondary vertex mass, SecVtxMass, of the leading tagged jet for double tags.

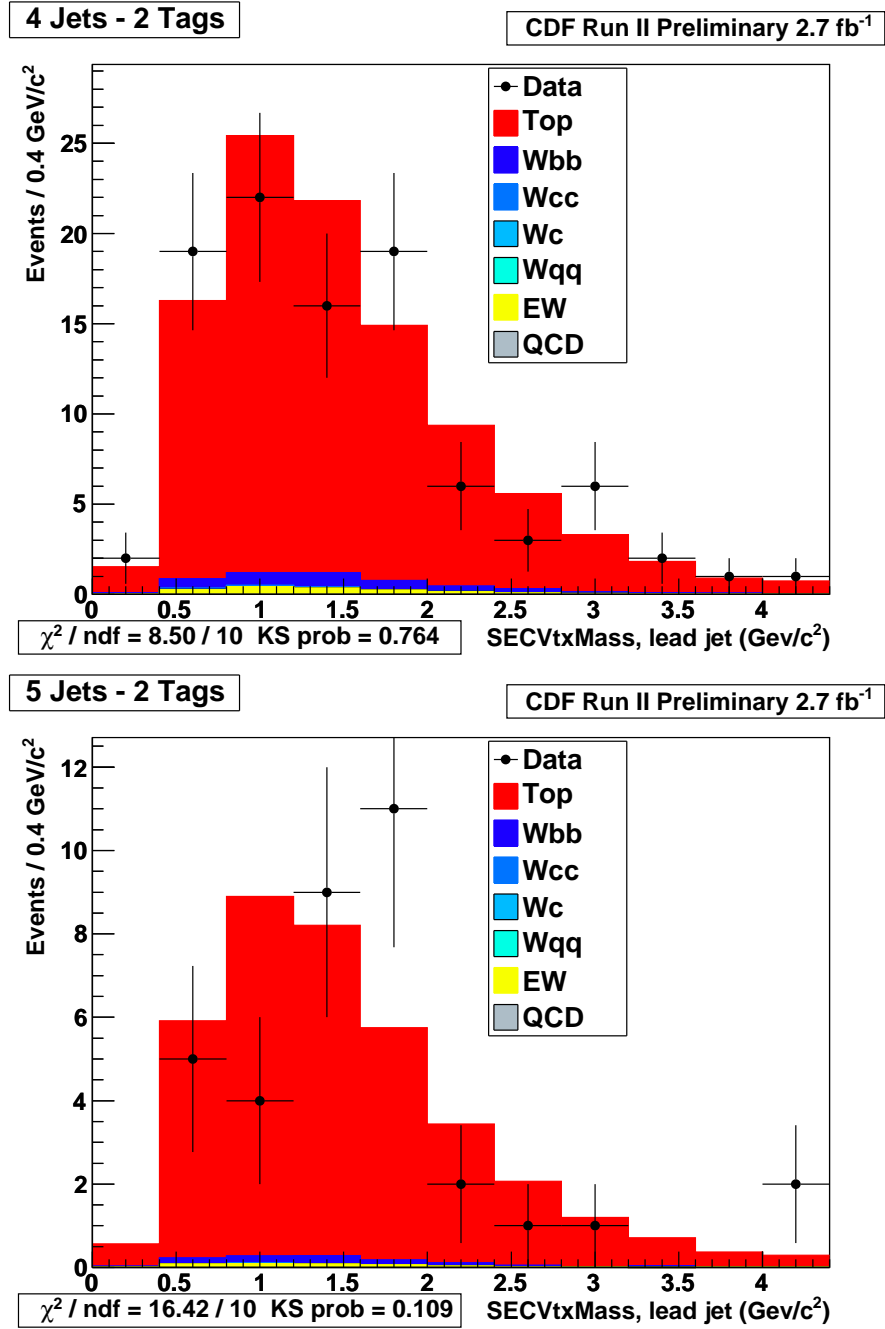


Figure 9.64: Validation plots of the secondary vertex mass, SecVtxMass, of the leading tagged jet for double tags.

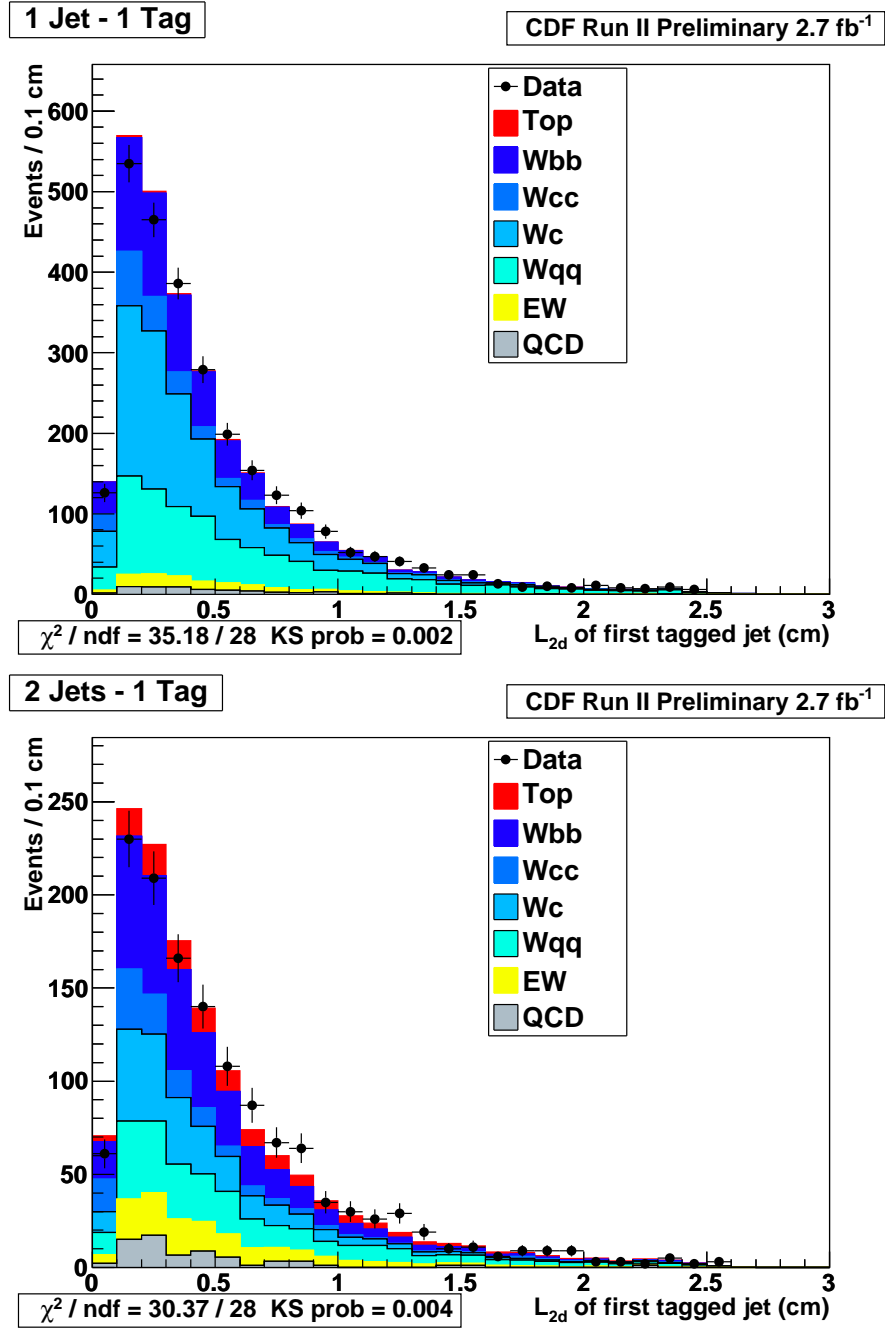


Figure 9.65: Validation plots of the two-dimensional secondary vertex displacement vector, L_{2d} , of the leading tagged jet for single tags.

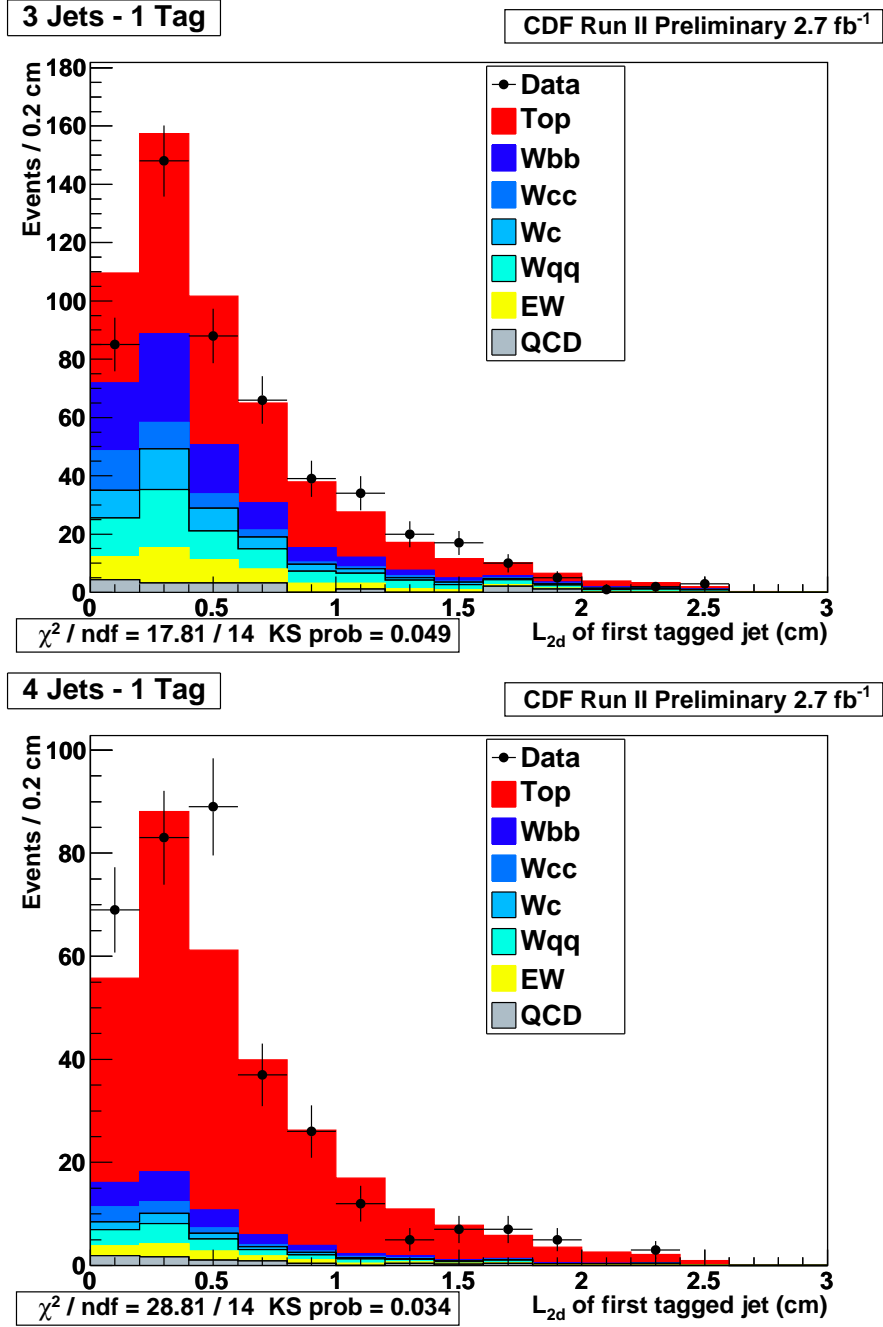


Figure 9.66: Validation plots of the two-dimensional secondary vertex displacement vector, L_{2d} , of the leading tagged jet for single tags.

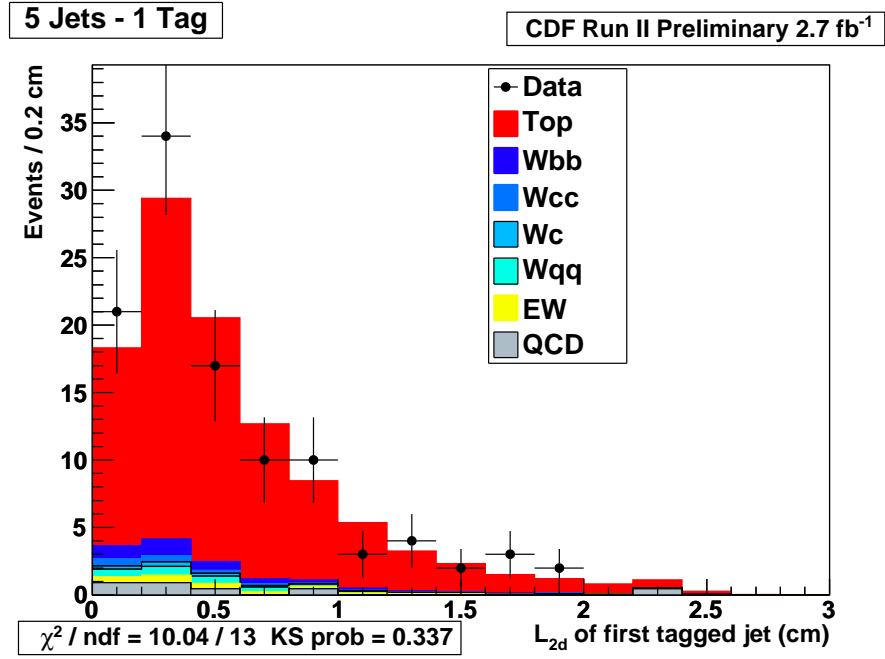


Figure 9.67: Validation plots of the two-dimensional secondary vertex displacement vector, L_{2d} , of the leading tagged jet for single tags.

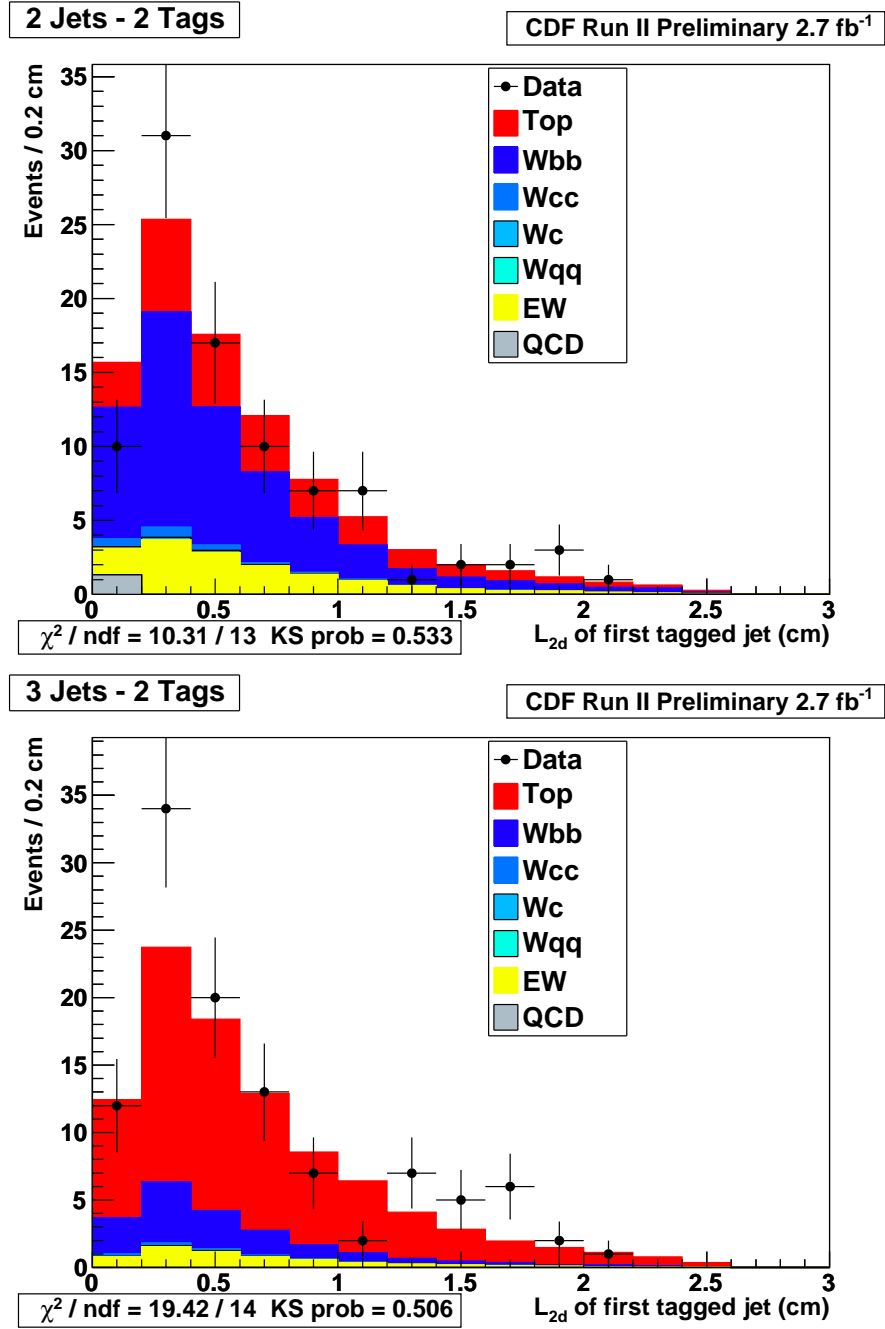


Figure 9.68: Validation plots of the two-dimensional secondary vertex displacement vector, L_{2d} , of the leading tagged jet for double tags.

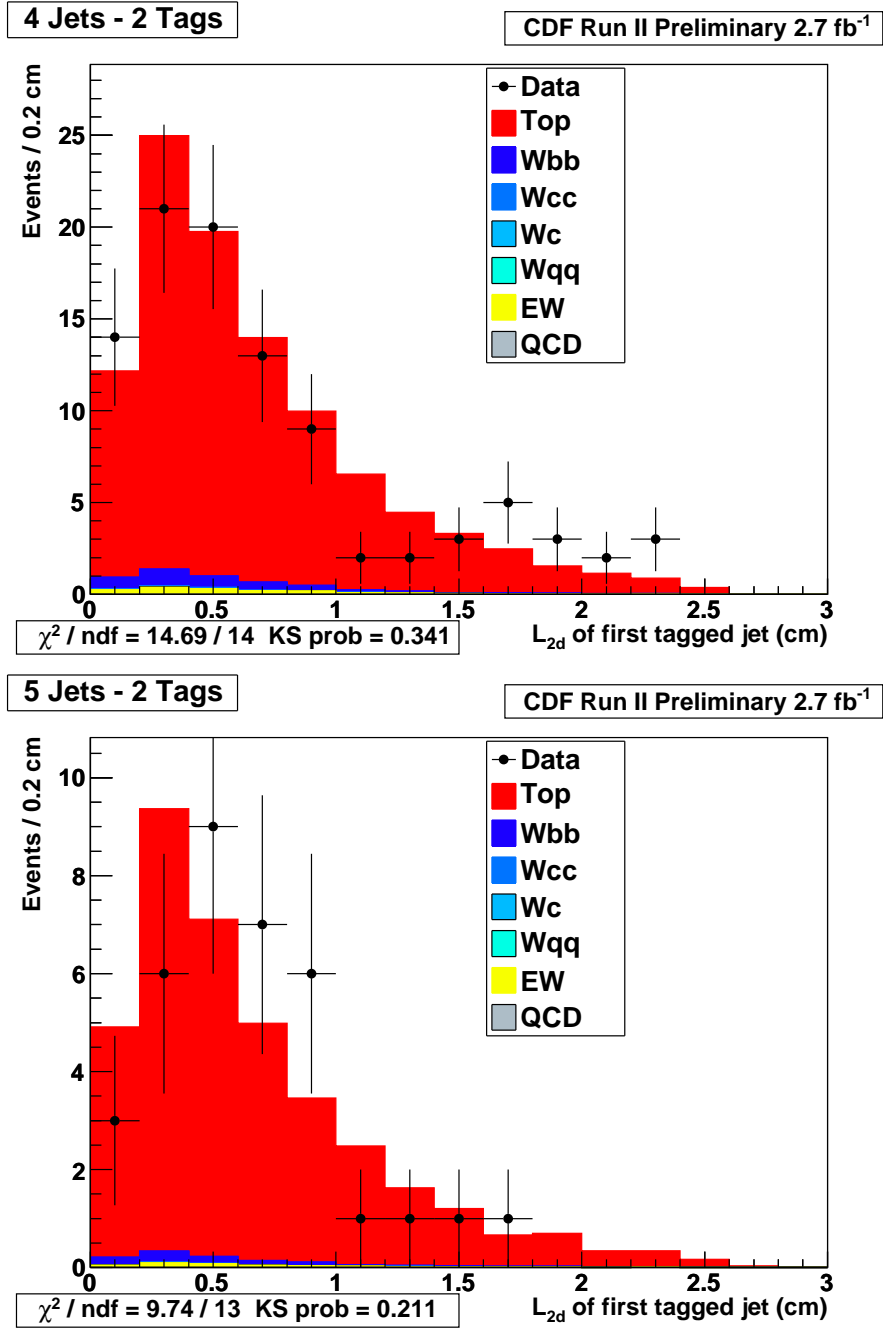


Figure 9.69: Validation plots of the two-dimensional secondary vertex displacement vector, L_{2d} , of the leading tagged jet for double tags.

Chapter 10

Conclusions and Outlook

We measure the $t\bar{t}$ production cross section with $2.7 \pm 0.2 \text{ fb}^{-1}$ of data obtained by CDF. Using a new procedure, called the Simultaneous Heavy Flavor Fraction and Top Cross Section Measurement (SHyFT, though generally referred to as METHOD III), we measured the top signal and background normalizations using simultaneous kinematic fits in the b -tagged lepton-plus-jets sample.

This novel approach allowed us to determine the normalizations, cross sections, and scale factors of multiple processes at once, reducing the dependence on modeling assumptions. We measured $\sigma_{t\bar{t}} = 7.64 \pm 0.57(\text{stat} + \text{syst}) \pm 0.45(\text{lumi}) \text{ pb}$ and $K_{Wb\bar{b}} = 1.57 \pm 0.25$ consistent with existing measurements; the measured top cross section is also consistent with the theoretical value. More data will reduce the systematic uncertainties and will lead to the best precision of any single analysis to date. We ran an additional 24,000 pseudoexperiments assuming a data-set size four times as

large as the one used in this analysis — this corresponds to the amount of data CDF is expected to collect before the Tevatron turns off. These new pseudoexperiments showed, as seen in Figure 10.1, that the uncertainty on the top cross section will decrease from 0.57 pb to approximately 0.37 pb — an improvement of 35%.

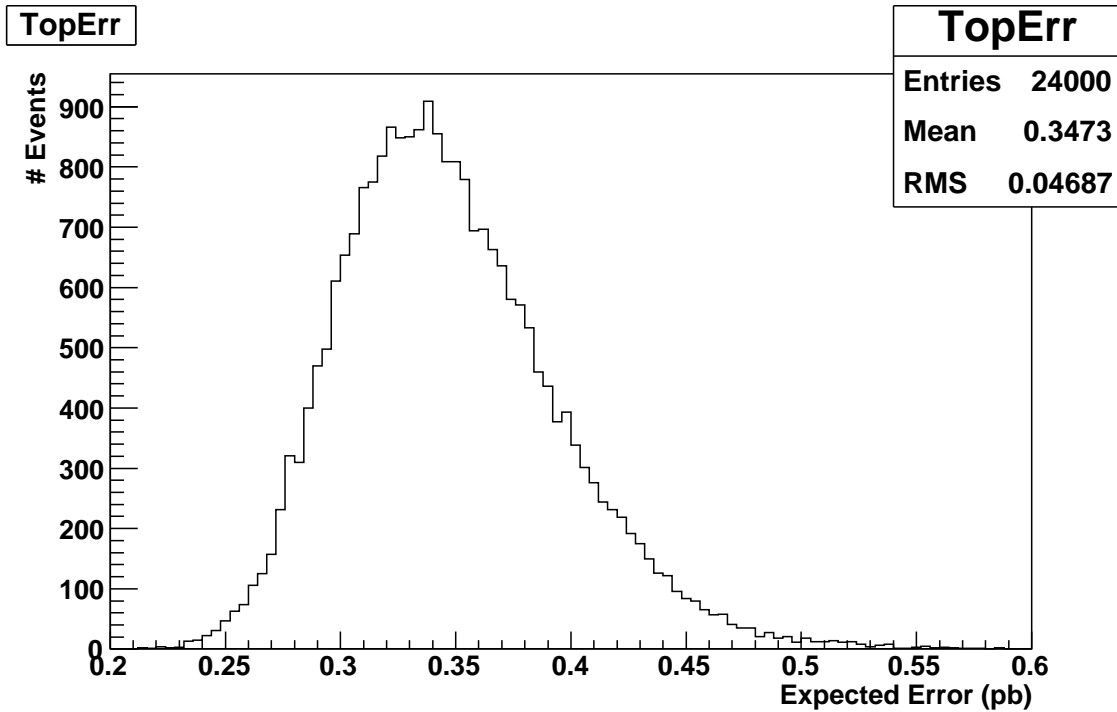


Figure 10.1: Expected uncertainty on the top cross section assuming four times as much data as currently used. The uncertainty should be reduced by approximately 35%.

The measured top production cross section’s consistency with the theoretical value indicates that there is no evidence of physics beyond the Standard Model. Given that the measurement has a relatively high uncertainty of 10% (7.5% excluding the luminosity uncertainty), however, there is still a need for improvement. The theoretical cross section depends largely on the parton distribution functions, so improvements

on the determination of those will help constrain new models of physics, especially in conjunction with more precise cross section measurements.

This same analysis is being done at the Large Hadron Collider as well (at the Compact Muon Solenoid experiment), and this work is the foundation for that analysis. In fact, at CMS, this procedure has additional motivation since it is the only way to measure the $Wb\bar{b}$ + jets contribution. The W + 1 jet bin, which is normally used to measure this contribution, is heavily polluted by top pairs and single top at those higher energies. This procedure will also likely be used to measure the W + jets cross sections.

Appendix A

Trigger Paths

There are two triggers used to collect the data for this analysis: the high- p_T electron trigger and the high- p_T muon trigger. The trigger selection is done using an overall trigger bit — the specific trigger paths that make up the overall trigger bit change on a per-run basis. These individual trigger paths are checked for each run using a small piece of software called the TRIGGER TOOL.

The high- p_T electron trigger simply requires the ELECTRON_CENTRAL_18_V overall bit to be set. The high- p_T muon trigger has different requirements for certain runs. For run numbers larger than 229763, it requires the bit for MUON_CMUP18_V to be set. For run numbers smaller than 229763, it requires the bit for MUON_CMUP18_V or MUON_CMUP_L2_PT15_V (or both) to be set. There are some special runs which require the bit for MUON_CMUP18_L2_LOOSE_DPS_V to be set. These runs are 262548, 262550, 262564, 262565, 262602, 262603, 262604, 262618, 262619, 262652, 262653,

262668, 262670, 262671, 262673, 262687, 262759, 262776, 262780, 262806, 262807,
262808, and 262823.

Appendix B

Analysis Appendices

B.1 Monte Carlo Simulation Parameters

Tables B.1 and B.2 show the Monte Carlo simulation parameters used for the samples in this analysis.

Table B.1: The ALPGEN v2.10' parameters used in the generation of the Monte Carlo simulation samples.

Parameter	Setting	Meaning
Gen p_T^j	15.0	Minimum parton p_T
Gen $ \eta_j $	3.0	Maximum light parton η
Gen dR_{jj}	0.4	Minimum parton-parton (and Q-parton) separation
Gen heavy flavor Pt	8.0	Minimum b/c parton p_T or $b\bar{b}/c\bar{c}$ p_T
Gen heavy flavor $ \eta_{max} $	3.0	Maximum b/c parton η
Gen heavy flavor ΔR_{min}	0.0	Minimum b - b (c - c) separation
Gen p_T^ℓ	1.0	Minimum lepton p_T
Gen $ \eta_\ell $	5.0	Maximum lepton η
Gen $\Delta R_{\ell j}$	0.0	Minimum ΔR between lepton and jets
Match Hepg-jet p_T	15.0	Minimum matching cluster E_T
Match Hepg-jet $ \eta_{max} $	3.0	Maximum matching η
Match Hepg-jet ΔR_{min}	0.4	Matching parton-parton (and Q-parton) minimum separation
MET_{MIN}	0.0	Minimum \cancel{E}_T
Qscale	$\text{qfrac } \sqrt{m_W^2 + \Sigma_{jets}(m_{tr}^2)}$	Q^2 scale choice pdfs.
QFACTOR	1.0	Scale factor on pdf Q^2 scale
KTFACTOR	1.0	Scale factor on vertex Q^2 scale
CLUOPT	1.0	Vertex Q^2 choice
m_t	174.3 GeV/ c^2	Top quark mass
m_b	4.7 GeV/ c^2	Bottom quark mass
PDF	CTEQ5L	Parton distribution function

Table B.2: The PYTHIA v6.326 parameters used in the generation of the Monte Carlo simulation samples. In addition to those listed, an underlying event tune is required, and EvtGen handles the decays of b and c quarks. Other settings not explicitly listed are either verified to match default CDF PYTHIA version or to have no effect. The top block shows Initial State Radiation-related parameters, the second block shows underlying event parameters, and the bottom block shows other settings.

Parameter	Setting	Meaning
PARP(67)	1.00	ISR Scale Factor
PARP(64)	0.20	Evolution scale, k_T^2 , for α_s and PDFs
PARP(62)	1.25	Q_{min}^2
MSTP(91)	1	Gaussian k_T distribution
PARP(91)	2.10	k_T distribution width
PARP(93)	15.00	k_T distribution maximum
MSTP(81)	1	Multiple parton interaction (MPI) switch
MSTP(82)	4.00	Double Gaussian structure of MPI
PARP(82)	1.70	MPI Cut-off
PARP(83)	0.50	Warm core double gaussian parameters
PARP(84)	0.40	Warm core double gaussian parameters
PARP(85)	1.00	Color connections to nearest neighbor
PARP(86)	1.00	Color connections to nearest neighbor
PARP(89)	1800.00	Energy dependence (E0)
PARP(90)	0.25	Energy dependence (exponent)
EvtGen version	1.42	Version of EvtGen used for b hadron decays
m_b	4.8 GeV/ c^2	Bottom quark mass
PDF	CTEQ5L SET 46	Parton distribution function

B.2 Monte Carlo Simulation Data-sets

Shown in Tables B.3 – B.11 are all of the Monte Carlo simulation data-sets used in this analysis. More details about the datasets used can be found on the CDF Top Group’s webpage [36].

Table B.3: The data-set names, cross sections (in picobarns), and number of events for the $t\bar{t}$, single top, and di-boson Monte Carlo simulation samples.

Sample	Data-set Name	Cross Section	Number of Events
$t\bar{t}$	ttop75	6.7	4,719,385
Single top, s -channel	stop00	0.29	918,173
Single top, t -channel	stopm0	0.64	1,012,502
WW	ihht1a	12.4	4,880,529
WZ	jhht1a	3.7	4,881,464
ZZ	khht1a	3.8	4,926,630

Table B.4: The data-set names, cross sections (in picobarns), and number of events for the $Z + \text{jets}$ Monte Carlo simulation samples. The top block gives the $Z + \text{light flavor}$ samples, the lower two blocks give the $Z + \text{heavy flavor}$ samples.

Sample	Data-set Name	Cross Section	Number of Events
$Z \rightarrow e^+e^- + 0p$	ztopp0	158	2,639,520
$Z \rightarrow e^+e^- + 1p$	ztop1p	21.6	536,159
$Z \rightarrow e^+e^- + 2p$	ztopzb	3.46	4,641,816
$Z \rightarrow e^+e^- + 3p$	ztop3p	0.550	528,491
$Z \rightarrow e^+e^- + 4p$	ztop4p	0.099	525,065
$Z \rightarrow \mu^+\mu^- + 0p$	ztopp5	158	2,665,104
$Z \rightarrow \mu^+\mu^- + 1p$	ztop6p	21.6	536,159
$Z \rightarrow \mu^+\mu^- + 2p$	ztopzt	3.46	4,710,842
$Z \rightarrow \mu^+\mu^- + 3p$	ztop8p	0.548	536,159
$Z \rightarrow \mu^+\mu^- + 4p$	ztop9p	0.0992	536,159
$Z \rightarrow \tau^+\tau^- + 0p$	ztopt3	158	5,860,164
$Z \rightarrow \tau^+\tau^- + 1p$	ztopt1	21.5	1,156,836
$Z \rightarrow \tau^+\tau^- + 2p$	ztopt2	4.14	2,273,221
$Z \rightarrow e^+e^- + b\bar{b} + 0p$	ztopb0	0.511	532,205
$Z \rightarrow e^+e^- + b\bar{b} + 1p$	ztopb1	0.134	525,955
$Z \rightarrow e^+e^- + b\bar{b} + 2p$	ztopb2	0.039	519,500
$Z \rightarrow \mu^+\mu^- + b\bar{b} + 0p$	ztopb5	0.511	530,793
$Z \rightarrow \mu^+\mu^- + b\bar{b} + 1p$	ztopb6	0.134	525,695
$Z \rightarrow \mu^+\mu^- + b\bar{b} + 2p$	ztopb7	0.039	536,159
$Z \rightarrow \tau^+\tau^- + b\bar{b} + 2p$	ztopbt	0.625	1,456,737
$Z \rightarrow e^+e^- + c\bar{c} + 0p$	ztopc0	1.08	699,861
$Z \rightarrow e^+e^- + c\bar{c} + 1p$	ztopc1	0.331	710,734
$Z \rightarrow e^+e^- + c\bar{c} + 2p$	ztopc2	0.107	663,518
$Z \rightarrow \mu^+\mu^- + c\bar{c} + 0p$	ztopc5	1.08	710,734
$Z \rightarrow \mu^+\mu^- + c\bar{c} + 1p$	ztopc6	0.332	710,734
$Z \rightarrow \mu^+\mu^- + c\bar{c} + 2p$	ztopc7	0.107	705,108
$Z \rightarrow \tau^+\tau^- + c\bar{c} + 2p$	ztopct	1.28	1,966,881

Table B.5: The data-set names, cross sections (in picobarns), and number of events for the W + heavy flavor Monte Carlo simulation samples.

Sample	Data-set Name	Cross Section	Number of Events
$W \rightarrow q\bar{q}' + b\bar{b} + 0p$ ($e\nu$)	btop0w	2.98	1,542,539
$W \rightarrow q\bar{q}' + b\bar{b} + 1p$ ($e\nu$)	btop1w	0.888	1,545,970
$W \rightarrow q\bar{q}' + b\bar{b} + 2p$ ($e\nu$)	btop2w	0.287	1,498,550
$W \rightarrow q\bar{q}' + b\bar{b} + 0p$ ($\mu\nu$)	btop5w	2.98	1,524,880
$W \rightarrow q\bar{q}' + b\bar{b} + 1p$ ($\mu\nu$)	btop6w	0.889	1,508,029
$W \rightarrow q\bar{q}' + b\bar{b} + 2p$ ($\mu\nu$)	btop7w	0.286	1,506,613
$W \rightarrow q\bar{q}' + b\bar{b} + 0p$ ($\tau\nu$)	dtop0w	2.98	1,503,024
$W \rightarrow q\bar{q}' + b\bar{b} + 1p$ ($\tau\nu$)	dtop1w	0.888	1,523,791
$W \rightarrow q\bar{q}' + b\bar{b} + 2p$ ($\tau\nu$)	dtop2w	0.286	1,478,875
$W \rightarrow q\bar{q}' + c\bar{c} + 0p$ ($e\nu$)	ctop0w	5.00	2,008,023
$W \rightarrow q\bar{q}' + c\bar{c} + 1p$ ($e\nu$)	ctop1w	1.79	1,987,389
$W \rightarrow q\bar{q}' + c\bar{c} + 2p$ ($e\nu$)	ctop2w	0.628	1,926,322
$W \rightarrow q\bar{q}' + c\bar{c} + 0p$ ($\mu\nu$)	ctop5w	5.00	1,985,033
$W \rightarrow q\bar{q}' + c\bar{c} + 1p$ ($\mu\nu$)	ctop6w	1.79	1,979,810
$W \rightarrow q\bar{q}' + c\bar{c} + 2p$ ($\mu\nu$)	ctop7w	0.628	1,990,504
$W \rightarrow q\bar{q}' + c\bar{c} + 0p$ ($\tau\nu$)	etopw0	5.00	1,978,370
$W \rightarrow q\bar{q}' + c\bar{c} + 1p$ ($\tau\nu$)	etopw1	1.80	1,985,097
$W \rightarrow q\bar{q}' + c\bar{c} + 2p$ ($\tau\nu$)	etopw2	0.628	1,921,088
$W \rightarrow q\bar{q}' + c + 0p$ ($e\nu$)	stopw0	17.1	1,960,065
$W \rightarrow q\bar{q}' + c + 1p$ ($e\nu$)	stopw1	3.39	1,964,891
$W \rightarrow q\bar{q}' + c + 2p$ ($e\nu$)	stopw2	0.507	1,976,553
$W \rightarrow q\bar{q}' + c + 3p$ ($e\nu$)	stopw3	0.083	1,982,654
$W \rightarrow q\bar{q}' + c + 0p$ ($\mu\nu$)	stopw5	17.1	1,992,335
$W \rightarrow q\bar{q}' + c + 1p$ ($\mu\nu$)	stopw6	3.39	1,979,964
$W \rightarrow q\bar{q}' + c + 2p$ ($\mu\nu$)	stopw7	0.507	1,980,674
$W \rightarrow q\bar{q}' + c + 3p$ ($\mu\nu$)	stopw8	0.083	1,993,173
$W \rightarrow q\bar{q}' + c + 0p$ ($\tau\nu$)	stopwa	17.1	1,532,572
$W \rightarrow q\bar{q}' + c + 1p$ ($\tau\nu$)	stopwb	3.39	1,532,908
$W \rightarrow q\bar{q}' + c + 2p$ ($\tau\nu$)	stopwc	0.507	1,504,501
$W \rightarrow q\bar{q}' + c + 3p$ ($\tau\nu$)	stopwd	0.083	1,512,907

Table B.6: The data-set names, cross sections (in picobarns), and number of events for the W + light flavor Monte Carlo simulation samples.

Sample	Data-set Name	Cross Section	Number of Events
$W \rightarrow q\bar{q}' + 0p$ ($e\nu$)	ptopw0	1800	4,928,812
$W \rightarrow q\bar{q}' + 1p$ ($e\nu$)	ptopw1	225	4,909,767
$W \rightarrow q\bar{q}' + 2p$ ($e\nu$)	ptop2w	35.3	1,003,193
$W \rightarrow q\bar{q}' + 3p$ ($e\nu$)	ptop3w	5.59	1,003,040
$W \rightarrow q\bar{q}' + 4p$ ($e\nu$)	ptop4w	1.03	989,607
$W \rightarrow q\bar{q}' + 0p$ ($\mu\nu$)	ptopw5	1800	5,017,218
$W \rightarrow q\bar{q}' + 1p$ ($\mu\nu$)	ptopw6	225	5,003,166
$W \rightarrow q\bar{q}' + 2p$ ($\mu\nu$)	ptop7w	35.3	1,002,804
$W \rightarrow q\bar{q}' + 3p$ ($\mu\nu$)	ptop8w	5.59	1,013,373
$W \rightarrow q\bar{q}' + 4p$ ($\mu\nu$)	ptop9w	1.03	988,545
$W \rightarrow q\bar{q}' + 0p$ ($\tau\nu$)	utopw0	1800	4,885,557
$W \rightarrow q\bar{q}' + 1p$ ($\tau\nu$)	utopw1	225	4,987,134
$W \rightarrow q\bar{q}' + 2p$ ($\tau\nu$)	utop2w	35.4	923,989
$W \rightarrow q\bar{q}' + 3p$ ($\tau\nu$)	utop3w	5.60	1,008,221
$W \rightarrow q\bar{q}' + 4p$ ($\tau\nu$)	utop4w	1.03	986,494

Table B.7: The data-set names, cross sections (in picobarns), and number of events for the Monte Carlo simulation samples used for the ISR/FSR and parton showering systematic studies.

Sample	Data-set Name	Cross Section	Number of Events
ISR/FSR increased	otop03	6.7	2,001,152
ISR/FSR decreased	otop04	6.7	1,997,900
Herwig showering	otop1s	6.7	3,950,060

Table B.8: The data-set names, cross sections (in picobarns), and number of events for the $W + \text{heavy flavor}$ $Q^2 = 0.5$ systematics Monte Carlo simulation samples.

Sample	Data-set Name	Cross Section	Number of Events
$W \rightarrow q\bar{q}' + b\bar{b} + 0p$ ($e\nu$)	qtopw0	4.14	700,381
$W \rightarrow q\bar{q}' + b\bar{b} + 1p$ ($e\nu$)	qtopw1	1.64	680,107
$W \rightarrow q\bar{q}' + b\bar{b} + 2p$ ($e\nu$)	qtopw2	0.615	699,368
$W \rightarrow q\bar{q}' + b\bar{b} + 0p$ ($\mu\nu$)	qtopw6	4.14	700,381
$W \rightarrow q\bar{q}' + b\bar{b} + 1p$ ($\mu\nu$)	qtopw7	1.64	700,381
$W \rightarrow q\bar{q}' + b\bar{b} + 2p$ ($\mu\nu$)	qtopw8	0.616	700,381
$W \rightarrow q\bar{q}' + b\bar{b} + 0p$ ($\tau\nu$)	qtopwc	4.14	612,063
$W \rightarrow q\bar{q}' + b\bar{b} + 1p$ ($\tau\nu$)	qtopwd	1.64	700,381
$W \rightarrow q\bar{q}' + b\bar{b} + 2p$ ($\tau\nu$)	qtopwe	0.614	700,381
$W \rightarrow q\bar{q}' + c\bar{c} + 0p$ ($e\nu$)	qtopwi	6.87	699,087
$W \rightarrow q\bar{q}' + c\bar{c} + 1p$ ($e\nu$)	qtopwj	3.19	1,050,580
$W \rightarrow q\bar{q}' + c\bar{c} + 2p$ ($e\nu$)	qtopwk	1.30	1,400,788
$W \rightarrow q\bar{q}' + c\bar{c} + 0p$ ($\mu\nu$)	qtopwo	6.88	1,225,946
$W \rightarrow q\bar{q}' + c\bar{c} + 1p$ ($\mu\nu$)	qtopwp	3.18	1,400,788
$W \rightarrow q\bar{q}' + c\bar{c} + 2p$ ($\mu\nu$)	qtopwq	1.30	1,393,051
$W \rightarrow q\bar{q}' + c\bar{c} + 0p$ ($\tau\nu$)	qtopwu	6.88	1,295,141
$W \rightarrow q\bar{q}' + c\bar{c} + 1p$ ($\tau\nu$)	qtopwv	3.18	1,400,788
$W \rightarrow q\bar{q}' + c\bar{c} + 2p$ ($\tau\nu$)	qtopww	1.30	1,387,859
$W \rightarrow q\bar{q}' + c + 0p$ ($e\nu$)	ctopq0	23.3	1,400,788
$W \rightarrow q\bar{q}' + c + 1p$ ($e\nu$)	ctopq1	5.72	1,400,788
$W \rightarrow q\bar{q}' + c + 2p$ ($e\nu$)	ctopq2	1.02	1,400,788
$W \rightarrow q\bar{q}' + c + 3p$ ($e\nu$)	ctopq3	0.190	1,400,788
$W \rightarrow q\bar{q}' + c + 0p$ ($\mu\nu$)	ctopq8	23.3	1,317,277
$W \rightarrow q\bar{q}' + c + 1p$ ($\mu\nu$)	ctopq9	5.72	1,397,425
$W \rightarrow q\bar{q}' + c + 2p$ ($\mu\nu$)	ctopqa	1.02	1,398,031
$W \rightarrow q\bar{q}' + c + 3p$ ($\mu\nu$)	ctopqb	0.189	1,393,952
$W \rightarrow q\bar{q}' + c + 0p$ ($\tau\nu$)	ctopqg	23.3	1,400,788
$W \rightarrow q\bar{q}' + c + 1p$ ($\tau\nu$)	ctopqh	5.72	1,400,788
$W \rightarrow q\bar{q}' + c + 2p$ ($\tau\nu$)	ctopqi	1.03	1,397,708
$W \rightarrow q\bar{q}' + c + 3p$ ($\tau\nu$)	ctopqj	0.189	1,400,788

Table B.9: The data-set names, cross sections (in picobarns), and number of events for the W + light flavor $Q^2 = 0.5$ systematics Monte Carlo simulation samples.

Sample	Data-set Name	Cross Section	Number of Events
$W \rightarrow q\bar{q}' + 0p$ ($e\nu$)	otop0m	1919.0	1,490,702
$W \rightarrow q\bar{q}' + 1p$ ($e\nu$)	otop0k	302.9	2,502,270
$W \rightarrow q\bar{q}' + 2p$ ($e\nu$)	otop0i	57.74	484,180
$W \rightarrow q\bar{q}' + 3p$ ($e\nu$)	otop0g	10.8	500,426
$W \rightarrow q\bar{q}' + 4p$ ($e\nu$)	otop0e	2.25	307,501
$W \rightarrow q\bar{q}' + 0p$ ($\mu\nu$)	otop0w	1917.86	2,502,270
$W \rightarrow q\bar{q}' + 1p$ ($\mu\nu$)	otop0u	303.2	2,502,270
$W \rightarrow q\bar{q}' + 2p$ ($\mu\nu$)	otop0s	57.8	495,049
$W \rightarrow q\bar{q}' + 3p$ ($\mu\nu$)	otop0q	10.81	489,683
$W \rightarrow q\bar{q}' + 4p$ ($\mu\nu$)	otop0o	2.25	500,426
$W \rightarrow q\bar{q}' + 0p$ ($\tau\nu$)	wtopq0	1911.72	2,502,270
$W \rightarrow q\bar{q}' + 1p$ ($\tau\nu$)	wtopq1	303.2	2,502,270
$W \rightarrow q\bar{q}' + 2p$ ($\tau\nu$)	wtopq2	57.6	500,471
$W \rightarrow q\bar{q}' + 3p$ ($\tau\nu$)	wtopq3	10.82	500,471
$W \rightarrow q\bar{q}' + 4p$ ($\tau\nu$)	wtopq4	2.25	495,139

Table B.10: The data-set names, cross sections (in picobarns), and number of events for the $W + \text{heavy flavor}$ $Q^2 = 2.0$ systematics Monte Carlo simulation samples.

Sample	Data-set Name	Cross Section	Number of Events
$W \rightarrow q\bar{q}' + b\bar{b} + 0p$ ($e\nu$)	qtopw3	2.30	700,381
$W \rightarrow q\bar{q}' + b\bar{b} + 1p$ ($e\nu$)	qtopw4	0.550	700,381
$W \rightarrow q\bar{q}' + b\bar{b} + 2p$ ($e\nu$)	qtopw5	0.152	700,381
$W \rightarrow q\bar{q}' + b\bar{b} + 0p$ ($\mu\nu$)	qtopw9	2.30	437,156
$W \rightarrow q\bar{q}' + b\bar{b} + 1p$ ($\mu\nu$)	qtopwa	0.550	700,381
$W \rightarrow q\bar{q}' + b\bar{b} + 2p$ ($\mu\nu$)	qtopwb	0.152	700,229
$W \rightarrow q\bar{q}' + b\bar{b} + 0p$ ($\tau\nu$)	qtopwf	2.30	700,381
$W \rightarrow q\bar{q}' + b\bar{b} + 1p$ ($\tau\nu$)	qtopwg	0.551	440,683
$W \rightarrow q\bar{q}' + b\bar{b} + 2p$ ($\tau\nu$)	qtopwh	0.152	700,277
$W \rightarrow q\bar{q}' + c\bar{c} + 0p$ ($e\nu$)	qtopwl	3.89	701,247
$W \rightarrow q\bar{q}' + c\bar{c} + 1p$ ($e\nu$)	qtopwm	1.08	878,680
$W \rightarrow q\bar{q}' + c\bar{c} + 2p$ ($e\nu$)	qtopwn	0.322	917,363
$W \rightarrow q\bar{q}' + c\bar{c} + 0p$ ($\mu\nu$)	qtopwr	3.89	1,393,165
$W \rightarrow q\bar{q}' + c\bar{c} + 1p$ ($\mu\nu$)	qtopws	1.08	1,400,788
$W \rightarrow q\bar{q}' + c\bar{c} + 2p$ ($\mu\nu$)	qtopwt	0.322	1,216,926
$W \rightarrow q\bar{q}' + c\bar{c} + 0p$ ($\tau\nu$)	qtopwx	3.89	1,393,372
$W \rightarrow q\bar{q}' + c\bar{c} + 1p$ ($\tau\nu$)	qtopwy	1.08	1,400,788
$W \rightarrow q\bar{q}' + c\bar{c} + 2p$ ($\tau\nu$)	qtopwz	0.323	1,400,788
$W \rightarrow q\bar{q}' + c + 0p$ ($e\nu$)	ctopq4	13.8	1,400,788
$W \rightarrow q\bar{q}' + c + 1p$ ($e\nu$)	ctopq5	2.30	1,400,788
$W \rightarrow q\bar{q}' + c + 2p$ ($e\nu$)	ctopq6	0.294	1,371,123
$W \rightarrow q\bar{q}' + c + 3p$ ($e\nu$)	ctopq7	0.042	1,339,400
$W \rightarrow q\bar{q}' + c + 0p$ ($\mu\nu$)	ctopqc	13.8	1,400,788
$W \rightarrow q\bar{q}' + c + 1p$ ($\mu\nu$)	ctopqd	2.30	1,395,613
$W \rightarrow q\bar{q}' + c + 2p$ ($\mu\nu$)	ctopqe	0.294	1,400,788
$W \rightarrow q\bar{q}' + c + 3p$ ($\mu\nu$)	ctopqf	0.042	1,398,030
$W \rightarrow q\bar{q}' + c + 0p$ ($\tau\nu$)	ctopqk	13.8	1,400,788
$W \rightarrow q\bar{q}' + c + 1p$ ($\tau\nu$)	ctopql	2.30	1,400,788
$W \rightarrow q\bar{q}' + c + 2p$ ($\tau\nu$)	ctopqm	0.294	1,400,788
$W \rightarrow q\bar{q}' + c + 3p$ ($\tau\nu$)	ctopqn	0.042	1,400,788

Table B.11: The data-set names, cross sections (in picobarns), and number of events for the W + light flavor $Q^2 = 2.0$ systematics Monte Carlo simulation samples.

Sample	Data-set Name	Cross Section	Number of Events
$W \rightarrow q\bar{q}' + 0p$ ($e\nu$)	otop0n	1772.9	2,485,992
$W \rightarrow q\bar{q}' + 1p$ ($e\nu$)	otop0l	182.7	2,502,270
$W \rightarrow q\bar{q}' + 2p$ ($e\nu$)	otop0j	24.65	495,337
$W \rightarrow q\bar{q}' + 3p$ ($e\nu$)	otop0h	3.37	500,426
$W \rightarrow q\bar{q}' + 4p$ ($e\nu$)	otop0f	0.54	382,458
$W \rightarrow q\bar{q}' + 0p$ ($\mu\nu$)	otop0x	1771.66	2,496,463
$W \rightarrow q\bar{q}' + 1p$ ($\mu\nu$)	otop0v	182.7	2,502,270
$W \rightarrow q\bar{q}' + 2p$ ($\mu\nu$)	otop0t	24.62	500,426
$W \rightarrow q\bar{q}' + 3p$ ($\mu\nu$)	otop0r	3.38	500,426
$W \rightarrow q\bar{q}' + 4p$ ($\mu\nu$)	otop0p	0.54	500,426
$W \rightarrow q\bar{q}' + 0p$ ($\tau\nu$)	wtopq5	1767.66	2,502,270
$W \rightarrow q\bar{q}' + 1p$ ($\tau\nu$)	wtopq6	182.9	2,502,270
$W \rightarrow q\bar{q}' + 2p$ ($\tau\nu$)	wtopq7	24.57	500,471
$W \rightarrow q\bar{q}' + 3p$ ($\tau\nu$)	wtopq8	3.37	500,471
$W \rightarrow q\bar{q}' + 4p$ ($\tau\nu$)	wtopq9	0.54	500,471

B.3 Building and Using the Fitter

The METHOD III fitter is available in CDF's Concurrent Versioning System in the package Jhu/Top. The README file contains instructions on how to build and run the fitter.

B.4 Fitter PolyNoids

All of the Polynoids used by the METHOD III fitter are shown in Figures B.1 – B.17. Specific details about the functions are described in Tables B.12 - B.16. Unless otherwise specified, each PolyNoid is a second-order polynomial, having the form

$$A + BR_x + CR_x^2.$$

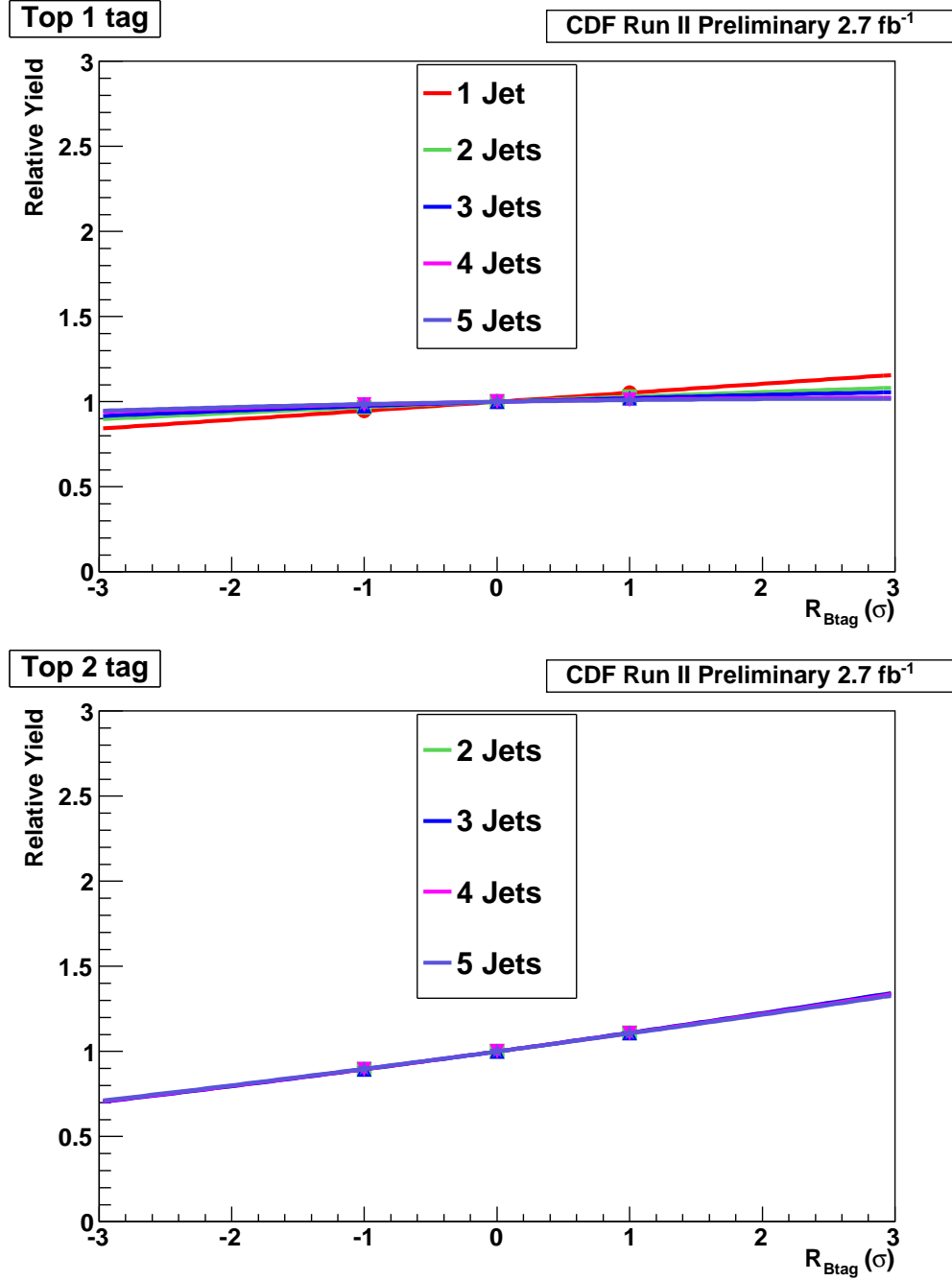


Figure B.1: Function parameterizing the form of the Btag uncertainty in the Top sample.

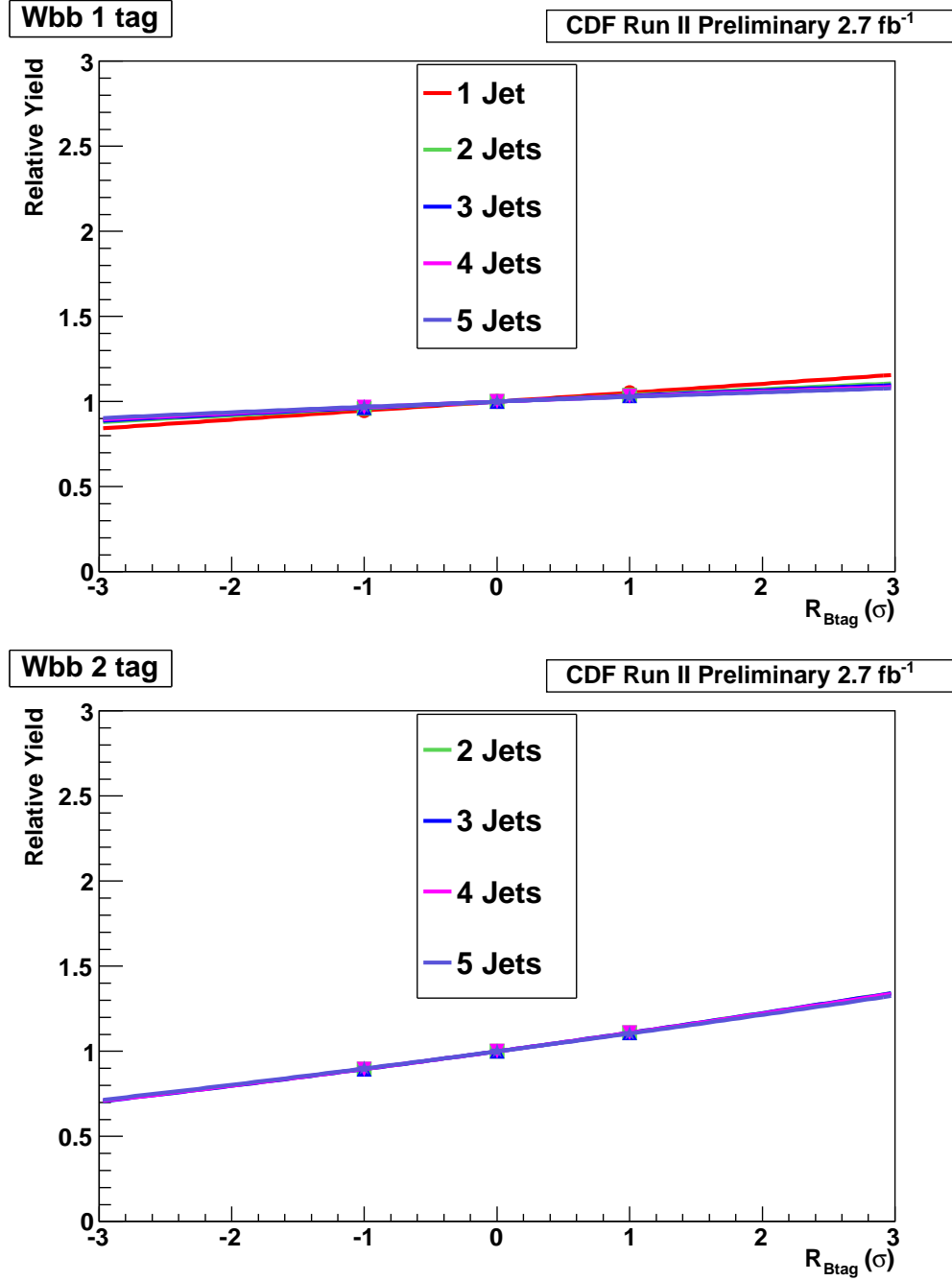


Figure B.2: Function parameterizing the form of the Btag uncertainty in the $Wb\bar{b}$ sample.

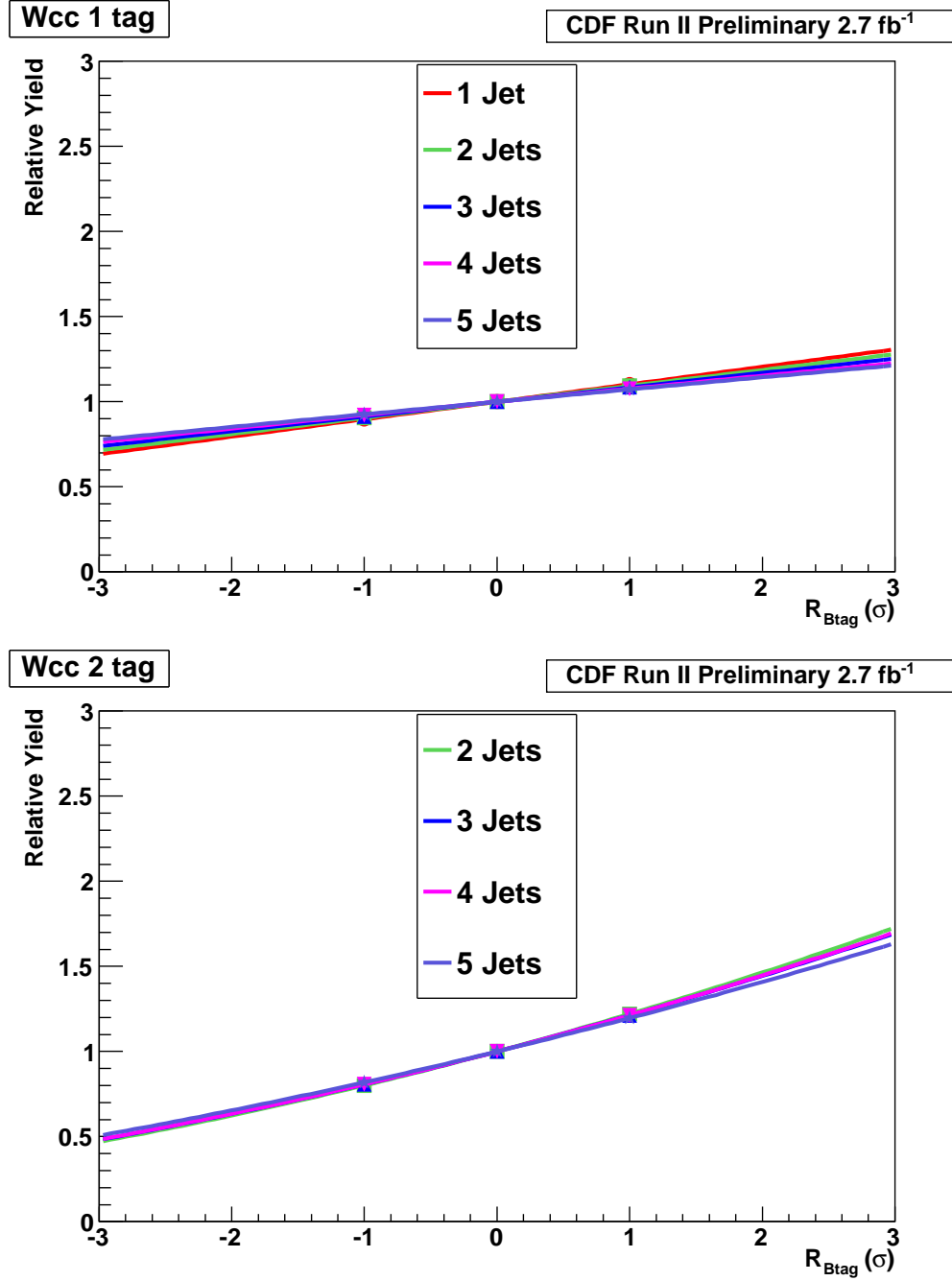


Figure B.3: Function parameterizing the form of the Btag uncertainty in the $Wc\bar{c}$ sample.

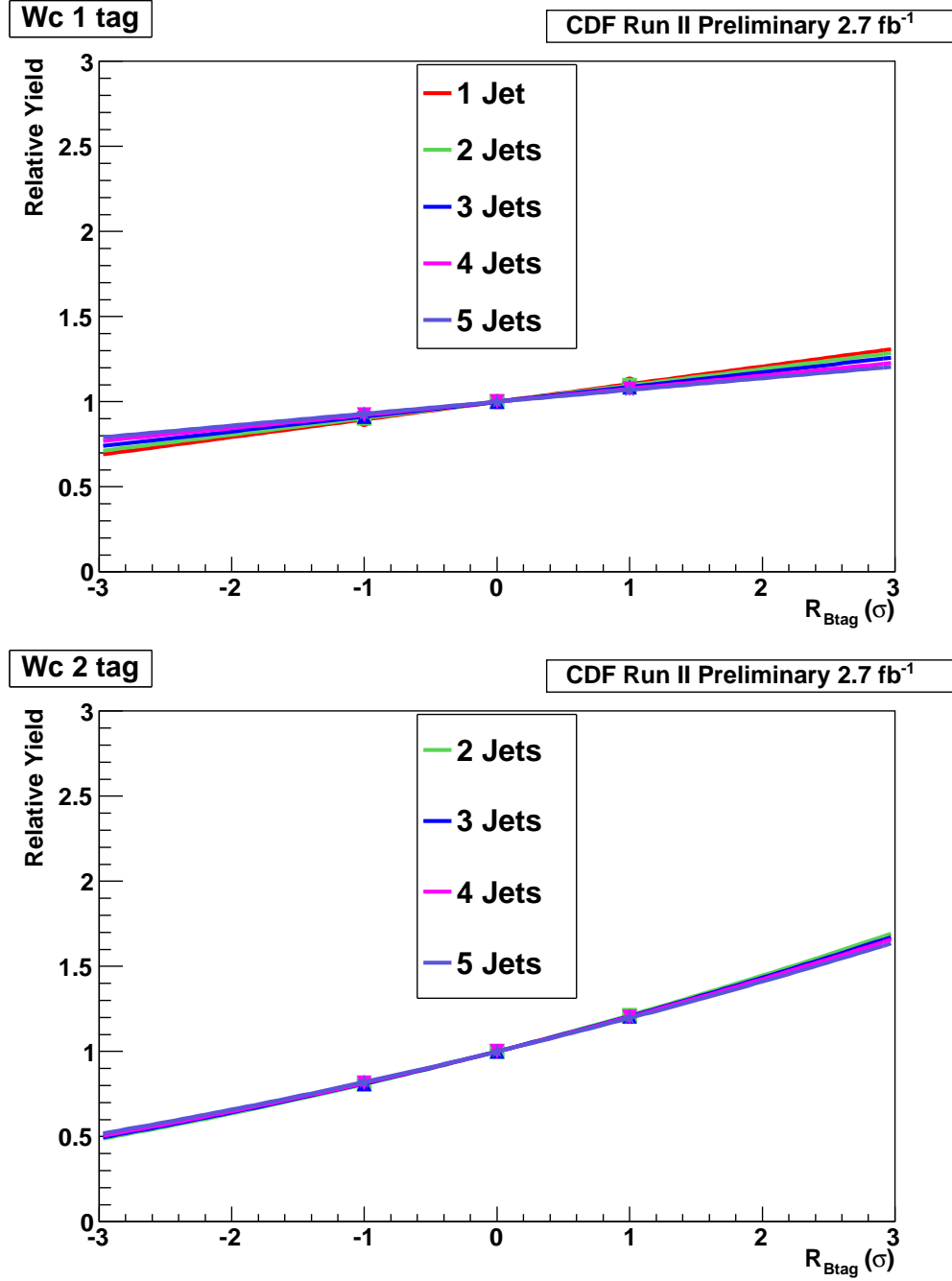


Figure B.4: Function parameterizing the form of the Btag uncertainty in the Wc sample.

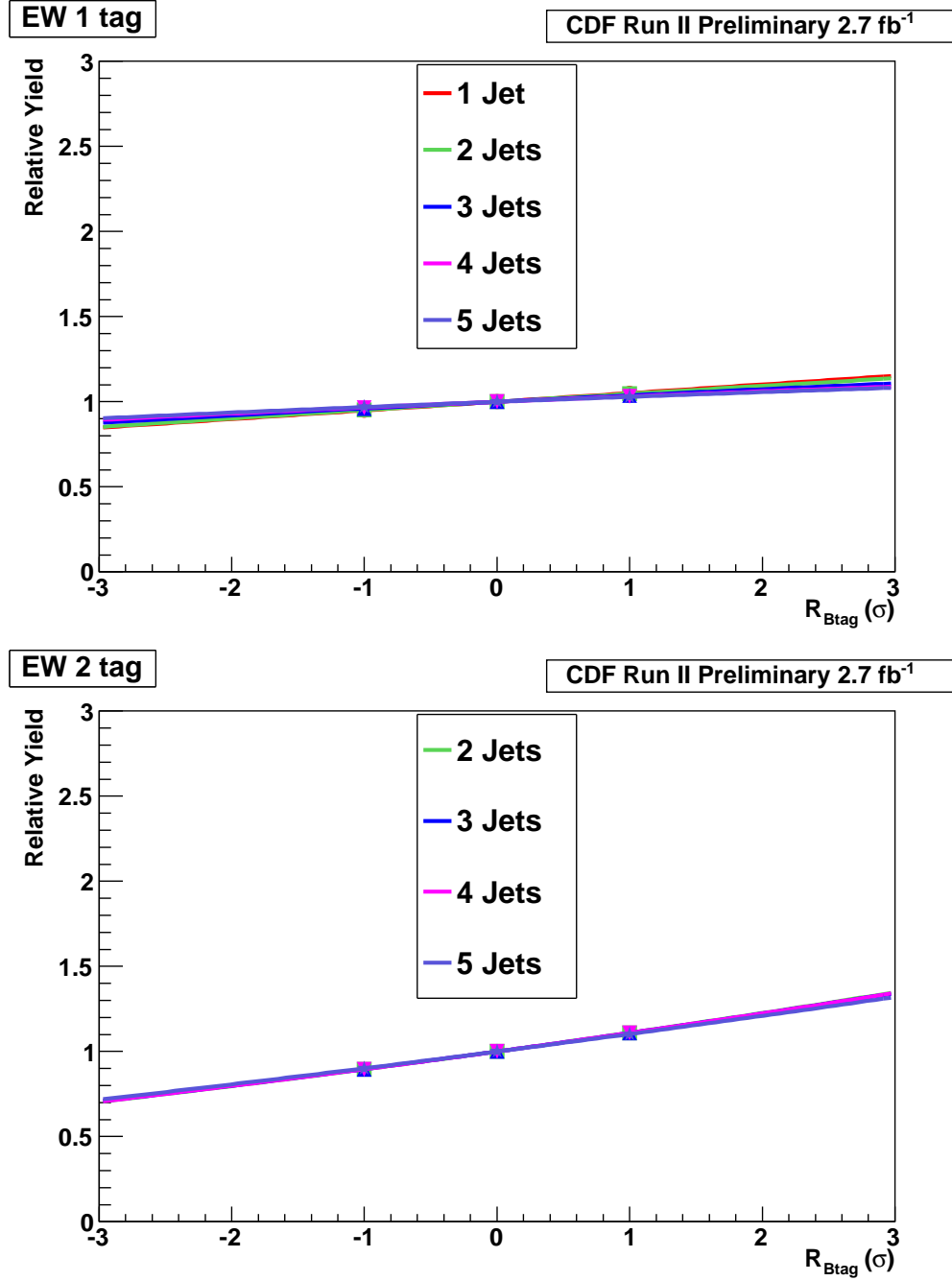


Figure B.5: Function parameterizing the form of the Btag uncertainty in the Electroweak sample.

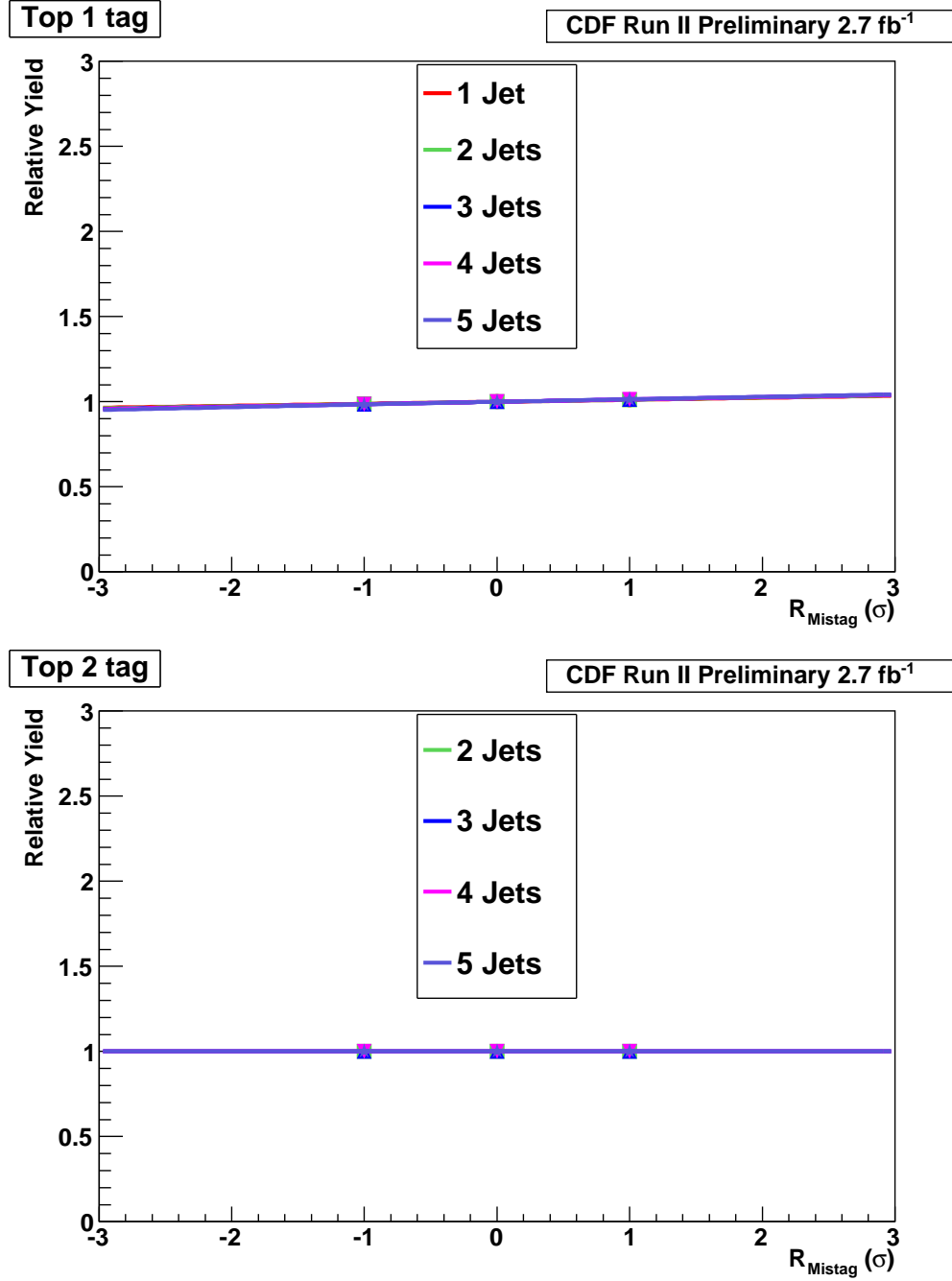


Figure B.6: Function parameterizing the form of the Mistag uncertainty in the Top sample.

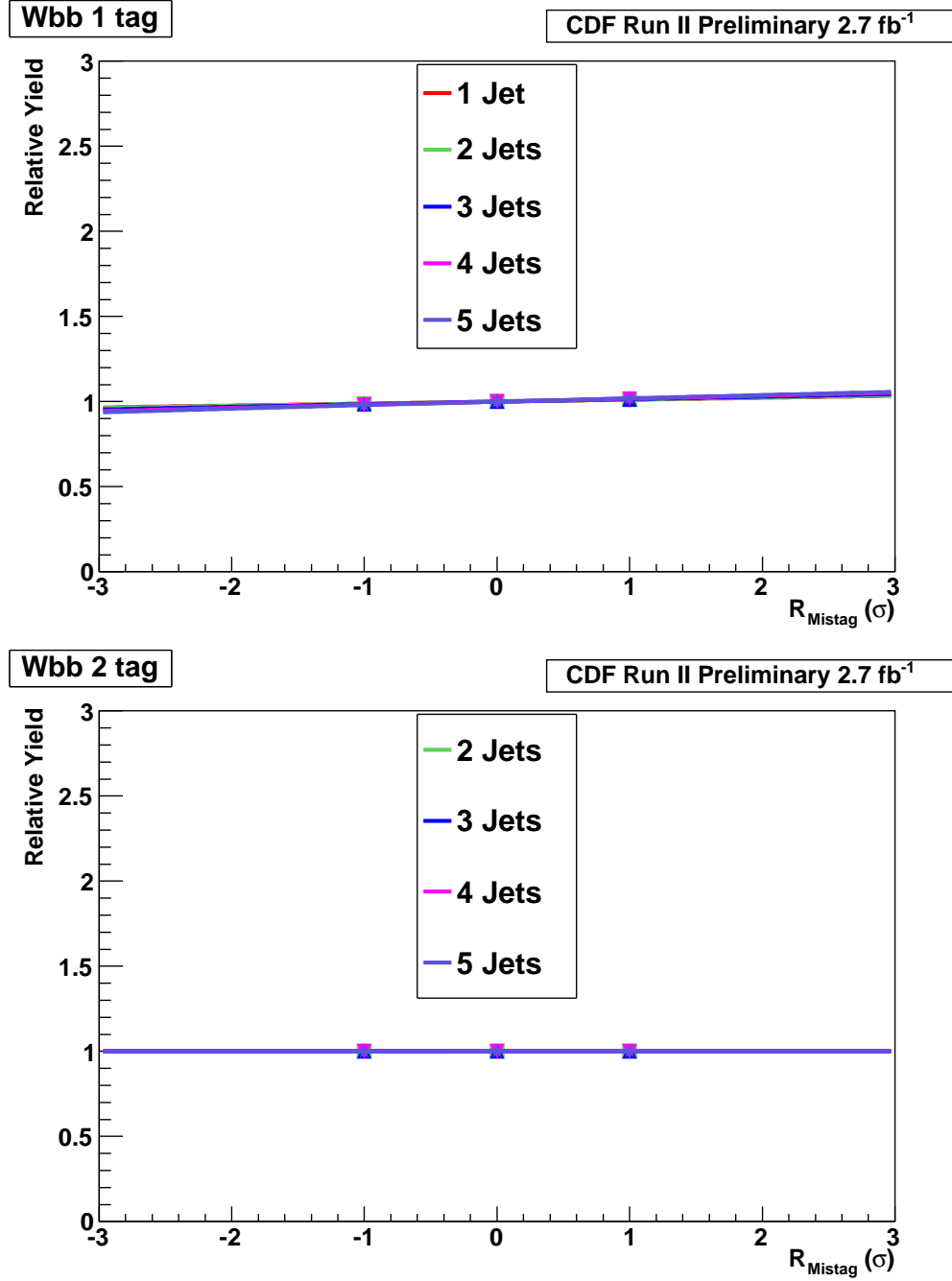


Figure B.7: Function parameterizing the form of the Mistag uncertainty in the $Wb\bar{b}$ sample.

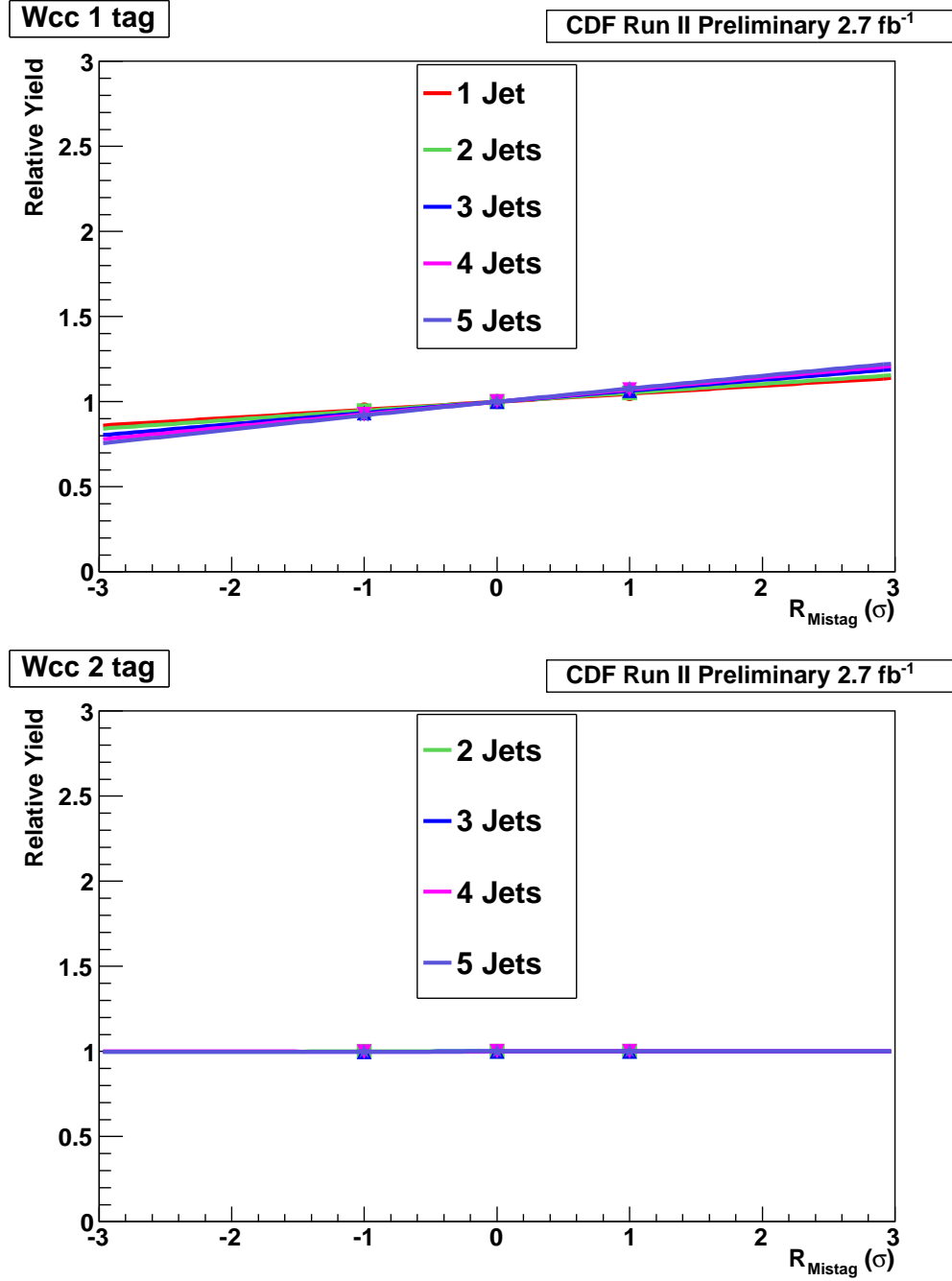


Figure B.8: Function parameterizing the form of the Mistag uncertainty in the $Wc\bar{c}$ sample.

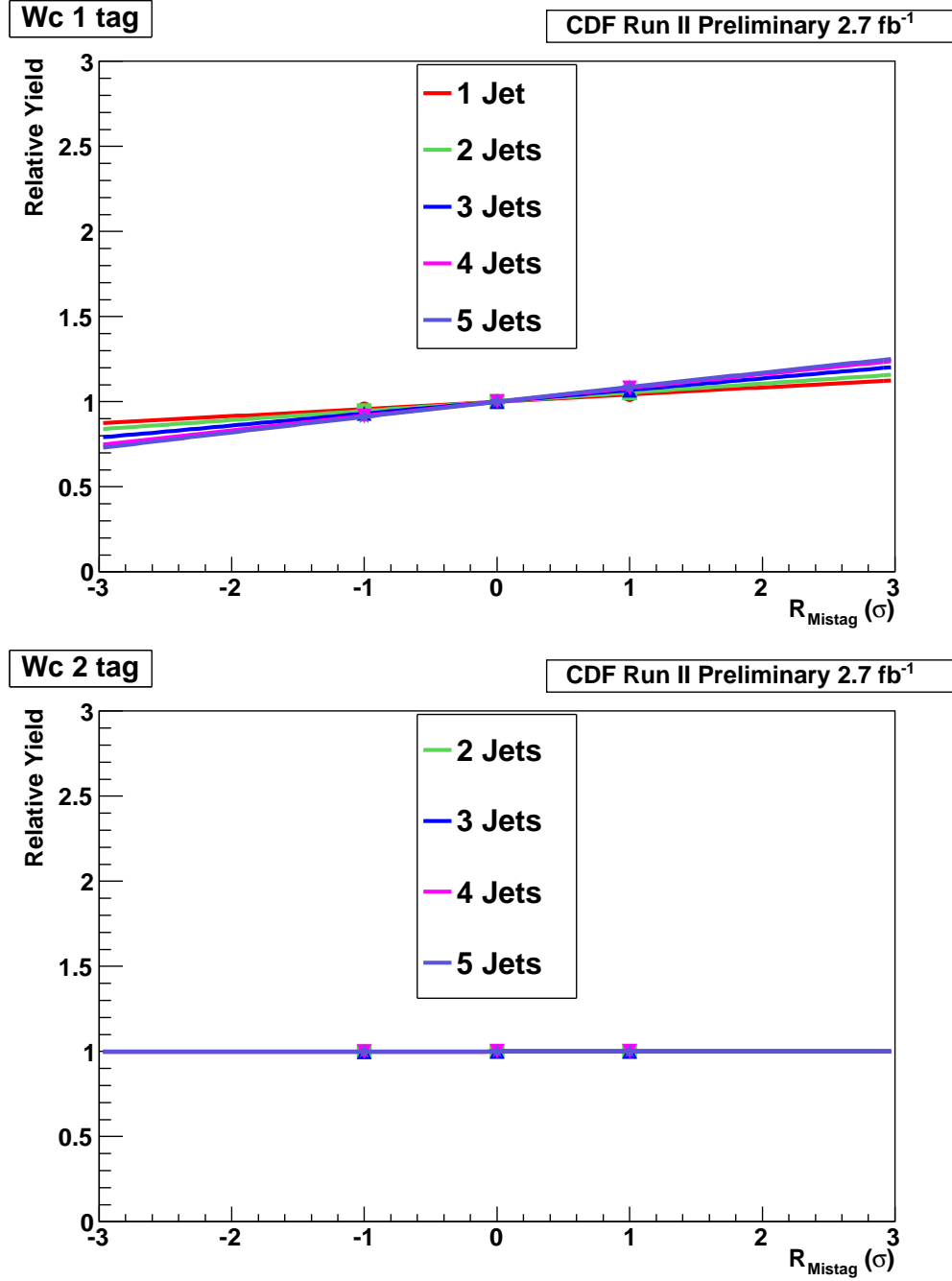


Figure B.9: Function parameterizing the form of the Mistag uncertainty in the Wc sample.

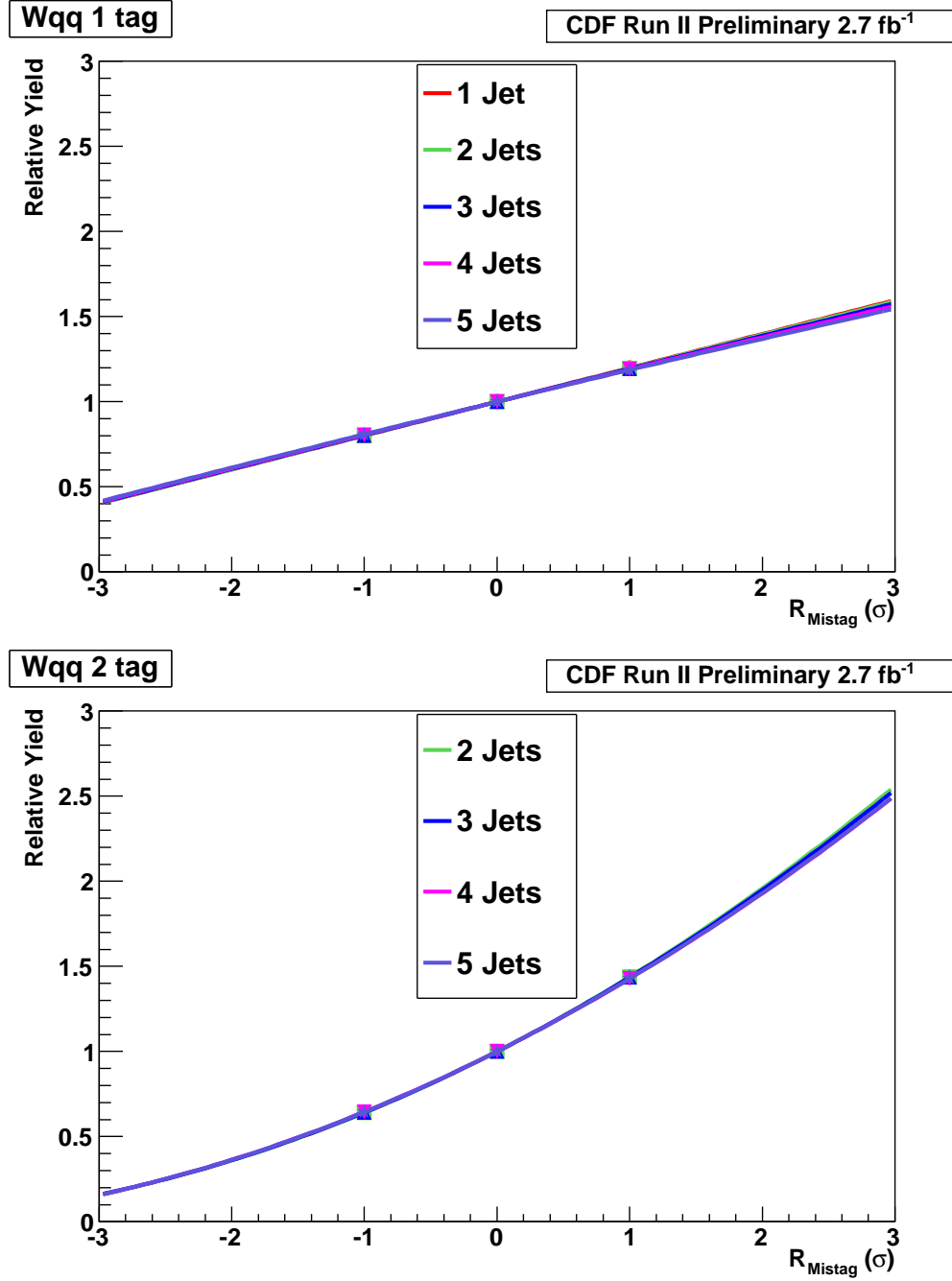


Figure B.10: Function parameterizing the form of the Mistag uncertainty in the $Wq\bar{q}$ sample.

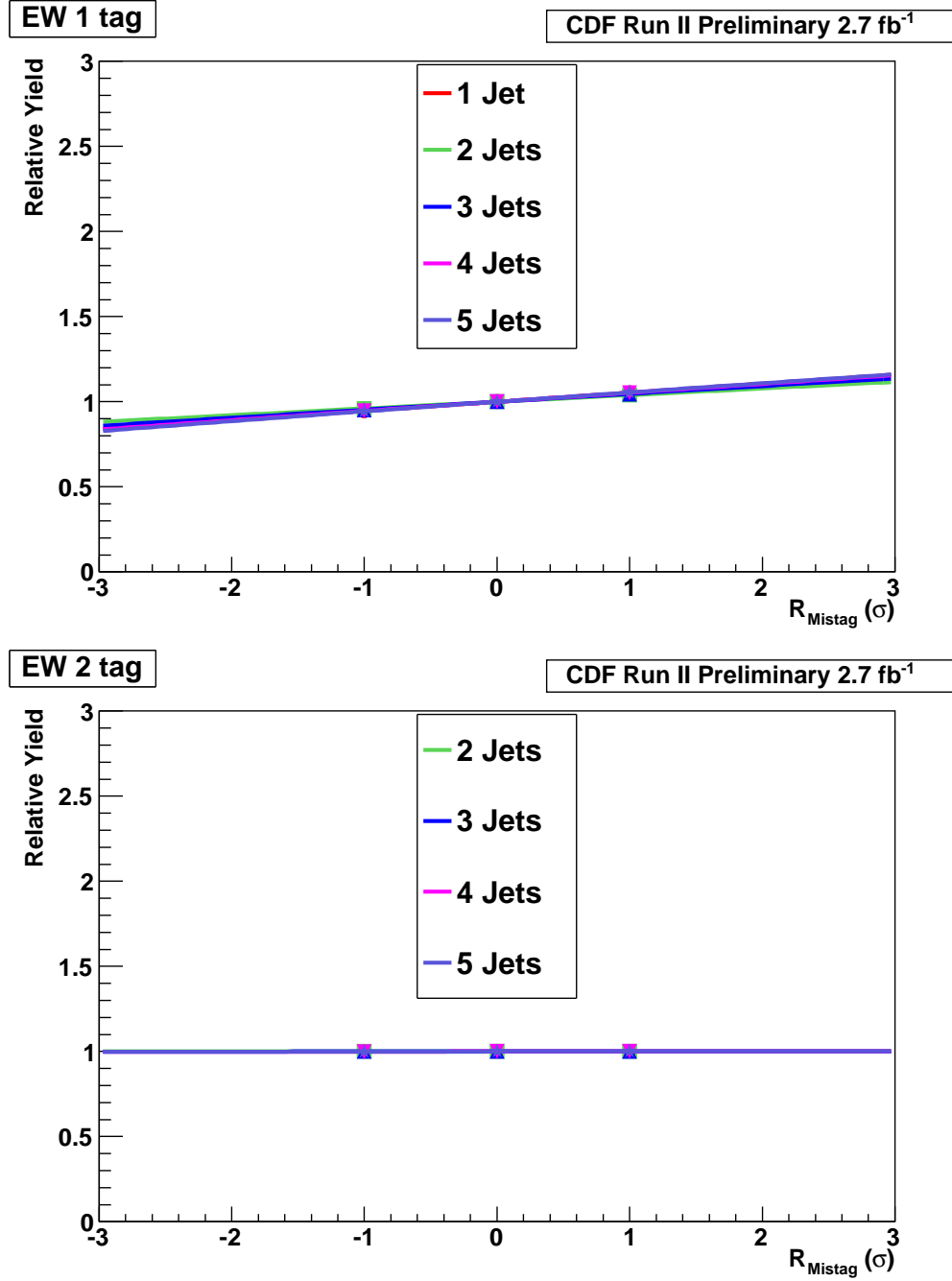


Figure B.11: Function parameterizing the form of the Mistag uncertainty in the Electroweak sample.

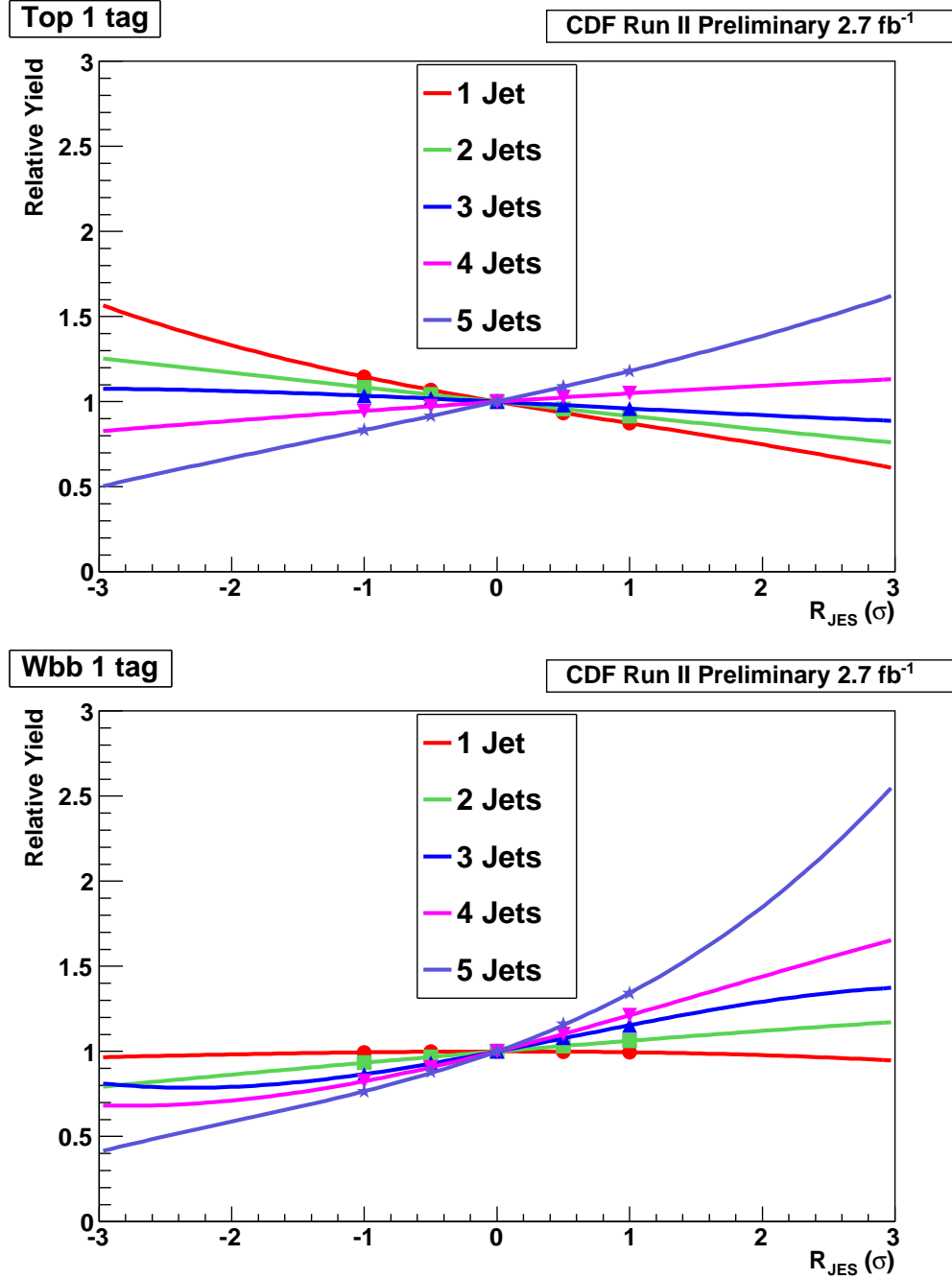


Figure B.12: Function parameterizing the form of the Jet Energy Scale uncertainty in the Top and $Wb\bar{b}$ samples.

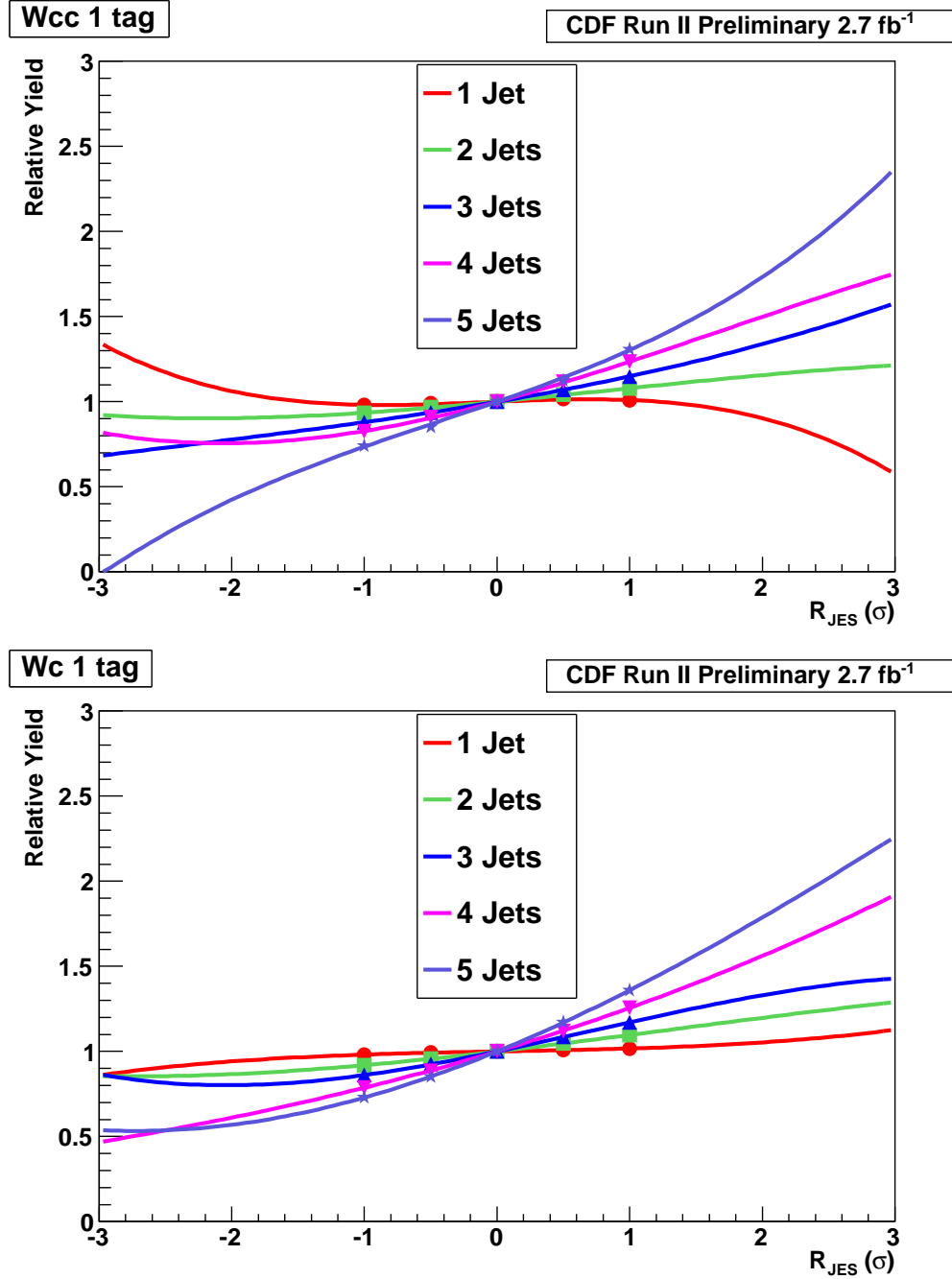


Figure B.13: Function parameterizing the form of the Jet Energy Scale uncertainty in the $Wc\bar{c}$ and Wc samples.

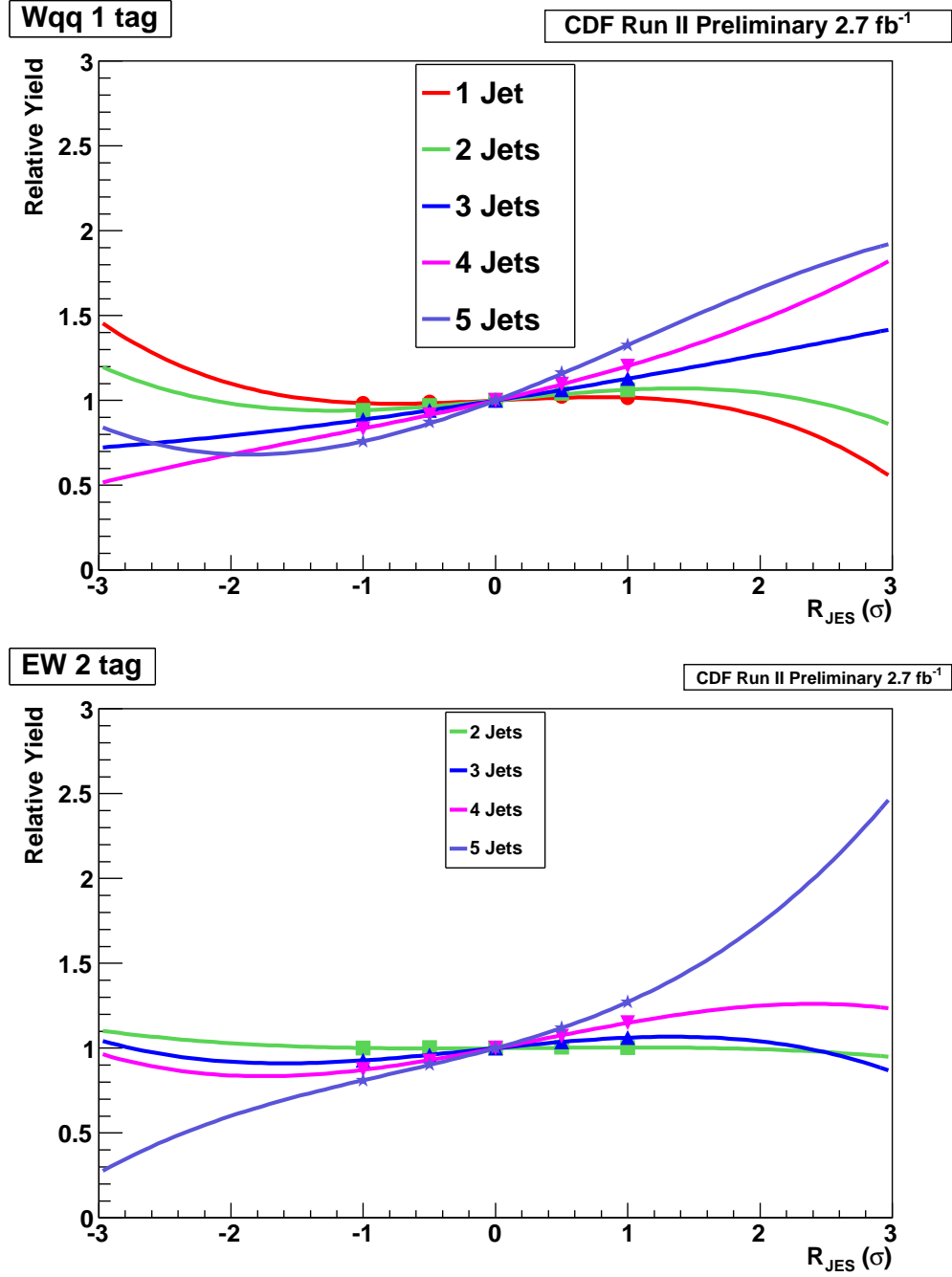


Figure B.14: Function parameterizing the form of the Jet Energy Scale uncertainty in the $Wq\bar{q}$ and Electroweak samples.

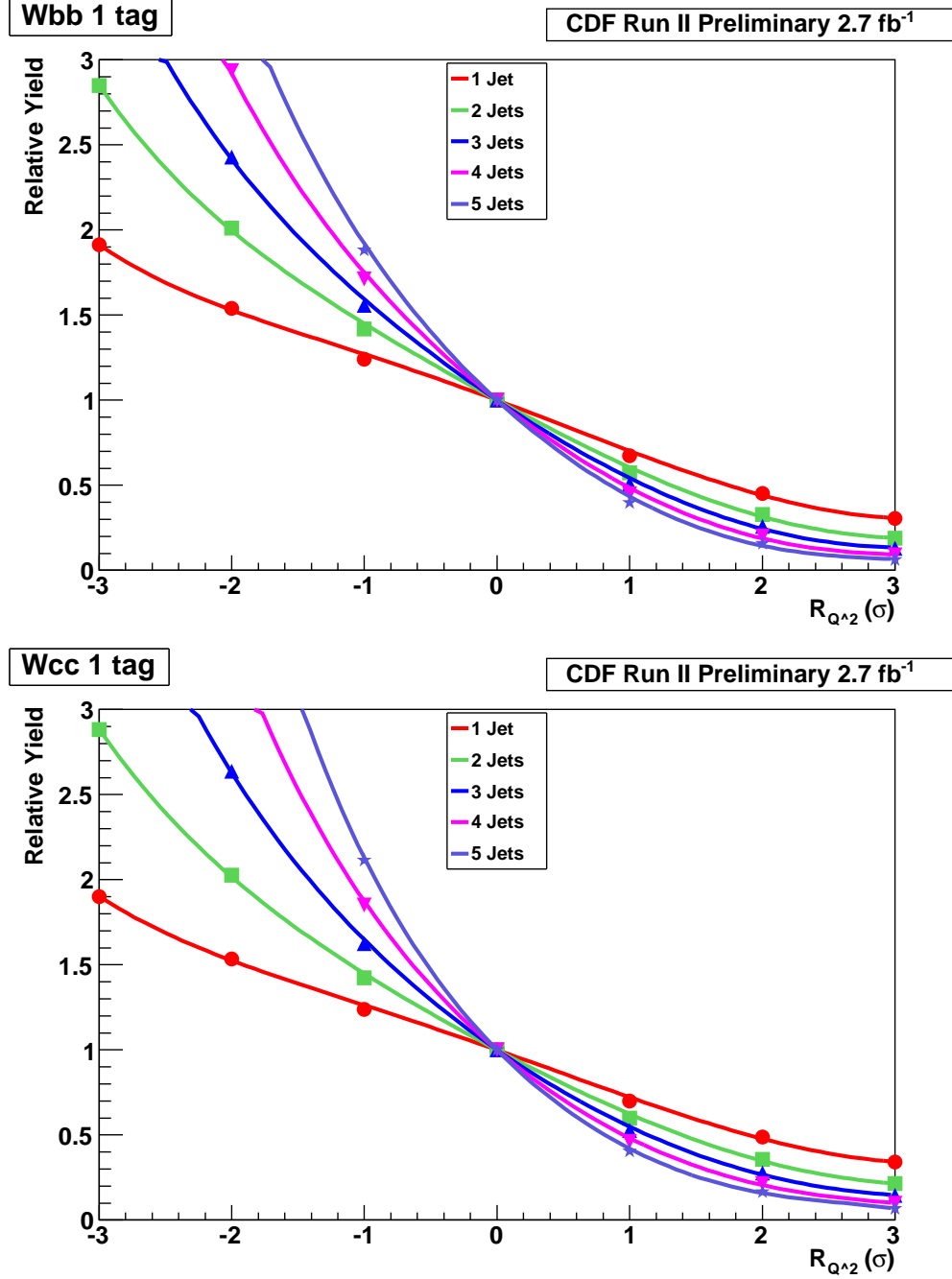


Figure B.15: Function parameterizing the form of the Q^2 energy scale uncertainty in the $Wb\bar{b}$ and $Wc\bar{c}$ samples.

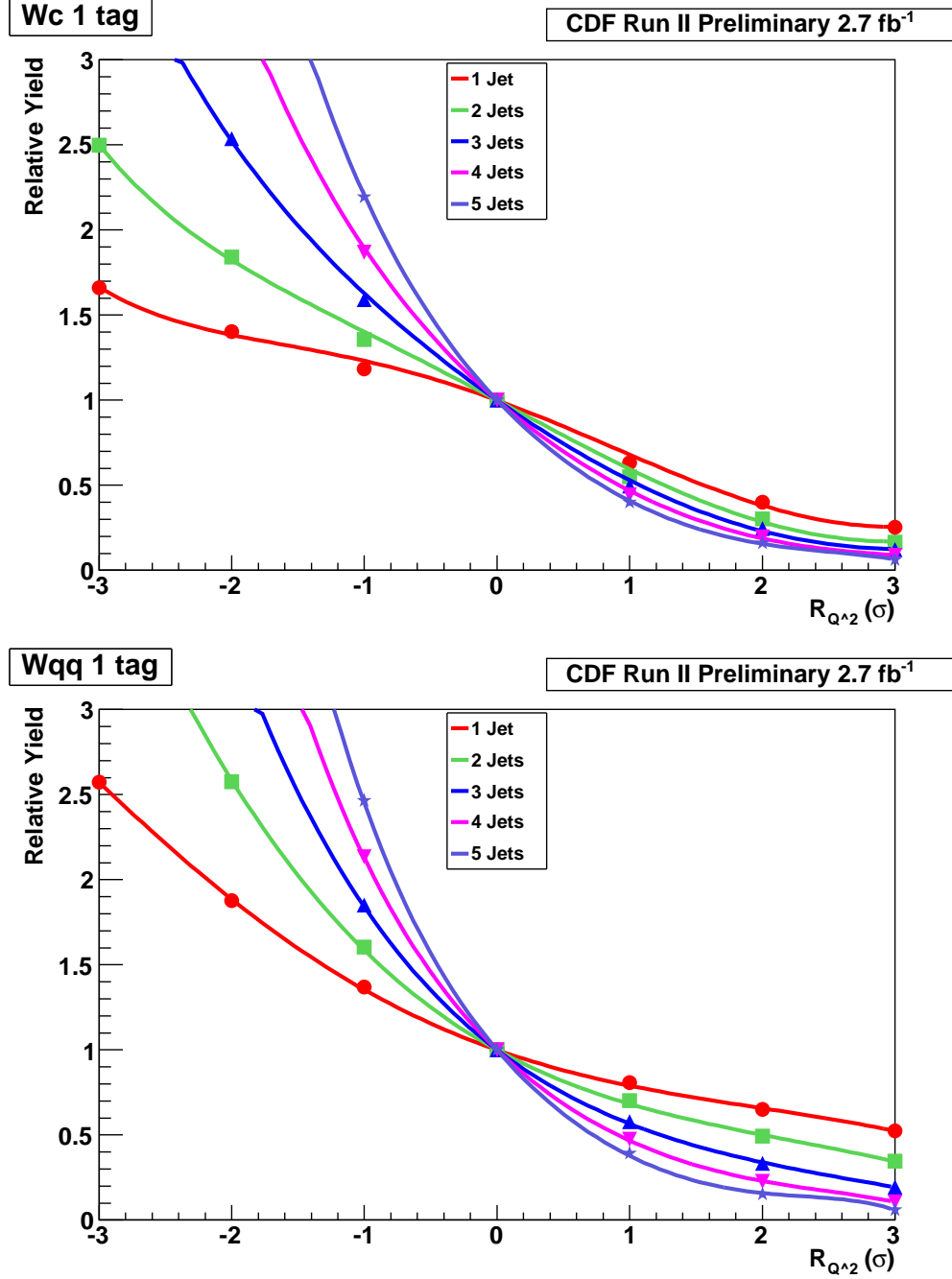


Figure B.16: Function parameterizing the form of the Q^2 energy scale uncertainty in the Wc and $Wq\bar{q}$ samples.

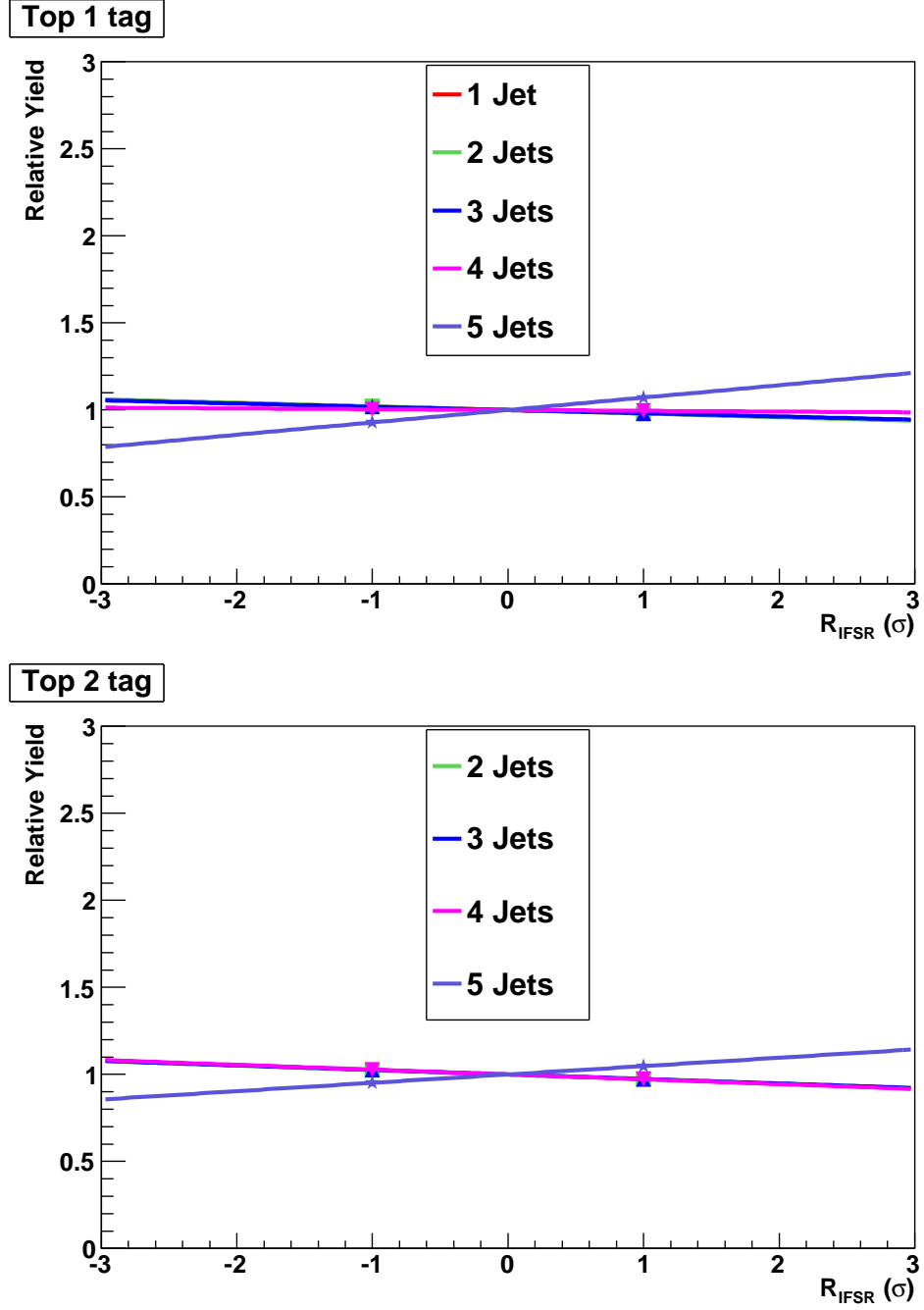


Figure B.17: Function parameterizing the form of the I/FSR uncertainty in the Top sample.

Table B.12: The parameters that define the functional form for the b -tag scale factor uncertainty.

n_{jet}, n_{tag}	Sample	A	B	C
1, 1	EW	1.0	0.050808601693199	0.000002667817740
2, 1	EW	1.0	0.047805720646437	-0.000566632860722
3, 1	EW	1.0	0.038514117860483	-0.000811189415222
4, 1	EW	1.0	0.032685118389686	-0.000948482793874
5, 1	EW	1.0	0.030005551237706	-0.000852808597110
2, 2	EW	1.0	0.107267772822832	0.002911291211040
3, 2	EW	1.0	0.106096702953553	0.002794813606327
4, 2	EW	1.0	0.106503649895311	0.002737646737662
5, 2	EW	1.0	0.100514120449439	0.002081811842546
1, 1	Wc	1.0	0.103801533749312	-0.000020878727592
2, 1	Wc	1.0	0.096510628436930	-0.000032636538176
3, 1	Wc	1.0	0.087118412449969	-0.000079778775683
4, 1	Wc	1.0	0.076966792917573	-0.000148026755266
5, 1	Wc	1.0	0.069540484282818	-0.000191735035271
2, 2	Wc	1.0	0.202551060029109	0.010240954220074
3, 2	Wc	1.0	0.197916928092812	0.009569152981680
4, 2	Wc	1.0	0.193938661346831	0.009285545207509
5, 2	Wc	1.0	0.187884520879665	0.008770722309597
1, 1	Wcc	1.0	0.102577487760930	0.000000471262974
2, 1	Wcc	1.0	0.094262476590790	-0.000368340803557
3, 1	Wcc	1.0	0.085673665472031	-0.000470938851759
4, 1	Wcc	1.0	0.077606218783834	-0.000637217789369
5, 1	Wcc	1.0	0.072837839387508	-0.000510195201096
2, 2	Wcc	1.0	0.209947146724235	0.011019851798308
3, 2	Wcc	1.0	0.202551587227643	0.009794495152068
4, 2	Wcc	1.0	0.203171628453488	0.010222052649570
5, 2	Wcc	1.0	0.188510838584675	0.007865906022415

Continued on next page

Table B.12—Continued

n_{jet}, n_{tag}	Sample	A	B	C
1, 1	Wbb	1.0	0.052617952797275	−0.000049028066704
2, 1	Wbb	1.0	0.038349856613444	−0.000774653743269
3, 1	Wbb	1.0	0.034915143305072	−0.000887029469412
4, 1	Wbb	1.0	0.031912673385848	−0.000986596728353
5, 1	Wbb	1.0	0.029187908953503	−0.001029679466286
2, 2	Wbb	1.0	0.106704594916124	0.002854374611364
3, 2	Wbb	1.0	0.106690498477592	0.002796920387805
4, 2	Wbb	1.0	0.105830757436527	0.002618922484992
5, 2	Wbb	1.0	0.102587916430385	0.002305413708222
1, 1	Top	1.0	0.052816331954326	−0.000001193206373
2, 1	Top	1.0	0.030939110692378	−0.001159090523290
3, 1	Top	1.0	0.023300390548155	−0.001550856986506
4, 1	Top	1.0	0.014243501850230	−0.001941695615134
5, 1	Top	1.0	0.011672273835828	−0.001981496219160
2, 2	Top	1.0	0.107163500354419	0.002870617879131
3, 2	Top	1.0	0.107297659449893	0.002675990705511
4, 2	Top	1.0	0.105653729843393	0.002412860314518
5, 2	Top	1.0	0.103507136030461	0.002217572360723

Table B.13: The parameters that define the functional form for the uncertainty due to the Mistag parameterization.

n_{jet}, n_{tag}	Sample	A	B	C
1, 1	EW	1.0	0.053217706826766	0.000000222785621
2, 1	EW	1.0	0.039180989683471	−0.000082889653974
3, 1	EW	1.0	0.046532510365108	−0.000232854532083
4, 1	EW	1.0	0.053349942894600	−0.000413497662794
5, 1	EW	1.0	0.055775800657878	−0.000653753672691
2, 2	EW	1.0	0.000001900074604	0.000000196203356
3, 2	EW	1.0	0.000006314014971	0.000000617753456
4, 2	EW	1.0	0.000023383894431	0.000002284470269
5, 2	EW	1.0	0.000094978929715	0.000009103312531

Continued on next page

Table B.13—Continued

n_{jet}, n_{tag}	Sample	A	B	C
1, 1	Wqq	1.0	0.199164314559183	−0.000020142546910
2, 1	Wqq	1.0	0.198214825212284	−0.000356694658003
3, 1	Wqq	1.0	0.195611792715817	−0.000863676453889
4, 1	Wqq	1.0	0.192555989685214	−0.001468124450470
5, 1	Wqq	1.0	0.188891970810473	−0.002170888988865
2, 2	Wqq	1.0	0.399999989762667	0.039999936983531
3, 2	Wqq	1.0	0.396797775801832	0.038768449158437
4, 2	Wqq	1.0	0.391314907713090	0.036678434282730
5, 2	Wqq	1.0	0.391806384055013	0.036865196273873
1, 1	Wc	1.0	0.042279241759683	−0.000001297294564
2, 1	Wc	1.0	0.053626248245832	−0.000110462029422
3, 1	Wc	1.0	0.069251149814338	−0.000340919143700
4, 1	Wc	1.0	0.082253145048066	−0.000707622282204
5, 1	Wc	1.0	0.087828718370673	−0.001064058482448
2, 2	Wc	1.0	0.000001638102605	0.000000169623139
3, 2	Wc	1.0	0.000216565418562	0.000057409181454
4, 2	Wc	1.0	0.000504580601111	0.000049259146858
5, 2	Wc	1.0	0.000576313925999	0.000054637199330
1, 1	Wcc	1.0	0.046870505557367	0.000000159544072
2, 1	Wcc	1.0	0.052703847855070	−0.000144456016792
3, 1	Wcc	1.0	0.064856437856421	−0.000361299447168
4, 1	Wcc	1.0	0.072298033776084	−0.000643801501756
5, 1	Wcc	1.0	0.078858360672987	−0.001181474897175
2, 2	Wcc	1.0	0.000006878561627	0.000000706069256
3, 2	Wcc	1.0	0.000019177679721	0.000001910289969
4, 2	Wcc	1.0	0.000178251322712	0.000115932693317
5, 2	Wcc	1.0	0.000032151208241	0.000003146203975

Continued on next page

Table B.13—Continued

n_{jet}, n_{tag}	Sample	A	B	C
1, 1	Wbb	1.0	0.011577581660612	−0.000000023754578
2, 1	Wbb	1.0	0.012302079898210	−0.000047551163979
3, 1	Wbb	1.0	0.015094441867364	−0.000103591286965
4, 1	Wbb	1.0	0.018053611576978	−0.000186061196853
5, 1	Wbb	1.0	0.020090619847282	−0.000294911582357
2, 2	Wbb	1.0	0.000000038629323	−0.000000009324319
3, 2	Wbb	1.0	0.000002226399795	0.000000004516024
4, 2	Wbb	1.0	0.000001823622836	0.000000182362284
5, 2	Wbb	1.0	0.000027230453504	0.000006104797136
1, 1	Top	1.0	0.011719226547266	0.000000002875497
2, 1	Top	1.0	0.012735177520243	−0.000081262075693
3, 1	Top	1.0	0.014005209046387	−0.000143172999682
4, 1	Top	1.0	0.014186264203054	−0.000199904928374
5, 1	Top	1.0	0.015459179719585	−0.000269200445437
2, 2	Top	1.0	0.000000000000000	0.000000000000000
3, 2	Top	1.0	0.000001167120433	0.000000352258167
4, 2	Top	1.0	0.000001283846432	0.000000204476847
5, 2	Top	1.0	0.000002221240991	0.000000253173704

Table B.14: The parameters that define the functional form for the Jet Energy Scale uncertainty. This parameterization takes the form $A + BR_x + CR_x^2 + DR_x^3$.

n_{jet}, n_{tag}	Sample	A	B	C	D
1, 1	EW	1.0	-0.033699906289850	0.001657901954130	0.001218591400012
2, 1	EW	1.0	0.021783968277624	-0.002276482324367	-0.000512523558700
3, 1	EW	1.0	0.104107690384997	0.007904150820242	-0.000858045207922
4, 1	EW	1.0	0.168291890310726	0.013200883176242	0.000061625370589
5, 1	EW	1.0	0.224302299005892	0.017041384717577	0.017595807645817
2, 2	EW	1.0	0.005003362355104	0.002995721524191	-0.003483585174847
3, 2	EW	1.0	0.079193083827693	-0.004943609634969	-0.012281082362094
4, 2	EW	1.0	0.150236957506360	0.011274861537502	-0.011866380473150
5, 2	EW	1.0	0.212803657870464	0.041977199859153	0.017616328579582
1, 1	Wqq	1.0	0.038025944914257	0.000837995590909	-0.021411513103311
2, 1	Wqq	1.0	0.075218414254744	0.003370470534047	-0.014885163114184
3, 1	Wqq	1.0	0.121410500241374	0.007970084010339	-0.000530080681448
4, 1	Wqq	1.0	0.179423515624746	0.019186108548987	0.004523781580549
5, 1	Wqq	1.0	0.296522178164656	0.043227731172598	-0.012996986787993
2, 2	Wqq	1.0	-0.166909453538851	1.476411024624356	1.943580335218650
3, 2	Wqq	1.0	0.016523325470551	0.026124764380319	0.006759130668968
4, 2	Wqq	1.0	0.073611401320337	0.052631112183558	-0.055528937120565
5, 2	Wqq	1.0	0.013108862991026	-0.174571495930435	0.165560963453268

Continued on next page

Table B.14—Continued

n_{jet}, n_{tag}	Sample	A	B	C	D
1, 1	Wc	1.0	0.014577363605418	−0.000687949117719	0.003340695748187
2, 1	Wc	1.0	0.090866466081534	0.008003657699068	−0.002040135003288
3, 1	Wc	1.0	0.162781562336890	0.016443342094592	−0.007676428791096
4, 1	Wc	1.0	0.233933031815768	0.021564235489930	0.000923834451660
5, 1	Wc	1.0	0.318440308394641	0.044474438416964	−0.003476161541207
2, 2	Wc	1.0	0.061939246209479	0.024141674970033	−0.011650738729042
3, 2	Wc	1.0	0.243342727196350	−0.014434735549009	−0.139417920795108
4, 2	Wc	1.0	0.002310253987623	0.005351697762229	0.097027290794095
5, 2	Wc	1.0	0.429909212912045	0.145065757774428	−0.081406336499241
1, 1	Wcc	1.0	0.031704162565828	−0.004294203275864	−0.017858354312144
2, 1	Wcc	1.0	0.074701524502724	0.007507632293231	−0.002909290924088
3, 1	Wcc	1.0	0.132734292037898	0.014475419061293	0.001857353659193
4, 1	Wcc	1.0	0.209909409710662	0.031957520558768	−0.006065803218439
5, 1	Wcc	1.0	0.269568459863576	0.019493572985822	0.014377218959165
2, 2	Wcc	1.0	0.054383260064302	0.000516808647151	0.008008793048873
3, 2	Wcc	1.0	0.071602924154049	−0.055787445620634	0.018227411300959
4, 2	Wcc	1.0	0.153194562905449	0.090914752188633	0.088786093965299
5, 2	Wcc	1.0	0.109782970130490	−0.102601269835641	0.103739892290681

Continued on next page

Table B.14—Continued

n_{jet}, n_{tag}	Sample	A	B	C	D
1, 1	Wbb	1.0	0.000709240130018	−0.004894351353632	−0.000446443576545
2, 1	Wbb	1.0	0.0647444494652281	−0.001971828926330	−0.000128610146666
3, 1	Wbb	1.0	0.150233218772678	0.010520256663969	−0.006296734351999
4, 1	Wbb	1.0	0.197806389206694	0.018941121741821	−0.003909409903490
5, 1	Wbb	1.0	0.279436259067293	0.054600707256041	0.009012467408394
2, 2	Wbb	1.0	0.044511153170422	−0.007359976394973	−0.001692791984064
3, 2	Wbb	1.0	0.121095479019738	0.003236312381424	−0.004077843156005
4, 2	Wbb	1.0	0.185633944900617	0.003990194633886	−0.006082656822872
5, 2	Wbb	1.0	0.224855098307426	0.049104378241080	0.022312884537035
1, 1	Top	1.0	−0.133475777069975	0.010050792237226	−0.003061963588035
2, 1	Top	1.0	−0.084071883458606	0.000820326477997	0.000132892697341
3, 1	Top	1.0	−0.038508642316763	−0.002013485923806	0.000778417342456
4, 1	Top	1.0	0.052039162778107	−0.002231148327747	−0.000107682544795
5, 1	Top	1.0	0.171803448408105	0.007139290621649	0.001833219551205
2, 2	Top	1.0	−0.069567422953781	0.002764463386149	0.003059992035147
3, 2	Top	1.0	−0.040707457421119	0.000849054525873	−0.003756333966128
4, 2	Top	1.0	0.039240405297156	−0.004703684429933	0.000643152311970
5, 2	Top	1.0	0.158022257528968	0.007001229091178	−0.000432942957315

Table B.15: The parameters that define the functional form for the Q^2 uncertainty. This parameterization takes the form $1 + BR_x + CR_x^2 + DR_x^3 + ER_x^4 + FR_x^5$, and the same parameterization is used in both the single and double tag cases.

n_{jet}	Sample	B	C	D	E	F
1	Wbb	-0.289693323600004	-0.016445948574428	0.006069191166668	0.003198045349237	-0.000405867566667
2	Wbb	-0.425495843433339	0.024122349189567	0.003909258937503	0.003759008052799	-0.000658415504167
3	Wbb	-0.523117454383337	0.063071596807570	-0.001202860770832	0.004859599576018	-0.000929684845833
4	Wbb	-0.619664666033333	0.110805402890585	-0.010532602520833	0.006989534340331	-0.001342702445833
5	Wbb	-0.715364238100005	0.166511901944020	-0.024837297708331	0.010829794185751	-0.002029310691667
1	Wcc	-0.274282781933337	-0.010083952778626	0.004379804041668	0.002636191538168	-0.000312022108333
2	Wcc	-0.413061099333338	0.032924999643129	0.001062539458336	0.003140284059160	-0.000511440125000
3	Wcc	-0.538301742066674	0.093467489541349	-0.009889077624996	0.004626715305980	-0.000769180308334
4	Wcc	-0.664249624333342	0.168720228717556	-0.029533831583329	0.008805735209924	-0.001404493583334
5	Wcc	-0.791314715466673	0.256242069610050	-0.059472256145830	0.017938255464377	-0.002927127887500

Continued on next page

Table B.15—Continued

n_{jet}	Sample	B	C	D	E	F
1	Wc	-0.286606476550005	-0.049105149062023	0.011626956145836	0.004974565541031	-0.000650479595834
2	Wc	-0.412950040950001	-0.005550125653626	0.010613903354167	0.004761235663168	-0.000878862404167
3	Wc	-0.544893219550004	0.073331009824746	-0.002992984479165	0.005221789803117	-0.001003795970833
4	Wc	-0.681267284316677	0.171083887867367	-0.029381271166662	0.009532924468511	-0.001585162516667
5	Wc	-0.822475388133334	0.284140255500637	-0.071058199500000	0.021689906804707	-0.003553822366667
1	Wqq	-0.272751015166666	0.073371227722647	-0.009208798395834	-0.001377604602417	0.000174813562500
2	Wqq	-0.427834191399997	0.134012870879135	-0.023759172687501	0.000420049855598	0.000123364087500
3	Wqq	-0.593413488799997	0.197069829192112	-0.042617063479168	0.006134501771628	-0.000604447720833
4	Wqq	-0.754986839566681	0.280184930739821	-0.072334404395827	0.017339196124682	-0.002471624537501
5	Wqq	-0.914417665050000	0.374721565374362	-0.114741884291666	0.038713982820293	-0.006615707158333

Table B.16: The parameters that define the functional form for the I/FSR uncertainty. This parameterization takes the form $A + BR_x$.

n_{jet}, n_{tag}	Sample	A	B
1, 1	Top	1.0	-0.019828645978032
2, 1	Top	1.0	-0.020684829966532
3, 1	Top	1.0	-0.018510771683614
4, 1	Top	1.0	-0.004485825520576
5, 1	Top	1.0	0.071256903108716
2, 2	Top	1.0	-0.025729642740566
3, 2	Top	1.0	-0.026051261582274
4, 2	Top	1.0	-0.027823917844624
5, 2	Top	1.0	0.048027569837480

Glossary

ALPGEN Software used to simulate events.

bhelxx High- p_T central electron-triggered data-sets.

bhmuxx High- p_T central muon-triggered data-sets.

σ Cross section. A measure of the probability of an interaction occurring.

CDF Collider Detector at Fermilab.

CEM Central Electromagnetic Calorimeter for CDF detector.

CHA Central Hadronic Calorimeter for CDF detector.

CLC Cerenkov Luminosity Counters. Measure the beam luminosity at CDF.

CMP Central Muon Detector Upgrade for CDF detector.

CMU Central Muon Detector for CDF detector.

CMX Central Muon Detector Extension for CDF detector.

COT Central Outer Tracker. Tracking chamber for CDF detector.

d_0 Impact parameter. Shortest distance between the interaction point and the trajectory of a track.

Data Quality Monitoring group This group creates a Good Run List based on availability of detector components.

E_T Transverse energy. Energy in the plane perpendicular to the beam direction.

η Pseudorapidity. A measure of the angle from the vertical.

eV Electron volt. Unit of energy where 1 eV is 1.6×10^{-19} J. Energies are typically measured in millions (MeV) or billions (GeV) of electron volts.

ISL Intermediate Silicon Layers. Used for linking tracks between SVX and COT. Also for silicon standalone tracks.

Jet Collection of tracks originating from the same point and in the same general direction. These tracks show up in the calorimeters.

Jet energy scale Energy discrepancy between the true energy of a jet and the raw energy measured in the calorimeters.

KIT Karlsruhe Institute of Technology's flavor separator. Uses a neural net to determine the flavor of a jet.

L00 Layer 00. Innermost silicon detector at CDF. Used for better impact parameter measurement.

Luminosity Measure of the beam intensity. When integrated over time it provides a measure of the size of the dataset.

\cancel{E}_T Missing transverse energy. This is calculated by negating the vector sum of the transverse energies of the event.

Mistag parameterization Separate algorithm applied to simulations to correctly model the mistag rate.

Pythia Software used to simulate events.

PEM Plug Electromagnetic Calorimeter for CDF detector.

PHA Plug Hadronic Calorimeter for CDF detector.

QCD Quantum Chromodynamics. The relativistic quantum field theory describing the strong nuclear interaction. Also used to describe background processes originating from these interactions.

QED Quantum Electrodynamics. The relativistic quantum field theory describing the electromagnetic interaction.

Secvtx Secondary Vertex tagger for CDF.

SVX Silicon Vertex Detector. Primary silicon detector for CDF.

Bibliography

- [1] R. P. Feynman, *Mathematical Formulation of the Quantum Theory of Electromagnetic Interaction*, Phys. Rev. **80** (1950), 440–457.
- [2] M. Gell-Mann, *A schematic Model of Baryons and Mesons*, Phys. Lett. **8** (1964), 214–215.
- [3] C. Amsler et al. (Particle Data Group Collaboration), *The Review of Particle Physics*, Phys. Lett. **B667** (2008), 1.
- [4] H. D. Politzer, *Asymptotic Freedom: An Approach to Strong Interactions*, Phys. Rept. **14** (1974), 129–180.
- [5] D. J. Gross and F. Wilczek, *Asymptotically Free Gauge Theories. 1*, Phys. Rev. **D8** (1973), 3633–3652.
- [6] F. Halzen and A. D. Martin, *Quarks & Leptons: An Introductory Course in Modern Particle Physics*, 1984.

- [7] P. Higgs, *Broken Symmetries and the Masses of Gauge Bosons*, Phys. Rev. Lett. **13** (1964), 508.
- [8] N. Kidonakis and R. Vogt, *The Theoretical Top Quark Cross Section at the Tevatron and the LHC*, Phys. Rev. **D78** (2008), 074005.
- [9] J. Pumplin et al., *New Generation of Parton Distributions with Uncertainties From Global QCD Analysis*, JHEP **07** (2002), 012, See also <http://www.phys.psu.edu/cteq/>.
- [10] I. Bigi, Y. Dokshitzer, V. Khoze, J. Khn, and P. Zerwas, *Production and Decay Properties of Ultra-Heavy Quarks*, Physics Letters B **181** (1986), no. 1-2, 157 – 163.
- [11] K. Ackerstaff et al. (OPAL Collaboration), *Measurement of the W boson mass and W^+W^- production and decay properties in e^+e^- collisions at $\sqrt{s} = 172$ GeV*, Eur. Phys. J. **C1** (1998), 395–424.
- [12] E. Palencia, *Observation of Electroweak Single Top Quark Production at the Tevatron*, (2009).
- [13] F. Abe et al. (CDF Collaboration), *Observation of Top Quark Production in $p\bar{p}$ Collisions*, Phys. Rev. Lett. **74** (1995), 2626–2631.
- [14] S. Abachi et al. (DØ Collaboration), *Observation of the Top Quark*, Phys. Rev. Letter. **74** (1995), 2632–2637.

- [15] *Operations Rookie Books*, accessed March 2010.
- [16] R. Blair et al. (CDF Collaboration), *The CDF II Detector: Technical Design Report*, 1996, Fermilab-PUB-96/390-E.
- [17] D. Acosta et al. (CDF Collaboration), *Measurement of the J/ψ Meson and b -Hadron Production Cross Sections in $p\bar{p}$ Collisions at $\sqrt{s} = 1960$ GeV*, Phys. Rev. **D71** (2005), 032001.
- [18] A. Sill et al. (CDF Collaboration), *CDF Run II Tracking Projects*, Nucl. Instrum. Meth. **A447** (2000), 1–8.
- [19] A. Affolder et al. (CDF Collaboration), *Intermediate Silicon Layers Detector for the CDF Experiment*, Nucl. Instrum. Meth. **A453** (2000), 84–88.
- [20] C. Hill (CDF Collaboration), *Operational Experience and Performance of the CDFII Silicon Detector*, Nucl. Instrum. Meth. **A530** (2004), 1–6.
- [21] A. Affolder et al. (CDF Collaboration), *CDF Central Outer Tracker*, Nucl. Instrum. Meth. **A526** (2004), 249–299.
- [22] L. Balka et al. (CDF Collaboration), *The CDF Central Electromagnetic Calorimeter*, Nucl. Instrum. Meth. **A267** (1998), 272–279.
- [23] M. Albrow et al. (CDF Collaboration), *The CDF Plug Upgrade Electromagnetic Calorimeter: Test Beam Results*, Nucl. Instrum. Meth. **A480** (2002), 524–546.

- [24] G. Ascoli et al. (CDF Collaboration), *CDF Central Muon Detector*, Nucl. Instrum. Meth. **A268** (1998), 33.
- [25] T. Dorigo (CDF Collaboration), *The Muon System Upgrade for the CDF II Experiment*, Nucl. Instrum. Meth. **A461** (2001), 560–562.
- [26] D. Acosta et al. (CDF Collaboration), *A Time-of-Flight Detector in CDF-II*, Nucl. Instrum. Meth. **A518** (2004), 605–608.
- [27] D. Acosta et al. (CDF Collaboration), *The Performance of the CDF Luminosity Monitor*, Nucl. Instrum. Meth. **A494** (2002), 57–62.
- [28] S. Klimenko, J. Konigsberg, and T. Liss, *Averaging of the Inelastic Cross Sections Measured by the CDF and the E811 Experiments*, FERMILAB-FN-0741 (2003).
- [29] E. J. Thomson et al. (CDF Collaboration), *Online Track Processor for the CDF Upgrade*, IEEE Trans. Nucl. Sci. **49** (2002), 1063–1070.
- [30] R. Downing et al. (CDF Collaboration), *Track Extrapolation and Distribution for the CDF-II Trigger System*, Nucl. Instrum. Meth. **A570** (2007), 36–50.
- [31] D. Acosta et al. (CDF Collaboration), *Measurement of $t\bar{t}$ Production Cross Section in $p\bar{p}$ Collisions at $\sqrt{s} = 1.96$ TeV Using Lepton + Jets Events with Secondary Vertex b -Tagging*, Phys. Rev. D. **D71** (2005), 052003.
- [32] A. Holloway et al. (CDF Collaboration), *SecVtx Tagging Scale Factor for 5.3.3 Analysis*, /CDF/DOC/SEC_VTX/CDFR/7333 (2004).

- [33] S. Richter (CDF Collaboration), *Search for the Electroweak Single Top-Quark Production with the CDF II Experiment*, Ph.D. thesis, Universität Karlsruhe, 2007.
- [34] *CDF Data Quality Monitoring Group Webpage*, <http://www-cdf.fnal.gov/internal/dqm/dqm.html>, 2010.
- [35] P. Dong (CDF Collaboration), *Measurement of Electroweak Single Top Quark Production in Proton-Antiproton Collisions at 1.96 TeV*, Ph.D. thesis, University of California at Los Angeles, 2008.
- [36] *CDF Top Group Webpage*, <http://www-cdf.fnal.gov/internal/physics/top/RunIIMC/topmc6/index.shtml>, 2008.
- [37] J. Alwall et al., *Comparative Study of Various Algorithms for the Merging of Parton Showers and Matrix Elements in Hadronic Collisions*, Eur. Phys. J. **C53** (2008), 473–500.
- [38] M. L. Mangano, M. Moretti, F. Piccinini, and M. Treccani, *Matching Matrix Elements and Shower Evolution for Top-Quark Production in Hadronic Collisions*, JHEP **0701** (2007), 013.
- [39] D. Hare, E. Halkiadakis, and S. Rolli, *Electron ID Efficiencies and Scale Factors for Periods 9 to 12*, CDF/ANAL/CDFR/9085 (2007).
- [40] S. Rolli, L. Lovas, and E. James, *High- p_T Muons ID, Reconstruction and*

- Trigger Efficiencies and Scale Factors for Period 9 Through Period 12 Data*, CDF/DOC/ELECTRON/CDFR/9148 (2008).
- [41] B. Cooper and A. Messina (CDF Collaboration), *Estimation of the Background to $W^\pm \rightarrow e^\pm \nu + n$ Jet Events*, /CDF/PHYS/JET/PUBLIC/7760 (2005).
- [42] *CDF Top Group Data Skims Webpage*, <http://www-cdf.fnal.gov/internal/physics/top/gen6skims.shtml>, 2010.
- [43] T. Altonen et al. (CDF Collaboration), *Measurement of Cross Sections for b Jet Production in Events with a Z Boson in $p\bar{p}$ Collisions at $\sqrt{s} = 1.96$ TeV*, Phys. Rev. **D79** (2009), 052008.
- [44] W. Johnson and T. Junk, *SECVTX Mistag Matrices for 4.1 fb^{-1} of Data up to $P22$* , CDF/DOC/SEC_VTX/CDFR/9816 (2009).
- [45] F. James, *Function Minimization and Error Analysis*, 2010.
- [46] R. Brun and F. Rademakers, *ROOT - An Object Oriented Data Analysis Framework*, Nucl. Inst. & Meth. in Phys. Res. **A 389** (1997), 81–86, See also <http://root.cern.ch/>.
- [47] T. Sjostrand, L. Lonnblad, S. Mrenna, and P. Skands, *PYTHIA 6.3 Physics and Manual*, 2003.
- [48] A. Bhatti et al., *Determination of the Jet Energy Scale at the Collider Detector at Fermilab*, Nucl. Instrum. Meth. **A566** (2006), 375–412.

- [49] *CDF JES Group Webpage*, <http://www-cdf.fnal.gov/internal/physics/top/jets/corrections.html>, 2010.
- [50] S. Grinstein and T. Lazovich, *SECVTX Scale Factor for P0-P17 Using the Electron Method*, CDF/DOC/SEC_VTX/CDFR/9478 (2008).
- [51] J. Freeman and S. Grinstein, *SECVTX Mistag Asymmetry Corrections Through 2.2 fb⁻¹*, CDF/ANAL/TOP/CDFR/9277 (2008).
- [52] T. Schwarz, A. Ivanov, and R. Erbacher (CDF Collaboration), *Measurement of the Top Pair Cross Section in the Lepton Plus Jets Decay Channel with 2.7 fb⁻¹*, /CDF/PUB/TOP/PUBLIC/9462 (2008).

Vita

Mark Mathis was born in Syracuse, New York, on August 6, 1981. He graduated West Genesee Senior High School in Camillus, New York, and subsequently enrolled at The American University in Washington, DC, where he received a Bachelor of Science in Physics and Applied Mathematics in 2003. While an undergraduate, he served as an active member of the Society of Physics Students for three years, including two years as president. Additionally, he received the Dr. Jacob Kastner Memorial Award for 2001–2002 for outstanding academic achievement and service.

In 2003, he started his graduate studies in Physics at The Johns Hopkins University and also worked as a teaching assistant for one year. After receiving his Master of Arts degree in Physics in 2006, he moved to Illinois the following year to conduct research at the Collider Detector at Fermilab. His research is now complete, and he expects to receive his Doctor of Philosophy degree in Experimental Particle Physics in 2010.